UNIVERSITY OF CAMBRIDGE

Cavendish Laboratory

OPTOFLUIDICS GROUP

In-situ monitoring of photocatalytic reactions in optofluidic microreactors

---

Takashi S. Lawson

Corpus Christi College

A thesis submitted for the degree of *Doctor of Philosophy*

Dedicated to my parents for their endless belief and support

Abstract

In-situ monitoring of photocatalytic reactions in optofluidic microreactors

Takashi S. Lawson

To advance the state-of-the-art technology in photocatalysis, there is a growing need to develop optically efficient microreactors that allow rapid changes in reaction conditions for catalyst screening. In addition, such microreactors should offer strong light-matter interactions for the *in-situ* spectroscopic detection of chemical species. Motivated by these challenges, this thesis marries the fields of fibre-based optofluidics and photocatalysis to generate scientific insights into how promising new photocatalysts behave.

Novel types of optical fibre were optimised and characterised for liquid phase spectroscopy on sub-microlitre samples; these fibres included kagomé-style and single-ring hollow-core photonic crystal fibres (HC-PCFs). New kinetic insights were obtained into the photoactivity of carbon nanodots (CDs) through systematic screening of a wide range of reaction conditions within kagomé-style HC-PCF microreactors.

Spectrokinetic insights across twenty-nine reaction conditions were studied with a cumulative sample volume of $< 1.5\,\mathrm{mL}$, using viologen species as indicators of electron transfer from CDs. First, amorphous and graphitic CDs were benchmarked against the well-known photocatalyst $[\mathrm{Ru(bpy)_3}]^{2+}$. This study was then extended to replace the viologen indicator with hydrogen-evolving cobaloxime electrocatalysts, to probe catalytic intermediate states.

To give further insight into the electron transfer from carbon nanodots to viologens, transient absorption spectroscopy was then performed to probe changes on timescales of 1 nanosecond to 1 millisecond.

Finally, a new ultralow volume fibre-based fluorescence spectroscopy method was realised. As a proof of principle, the photoredox catalyst 4CzIPN was combined with the fluorescence quenchers tetrabutylammonium azide and cyclohexylamine. The extracted bimolecular Stern-Volmer quenching coefficients were compared with conventional fluorometer-based approaches, which were taken on much larger sample volumes.

This thesis provides a foundation for developing continuous-flow photocatalytic screening systems based on HC-PCFs, which minimise the consumption of precious reagents.

Acknowledgements

The making of this thesis has been a personal journey that has relied on the support of many. Along the way, I have had some unforgettable experiences, and I am grateful to have these memories with me for many years to come.

Firstly, I am extremely thankful to my supervisor, Dr Tijmen Euser, for taking me on as a new PhD student back in 2018 and for his incredible guidance throughout. I have learnt so much under your wing, and the lab atmosphere you have fostered has been inspiring. Thank you for all the time you have given me and everyone in the lab – I really appreciate how responsive and caring you have been to my questions and needs.

I also want to express my deepest gratitude to Prof Erwin Reisner, for his co-supervision and making me feel so welcome in his research group. I have always felt part of the Reisner Lab, which is not an easy feat given how little time I spent in the Chemistry Department. Thank you for your constructive advice, for including me in group activities (Cheddar Gorge 2018 was a personal highlight!) and for being patient with me as a non-chemist.

The work undertaken here has relied on many fellow scientists across the Optofluidics Group, Reisner Lab and Stranks Lab. I am especially thankful to Dr Alex Gentleman, for being so motivating, supportive and positive, particularly when experiments didn't work. You have been my sounding board for just about everything. I will miss those evening lab sessions with Thai Cricketers, and the Egyptian Creams in the Maypole.

Thank you also to Dr Ermanno Miele, Dr Ralf Mouthaan, Jan Heck, Megan Groom, Jonathan Pinnell, Matthew Ellis, Dr Philipp Koehler and Dr Omid Siddiqui from the Optofluidics Group. The daily interactions we had in the lab might not seem much but have been so helpful for troubleshooting problems and keeping me enthused. I am grateful to Ava Lage, Dr Carla Casadevall Serrano, Dr Daniel Antón García and Dr Annika Eisenschmidt, for being so easy to work with in the Reisner Lab, and for the fruitful discussions about carbon dots and cobaloximes. Thanks also to Stuart MacPherson and Dr Paolo Andrich from the Stranks Lab, for teaching me transient absorption spectroscopy, and the additional insights this technique can bring.

I am grateful to Dr Alex Cresswell and Jacob Turner-Dore from the University of Bath, for all their help with 4CzIPN and Stern-Volmer analysis. I hope this initial project fuels further collaborations on screening photocatalysts.

I can't thank Dr Karishma Jain and Kim Cole from the NanoDTC enough. The NanoDTC programme has been fantastic, and I feel so lucky to have been part of c2017. Thanks for the sense of community you have nurtured across the university and all the memories you have helped create - particularly Grenoble 2018 and JapaNano 2019. Before coming to Cambridge, I never thought I would appear with an intelligent toilet on ITV News! Thanks also to Akhila, Bluebell, Greg, Jędrzej, Josh, Kevin, Roger, Ryan, Theo and Tom for being such a great cohort to share the PhD experience with.

To my closest friends, Sarah Rafferty, Luke Pattison, Katie Barker, Rosie Bell and Harriet Gilbert Savage: you have seen me through some of the toughest years of my life. I owe you much more than what can be written down. Thank you for being a source of strength and fun - I wouldn't want to live through a pandemic with anyone else.

Finally, to Mum, Dad and Alex, thanks for believing in me. I would not have completed this PhD without your unconditional support. Thank you for all that you've done for me and all that you're still doing.

Monday 1st November, 2021
Cambridge

List of Publications

This thesis contains results published in the following peer-reviewed publications:

Alexander S. Gentleman[†], <u>Takashi Lawson</u>[†], Molly Davis, Jacob Turner-Dore, Michael Frosz, Alexander J. Cresswell, Erwin Reisner and Tijmen G. Euser. 'Stern-Volmer analysis of fluorescence quenching of photocatalysts within hollow-core photonic crystal fibre microreactors'. **(in preparation)**.

<u>Takashi Lawson</u>, Alexander S. Gentleman, Ava Lage, Carla Casadevall, Michael H. Frosz, Erwin Reisner, and Tijmen G. Euser. 'Low volume reaction monitoring of carbon nanodot light absorbers in optofluidic microreactors'. **(in preparation)**.

<u>Takashi Lawson</u>,[†] Alexander S. Gentleman,[†] Annika Eisenschmidt, Daniel Antón-García, Michael H. Frosz, Erwin Reisner, and Tijmen G. Euser. 'In-operando detection of cobaloxime intermediate states during photocatalytic water-splitting'. **(in preparation)**.

[†] authors contributed equally

Contributions were also made to the following publications but were not included in this thesis:

Philipp Koehler, <u>Takashi Lawson</u>, Julian Neises, Janina Willkomm, Benjamin C. M. Martindale, Georgina A. M. Hutton, Daniel Antón-García, Ava Lage, Alexander S. Gentleman, Michael H. Frosz, Philip St.J. Russell, Erwin Reisner, and Tijmen G. Euser. 'Optofluidic photonic crystal fiber microreactors for in-situ studies of carbon nanodot-driven photoreduction'. Anal. Chem. 2021, 93, 2, 895–901. `https://doi.org/10.1021/acs.analchem.0c03546`.

Virgil Andrei, Geani M. Ucoski, Chanon Pornrungroj, Chawit Uswachoke, Qian Wang, Demetra S. Achilleos, Hatice Kasap, Robert A. Jagt, Haijiao Lu, <u>Takashi Lawson</u>, Andreas Wagner, Sebastian D. Pike, Dominic S. Wright, Robert L. Z. Hoye, Judith L. MacManus-Driscoll, Hannah J. Joyce, Richard H. Friend, and Erwin Reisner. 'Lightweight perovskite-$BiVO_4$ PEC devices for scalable unassisted solar fuel production'. Nature 2021 **(in revision)**.

Contents

List of Abbreviations

4CzIPN	2,4,5,6-tetra(9H-carbazol-9-yl)isophthalonitrile
AA	Ascorbic Acid
aCD	Amorphous Carbon Nanodot
AgNPs	Silver Nanoparticles
ARROW	Anti-Resonant Reflection Optical Waveguide
BS	Beam Splitter
Bu_4NN_3	Tetrabutylammonium Azide
BV	Benzyl Viologen
CD	Carbon Nanodot
CHA	Cyclohexylamine
$Co(dmgH)(dmgH_2)$	Cobalt Tetradentate Dimethylglyoximato Dimethylglyoxime
CoP	Cobaloxime with phosphonic acid moiety
CV	Cyclic Voltammetry
DFT	Density Functional Theory
DHA	Deyhydroascorbic Acid
DSP	Dye-Sensitised Photocatalyst
EDTA	Ethylenediaminetetraacetic Acid
EH	Hybrid Modes
EnT	Energy Transfer
ETFE	Ethylene tetrafluoroethylene
EV	Ethyl Viologen
FWHM	Full-Width Half-Maximum
GC	Gas Chromatography
gCD	Graphitic Carbon Nanodot
HAT	Hydrogen Atom Transfer
HC-NCF	Hollow-Core Negative Curvature Fibre
HC-PBGF	Hollow-Core Photonic Band Gap Fibre

HC-PCF	Hollow-Core Photonic Crystal Fibre
HEC	Hydrogen Evolution Catalyst
HOMO	Highest Occupied Molecular Orbital
HOMs	Higher Order Modes
ITO	Indium Tin Oxide
LED	Light Emitting Diode
LG	Laguerre-Gaussian
LIC	Low Index Coating
LP	Linearly Polarised
LSPR	Localised Surface Plasmon Resonance
LUMO	Lowest Unoccupied Molecular Orbital
LVRPA	Local Volumetric Rate of Photon Absorption
MFD	Mode Field Diameter
MLCT	Metal-to-Ligand Charge Transfer
MMF	Multimode Fibre
MS	Marcatili-Schmeltzer
MV	Methyl Viologen
NA	Numerical Aperture
NADH	Nicotinamide Adenine Dinucleotide Hydride
ND	Neutral Density
NgCD	Nitrogen-Doped Graphitic Carbon Nanodot
NHE	Normal Hydrogen Electrode
PC	Photocatalyst
PDMS	Polydimethylsiloxane
PEEK	Polyether ether ketone
PL	Photoluminescence
PS	Photosensitiser
Re	Reynolds Number
RHE	Reversible Hydrogen Electrode
ROS	Reactive Oxygen Species
SC	Supercontinuum
SED	Sacrificial Electron Donor
SEM	Scanning Electron Microscope
SET	Single Electron Transfer

SMF	Single Mode Fibre
TA	Transient Absorption
TC-SPC	Time Correlated Single-Photon Counting
TCEP	Tris(carboxyethyl)phosphine
TE	Circular Electric Modes
TEA	Triethylamine
TEOA	Triethanolamine
TIR	Total Internal Reflection
TM	Circular Magnetic Modes
TMEDA	Tetramethylethylenediamine
TOF	Turnover Frequency
TON	Turnover Number
TPE	Two-Photon Excitation
UV	Ultraviolet

List of Figures

List of Tables

Chapter 1

Introduction

1.1 Motivation

The development of low-carbon energy sources is essential to achieve the UK government target of net zero emissions by 2050. This development is especially significant in decarbonising hard-to-abate emission sources, for example, long-haul transport, steel production, chemicals manufacture and high-temperature industrial processing. It is worth noting that 80% of energy demand by end-users is for carbon-containing fuels, not electricity.[1] While electrification using clean sources is an enticing solution, these energy sources are generally intermittent and reliant on grid-balancing systems.[2] Solar fuels are viable energy carriers capable of interseasonal storage and transport, which store energy in molecular bonds by employing sunlight to drive endothermic chemical reactions. Hydrogen is an example of a solar fuel, as it can be derived by splitting water through photoredox catalysis with oxygen as a co-product - a process akin to photosynthesis. More complex chemical feedstocks can be produced by tuning the photocatalyst for the desired chemistry (see Figure 1.1). It is striking to note that the majority of hydrogen produced today is from fossil fuels. Less than 0.7% is produced from renewables ('green hydrogen'), and from fossil fuel plants equipped with carbon capture, utilisation and storage (CCUS, 'blue hydrogen').[1]

The development of solar fuels is a major scientific and technological challenge, and a route that remains largely untapped despite its potential significance. Although photovoltaic-electrolysis systems currently report solar-to-hydrogen efficiencies of over 30%,[3] direct photocatalytic water-splitting at similar efficiencies is evasive. Photocatalytic water splitting currently has efficiencies of around 1%.[4] Barriers to development include the slow optimisation of reaction parameters, and the lack of mechanistic understanding for the guided design of photocatalysts with greater turnover. Reaction analysis is overwhelmingly through *ex-situ* methods such as gas chromatography or mass spectrometry, without the direct study of the active catalyst species. These methods generally rely on extracting a sample at regular time intervals ($> 5\,\mathrm{min}$) from a reactor, and measuring samples off-line. *Ex-situ* methods may not necessarily reflect the system under real catalytic conditions, and therefore lead to poor reaction optimisation decisions. *In-operando* optical spectroscopy

provides a solution, enabling the analysis of steady-state reaction conditions and to study catalyst speciation. Such methods generally employ microreactors that enable reactions to be monitored within sub-μL volumes. However, typical microreactors are surface-limited or rely on flow cells with short light-matter interaction lengths. While some progress towards mechanistic understanding has been achieved through these techniques, their inherently limited path lengths significantly restrict their sensitivity, and hence application.

What could the production and use of solar fuels look like?

Sunlight is used to split water into hydrogen and oxygen

Sunlight is used to produce carbon-based fuels from water and carbon dioxide. A source of carbon dioxide could be a coal-burning power station fitted with carbon capture technology

Hydrogen is used as a transport fuel

Hydrogen and simple carbon-based fuels are used as raw materials (feedstocks) by many industries

New technologies

Solar fuels

H   Hydrogen (H$_2$)

C   Carbon-based fuels such as methane (CH$_4$), carbon monoxide (CO) and methanol (CH$_3$OH)

Existing technologies

• Fertiliser
• Plastics
• Pharmaceuticals
• Synthetic fuels for transport

www.rsc.org/solar-fuels

Figure 1.1: Solar fuels could displace fossil fuels and reduce CO_2 emissions from transportation and industrial processes. Reproduced with permission from the Royal Society of Chemistry. https://edu.rsc.org/.

To advance the state-of-the-art technology in photocatalysis, there is a growing need to develop optofluidic microreactors, allowing rapid changes in reaction conditions for catalyst screening, and strong light-matter interactions for the detection of chemical species present in the nanomolar regime. Motivated by these challenges, this project aims to marry the fields of optofluidics and solar fuel synthesis to help elucidate reaction mechanisms. With an improved understanding of how these reactions proceed, photocatalysts can be optimized for quantum efficiency and turnover, making such technology economically viable and practically useful.

1.2 Outline

A synopsis of objectives and key results achieved are outlined here, together with short chapter summaries describing the layout of this thesis.

1.2.1 Objectives

This project aims to exploit fibre-based optofluidic microreactors for ultra-low volume reaction kinetics analysis, and to deliver mechanistic insight into elusive photocatalytic systems. Utilising the wave-guiding properties of hollow-core photonic crystal fibres (HC-PCFs), an assortment of optical techniques are employed to study photochemical reactions *in-operando*. These optical techniques can be used to categorise this research into four main areas of investigation:

1. Electronic absorption spectroscopy to screen light absorbers for photocatalysis;

2. Electronic absorption spectroscopy to identify catalytic intermediate species;

3. Fluorescence quenching to determine the reactivity of the excited state of photocatalysts and

4. Transient absorption spectroscopy to probe electron transfers from light absorbers.

Carbon nanodots are explored in detail as a novel light absorber that offers a unique combination of scalability, biocompatibility, water solubility and stable optical properties. This thesis provides a platform to screen state-of-the-art photocatalysts for reaction development, in addition to laying the foundations for new fibre-based optical techniques to comprehend the underlying mechanisms behind photocatalysis.

1.2.2 Key results

The key results and new science shown in this thesis include:

- A thorough study into the photoactivity of carbon dots with various electron acceptors and sacrificial electron donors commonly used in solar fuel synthesis;

- Insights into the electron-transfer processes at the carbon dot - catalyst interface through time-resolved spectroscopy;

- The detection of cobaloxime catalyst intermediate states *in-operando*;

- Fluorescence spectroscopy on Coumarin dyes and 4CzIPN and

- Stern-Volmer analysis on 4CzIPN with microlitre volumes.

Coumarin dyes are first explored due to their well-characterised fluorescence, before moving onto 4CzIPN, an emerging photoredox catalyst for organic transformations. The new methodologies and tools created include:

- Two complete optical set-ups built to facilitate fibre-based experiments, for both electronic absorption and fluorescence studies;

- A new approach for mounting fibres, giving improved temporal stability without significant drift or undue stress applied to fibre walls;

- A thorough characterisation of liquid-filled kagomé HC-PCFs and hollow-core negative curvature fibres (HC-NCFs) and

- Python code to process, analyse and present large sets of time-resolved spectroscopic data, which is available as a Python package online.

1.2.3 Layout

This thesis is structured into a number of chapters.

Chapter 2 reviews the fundamentals of optical fibres, and developments that have improved the applicability of fibre-based optofluidics to reaction screening and monitoring, particularly in the context of solar fuel production. It considers the key electron-transfer processes enabling photocatalysis in hybrid colloidal systems, specifically carbon nanodot photosensitisers with cobaloxime proton reduction catalysts.

Chapter 3 introduces detail on the transmission characteristics of the HC-PCFs utilised. In addition, a description of the optical set-ups designed and built is provided, along with the fluidic considerations of sample delivery to the HC-PCFs.

Chapter 4 details the use of absorption spectroscopy to study carbon nanodot driven photoreduction in fibre-based microreactors. A systematic screening investigation has been carried out with various electron acceptors and donors, coupled with concentration sweeps of constituent components.

Chapter 5 describes the use of absorption spectroscopy in fibre-based microreactors to identify catalytic intermediate states formed during photocatalysis. A study with various cobaloxime proton reduction catalysts, combined with a Ruthenium-based photosensitiser, was performed.

Chapter 6 presents the use of fluorescence spectroscopy in fibre-based microreactors for ultralow volume Stern-Volmer analysis. A quenching study with Coumarin dyes and 4CzIPN was carried out and compared with conventional fluorometer measurements.

Chapter 7 reports the study of carbon nanodots by transient absorption spectroscopy to probe the electron transfer timescale between carbon nanodots and an electron-accepting viologen species. Comparisons in carbon nanodot behaviour between steady-state absorption and transient absorption are discussed.

Chapter 8 provides concluding remarks and outlooks on the use of fibre-based microreactors for monitoring photocatalytic reactions. It identifies further areas for potential investigation.

Chapter 2

Optofluidics for photocatalysis: a literature review

This chapter reviews the fundamentals of photocatalysis, and the challenges involved with producing green hydrogen more efficiently. The key electron-transfer processes enabling catalysis in hybrid colloidal systems with carbon nanodot photosensitisers is explored. The focus of this review then shifts towards how optofluidic techniques can shed new insight into the mechanisms behind photocatalysis, with a particular focus on hollow-core photonic crystal fibre microreactors. The advantages of such an approach are discussed in detail with a number of examples in the literature.

2.1 Photocatalysis

Photochemistry is a vast research area, including processes such as electron and energy transfers, ligand substitution and isomerisation.[5] The general aim of photochemistry is to use UV-visible light to drive an 'up-hill' chemical reaction,[6] and overcome an activation energy barrier. Photochemistry is of paramount importance to the terrestrial energy cycle, specifically photosynthesis,[7] where plants can convert raw materials (CO_2 and H_2O) into carbohydrates.

However, limited spectral absorption of natural photosystems and internal losses such as metabolic processes reduce the overall solar conversion efficiency of natural photosynthesis to $< 3\%$.[8] Substituting natural photosystems with artificial photosensitisers and catalysts can lead to systems with higher solar conversion efficiencies than natural photosynthesis, and generate industrially useful products.

Comparisons between thermal reactions and photochemical reactions, with and without a catalyst, are shown in Figure 2.1. The case shown is for an exothermic reaction with photocatalysis via energy transfer (EnT), however endothermic reactions with photocatalysis via electron transfers can also be driven by solar radiation, which will become important when water-splitting is considered.
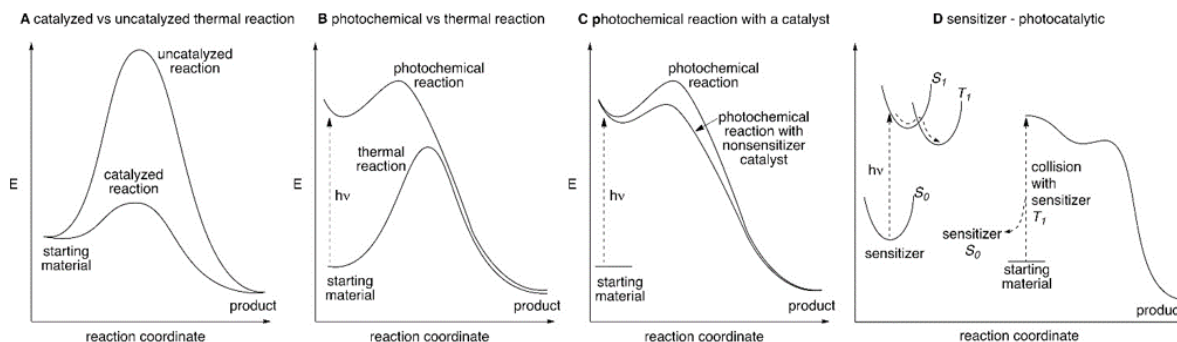
Figure 2.1: A comparison of photochemical and thermal reactions, with and without a catalyst. A photosensitiser can transfer energy to a catalyst through a collision, typically with a photoexcited sensitizer in a triplet state (depicted in D), or through electron transfer. Reprinted with permission. [7] ©2016 American Chemical Society.

Photoredox catalysis is mediated by electron transfers. In the general case, a photoredox catalysis cycle is formed of three key steps. First, the absorption of a photon to promote a catalyst in its ground state to an excited state. Second, an excited photocatalyst and substrate must diffuse towards one another to form an encounter complex, such that an electron transfer can take place. This process competes with excited-state relaxation. The photocatalyst and product must then separate to prevent an unwanted back-transfer of the electron. Third, the catalyst needs to be re-generated through another photocatalyst-substrate encounter, for the cycle to be closed. The cyclic nature of this process identifies the first trait of a photoredox catalyst: it must display reversible electrochemical behaviour. Other desirable properties include wide-range absorption, stability, long excited-state lifetimes and strong redox power. [9,10,11] Specifically, the excited-state lifetime must be long enough for diffusion to the substrate to occur - a practical lower limit is $\sim 1\,\text{ns}$. [5]

One application of photoredox catalysis is the sustainable production of solar fuels via water-splitting. [12,13] Hydrogen is particularly attractive due to its high energy density and clean products on combustion. [14] Hydrogen contains $120.1\,\text{MJ}\,\text{kg}^{-1}$, 3 times that of gasoline. [1] Moreover, there is great global demand for pure hydrogen as a feedstock for the Haber-Bosch process to produce ammonia, and for oil refining. These two activities require 70 million tonnes of hydrogen a year. Additionally, there is demand for hydrogen in gas mixtures, for example the generation of syngas for the Fischer–Tropsch process to produce liquid hydrocarbon fuels, and for steel production. These two further activities bring total global hydrogen demand to 115 million tonnes a year. [1]

Scientists have known how to split water electrochemically for more than 200 years, however, the bottleneck in electrochemical methods has been the cost of implementation, particularly with renewable energy sources, meaning that most of the hydrogen produced today comes from the steam reforming of natural gas. [1,15]

Although water-splitting will be the focus here, alternative reactions can be driven by captured solar energy. Examples include the reduction of CO_2 to feedstocks such as formic

6

acid[16,17] or methanol,[6,11] nitrogen fixation to ammonia,[18] or the co-enzyme regeneration of NADH (nicotinamide adenine dinucleotide hydride), which is a key process for carbohydrate production in plants.[11]

2.1.1   Water-splitting systems

The overarching aim in solar fuel photocatalysis is to capture and store solar energy in chemical bonds and to selectively produce useful molecules.[19] In all systems this initially relies on the excitation of an electron across a semiconductor band gap or molecular HOMO/LUMO gap. For a water-splitting system, this excited electron must then be transferred to a catalytic surface to reduce protons to hydrogen. The remaining hole must be transferred to a separate catalytic site to oxidise water to oxygen. This is a significant step in natural photosynthesis, and artificial systems are often inspired by the protein complex photosystem two (PSII).[20]

The full reaction can be written $2\,H_2O \longrightarrow 2\,H_2 + O_2$ ($\Delta G^\circ = +\,237\,\text{kJ}\,\text{mol}^{-1}$).[21] This multielectron redox process can be summarised as two electron half-equations. Standard reduction potentials referenced to the reversible hydrogen electrode (RHE) are shown for comparison.[19]

$$2\,H^+ + 2\,e^- \longrightarrow H_2 \qquad E^\circ = 0\,\text{V}\ \textit{vs.}\ \text{RHE}$$
$$4\,H^+ + 4\,e^- + O_2 \longrightarrow 2\,H_2O \qquad E^\circ = +\,1.23\,\text{V}\ \textit{vs.}\ \text{RHE}$$
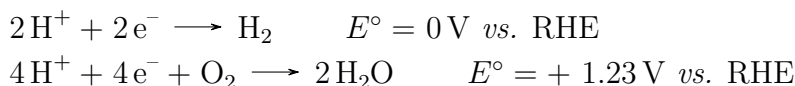
In a closed redox system, electron transfer is achieved through a redox mediator, such as iodate,[22] or methyl viologen.[23,24] The highest values for quantum efficiency under visible light irradiation in a closed redox system were reported by Maeda *et al.* using Pt-loaded ZrO_2 / TaON (hydrogen evolution catalyst) and Pt-loaded WO_3 (oxygen evolution catalyst), with an IO_3^-/I^- redox mediator. They report a quantum efficiency of 6.3% under irradiation by 420.5 nm monochromatic light.[25] However, scale-up is restricted by the expense of certain materials (i.e. platinum, tantalum), limited use of the full visible spectrum and poor utilisation in terms of catalytically active atomic sites.

Breaking down the closed redox system into two separate half-reactions enables the detailed study of photocatalysts, so that individual components can be optimised.[20] For the proton reduction half-reaction, hole scavengers or sacrificial electron donors (SEDs) are used for this purpose.[19,21,26] SEDs also play a secondary role in buffering a reaction solution at a desired pH value.[19] Typical SEDs for solar fuel chemistry include triethylamine (TEA), triethanolamine (TEOA), ethylenediaminetetraacetic acid (EDTA) and ascorbic acid (AA).[20] These SEDs are discussed in detail in Section 2.1.4.

So we have a system of three components, namely the photosensitiser (PS), the hydrogen evolution catalyst (HEC) and the sacrificial electron donor (SED). Two reaction schemes are possible, and can be identified by the component which interacts with the excited state of the photosensitiser (PS*):

(1) $PS^* + SED \longrightarrow PS^- + SED^+$

(2) $PS^* + HEC \longrightarrow PS^+ + HEC^-$
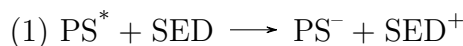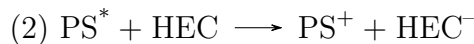
In Case 1, PS^* is reduced by the SED, followed by regeneration of PS by the HEC. In Case 2, PS^* is oxidised by the HEC, followed by regeneration of PS by the SED. Whether PS^* participates in a reductive quench or oxidative quench depends on the system and reaction conditions in question.[20]

Proton-coupled processes, such as hydrogen evolution, are pH sensitive. Reynal *et al.* suggest that the optimal pH of a hydrogen evolution system is a compromise between having a reservoir of hydrogen ions to protonate the catalyst, and the decline in electron-donating ability of sacrificial electron donors as they themselves are protonated, leading to an anodic shift in reduction potential.[27] In addition, the pH can also affect the surface chemistry of the photosensitiser, including the position of the conduction band, the affinity of the anchoring groups for the semiconductor and the activity of the catalyst.[19]

Photocatalytic systems may be homogeneous and comprise of fully-soluble molecular components. For example, soluble ruthenium tris-2,2'-bipyridine complexes ($[Ru(bpy)_3]^{2+}$; bpy = bipyridine), have been employed in photoredox catalysis in aqueous solutions.[28,29,30] Alternatively, the photosensitiser may be heterogeneous and contain catalysts in suspension and/or semiconductor colloids. A hybrid system is a system that contains both homogeneous and heterogeneous components.

Hybrid colloidal systems comprising of a photosensitiser in conjunction with a hydrogen evolution catalyst (HEC) have been proposed for H_2 generation from water.[19,31] A schematic for this system is depicted in Figure 2.2a, showing the electron transfers required to drive the water-splitting reaction. Electron-hole pairs generated in the semiconductor provide two electrons to the catalyst to drive proton reduction. The remaining two holes are filled by a SED.

Photosensitiser   The photosensitiser in hybrid colloidal systems is usually a semiconductor; a few examples are depicted in Figure 2.2b. For water splitting, the position of the bottom edge of the conduction band must be more negative than $0\,V$ *vs.* RHE, while the top edge of the valence band must be more positive than $1.23\,V$ *vs.* RHE.[19,21] Although this suggests that $1.23\,eV$ is the minimum energy requirement for water-splitting, this requirement is generally considered to be $> 2\,eV$ due to parasitic losses. These losses generally relate to electron-hole recombination, which is promoted by slow surface kinetics, short charge carrier diffusion lengths and rapid charge trapping.[32]

Narrow band gap semiconductors which absorb in the visible wavebands, such as CdS, often suffer from photo-corrosion and have poor stabilities in water ($CdS + 2\,h^+ \longrightarrow Cd^{2+} + S$).[21] Wide band gap semiconductors are stable in aqueous media, but absorption is shifted towards UV wavebands. One approach to maximise the use of the visible wavebands is to use molecular dyes with wide band gap semiconductors, termed dye-sensitised photocatalysis (DSP). Together, the molecular dye and colloidal semiconductor can absorb UV and visible wavelengths, with the colloidal semiconductor also functioning as a

linker from the molecular dye to the catalyst. A common molecular dye utilised for sensitising nanoparticles in hybrid colloidal systems is phosphonated $[Ru(bpy)_3]^{2+}$,[33,19] often called RuP. The phosphate group anchors the molecular dye to the nanoparticle surface. Alternative anchors are discussed in detail in a review by Dalle et al..[34]
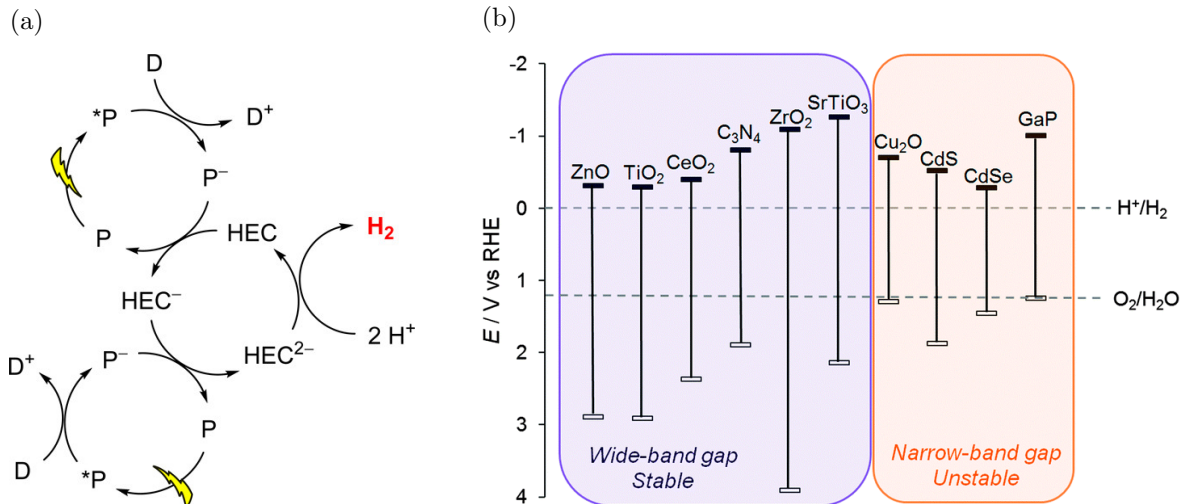
Figure 2.2: (a) Components of a hydrogen evolution photosystem. D = sacrificial electron donor, P = photosensitiser/light-absorber, HEC = hydrogen evolution catalyst. Reprinted with permission.[31] ©2017 American Chemical Society. (b) Semiconductor band positions for a selection of typical photosensitisers, with the electrochemical standard potentials for water oxidation and proton reduction shown for comparison. Reprinted with permission from the Royal Society of Chemistry.[19] Licensed under CC BY 3.0.

Degussa P25 TiO_2, composed of anatase/rutile mixed-phase microparticles, is generally considered the archetypal semiconductor and benchmark for new photocatalysts.[35] P25 TiO_2 limits recombination events by forming heterojunctions at the anatase/rutile phase boundary, enabling efficient separation of electron-hole pairs.[36] Agglomeration of TiO_2 nanoparticles is also though to have a beneficial effect on photoactivity by forming a conductive network, which increases the spatial separation between the photoexcited electron in the conduction band, and its corresponding hole in the valence band.[37]

The advantages of P25 TiO_2 are its low cost, high photostability and aligned band potentials for both water oxidation and proton reduction.[38] However, TiO_2 has poor solubility in water, which limits its use to heterogeneous systems,[39] and poor absorption in the visible region of the solar spectrum, due to its large bandgap of $\approx 3.2\,\text{eV}$.[32,33] Alternative metal oxides employed in photocatalysis include haematite (α-Fe_2O_3), WO_3, $BiVO_4$ and $SrTiO_3$.[40] Carbon nanodots are an example of an emerging, competitive photosensitiser and are discussed in Section 2.1.2.

With the vast majority of photocatalysts, electrons can also interact with molecular oxygen, forming superoxide ($O_2 + e^- \longrightarrow O_2^{\bullet-}$) and peroxide ($O_2^{\bullet-} + e^- \longrightarrow O_2^{2-}$) species, together termed reactive oxygen species (ROS). These processes are generally competitive with the desired reaction, and purging reaction mixtures of oxygen prior to use is commonplace.

Catalyst   Platinum is a benchmark hydrogen evolution catalyst, operating close to the thermodynamic minimum for proton reduction.[41] However, Pt is a rare and costly precious metal,[42] and therefore alternative catalysts containing more abundant and cheaper elements are sought. Molecular catalysts based on 3d transition metals such as nickel, iron and cobalt have been utilised to achieve this purpose.[9,26,27,43,44]

Importantly, these molecular catalysts must exist in at least three oxidation states to enable the proton reduction process: the initial oxidation state of the catalyst plus the temporary storage of two electrons. Moreover, the catalyst needs to be stable enough in its reduced forms to be regenerated over the course of multiple turnovers.[5]

Table 2.1 lists potential candidates for CD-driven photocatalysis. NiP is one of the most developed Ni-based hydrogen evolution catalysts. It is a DuBois-type catalyst that consists of bis(diphosphine) ligation.[34] [NiFeSe]-H_2ase is a redox enzyme that can be coupled with tertiary-amine terminated CDs (CD-NHMe$_2$) for enzymatic hydrogen evolution.

The proximity of the light harvester to the catalyst is important to improve the rate of electron transfer. It has been shown that pre-assembly of the photosensitiser and catalyst can lead to improvements in solar conversion efficiencies.[33]

Catalyst performance is generally defined through two measures: turnover number (TON) and turnover frequency (TOF). The TON is a stability measure, and for hydrogen-evolving catalysts gives the total number of moles of hydrogen produced per mole of catalyst active site before the catalyst becomes inactive. The TOF is an activity measure, and for hydrogen-evolving catalysts gives the mean number of moles of hydrogen produced per mole of catalyst active site per hour. An ideal photocatalytic system permits a catalyst to operate at its optimal TOF, with no compromise to its stability.[39]

Photosensitiser	Catalyst	SED	TOF / h^{-1}	TON
aCD	NiP	EDTA	41	64
aCD	NiP	TCEP/AA	53	1094
gCD	NiP	EDTA	12	45
NgCD	NiP	EDTA	143	277
aCD-NHMe$_2^+$	[NiFeSe]-H_2ase	EDTA	5,100	44,000

Table 2.1: Table showing the turnover frequency (TOF) and turnover number (TON) for carbon nanodot-based hydrogen-evolving photosystems. aCD = amorphous carbon dots, gCD = graphitic carbon dots, NgCD = nitrogen-doped graphitic carbon dots, SED = sacrificial electron donor. Adapted with permission from the Royal Society of Chemistry.[45]

2.1.2   Carbon nanodots

Carbon nanodots (CDs) were first discovered whilst purifying carbon nanotubes synthesised by arc-discharge methods in 2004.[46,47] They are quasi-spherical nanosized particles, generally less than 10 nm in size,[10,48] and can exist in two allotropic forms: crystalline with sp^2 character (graphite) or amorphous.[45] Crystalline nanodiamonds possessing sp^3 char-

acter are generally not considered under the definition of carbon nanodots.[49] Graphitic carbon nanodots display much higher absorption than amorphous carbon nanodots, due to the greater number of $\pi - \pi^*$ transitions present.[45] Their absorption can tail up to 650 nm, which resembles the absorption of graphene and graphene oxide.[50] The structure of carbon nanodots remains a matter of debate. Luo *et al.* suggest that the main structural motif of the CDs is formed of furan molecules, linked by direct C-C bonds or through a methine or methylene bridge.[50] Margraf *et al.* used semi-empirical molecular orbital theory to show that amorphous carbon dots contain hexagonal carbon networks, and are partially sp^2 hybridised. They found that the geometry of amorphous carbon dots was the most significant factor affecting electronic structure, with atomic hybridisation and heteroatom content having a much lesser effect.[51]

Carbon nanodots are surface-passivated with oxygen-containing functional groups such as carboxyls and alcohols, enabling exceptional water solubility and the ability to tune their surface functionalities.[49,52,53] They display broad photoluminescence (PL) emission across the UV-visible bands, in contrast to nanodiamonds with narrow PL emission from point defects within the bulk structure.[49] Doping of carbon nanodots with Cl[54] and N[55,56] has been reported to enhance the separation of photoexcited charge carriers, and therefore prolong the lifetime of photogenerated charges.

At the time of writing, the highest reported PL quantum efficiency for carbon nandots was 99.3% (excitation at $\lambda = 320$ nm), for nitrogen-doped hydroxyl-functionalised CDs synthesised from citric acid and tris(hydroxylmethyl)aminomethane.[57] Meiling *et al.* report similar PL quantum efficiencies of between $80\% - 90\%$ (excitation at $\lambda = 340$ nm).[56]

Radiative $n - \pi^*$ transitions involving C=O, COOH and C-O-C moieties are thought to contribute to PL emission, given observed dependencies on surface functionalisation and pH.[50,58] CDs display a dependence on excitation wavelength[59,60] with red-shift apparent at longer excitation wavelengths. These dependencies are not fully understood, but have been suggested to be a consequence of radiative recombination primarily at surface states, rather than in the bulk sp^2 carbon network, and broad particle size distributions.[45,56]

Luo *et al.* report that the PL emission originates from very similar emissive states involving oxygen functional groups (i.e., C=O and COOH). They show that absorption below 300 nm does not populate emissive states, with PL originating from excited states at low density, or with small absorption coefficients, given no strong absorption peaks can be resolved above 300 nm. Absorption near 300 nm is subsequently followed by non-radiative recombination, specifically phonon-assisted relaxation to the ground state through the sp^2 carbon network.[50]

Margraf *et al.* suggest the PL excitation-dependence is due to the diversity of the underlying CD structures. Through semi-empirical molecular orbital theory, they modelled the electronic density of states of a 2 nm amorphous carbon dot, and showed that while states in the continuous band regions were relatively delocalised, mid-gap states were localized to the surface of the dots. Moreover, the inhomogeneity of the CD structure was found

to localise charge, and in consequence result in the localisation of reactivity to specific surface sites.[51] It must be noted inhomogeneity is also associated with graphitic carbon nanodots, with Luo *et al.* confirming the inhomogeneity in graphite (001) plane spacings within the same carbon nanodot sample via high resolution scanning transmission electron microscopy.[50]

CD photoluminescence can be quenched efficiently by electron acceptor molecules in solution, which is promising for rapid electron transfer to a catalytic site. Ren *et al.* suggest that electron transfer from CDs occurs via surface carboxyl groups. Further favourable characteristics include resistance to photobleaching and low toxicity compared to current metal-based systems such as cadmium-based quantum dots and lead-based perovskites.[56] CD synthesis is cheap, simple and scalable, with the potential for feedstocks to be derived from sustainable sources such as lignocellulosic biomass waste.[49,61] Synthesis can be achieved through a number of routes including thermolysis of citric acid,[62] arc-discharge,[46] laser ablation,[63] electrochemical,[59] combustion[58] and microwave pyrolysis methods.[64]

Martindale *et al.* utilised methyl viologen (MV^{2+}) as a probe to study photo-induced electron transfer from CDs, where $MV^{2+} + e^- \longrightarrow MV^{+\bullet}$. The reduced methyl viologen radical ($MV^{+\bullet}$) absorbs strongly at 600 nm, enabling its evolution to be tracked over time via UV-Vis absorption spectroscopy.[62,65,66] CD-Viologen reactions thus form an excellent test system to understand photoredox mechanisms independently from catalysis requirements. Additionally, viologen redox couples have been implemented as electron relays in some hydrogen-evolving systems.[23,24] Strauss *et al.* performed zeta-potential measurements of CDs in the presence and absence of MV^{2+}. They found that CDs feature a negatively charged surface, whose zeta-potential magnitude decreases on addition of MV^{2+}. They therefore hypothesize that the positively charged MV^{2+} and negatively charged CDs form a pre-organised electrostatically bound complex, which results in stronger luminescence quenching over neutral substrates such as TEOA.[67]

2.1.3 Cobaloximes

Conventional hydrogen evolution catalysts, such as platinum and hydrogenases, have been shown to operate at low overpotentials, however these catalysts suffer from limitations related to commercial scale-up. Hydrogenases are enzymes that can be divided into three distinct classes: [NiFe], [FeFe] and [Fe].[68] All hydrogenase classes are difficult to purify and are considered to be fragile. Moreover, the low abundance of platinum leads to its considerable expense. On the other hand, molecular catalysts have the potential to be produced cheaply, are tunable by modifying ligands, metal centres and anchoring groups, and can possess high atom-efficiencies with full utilisation of metal centres for catalysis.[69,19,70]

Shaw *et al.* suggest that not only is the primary coordination sphere surrounding the metal centre in a molecular catalyst important, but the outer coordination sphere which interacts with the reaction substrate heavily influences the turn-over frequency of molecular

catalysts.[71] Surface-functionalities of molecular catalysts can be designed and tuned to purpose, offering a significant advantage over conventional heterogeneous catalysts, where selectivity is generally poor. This attribute is especially important for complex reactions such as CO_2 reduction and N_2 fixation, where a variety of products are possible.[72]

Established and popular molecular catalysts are usually based on rare and/or toxic ruthenium(II) and iridium (III) metal centres. This imposes a barrier to adoption of this technology in industry. There has been a recent emergence of molecular catalysts based on earth-abundant metal centres such as nickel, iron, cobalt and manganese.[69,73,74]

Cobaloximes are cobalt-based metal complexes. Those containing dimethylglyoximato (dmgH) ligands (see Figure 2.3a) have been shown to be effective proton reduction catalysts in aqueous solutions, remaining active under aerobic O_2 conditions.[74,75,76] The cobaloxime $[Co(dmgH)_2(H_2O)_2]$ has a small proton reduction wave at an onset potential of -0.65 V $vs.$ NHE, corresponding to the reduction of Co^{II} to Co^{I}. Wakerley et $al.$ showed that the addition of pyridine to a solution of $[Co(dmgH)_2(H_2O)_2]$ formed $[Co(dmgH)_2(py)]$, which possessed a catalytic wave at a lower onset potential of -0.54 V $vs.$ NHE. A reversible Co^{III}/Co^{II} couple was also identified at -0.03 V $vs.$ NHE. Moreover, they showed that H_2 evolution activity of cobaloximes decreased by less than 5% between aerobic and anaerobic conditions.[74]

(a)

(b)
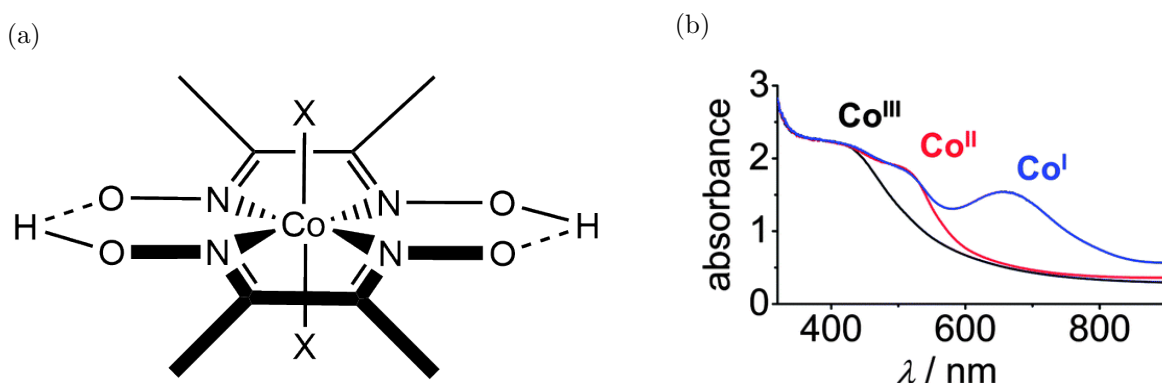
Figure 2.3: (a) General cobaloxime molecular structure, with the axial ligands X depicting a halide, pyridine or attached solvent molecule. (b) Absorption spectra obtained by spectroelectrochemistry for a phosphonated cobaloxime on a mesoporous ITO substrate, for different Co oxidation states in DMF. Adapted with permission from the Royal Society of Chemistry.[19] Licensed under CC BY 3.0.

Willkomm et $al.$ report enhanced performance from the 'CoP' class of cobaloximes containing a phosphonic acid moiety, due to improved immobilisation to metal oxides.[77] This system was first reported by Lakadamyali et $al.$ in 2011.[78] The utilisation of their CoP^1 catalyst in a hydrogen-evolving dye-sensitised system consisting of $[Ru^{II}(2,2\text{-bipyridine})_2(2,2\text{-bipyridine-4,4-bisphosphonic acid})]Br_2$ with TiO_2 nanoparticles, was found to have a peak turnover frequency of $44.0\,h^{-1} \pm 0.9\,h^{-1}$ and a turnover number of 56.6 ± 2.2 after four hours.[77]

Figure 2.4: The structure of Co(dmgH)$_2$pyCl synthesised by Cao *et al.*, compared with the structures of the phosphonated cobaloxime catalysts CoP^1, CoP^2 and CoP^3 first synthesised by Lakadamyali *et al.*,[78] Muresan *et al.*,[79] and Willkomm *et al.*,[77] respectively.

Figure 2.5: (A) Electron and proton transfer steps, with red indicating the classical pathway with protonation of the Co centre only, and blue indicating the bridge-protonated pathway, which involves the protonation of the O-H-O functional group. (B) and (C) refer to two classical routes for the final hydrogen evolution step. (B) refers to a pathway with the protonation of one cobalt-hydride species. (C) refers to a pathway involving two cobalt-hydride species. L depicts the ligands. Reprinted from Willkomm *et al.*.[80] ©Japan Society of Coordination Chemistry.

Cobaloximes have characteristic absorption spectra dependent on the oxidation state of the cobalt metal centre (see Figure 2.3b).[72,80,79] Therefore, time-resolved spectroscopy can be used to identify the intermediate states and their lifetime *in operando*. Rosser *et al.* immobilised CoP^2 and CoP^3 on mesoporous ITO electrodes for UV-Vis spectroelectrochemistry. They identified the active species for proton reduction as Co^I, as its characteristic absorption peak at $\lambda = 655\,$nm appeared on applying a potential of $-0.6\,$V *vs.* NHE. The peak immediately depleted within a few seconds, attributed to proton reduction with concomitant oxidation of the cobalt metal centre to form Co^{III}-hydride.[72] This classical pathway is depicted in Figure 2.5A.

Cao *et al.* explored the performance of Co(dmgH)$_2$pyCl with g-C$_3$N$_4$, and report the appearance of an absorbance peak at $525\,$nm after light irradiation. They attribute this to a Co^I intermediate species.[81] The Co^I species, being highly nucleophilic, are rapidly protonated to form Co^{III}-hydrides. The subsequent protonation of Co-H species to release H$_2$ has been suggested to be the rate-limiting step for cobaloxime-based hydrogen generation (see Figure 2.5B).[74,82] Willkomm *et al.* propose a second 'bridge-protonated' pathway in contrast to the classical pathway described. Both pathways are summarised in Figure 2.5, with the exact sequence of steps in the reaction mechanism remaining evasive.

To perform mechanistic studies and to identify reaction steps such as those in Figure 2.5, it is useful to characterise catalyst intermediate states - catalyst speciation - and elucidate the factors that control catalyst performance.[83]

2.1.4 Sacrificial electron donors

Sacrificial electron donors (SEDs) include a wide variety of small molecules, such as tertiary aliphatic amines, thiols and carboxylic acids. On electron donation to a photosensitiser, an oxidised species will form. These oxidised species will accumulate, and dependent on the sacrificial electron donor, may interact further with the photocatalyst. The ideal SED will be irreversibly oxidised into inert molecules, and its oxidised form will not recombine with its electron-transfer counterpart. Recombination is a difficult process to control, as an electron transfer in the donor-acceptor encounter complex, $[D-A] \longrightarrow [D^+-A^-]$, can result in attractive Coulombic interactions between oxidised donor (D^+) and reduced acceptor (A^-). The probability of the donor escaping the potential well of the acceptor is commonly termed the solvent cage escape yield, and is dependent on the donor, acceptor and solvent in question.

Sacrificial electron donors are usually pH sensitive with their pK$_a$ indicating transition points in their behaviour. The pK$_a$ refers to the equilibrium constant for dissociation of a weak acid, $HA \rightleftharpoons H^+ + A^-$, where

$$\mathrm{pK}_a = -\log_{10} \frac{[A^-][H^+]}{[HA]} \qquad \Rightarrow \qquad \mathrm{pH} - \mathrm{pK}_a = \log_{10} \frac{[A^-]}{[HA]} \qquad (2.1)$$

This means if the pH is lowered below the pK_a of a SED, the dominant species will transition from a deprotonated form to a protonated form. Herein, the degradation pathway of three common SEDs for solar fuel catalysis are reviewed.

Ethylenediaminetetraacetic acid (EDTA) is one of the most common SEDs employed in neutral or alkaline conditions, with a pH-dependent oxidation potential in the range 0.57 V *vs.* NHE to 0.92 V *vs.* NHE.[20,84] Given EDTA is a diamine with four carboxylic acid moieties, it is characterised by 6 pK_a values (0.0, 1.5, 2.0, 2.7, 6.1, 10.2).[20] Between pH 7 and pH 9, EDTA exists in a monoprotonated form. The reducing ability of EDTA decreases in its highly protonated forms. The degradation pathway of EDTA upon electron donation is graphically depicted in Figure 2.6. The product upon monoelectronic oxidation is an aminyl radical. The aminyl radical is unstable and deprotonated by a nearby EDTA molecule to form a carbon-centred radical. This carbon-centred radical is highly reductive and can donate a further 'dark' electron to PS or HEC. Dependent on the available electron acceptors, the resultant species can eventually be hydrolysed to form inactive iminodiacetic acid (IDA).[43,85]
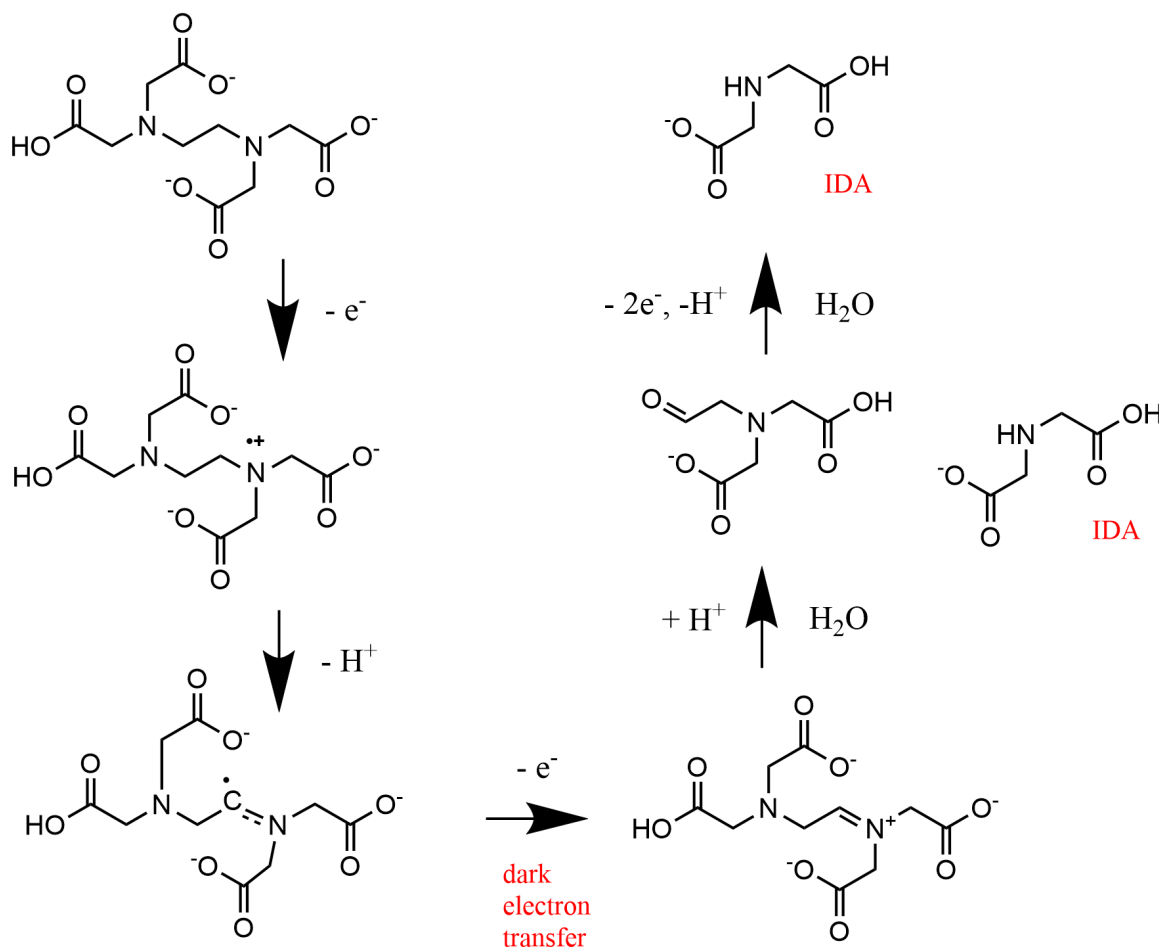
Figure 2.6: The major degradation pathway of EDTA upon electron donation to a photosensitiser. Upon monoelectronic oxidation, EDTA can donate a further 'dark' electron. Dependent on the electron acceptors available, the final product is expected to be iminodiacetic acid (IDA).
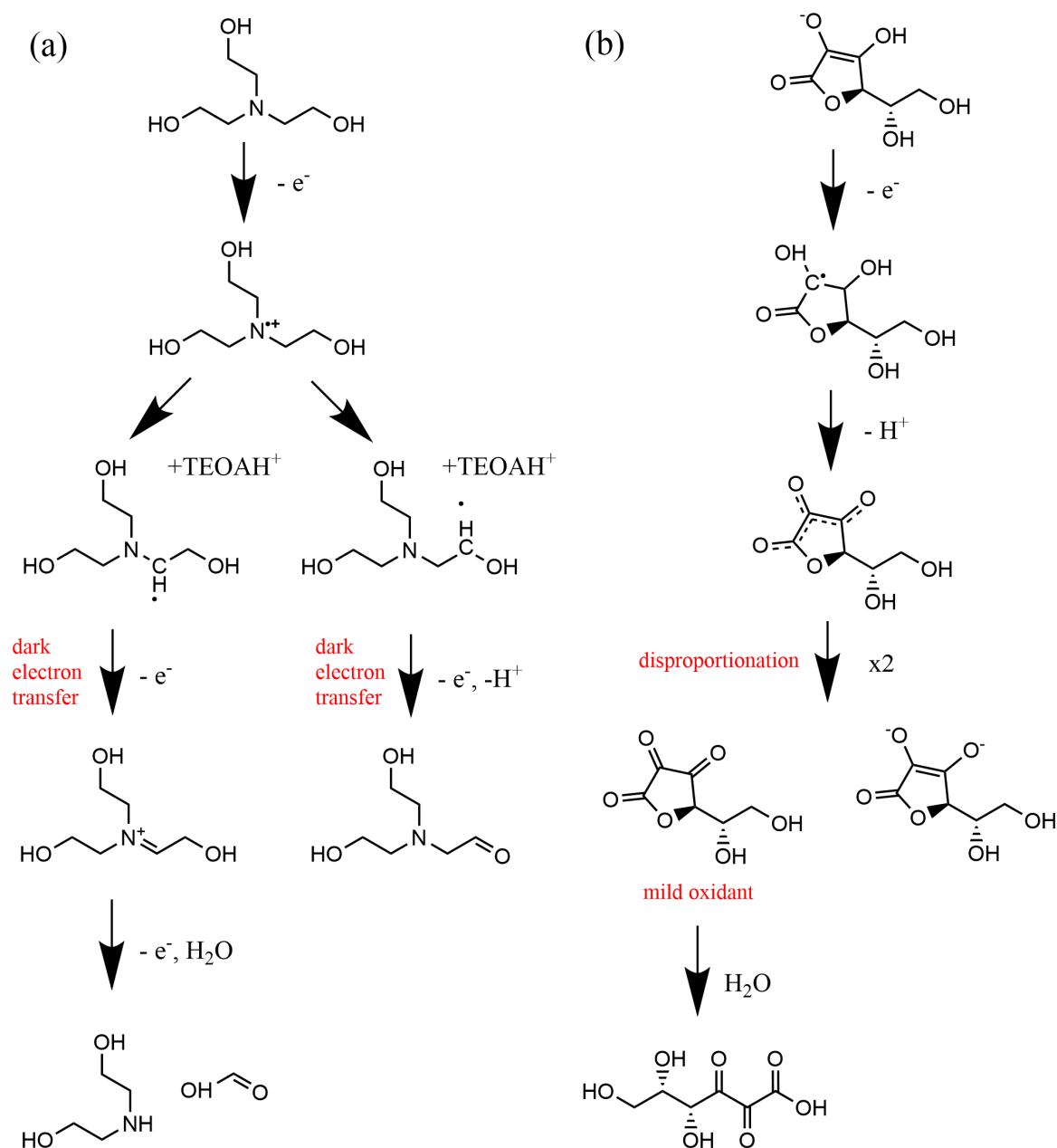
Figure 2.7: The degradation pathways of triethanolamine (a) and ascorbic acid (b) upon electron donation to a photosensitiser. Upon monoelectronic oxidation, triethanolamine can donate a further 'dark' electron before final degradation to ethanal and a secondary amine. The ascorbic acid degradation pathway results in the formation of dehydroascorbic acid, a mild oxidant. Although short-lived, this species can counter-productively interfere with the photocatalytic cycle by oxidising PS^- and HEC^-. This process competes with hydrolysis to form diketogulonic acid.

Triethanolamine (TEOA) is an example of a SED commonly used under alkaline conditions, with an oxidation potential in the range $0.57\,\mathrm{V}$ *vs.* NHE to $0.82\,\mathrm{V}$ *vs.* NHE. The degradation pathway of TEOA upon electron donation is graphically depicted in Figure 2.7a. The product of monoelectronic oxidation is an aminyl radical. The aminyl radical is unstable and deprotonated by a nearby TEOA molecule to form a carbon-centred radical. This carbon-centred radical is highly reductive and can donate a further electron to PS or HEC. The resultant iminium species is hydrolysed to inactive ethanal and secondary

amine. Hence, the quenching efficiency of TEOA is theoretically 2, however in practice is 0.5 at best because the cage escape yield is poor. The pK_a of TEOA is 7.9, so the deprotonation step of the aminyl radical becomes less likely as pH decreases.[20]

Ascorbic Acid (AA) is an example of a SED that can be employed in acidic conditions, with an oxidation potential of 0.46 V *vs.* NHE. It is characterised by 2 pK_a values (4.0, 11.3). Between pH 5 and pH 9, AA exists in a monodeprotonated form HA$^-$. The degradation pathway of HA$^-$ upon electron donation is graphically depicted in Figure 2.7b. The product of monoelectronic oxidation is HA$^\bullet$, which dissociates into A$^{\bullet-}$ and H$^+$. Two A$^{\bullet-}$ molecules disproportionate into A and A^{2-}. A is a mild oxidant and can counter-productively oxidise PS$^-$ and HEC$^-$. This process competes with hydrolysis to form diketogulonic acid. Martindale *et al.* used tris(carboxyethyl)phosphine (TCEP) to extend the lifetime of a carbon nanodot based solar H$_2$-evolving system by preventing the back-electron transfer from PS$^-$ to A. The regenerating TCEP/AA donor allowed photo-induced holes to be quenched by HA$^-$, followed by subsequent irreversible reduction of A back to HA$^-$ by TCEP.[43]

EDTA readily forms a charge-transfer complex with the substrate methyl viologen (MV^{2+}). The equilibrium constant for complexation, K_c, is pH-dependent with Mulazzani *et al.* reporting a value of 13 in the pH range 8.0-10.0.[86] The proportion of MV that is complexed, f_c can then be calculated by

$$f_c = \frac{K_c[EDTA]}{K_c[EDTA] + 1}, \tag{2.2}$$

which means for an EDTA concentration of 0.1 M, 56% of MV^{2+} exists in a MV-EDTA complex in a pH range typical for photocatalysis experiments.

2.2 Kinetics

The relaxation of the excited state, CD^*, is comprised of a radiative and non-radiative component. Both components are first-order with respect to CD^* such that

$$[CD^*] = [CD^*]_0 \exp\{-(k_r + k_{nr})t\} \tag{2.3}$$

where k_r and k_{nr} are the rate constants of the radiative and non-radiative components respectively. Coupled with a photoluminescence quantum efficiency (PLQE, Φ), we can write

$$k_{nr} = k_0(1 - \Phi) \tag{2.4}$$

where $k_0 = k_r + k_{nr}$. When we transfer an electron from the CD to an acceptor, k_{nr} now comprises of an additional electron-transfer term k_{ET}.[5] The kinetics of electron-transfer from the surface of a CD to a substrate can be described by non-adiabatic Marcus theory.[87] The charge distribution of the encounter complex changes following an electron transfer, resulting in the reorganisation of surrounding solvent molecules. The energetics of this process, alongside the structural changes to the CD surface and substrate following electron transfer, are defined together as a 'reorganisation energy'. This influences the

electron-transfer rate, k_{ET}, described by

$$k_{ET} = \frac{2\pi}{\hbar} |H_{AB}|^2 \frac{1}{\sqrt{4\pi\gamma k_B T}} \exp\left\{ \frac{(-\Delta G + \gamma)^2}{4\gamma k_B T} \right\} \tag{2.5}$$

where $\hbar$ is the reduced Planck constant, H_{AB} is the acceptor-donor electron coupling, γ is the reorganisation energy, ΔG is the driving force for the electron transfer, k_B is the Boltzmann constant and T is the temperature. H_{AB} is influenced by the relative orientation of CD and substrate, and their separation. [5]

In the case of proton reduction, tuning k_{ET} by selecting acceptor-donor pairs with a strong driving force, ΔG, and electronic coupling, H_{AB}, for the second reduction step is important. This is because the second electron transfer is often rate-limiting and has a lower driving force than the first transfer. [33] The separation of the photogenerated electron-hole pair must be on a time-scale faster than recombination to enable this electron transfer to take place.

Moreover, in the case of carbon nanodots, Ren *et al.* determine a difference in the ordering of water molecules surrounding a carbon nanodot following nitrogen doping. The faster generation of photoexcited electrons results in the accumulation of charge and subsequent polarization of the CD surface. The surface polarization orients water molecules with oxygen sites pointing toward the CD, leaving two hydrogen atoms available for hydrogen bonding. This seeds a structured interfacial water layer, [88] which likely affects the reorganisation energy for the electron transfer process. Therefore, the electron transfer kinetics between carbon nanodots is likely to differ.

The two main techniques to probe electron transfer kinetics in photocatalysis are transient absorption spectroscopy (TAS) and time correlated-single photon counting (TC-SPC).

TAS Transient absorption spectroscopy (TAS) provides information about short-lived transient species that absorb in the visible and near-infrared region. [89,90,91] TAS is a pump-probe technique, where the sample is subject to a short intense pulse of excitation light (pump) followed by a second broadband light source (probe). Spectra are collected as a function of the pump-probe time delay. [19] Changes in absorbance can indicate the generation of transient species, often referred to as photoinduced absorption (PIA, positive absorbance change), or the loss of the ground state species, often referred to as a ground state bleach (negative absorbance change). [89] The dynamics associated with changes of absorbance can give insight into the timescale of formation and disappearance of transient species, along with their nature.

TC-SPC Time correlated-single photon counting (TC-SPC) provides information about the excited state lifetime of photosensitiser and electron transfer kinetics. [44] Without an electron acceptor, the luminescence of the photosensitiser usually decays within nanoseconds, however, in the presence of an electron acceptor the luminescent decay is quenched, thus providing insight into the timescale and efficiency of electron transfer.

Figure 2.8 shows typical timescales for each electron pathway in a RuP dye-sensitised TiO_2 system, measured by TC-SPC. The generation of electron-hole pairs ($k = 10^{11}\,\text{s}^{-1}$) is faster than the recombination of electron-hole pairs in the dye ($k = 10^7\,\text{s}^{-1}$). The probability of recombination can be reduced by using a fast hole scavenger (SED), such that the electron-hole pair cannot recombine. The transfer of the photogenerated electron to the semiconductor ($k = 10^{10}\,\text{s}^{-1}$) is faster than their recombination with holes in the dye ($k = 10^3\,\text{s}^{-1}$).
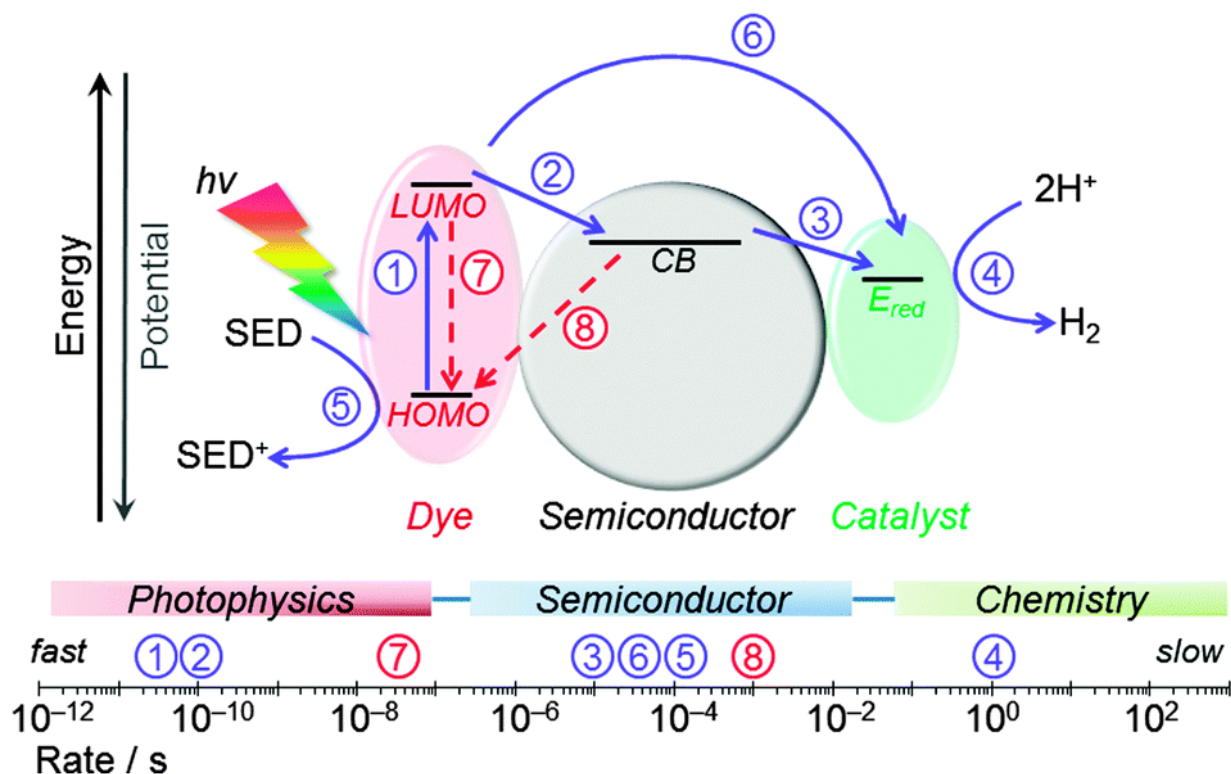
Figure 2.8: Electron pathways in a dye-sensitised hybrid colloidal system. Blue solid arrows depict desired electron transfer processes and red dashed arrows depict recombination pathways. Rates shown are for a RuP-sensitised TiO_2 system. Reprinted with permission from the Royal Society of Chemistry.[19] Licensed under CC BY 3.0.

Subsequent electron transfer from the semiconductor to the catalyst is on a $10^{-6}\,\text{s}$ to $1\,\text{s}$ time-scale.[45] This spans six orders of magnitude and relies heavily on the chemical structure of the catalyst in question. It must be noted that each electron transfer step in a multi-electron process will have different characteristic timescales. The challenge in photocatalytic systems is to match the rate of chemistry (proton reduction in our case), occurring on the $10^{-3}\,\text{s}$ to $1\,\text{s}$ time scale, to charge carrier lifetime.[19] Moreover, Yang *et al.* suggest that use of sacrificial electron donors can imbalance electron and hole extraction rates and result in the accumulation of charge in a photocatalytic system. They argue that this can negatively accelerate recombination kinetics and complicate extrapolation to systems which couple water oxidation to water reduction.[92] Therefore, it is also prudent to match the kinetics of hole extraction to electron extraction.

2.3   Optofluidics

The attention of this review now shifts towards how optofluidic techniques can provide new scientific insights into photocatalysis. Optofluidics combines micro- (or nano-) fluidics and optics in the same platform, to create functional devices resulting from their interaction.[93,94,95,96,97] In one type of optofluidic devices, fluids can be exploited to control the propagation of light, for applications including optical filters, optical routing, data storage and tunable liquid dye lasing.[94,96] Such applications are enabled by fluid mobility (avoiding the challenge of moving solid components), readily modified interfaces, and the ability to tune refractive index through changing fluid composition or concentration.[95,6] There has also been a great push to develop sensing applications using optofluidic waveguides. Fluids are used to transport substances for analysis through photonic circuits, for example, on-chip hollow waveguides, which are becoming increasingly important with the growing need for portable and miniaturised optical sensors.[98] Sensing can be achieved by analysing changes in absorbance, fluorescence, Raman scattering, effective refractive index or surface plasmon resonances.[96,98,99,100] Examples of optofluidic sensing devices are shown in Figure 2.9.
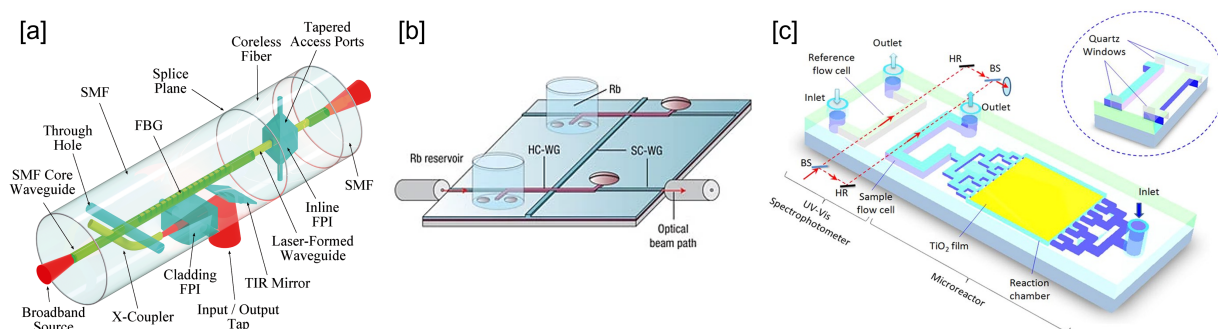
Figure 2.9: (a) Lab-in-fibre: optofluidic components can be integrated into the cladding of an optical fibre to perform sensing; SMF: single-mode fibre, FBG: fibre Bragg grating, FPI: Fabry-Perot interferometer, TIR: total internal reflection. Reprinted with permission from the Royal Society of Chemistry.[101] (b) Interconnected hollow-core waveguides (HC-WG) and solid-core waveguides (SC-WG) that form two vapour cells on a chip. Rubidium-filled reservoirs are attached at the open ends of the HC-WGs. Reprinted with permission.[97] ©Springer Nature 2007. (c) Schematic diagram of a photocatalytic microreactor with an on-chip integrated UV-Vis spectrophotometer. BS: beam splitter; HR: high-reflection mirror. Reprinted with permission from Wang *et al.*.[102] Licensed under CC BY 4.0.

On-chip optofluidic circuits suffer from short light-matter interaction lengths ($\approx 2\,cm$) due to optical confinement losses, or rely on surface-bound evanescent fields of embedded waveguides, for example, in infrared spectroscopy by attenuated total reflectance. This limits the detectability of low analyte concentrations or restricts sensing to regions close to the surface, often with poor overlap between the field and medium of interest.[93,95,96,103,104,105] This problem is even more significant in conventional photochemical reactors where only reaction media adjacent to the vessel wall (i.e., within $2\,mm$) is exposed to irradiation.[106]

Recently, Kim *et al.* demonstrated an optofluidic 'light cage', with high-aspect-ratio cylindrical dielectric strands surrounding a hollow core in a hexagonal arrangement. The light cage featured open space between the strands, allowing analytes to sideways access the core with faster diffusion dynamics over tubular structures. However, the optical losses were large $(0.58\,\mathrm{dB}\,\mathrm{mm}^{-1})$.[105]

A potential way to achieve better detection sensitivity is to use liquid-filled hollow-core photonic crystal fibres (HC-PCFs). This novel class of optical fibre facilitates the guidance of light though liquids, and localises the field within small spatial domains. This augments the fraction of power in the medium of interest. Conventional fibre optics guiding light by total internal reflection (TIR) require the refractive index of the core to be greater than the refractive index of the cladding - a condition generally unachievable with a liquid core. HC-PCFs overcome this constraint by guiding light through careful control of a photonic band gap or through anti-resonant reflection (see Section 2.3.3).

The following section will first introduce waveguide modes in conventional optical fibres, before introducing hollow capillaries and HC-PCFs.

2.3.1 Optical fibres as waveguides

Conventional step-index fibres have a central core and outer cladding where $n_{\mathrm{core}} > n_{\mathrm{clad}}$ (see Figure 2.12). Typically, the refractive index of core and cladding materials differs by around a percent.[107] The propagation of light through a step-index fibre is well-described and derived in Appendix A.

The simplified solutions to this derivation are the linearly polarised LP$_{lm}$ modes (see Figure 2.10), where l and m represent the azimuthal and radial orders of the modes respectively.

$$\mathrm{LP}_{lm} = F(r, \phi)e^{i\beta z}e^{-i\omega t} \tag{2.6}$$

where $F(r, \phi)$ is the transverse function dependent on a radical component, r, and an azimuthal component, ϕ. For each LP$_{lm}$ mode, there are two degenerate polarisation modes.
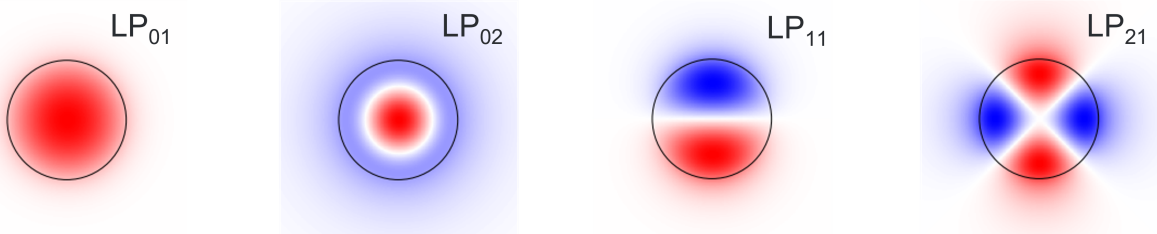
Figure 2.10: Electric field distributions for the the first four linearly polarised LP modes in the r-ϕ plane for a cylindrical waveguide. The black ring signifies the boundary between the higher refractive index core region and lower refractive index cladding. Plots generated using the LIBLP Python package available at https://github.com/xmhk/liblp.

2.3.2 Marcatili-Schmeltzer model

For conventional step-index fibres, $n_{core} > n_{clad}$. However, common liquid solvents (see Table 2.2) generally possess a refractive index below that of silica (1.45 at 600 nm).[108,109] Consequently, infiltrating a liquid through a hollow core results in $n_{core} < n_{clad}$, which changes the boundary conditions of the previously described step-index fibre. This new system - a capillary - requires the Marcatili-Schmeltzer (MS) model for a hollow cylindrical dielectric to describe the waveguiding properties.[110]

The capillary is a lossy system, as guidance by total internal reflection is not possible. The leaky mode solutions to the Helmholtz equation for a capillary can be categorised into three classes: the circular electric modes TE_{0m}, the circular magnetic modes TM_{0m}, and the hybrid modes EH_{lm}. Again, l and m represent the azimuthal and radial orders of the modes respectively. The TE_{0m} transverse modes have a vanishing E_z component, whereas the TM_{0m} transverse modes have a vanishing H_z component. The EH_{lm} modes have non-vanishing E_z and H_z components.[111,112]

Solvent	Refractive Index
Deionized water	1.333
Acetonitrile	1.344
Acetone	1.359
2-Propanol	1.378
Tetrahydrofuran	1.405
Dichloromethane	1.424
N,N-Dimethylformamide	1.431
Ethylene Glycol	1.432

Table 2.2: Refractive indices of common solvents at 589 nm.[113]
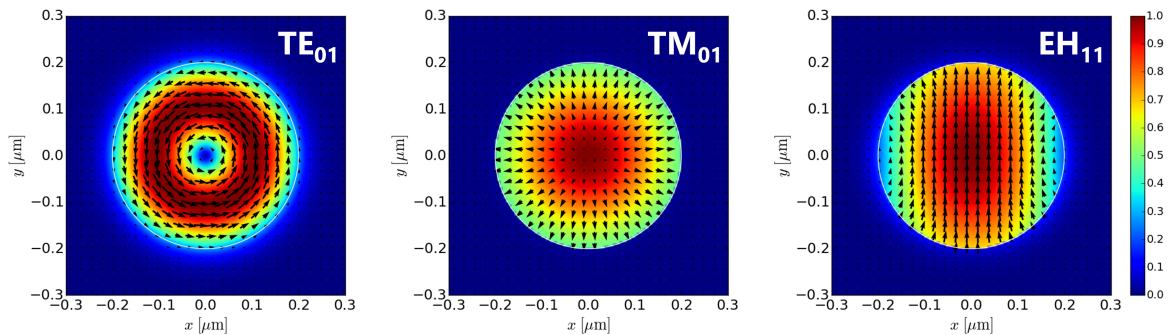
Figure 2.11: Electric field distributions for the TE_{01}, TM_{01} and EH_{11} modes in a cylindrical dielectric capillary. Plots generated using the PYMWM Python package available at https://github.com/mnishida/PyMWM.

The propagation constant, β_{lm}, for each mode in a hollow cylindrical dielectric capillary is defined through the MS model as

$$\beta_{lm} = \frac{2\pi}{\lambda}\left[1 - \frac{1}{2}\left(\frac{u_{l+1,m}\lambda}{2\pi a}\right)^2\right] \tag{2.7}$$

where $u_{l+1,m}$ is the mth root of the equation $J_l(u_{l+1,m}) = 0$ and λ is the wavelength.[110] The loss (attenuation) constant, α_{lm}, describing the $1/e$ decay length in the electric field for each mode is defined as

$$\alpha_{lm} = \left(\frac{u_{l+1,m}}{2\pi}\right)^2\frac{\lambda^2}{a^3}\frac{1}{\sqrt{n^2-1}}\begin{cases} 1 & \text{for } \mathrm{TE}_{0m}(l=0) \\ n^2 & \text{for } \mathrm{TM}_{0m}(l=0) \\ \frac{1}{2}(n^2+1) & \text{for } \mathrm{EH}_{lm}(l\neq 0) \end{cases} \tag{2.8}$$

where $u_{l+1,m}$ is the mth root of the equation $J_l(u_{l+1,m}) = 0$ and n is the refractive index of the capillary walls.[110] The attenuation scales as λ^2/a^3, meaning the confinement ability of capillaries are improved for short wavelengths and large core sizes. However, Marcatili *et al.* noted that bending losses scale with a^3, so dependent on application, a large core size may not necessarily result in a more efficient waveguide.

For the fundamental EH_{11} mode in a straight capillary ($u_{l+1,m} = 2.405$) this reduces to

$$\alpha_{11} = 0.073\frac{\lambda^2}{a^3}\frac{n^2+1}{\sqrt{n^2-1}} \tag{2.9}$$

which means typical capillary losses can be easily estimated. For comparison to loss values quoted elsewhere, a conversion to dB is made where $\alpha[\mathrm{dB}m^{-1}] = 10\log e \times \alpha[m^{-1}]$. Moreover, the loss constant in intensity is often quoted in literature. The loss constant in intensity is simply $\times 2$ the loss constant in electric field. Loss constants in terms of intensity are quoted herein.

For a capillary of radius $10\,\mu\text{m}$, and by taking the refractive index of silica as 1.45, a loss constant of $6.8 \times 10^2\,\mathrm{dB\,m}^{-1}$ is calculated at a wavelength of $600\,\text{nm}$. A similar calculation at a wavelength of $1050\,\text{nm}$ gives a loss constant of $2.0 \times 10^3\,\mathrm{dB\,m}^{-1}$. These losses reduce to $5.4\,\mathrm{dB\,m}^{-1}$ and $16.6\,\mathrm{dB\,m}^{-1}$ for a capillary of radius $50\,\mu\text{m}$.

In conclusion, it may be possible to use a $50\,\mu\text{m}$-radius capillary with acceptable losses in air over $<1\,\text{m}$ lengths, as the $1/e$ decay length is $0.8\,\text{m}$ for guidance at $600\,\text{nm}$. However, this system would be very sensitive to bending and restricts the minimisation of sample volumes by reducing core diameters.

2.3.3 Hollow-core photonic crystal fibres

Capillaries have significant confinement losses, especially at reduced diameters. It is apparent that a different guidance mechanism is required. Philip Russell conceived the idea of using photonic band gap effects to guide light in 1991. Following the experimental im-

plementation of guidance using these photonic band gaps,[114] new optical fibres based on antiresonant waveguides were established. These new classes of optical fibre were together called hollow-core photonic crystal fibres (HC-PCFs), which are now discussed in further detail.
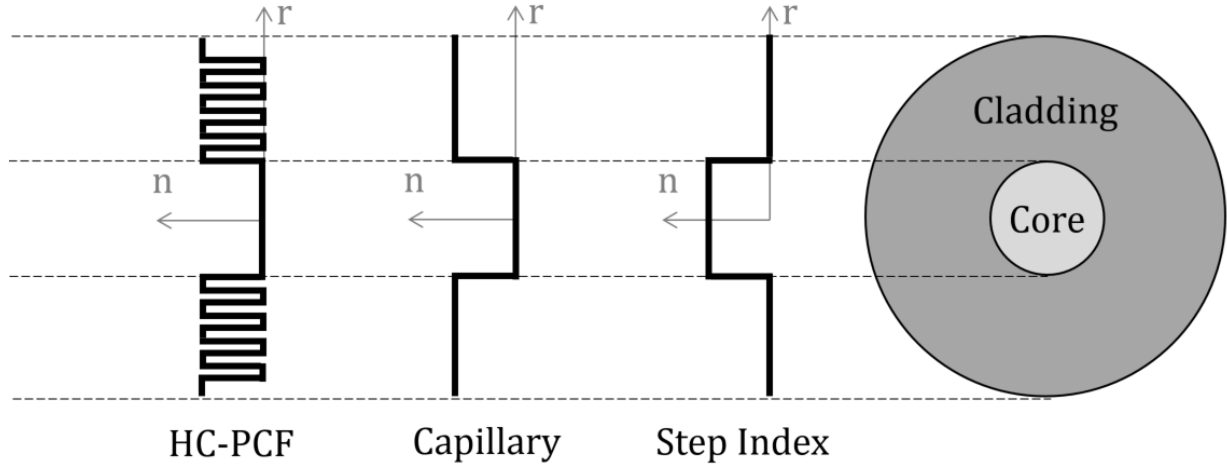
Figure 2.12: Schematic diagram of the refractive index profile, n, for a (1) HC-PCF (2) capillary and (3) step-index fibre, as a function of radial distance, r.

HC-PCFs are designed to reduce the significant attenuation and bend sensitivity characteristics of hollow capillaries. This is vital when extending light-matter interaction lengths, so there is an appreciable intensity of light that can interact with a sample throughout the entire length of the fibre. The lowest loss HC-PCF reported to date has an attenuation coefficient of $1.6\,\mathrm{dB\,km^{-1}}$ at $1050\,\mathrm{nm}$.[115] This is five orders of magnitude lower than a capillary with a similar core size ($1.0 \times 10^3\,\mathrm{dB\,m^{-1}}$).

HC-PCFs (see Figure 2.13) consist of a central cylindrical hollow channel with a typical radius of $5\,\mathrm{\mu m}$ to $30\,\mathrm{\mu m}$ (the core), surrounded by a periodic arrangement of smaller channels (the cladding), running along the entire length of the fibre.[116,117] The cladding consists of very little solid material (usually silica) with generally less than 10% filling fraction by area.[118] HC-PCFs are typically fabricated by a stack-and-draw technique. A preform that holds the structure of interest on a macroscopic scale is assembled by stacking capillaries and rods by hand. These preforms are typically a metre long and $10\,\mathrm{mm}$ in radius. The preform is then drawn on a fibre-drawing tower under high temperature ($\approx 2000\,^\circ\mathrm{C}$), substantially extending its length while reducing its cross-section.[107] Three distinct classes of HC-PCFs now exist: photonic band gap, Kagomé and negative curvature fibres.

HC-PBGFs Hollow-core photonic band gap fibres (HC-PBGFs) confine light to the fibre core using a photonic band gap in the cladding.[119,120] This photonic band gap prevents light within a narrow band of wavelengths and incident angles from propagating into the cladding. The first demonstration of a HC-PBGF was reported by Cregan *et al.* in 1999.[121]
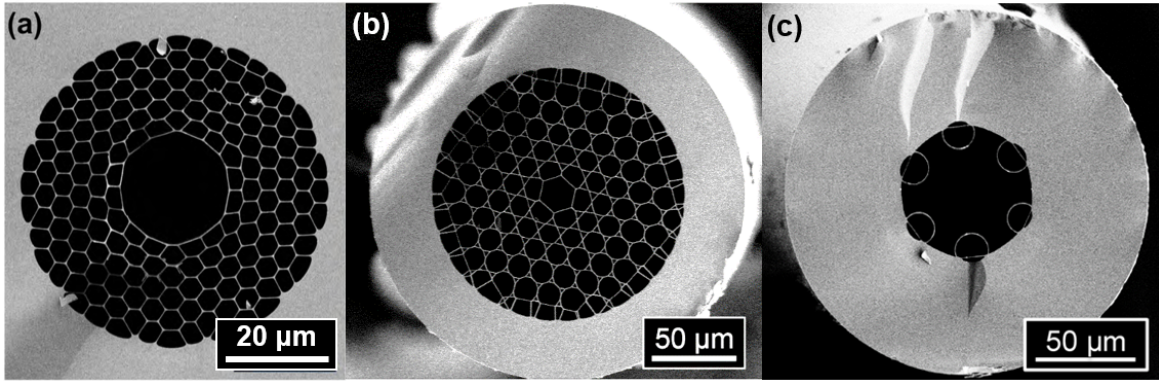
Figure 2.13: SEM images of three classes of HC-PCF. (a) Photonic band gap fibre, (b) Kagomé fibre and (c) Negative-curvature fibre. Images taken by Michael H. Frosz at the Max Planck Institute for the Science of Light.

The photonic band gap stems from the periodic modulation of the fibre's refractive index in the cladding, analogous to the periodic arrangement of atomic potentials in a semiconductor giving rise to an electronic band gap. A simple treatment considers the application of Bloch boundary conditions to the unit cell of the periodicity, such that the dispersion surface for each cladding mode can be generated through numerical techniques,

$$D_q(\omega, k_{\perp BZ}), \tag{2.10}$$

where q is the band index, ω is the angular frequency and $k_{\perp BZ}$ is the transverse wavevector within the first Brillouin Zone.[118,122] Where no cladding states exist in ω-D space for any band index, q, and any transverse wavevector $k_{\perp BZ}$, nearly lossless guidance can be realised through the core. Minor attenuations are limited by surface scattering loss from the intrinsic roughness of the silica-air interface.[118,120] It must be noted that this simple treatment assumes perfectly symmetric lattices of infinite extent, which may not necessarily provide a valid model for all HC-PBGFs. HC-PBGFs are commercially available with NKT Photonics producing a fibre with an attenuation of $< 250\,\mathrm{dB\,km^{-1}}$ at the design wavelength of $820\,\mathrm{nm}$ (HC-800-02). Losses below $100\,\mathrm{dB\,km^{-1}}$ for the visible region of the electromagnetic spectrum are difficult to achieve with HC-PBGFs because of the challenge of drawing smaller-pitch microstructures with similar surface uniformity to those designed for longer wavelengths. At these wavelengths, surface scattering losses (SSL) become the dominant loss mechanism, particularly as SSL scales with $1/\lambda^3$.[123] However, at infrared wavelengths the lowest documented HC-PBGF loss is $1.7\,\mathrm{dB\,km^{-1}}$ at $1565\,\mathrm{nm}$ and was obtained by Mangan *et al.* in 2004.[124]

Kagomé HC-PCFs A contrasting type of HC-PCF, kagomé HC-PCFs, consist of a silica-web cladding with a periodic hexagonal motif, which does not possess a photonic band gap. The first kagomé fibre was reported by Benabid *et al.* in 2002, with a loss of $1\,\mathrm{dB\,m^{-1}}$.[125] In contrast with HC-PBGFs, kagomé fibres possess a wide transmission window, meaning kagomé HC-PCFs are suitable for sensitive broadband spectral measure-

ments, especially coupled with the fact that kagomé HC-PCFs today can display losses below $100\,\mathrm{dB\,km^{-1}}$.[126] To date, the lowest loss reported for a kagomé fibre was fabricated by Maurel *et al.* with an attenuation of $8.5\,\mathrm{dB\,km^{-1}}$ at $1030\,\mathrm{nm}$.[127] Recently it was realised that the optical losses in kagomé HC-PCFs did not scale with the number of silica layers in the cladding, and broadband guidance with only the inner-most ring of the kagomé cladding is possible.[128]
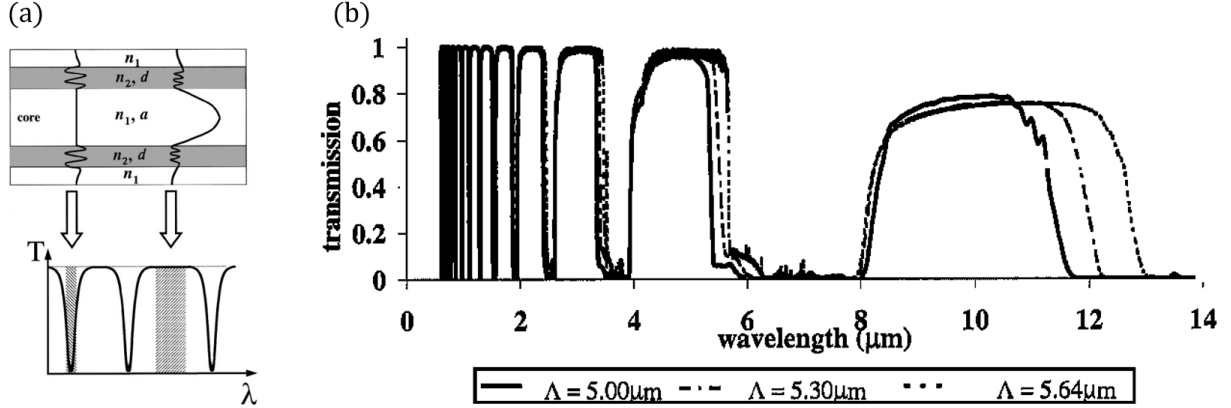
Figure 2.14: (a) Schematic of an ARROW and its associated transmission spectrum. (b) Simulated transmission spectra for a 1D 10-layer ARROW over the wavelength range $0.6\,\mu\mathrm{m}$ to $15\,\mu\mathrm{m}$. Spectra were plotted for three different lattice constants, Λ, defined as the sum of the high-index region thickness and low-index region thickness. The high-index region thickness was fixed at $3.437\,\mu\mathrm{m}$ in all three cases. Reprinted with permission.[129] ©The Optical Society.

Guidance in kagomé HC-PCFs can be explained through the anti-resonant reflection optical waveguide (ARROW) model,[129] where the silica web can be considered as an array of Fabry-Pérot resonators. In the simplest case, we can examine one silica strut in Figure 2.14a, such that our resonance condition is defined as

$$k_e d = \pi m \tag{2.11}$$

where k_e is the wavenumber in silica, t is the strut thickness and m is the resonance order. Given that

$$k_e = \sqrt{k_0^2 n_2^2 - \beta^2} \tag{2.12}$$

where k_0 is the wavenumber in free space, n_2 is the refractive index of silica and β is the propagation constant, we can write

$$k_0 d \sqrt{n_2^2 - 1} = \pi m \tag{2.13}$$

assuming $\beta \approx k_e$. The resonant wavelengths are thereby defined by

$$\lambda_{\mathrm{loss}} = \frac{2d}{m} \sqrt{n_2^2 - 1}. \tag{2.14}$$

At resonant wavelengths, light is transmitted through the silica strut (Figure 2.14a left), whereas off-resonance the light is confined to the fibre core (Figure 2.14a right).[121,122,130,131]

Litchinitser *et al.* simulated a 1D 10-layer geometry for three different lattice constants, Λ, resulting in the transmission spectra depicted in Figure 2.14b. The strut thickness of Kagomé fibres can be designed to guide in the wavelength region of interest for the chemistry under study.

Finger *et al.* showed that a modified Marcatili-Schmeltzer (MS) model with a wavelength-dependent effective core radius agrees with experimentally observed modal refractive indices in kagomé fibres. [132]

HC-NCFs The most recent developments in HC-PCFs center around hollow-core negative curvature fibres (HC-NCFs) or hypocycloid HC-PCFs. These fibres posses a ring of anti-resonant tubes around the core, and emerged from attempts to simplify the kagomé fibre design into a single ring (see Figure 2.15), [133] hence their alternative name: single ring HC-PCFs. The simplified design reduces the complexity of the stack-and-draw fabrication process. Debord *et al.* report a loss of $7.7\,\mathrm{dB\,km^{-1}}$ at $750\,\mathrm{nm}$ with a 8-tube HC-NCF, [123] and Gao *et al.* report a loss of $80\,\mathrm{dB\,km^{-1}}$ at $532\,\mathrm{nm}$ with a 6-tube HC-NCF. [134]

Compared to HC-PBGFs, HC-NCFs have lower spatial overlap of the fundamental LP_{01} mode with the silica cladding, resulting in a surface-scattering loss reduction of over one order of magnitude. [135] Furthermore, by controlling the diameter ratio of the anti-resonant tubes to the core (d/D), Uebel *et al.* were able to suppress the propagation of higher order modes (HOMs) to realise broadband single modedness. Their method is based on the promotion of coupling between core and cladding modes. By phase-matching the transverse component of the cladding (anti-resonant tubes) modes with the transverse component of core HOMs, the propagation of HOMs is made lossy due to core-cladding coupling. [136] However, core-cladding coupling is inhibited with the fundamental LP_{01} mode, due to a substantial transverse phase mismatch, along with the poor spatial overlap of the core LP_{01} mode with cladding modes. Figure 2.15 shows an example, where the LP_{11} mode in the core couples with the LP_{01} mode in the surrounding anti-resonant tubes.
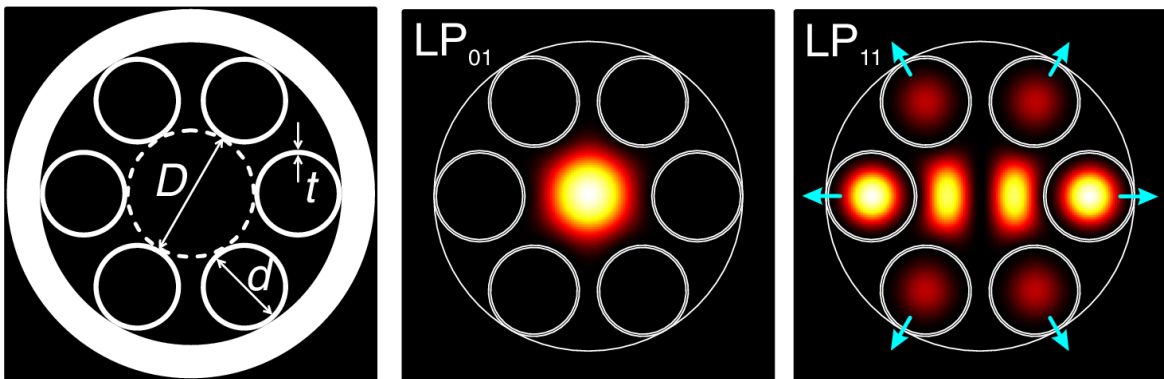
Figure 2.15: (a) Schematic of a HC-NCF fibre-end. (b) The fundamental LP_{01} core mode is strongly confined due to antiresonance with the surrounding tubes. (c) The higher order LP_{11} core mode experiences high losses due to transverse phase-matching with modes in the surrounding tubules. Reprinted with permission. [136] ©The Optical Society.

Confinement loss of the fundamental LP_{01} mode can be further minimised by introducing nested tubes[137] or conjoining anti-resonant tubes in the radial direction, with Gao *et al.* demonstrating losses below $2\,dB\,km^{-1}$ with a twin conjoin (see Figure 2.16).[135] Amrani *et al.* report the lowest loss HC-PCF to date with a hybrid cladding composed of a kagomé-tubular lattice, with an attenuation of $1.6\,dB\,km^{-1}$ at $1050\,nm$.[115]
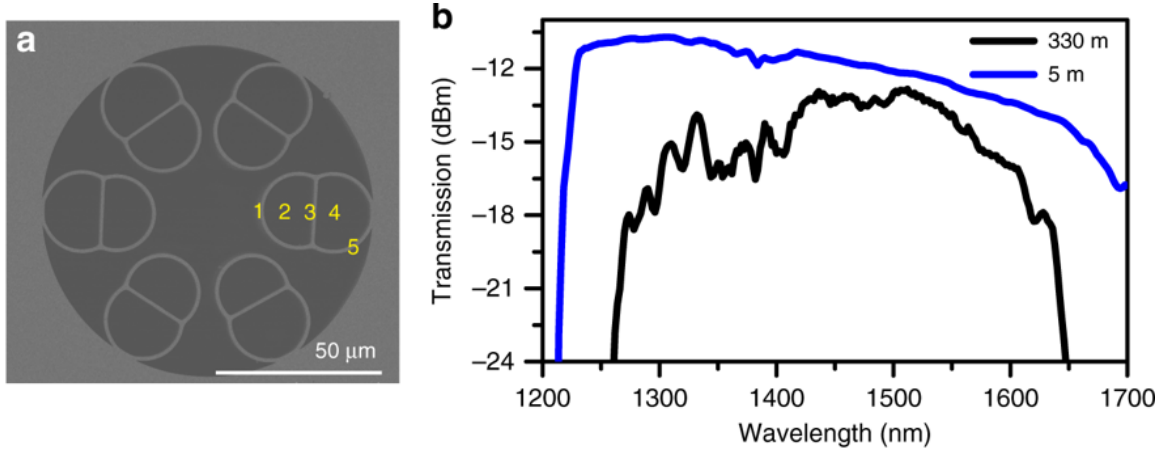
Figure 2.16: (a) SEM image of a conjoined-tube HC-NCF fibre-end with numbered labels indicating the five dielectric layers comprising the Fabry-Pérot resonator. (b) Transmission spectra of a conjoined-tube HC-NCF with a fibre length of $330\,m$ (black) and $5\,m$ (blue). Reprinted from Gao *et al.*.[135] Licensed under CC BY 4.0.

2.3.4 Liquid-filled HC-PCFs

HC-PCFs with extremely low visible light transmission losses now exist. However, for HC-PCFs to be useful for photochemistry, optical guidance must be maintained in liquids. The hollow core in HC-PCFs enables a liquid analyte to be loaded and then probed by the guided light in the same physical channel.[138,120] However, this leads to a shift in the transmission behaviour of the fibre. When a HC-PCF is fully infiltrated with a liquid sample with a refractive index n_1, and the cladding web (silica) has a refractive index n_2, then the transmission window found initially in air at wavelength λ_0 will shift to a wavelength λ given by

$$\lambda = \lambda_0 \left[\frac{n_2^2 - n_1^2}{n_2^2 - 1} \right]^{\frac{1}{2}} \qquad (2.15)$$

For example, when the fibre is infiltrated with water, the resonant wavelengths shift by a factor 0.54. Strictly speaking, this scaling law is valid under the *weak guidance* condition $(n_2 - n_1 \ll 1)$. However, Antonopoulos *et al.* compared transmission in air and heavy water (D_2O) and showed that the discrepancy between this scaling law and experimentally observed transmission bands in HC-PBGFs was small.[138] On top of the shift in transmission window, a smaller refractive index contrast between the infiltrated liquid and silica will also result in greater confinement and reduced bending losses. Cubillas *et al.* reduced these loss with higher refractive index organic solvents by fabricating fibres out of lead-silicate glass (Schott SF6). Lead-silicate glass has a higher refractive index (1.80 at $600\,nm$) than fused silica (1.45 at $600\,nm$), enabling guidance in toluene ($n = 1.49$ at $600\,nm$).[109] They

were able to demonstrate the photolysis of organometallic complexes in toluene, driven by an in-coupled 405 nm laser diode.

This brings us to one of the key advantages of using HC-PCFs as photochemical reactors. HC-PCFs have long light-matter interaction lengths, which enable sensitive detection of analytes at low concentration. We can express light-matter interaction length as

$$\int I(z)dz \tag{2.16}$$

where z lies along the length of the reaction vessel and $I(z)$ is the intensity of light. Maximising this quantity is particularly important for photochemical reactions with low quantum yields. For example, Williams *et al.* made use of the long interaction length in a HC-PCF to study the two-photon excitation (TPE) of fluorescein and rhodamine B. They report calculations of TPE cross-sections on subpicomole sample quantities, making HC-PCFs highly attractive for the assessment of newly developed fluorophores.[139] Chen *et al.* studied the photolysis of vitamin B_{12} in a HC-PCF, exploiting the long interaction length for boosting reaction rate. They report no conversion in a cuvette after 15 h of continuous irradiation at 9.5 mW, however in a HC-PCF the reaction completed within 10 min of irradiation at a power of 20 mW.[117,140]

The low cross-sectional area of HC-PCFs provides another key advantage: the reduction in typical sample volumes to below 1 µL (calculated here for a 1 m fibre length).[116,117] For comparison, conventional cuvette measurements require a sample volume of at least 2 mL to fill a 1-cm cuvette.[102] As an example, Cubillas *et al.* utilised electronic absorbance spectroscopy to monitor the photo-Fenton catalytic reaction, which results in the degradation of methylene blue (MB) in the presence of Fe^{2+}/H_2O_2 under visible light irradiation. They showed that cuvette-based time-resolved absorbance data was extremely noisy when the reaction was started with 1 µM MB. However, they observed clear first-order kinetics when this reaction was carried out in fibre on a sample volume 100, 000 times smaller than in cuvette.[117,141] The reduction in sample volume is particularly important for lowering screening costs, where multiple conditions may have to be tested with rare and expensive photocatalysts synthesised at research-scale.

Benabid *et al.* reported a useful figure of merit (f_{om}) to compare between reaction chambers, considering both interaction length and sample volume.[125]

$$f_{om} = \frac{L_{int}\lambda}{A_{eff}} \tag{2.17}$$

where L_{int} is defined as the interaction length at which the initial intensity drops by $1/e$ in the reference liquid and A_{eff} is the cross-sectional area of the sample cell. Typical figures of merit are plotted as a function of core diameter in Figure 2.17. Compared to a standard 1-cm cuvette, the efficacy of the light-matter interaction in a HC-PCF can be enhanced by 10^8 times.[119]
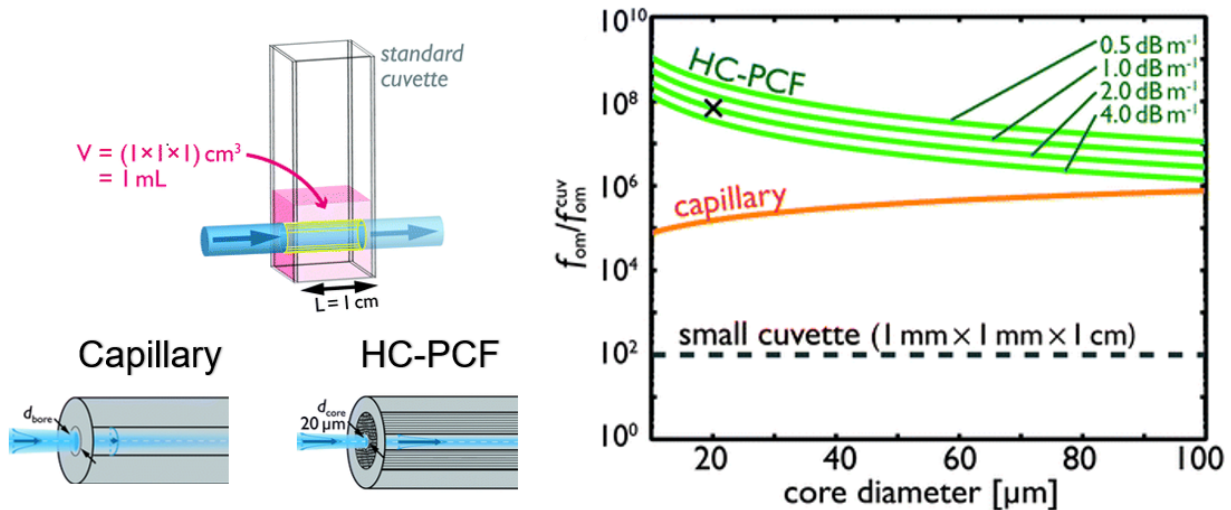
Figure 2.17: f_{om} for light-matter interactions, normalised to a standard cuvette. f_{om} is calculated for a small cuvette, a capillary, and a HC-PCF for a range of loss values. An experimental value for a kagomé HC-PCF is shown with a cross. Adapted with permission from the Royal Society of Chemistry. [119]

2.3.5 Exciting higher order modes

Higher-order modes (HOMs), which enable the spatial selection of certain regions in a fibre, can be excited within an optical fibre by using a 4-f setup and a spatial light modulator (SLM). [142,143] The SLM can introduce a phase shift between 0 and 2π and thus shape the wavefront of a spatially coherent illumination beam, [144] such that desired free-space Laguerre-Gaussian (LG) modes can be projected onto the end-facet of the fibre.

Bruning et al. report that for high coupling efficiencies into a step-index fibre, high spatial overlap is required between the desired fibre LP and free-space LG modes; this is generally achievable for LP modes of low radial order and far from their cut-off condition. At a beam-to-core radius ratio of 0.75, they achieved a LG mode overlap of about 0.99 for the LP_{01}, LP_{11} and, LP_{21} modes, and about 0.98 for the LP_{02} mode. [145]

Ruskuc et al. were able to achieve launch efficiencies of 10% to 20% up to the LP_{33} mode in a water-filled kagomé HC-PCF, and up to LP_{31} in a water-filled HC-PBGF (see Figure 2.18). [143] This built upon the work of Bruning et al. who demonstrated excitation of HOMs in step-index fibres, [145] and Euser et al. who demonstrated excitation of HOMs in air-filled HC-PBGFs and Kagomé HC-PCFs. [142] Other notable applications of SLM-excited modes in gas-filled HC-PCFs include mode-division multiplexing, [146] spatially-resolved atom spectroscopy, [147] and optical conveyor belts. [148] Utilising HOMs in liquid-filled HC-PCFs can be exploited to probe the surface adhesion of compounds to the fibre walls (for example, using a LP_{31} mode) or to selectively excite photocatalysts attached to the fibre walls.
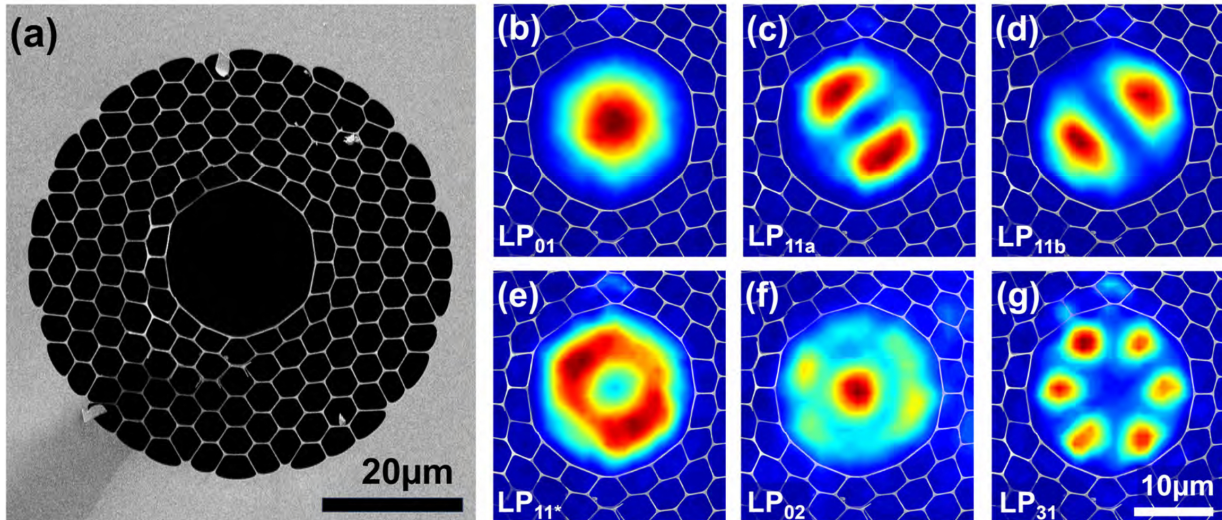
Figure 2.18: Excitation of higher order modes in a HC-PBGF. (a) SEM image of the HC-PBGF. (b-g) Intensity profiles of higher order modes up to LP_{31} at a wavelength of 800 nm. Reprinted from Ruskuc *et al.*.[143] Licensed under CC BY 4.0.

2.3.6   Photochemistry in HC-PCFs

A broad introduction to HC-PCFs has been provided. The focus now switches to how HC-PCFs have been utilised as optofluidic microreactors in the study of photochemistry. First, three spectroscopic techniques to track chemical reactions are discussed, after which microfluidic integration and heterogeneous catalysis are explored.

HC-PCFs are usually fabricated from chemically inert silica, with negligible scattering, absorbance and fluorescence. Therefore, HC-PCFs are an effective reaction vessel for spectroscopic studies of photochemical reactions. Reaction insights can be obtained through three light-matter phenomena: (1) electronic absorbance, (2) fluorescence and (3) Raman scattering.

Electronic absorption   Observing an electronic absorption signal gives an insight into the chemical species present in a reaction mixture, and their quantities, through the Beer-Lambert law,

$$\text{Abs} = -\log_{10}\left(\frac{I_s - I_b}{I_r - I_b}\right) = \epsilon l c, \tag{2.18}$$

where Abs is the absorbance, I_s is the sample intensity, I_b is the background intensity, I_r is the reference intensity (usually solvent), ϵ is the molar absorptivity, l is the path length and c is the concentration of the species of interest.[149,83]. For transient absorption (TA) spectroscopy, we use a slightly modified form of the Beer-Lambert law, where we express differential absorbance (ΔAbs) and differential molar absorptivity ($\Delta\epsilon$) terms such that

$$\Delta\text{Abs} = \Delta\epsilon l c \eta. \tag{2.19}$$

η is the fraction of molecules that are excited from the ground state to the excited state.[5] The wavelength at which a chemical species absorbs is characteristic of the electronic tran-

sitions present. The molar absorptivity, ϵ ($M^{-1}\,cm^{-1}$), describes the extent of absorption and can be related to an absorption cross section per molecule or particle, σ_a (m^2), by

$$\sigma_a = \frac{10 \ln 10}{N_A} \epsilon \tag{2.20}$$

where N_A is the Avogadro's constant.

Fluorescence Photocatalysts generally fluoresce under UV illumination, which is indicative of recombination across the band gap or HOMO/LUMO gap. Providing an electron-acceptor to the catalyst diminishes the fluorescence signal, as an electron can transfer from the photocatalyst to the electron-acceptor and therefore cannot take part in a recombination event. Alternatively, adding an electron-donor will result in a diminished signal, as the hole in the valence band is filled by the electron-donor preventing a recombination event. Both these processes describe fluorescence quenching.[9]

The excited-state (PS^*) lifetime of a photocatalyst decreases on the addition of a quencher and can be described through

$$\frac{d[PS^*]}{dt} = -(k_0 + k_q[Q])[PS^*] = -k_{obs}[PS^*] \tag{2.21}$$

where k_0 is the rate of decay of the excited state in the absence of quencher, k_q is the bimolecular quenching constant, $[Q]$ is the concentration of quencher and k_{obs} is the observed rate constant.[5] Dividing k_{obs} by k_0, we arrive at the Stern-Volmer equation[150,151]

$$\frac{k_{obs}}{k_0} = 1 + k_q \tau_0 [Q] \tag{2.22}$$

where τ_0 is the fluorescence lifetime in the absence of quencher ($\tau_0 = k_0^{-1}$). For pseudo first-order conditions where $[Q] \gg [PS^*]$, the fluorescence signal is proportional to k_{obs}. Therefore, by investigating the fluorescence signal as a function of quencher concentration, the activity of photocatalysts can be characterised. Arias-Rotondo *et al.* note that the fluorescence signal must be normalised to the absorbance of the sample at the excitation wavelength, as the absorbance of the sample will be partitioned between that of the photocatalyst and that of the substrate, which will change as the concentration of quencher is varied.[5]

Fluorescence measurements in HC-PCF were demonstrated by Smolka *et al.* in 2007.[152] The HC-PCF provides two benefits in this case: long interaction lengths for efficient excitation, and the integration of emitted counts along the entire length of the fibre for low concentration sensing. Williams *et al.* could detect down to 1.8 attomoles of fluorescein (10^6 molecules) in HC-PCF with a $90\,nL$ sample volume. However, the absorption and emission spectra of fluorescein overlap, resulting in the appreciable reabsorption of shorter emission wavelengths in the contained fibre environment. This manifests as a redshift in peak emission with increasing concentration of fluorescein.[153] More recently, Williams *et*

al. have demonstrated the sub-picomole detection of singlet oxygen ($^1O_2$) in HC-PCFs.[154]

Raman   One form of inelastic scattering from molecules is Raman scattering. This effect was first observed by C. V. Raman in 1928. The gain (anti-Stokes shift) or loss (Stokes shift) in energy gives an insight into the molecular vibrational states or phonons present in the molecules, hence helps identify chemical species present.[149,155] The energy difference between the inelastically scattered and incident photons is defined as the Raman shift, ν,

$$\nu[\text{cm}^{-1}] = 10^7 \left(\frac{1}{\lambda_i[\text{nm}]} - \frac{1}{\lambda_s[\text{nm}]} \right) \tag{2.23}$$

where λ_i is the wavelength of the incident light and λ_s is the wavelength of the scattered light. Stokes scattering is associated with positive Raman shifts and anti-Stokes with negative shifts. The Stokes scattering is generally used to identify chemical species, as the Raman intensity is stronger than that of anti-Stokes scattering due to the exponentially smaller population of molecules in higher energy states. This Boltzmann distribution in states means a molecular temperature, T, can be extracted from the relative intensities of the Stokes and anti-Stokes peaks,

$$\frac{S_{\text{anti-Stokes}}}{S_{\text{Stokes}}} = \left(\frac{\nu_i - \nu_s}{\nu_i + \nu_s} \right)^4 \exp\left\{ -\frac{h\nu_s}{kT} \right\} \tag{2.24}$$

where $S_{\text{anti-Stokes}}$ is the intensity of the anti-Stokes peak, S_{Stokes} is the intensity of the Stokes peak, and ν_i and ν_s are the frequencies of the incident and scattered light respectively.[156] Although Raman is a powerful technique, it is inefficient due to tiny scattering cross sections, of the order $10^{-30}\,\text{cm}^{-2}\,\text{sr}^{-1}$.[157] This means it is important to filter out the elastic Rayleigh scattering, usually using a notch filter, so that the spectrometer is not overwhelmed. The Raman intensity, I_r, can be calculated for a known differential cross section, $d\sigma/d\Omega$, by

$$I_r = \eta F_c n L \Omega_c I_0 \left(\frac{d\sigma}{d\Omega} \right) \tag{2.25}$$

where η is the detector efficiency, F_c is the collection factor, n is the number density of scattering centers, L is the interaction length, I_0 is the incident laser flux and Ω_c is the solid angle of collection. The collection factor, F_c, is the ratio of photons that enter the monochromator slits, to the total photons collected into Ω_c.[158] The quantity $L\Omega_c$ can be used as figure of merit for the efficacy of microreactors for Raman measurements.

Online reaction monitoring by Raman spectroscopy has been demonstrated in hollow-core photonic crystal fibres. Schorn *et al.* were able to track the esterification of methanol and acetic activity by the shift in the C=O Raman peak in kagomé-style HC-PCFs.[159] Surface-enhanced Raman spectroscopy (SERS) can also be exploited to amplify these inherently weak signals by trapping molecules of interest in localised regions of intense optical fields.[160] Enhancement is achieved through localised surface plasmon resonance (LSPR), with enhancement factors of between 10^4 and 10^{12} possible over a distance typically ex-

tending 10 nm - 30 nm from a plasmonic surface.[157,161] Tiwari *et al.* demonstrate SERS in a HC-PBGF, with contributions to the enhancement of R6G Raman signal from both the 60 nm ± 10 nm plasmonic Ag nanoparticles ($\sim$ 20 times), and the HC-PBGF ($\sim$ 16 times).[162,163] Plasmonic nanoparticles were suspended in the fluid with the analyte.

Microfluidics HC-PCFs can be interfaced with microfluidic chips,[164] making it convenient to monitor photochemical reaction processes *in operando* and under a continuous flow.[165] The precision provided by optofluidics in terms of light and fluidic control means hollow-core photonic crystal fibres can be used for the rapid optimisation of reactant concentrations using small sample volumes, with readily translatable results for up-scaling.[6,166,167] In fact, the fine control over the irradiation intensity enables behaviour in different reaction regimes to be observed. For example, at low intensities of incident light, the reaction may be photon-limited, whereas at high intensities of incident light, the reaction may be mass-transport (diffusion) limited, or limited by an electron transfer across an interface.[22] In addition, interfacing with microfluidic chips permits the addition of additional characterisation techniques *on-line*, such as mass spectrometry or gas chromatography.

Heterogeneous catalysis HC-PCFs provide a reactor with high surface-to-volume ratios for heterogeneous catalysis, where catalytic nanoparticles are attached to the fibre walls. Cubillas *et al.* selectively immobilised 25 nm Rhodium Rh particles on the inner core wall of a kagomé HC-PCF, and demonstrated the catalytic hydrogenation of Disperse Red 1 *in-fibra*. Together with a continuous flow of reactants, catalyst-decorated HC-PCFs greatly reduce the consumption of precious catalytic metals and reactants, permitting efficient measurement of catalytic activity on ultra-low sample volumes.[116] Moreover, the ability for photocatalysts to be washed *in-situ* without the need for downstream recovery saves turnover time between experiments.[116,22,168,169,166]

2.4 Conclusions

For the development of new photocatalytic systems, advanced, highly sensitive, *in-situ* screening techniques are essential, such that the kinetic and mechanistic detail can be probed. The use of spectroscopic tools in monitoring photocatalysis is generally restricted to sparse snapshots, rather than *in-operando* tracking.[170] Moreover, for the vast majority of photocatalysts, relatively little is known about their behaviour at high photon fluxes required to reach industrially-relevant conversions.[171] In general, a much deeper understanding of the reaction mechanisms behind photocatalysis is needed, with investigation into various operating conditions.[22] Fibre-based optofluidic microreactors are well-placed to tackle such challenges, due to a number of key advantages summarised below:

- metre-long interaction lengths that enable high sensitivity in analyte detection;

- nL/cm sampling volumes which reduce the consumption of precious reagents;

- controllable light-matter interactions through manipulating both the temporal and spatial extent of light-driven processes within the fibre-based microreactor and

- 10^8 enhancement in light-matter interactions over standard cuvettes, permitting measurements in previously inaccessible reaction regimes, or with photocatalysts that have low quantum yields.

In this project, the requirements of broadband visible guidance in liquids and reasonable fluid flows at low pressures, suggest that kagomé HC-PCFs and HC-NCFs are best-placed to monitor photocatalytic reactions. These two classes of fibre were investigated herein by experiment.

Chapter 3

Experimental methods

This project aims to track the evolution of chemical species during a photocatalytic reaction via optical techniques. In a previous project by Philipp Koehler at the University of Cambridge, an optical set-up was built for absorption spectroscopy in kagomé fibres.[172] Samples were infiltrated into the fibre through a home-built pressure cell, with the distal end contacted against a glass slide. Improvements to this optical set-up were made with new fibre-mounting processes to reduce drift of fibre facets and restrict the stress exerted on the fibres during sealing. This was found to reduce transmission losses and favour the excitation of lower-order modes. Both proximal and distal ends of the fibre were sealed with home-built pressure cells to improve temporal stability. Syringe pumps were also integrated into the optical set-ups with sample delivery tubing upgraded to those with lower elastic compliances, to limit residual flows during static measurements.

A new optical set-up was built for fluorescence measurements with fluorescent excitation possible through the side of the fibre, or by coupling the light from a 405 nm laser diode into the HC-PCF core.

This chapter details the optical set-ups designed to facilitate fibre-based optofluidic measurements along with the transmission properties of the HC-PCFs utilised in this project. In addition, the fluidic aspects of sample delivery are considered.

3.1   Optical setup

Two optical set-ups were utilised in this project, referred to as the Absorption setup and the Fluorescence setup. The Absorption setup consists of both an excitation source and a probe source, whereas the Fluorescence setup foregoes the probe source. Both optical setups were designed to have a modular excitation source that could be switched out, for example, to change the excitation wavelength.

Herein the light sources, pressure cells, fibre preparation processes and optical alignment processes are described with full details of the Absorption and Fluorescence setups provided.

3.1.1 Light sources

Three excitation sources to drive the photochemical reactions and two probe sources to monitor the photochemical reactions were used in experiments. The excitation sources consisted of HepatoChem EvoluChem LEDs at three different wavelengths: 365 nm, 405 nm and 450 nm. To ensure a homogeneous excitation profile, the sample was side-irradiated over a 5 cm length of the HC-PCF with an optical diffuser (Thorlabs DG20-220-MD) as shown in Figure 3.1. The irradiance was adjusted using 2" x 2" neutral density (ND) filters placed on a 3D-printed stage. The spectroscopic profiles of each source are shown in Figure 3.2, normalised to the power incident at the position of the fibre as measured by a Thorlabs S120VC photodiode, without any ND filter in place.
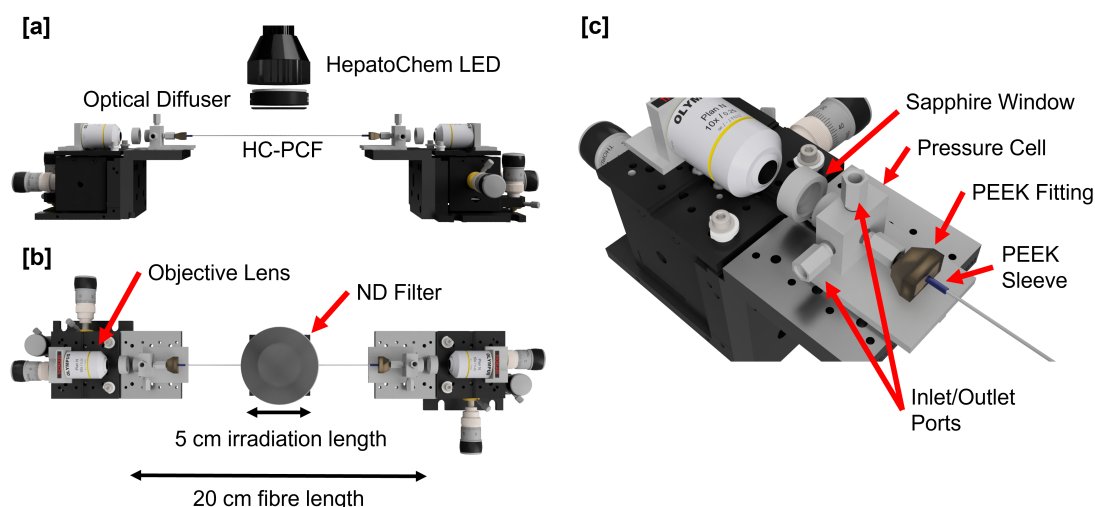
Figure 3.1: 3D renderings of the pressure cells, excitation geometry and fibre-coupling optics. The 3D-printed neutral density (ND) filter stage and inlet/outlet tubing are omitted for clarity. (a) Side view showing the excitation source with optical diffuser above the HC-PCF. (b) Top view showing the square ND filters used to modify the irradiance, together with the 5 cm irradiation and 20 cm fibre lengths. (c) Magnified rendering of the pressure cell. HC-PCFs were sealed using polyether ether ketone (PEEK) sleeves and commercially available microfluidic PEEK fittings.
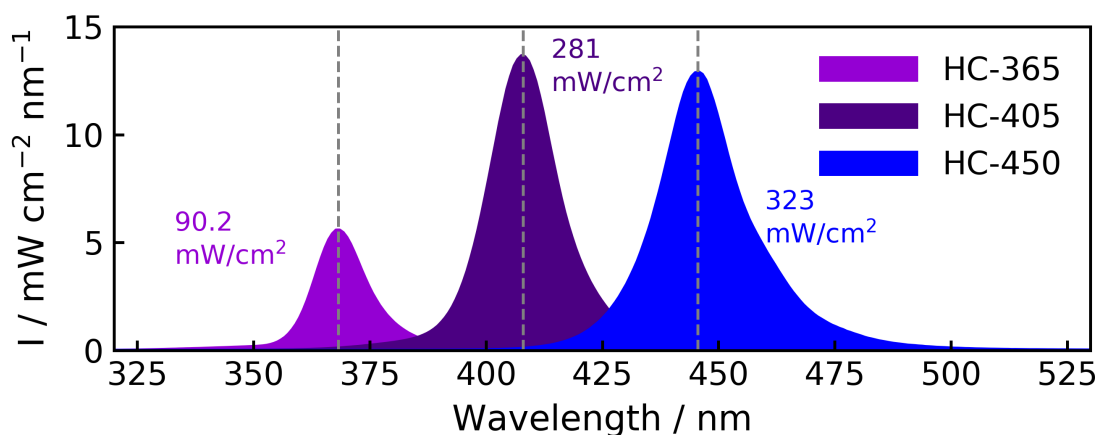
Figure 3.2: Spectroscopic profiles of the three excitation sources used in experiments, normalised to the incident power at the position of the fibre. Full-width half-maximum (FWHM) values of each source are 13 nm, 17 nm and 20 nm for the 365 nm, 405 nm and 450 nm sources respectively.

The probe source used for fibre-based measurements was a NKT SuperK Compact supercontinuum laser. The fibre-coupled output emits a slightly elliptical Gaussian beam with a mode field diameter that can be decomposed into an x-component of 656 µm and y-component of 706 µm. A 450 nm long-pass filter was placed in the beam path and the incident power coupled into the HC-PCF was reduced to 2.2 µW to prevent the probe source from driving the photochemical reaction. The probe geometry is shown in Figure 3.1c. For cuvette-based measurements, the probe source used was an Ocean Optics DH-2000 halogen lamp due to the larger spot size. The spectroscopic profiles for each probe source are shown in Figure 3.3.
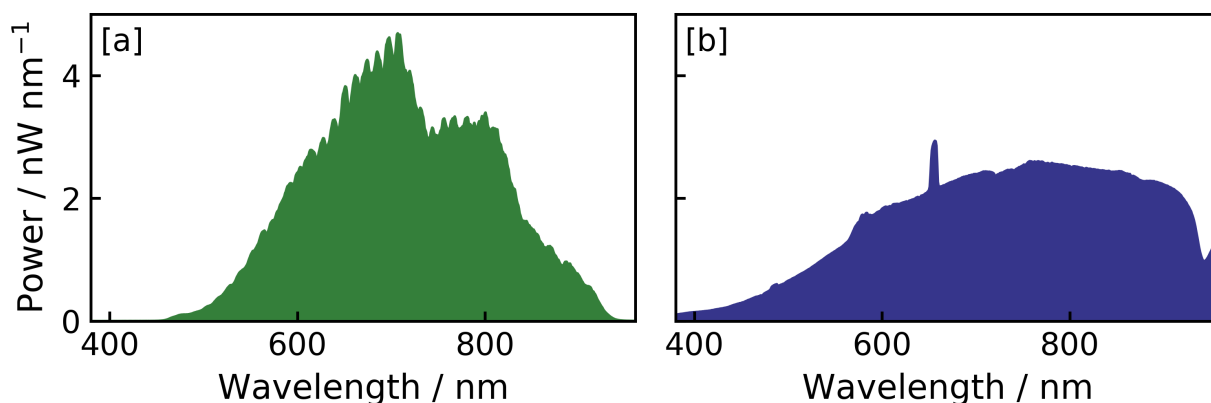
Figure 3.3: Spectroscopic profiles of the two probe sources used in experiments, normalised to 1 mW. The NKT SuperK Compact supercontinuum laser having passed through a 450 nm long-pass filter and a water-infiltrated kagomé-fibre is shown in (a), with the fibre-coupled output of the Ocean Optics DH-2000 halogen lamp shown in (b).

3.1.2   Pressure cells

Custom-designed pressure cells were manufactured to interface the HC-PCFs with microfluidic tubing, whilst retaining optical accessibility of the fibre facet. The CAD drawings of the pressure cell are shown in Figure 3.4.

The cell body is sealed with a cap containing a sapphire window. A polymer O-ring ensures that the cap creates a tight seal with the cell body. This polymer O-ring is placed within the labelled indent prior to sealing. The entry port on the pressure cell directs liquid sample to an enclosed volume with the fibre facet. The dead volume within the pressure cell is minimised to 50 µL by reducing this enclosed volume as far as possible and drilling out thin 1 mm channels. The exit port enables the enclosed volume to be drained where necessary. Closing the valve on the exit port forces the liquid sample through the HC-PCF, with the fluidic aspects of this sample loading considered in Section 3.2.

Concurrent to the loading process, the probe light can be coupled into the proximal end of the fibre through the transparent sapphire window, and the guided light transmitted out through the sapphire window at the distal end.
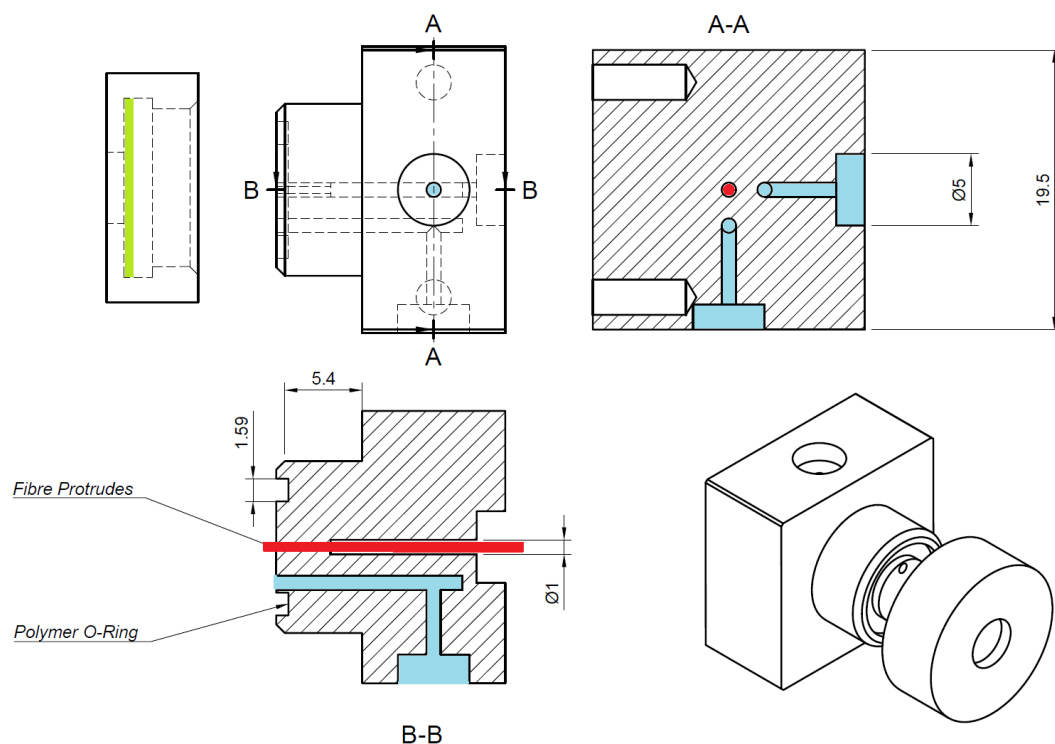
Figure 3.4: CAD drawing of the pressure cells used in these experiments. A vertical cross-section (A-A) is shown with the regions filled with liquid sample during a measurement coloured light blue. A horizontal cross-section (B-B) shows the protruding HC-PCF in red. A cap with a sapphire window (shown in green) is screwed onto the pressure cell to create a sealed volume, aided by a polymer O-ring which is placed in the 1.59 mm wide indent. All dimensions in mm.

3.1.3 Fibre preparation

HC-PCFs were prepared for experiments by cutting a 25 cm length from a spool. The HC-PCF was then stripped of its protective polymer coating using a razor blade. This removes the possibility of the polymer coating absorbing light from the excitation source, and was found to seal more effectively. The fibre was then threaded through a polyether ether ketone (PEEK) sleeve, which enable the fibre to be sealed with commercially available 1/16" microfluidic components. IDEX F-240 Blue sleeves were used with the kagomé fibre 20110315-02. The fibre and PEEK sleeve were then threaded through a commercially available microfluidic fitting and screwed loosely into the custom-built pressure cell as shown in Figure 3.1c. The fibre was then pushed through the pressure cell until the facet was protruding from the other side, and a ceramic cleaving tile used to create a surface crack. The end facet was then tapped with the ceramic tile to fracture the fibre leaving a clean flat facet. The fibre facet was then imaged using a microscope to check the quality of the cleave. The cleaving procedure was repeated if a flat cleave was not achieved. The fibre facet was then positioned within 1 mm of the sapphire window in the pressure cell and the microfluidic fitting tightened to seal off the fibre. The cleaving process was then repeated with the opposite end of the fibre. No glues were required to seal the fibre-PEEK sleeve interface.

3.1.4 Optical alignment

Optical coupling of light sources into the HC-PCF was achieved by using two mirrors and objective lenses mounted on Thorlabs MBT616D 3-axis stages. An Olympus PLN 10x objective with a 10.6 mm working distance was used for these purposes. The output from the laser source was directed into the centre of the objective lens using the two mirrors, which focusses the beam onto the fibre facet. Adjustments in all three planes of the stage were then performed to optimise the number of counts at the spectrometer. Following this, the set of two mirrors were used to *walk the beam*. This process is well described by Koehler.[172] The four degrees of freedom offered by two mirrors (x, y, θ_x, θ_y) enables the correct (x,y) position and incident angle (θ_x, θ_y) to be achieved for exciting the fundamental LP_{01} mode of the fibre. It is desirable for this fundamental mode to be excited since it has a well-defined intensity distribution across the hollow-core.

Preliminary work found that the propagation of additional higher order modes could also result in detrimental modal beating with an unstable baseline for absorption referencing. This effect was minimised by collecting all the light emitted from the fibre into a multi-mode fibre (MMF).

3.1.5 Absorption setup

An absorption spectroscopy setup was upgraded from previous work.[172] The upgraded setup is shown in Figure 3.5 and the individual components listed in Table 3.1. The changes made include sealing the HC-PCF at both ends using pressure cells to minimise drift of the fibre facets and evaporation of solvent. In previous work, the fibre was only sealed by a pressure cell at the distal end, and a glass slide used to contact the HC-PCF at the proximal end. The optical coupling to kagomé fibre 20110315-02 was also improved by replacing the 4x objective with a 10x objective. The fluidic delivery of sample was modified to include a syringe pump (Aladdin AL-1000) with flow rate control and the integration of 0.2 µm cellulose acetate filters to prevent particulate matter blocking the fibre. In previous work, a nitrogen gas overpressure in a sealed sample container was used to drive a sample into the pressure cell, with limited control of flow rate and no filtering.

The absorption setup also employs two flip mirrors to steer the beam through a 1 cm cuvette and then to the spectrometer for time-resolved preliminary measurements. This was unachievable with a conventional UV-Vis spectrophotometer. The cuvette was placed on a magnetic stirring stage to ensure sufficient mixing of the sample volume. An excitation source could then be placed at right angles to this probe beam to monitor the progress of a photochemical reaction.

3.1.6 Fluorescence setup

A Fluorescence spectroscopy setup was built based on the principles of the absorption setup. The major difference is the negated requirement for a broadband light source. This setup is shown in Figure 3.6 and the individual components listed in Table 3.2. Two excitation

Component	Part Identifier	Description
Camera	IDS uEye UI-3240LE-NIR-GL	
Spectrometer	Ocean Optics QE65000	
Broadband Source (1)	NKT Photonics SuperK Compact	Supercontinuum Laser
Broadband Source (2)	Ocean Optics DH2000	Halogen Lamp
M1-M6	Thorlabs PF05-03-P01	
FM1-FM2	Thorlabs PF05-03-P01	
O1, O2	Edmund Optics 86-813	10x
A1	Thorlabs D25S	Aperture
BS	Thorlabs BS010	Non-Polarizing
MMF	Thorlabs BFH37-300	Fibre Patch Lead
f=250mm	Thorlabs AC254-250-A-ML	
f=500mm	Thorlabs AC254-500-A-ML	
f=7.86mm	Thorlabs F240APC-A	Fibre Collimation Package
450nm LP Filter	Thorlabs FEL0450	

Table 3.1: Optical components used in the absorption setup to realise fibre-based spectroscopy.

geometries are possible: side-irradiation using the HepatoChem EvoluChem LEDs and an optical diffuser, or by coupling a laser diode into the HC-PCF core.

The output from a Thorlabs 405 nm laser diode could be coupled into the fibre core using two mirrors and a 10x objective as before. However, due to the elliptical nature of the diode output (3.8 mm x 1.8 mm), the laser beam was first coupled into a single mode fibre (SMF) to clean up the mode into a circular shape. This was achieved using an Olympus 10x objective. The cleaned beam profile was then enlarged by an Olympus 40x objective and collimated. Neutral density (ND) filters were used to adjust the irradiance.

The fluorescent light, either excited by side-irradiance or by coupling a laser diode into the HC-PCF core, was captured using an Olympus 10x objective and directed towards a beam splitter. This enabled both the transmitted mode to be analysed by a camera, and its spectrum by a spectrometer. An Olympus 20x objective and multi-mode fibre (MMF) were used to deliver the transmitted light to a spectrometer.

3.2   Fluidic setup

PEEK tubing was utilised to connect the syringe pump to the entrance port of the pressure cell, as shown in Figure 3.7a. Exit ports were connected to additional PEEK tubing with waste directed towards small glass beakers. To a load a sample, valves V1 and V3 were opened to fill the pressure cell. Once the pressure cell was flowed through with 500 µL of sample, valve V3 was closed and valve V2 was opened to fill the HC-PCF at a set flow rate of $20\,\mu L\,min^{-1}$ on the syringe pump. Once at least 1 µL was flowed through the HC-PCF, the syringe pump was stopped and valve V3 opened to relieve the residual pressure. The system was then left to equilibrate for 5 minutes, before all valves were closed and a spectroscopic measurement started.
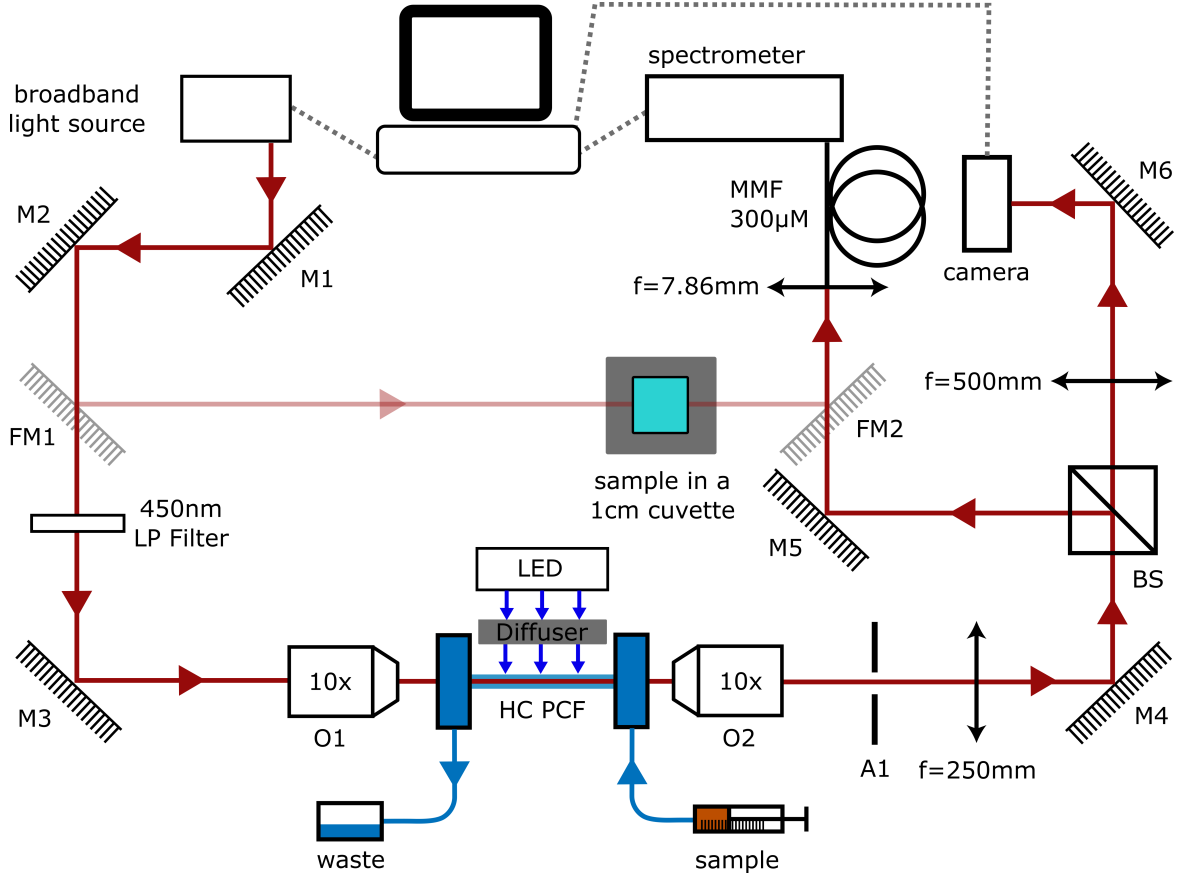
Figure 3.5: Schematic of the absorption setup (not to scale). The output from a broadband light source (top left) was passed through a 450 nm long-pass (LP) filter, then steered and coupled into a fibre using an Olympus 10x objective. On the out-coupling side, an Olympus 10x objective was used to form an intermediate image plane at the aperture (A1), where light from the core was spatially selected and light from the fibre walls was cut out. The beam was then collimated using a f = 250 mm lens and passed through a 50/50 beam splitter (BS). One path was focused onto a CCD using a f = 500 mm lens, whilst the other path was coupled into a 300 μm multi-mode fibre (MMF) using a f = 7.86 mm lens and delivered to the spectrometer. A flip mirror (FM1) enabled the beam to be steered through a cuvette for preliminary measurements.

To determine whether the flow through the core of a HC-PCF is in the laminar flow regime, the Reynolds number, Re, is calculated. This is defined as

$$\text{Re} = \frac{\rho}{\eta}\bar{v}d_H \tag{3.1}$$

where ρ is the mass density, η is the dynamic viscosity, $\bar{v}$ is the fluid velocity and d_H is the hydraulic diameter of the channel. For Re < 2100, the viscous interaction between the fluid and wall is strong, resulting in laminar flow.[173] For a fluid velocity of $10\,\text{cm}\,\text{s}^{-1}$ through a 20 μm channel with water at room temperature ($\rho = 10^3\,\text{kg}\,\text{m}^{-3}$, $\eta = 10^{-3}\,\text{N}\,\text{s}\,\text{m}^{-2}$), Re = 2, so we are comfortably in the laminar flow regime. The same calculation for acetonitrile ($\rho = 7.8 \times 10^2\,\text{kg}\,\text{m}^{-3}$, $\eta = 3.4 \times 10^{-5}\,\text{N}\,\text{s}\,\text{m}^{-2}$) results in Re = 46.
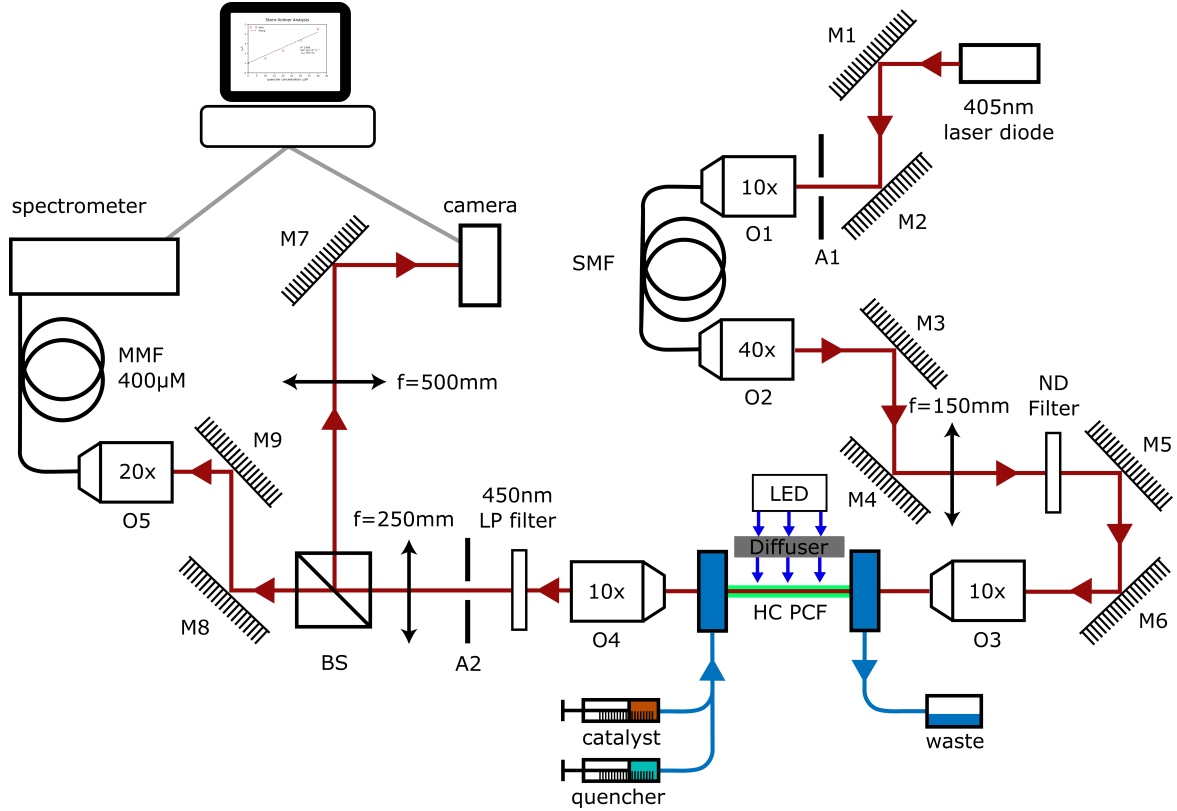
Figure 3.6: Schematic of the fluorescence setup (not to scale). The output from the 405 nm (top right) laser diode was cleaned by coupling the beam through a single mode fibre (SMF) using an Olympus 10x objective. On the out-coupling side, an Olympus 40x objective was used to form an intermediate image plane. The beam was then collimated using a f = 150 mm lens and passed through a neutral density (ND) filter. The beam was then steered and coupled into a HC-PCF using using an Olympus 10x objective. Alternatively, excitation could be achieved by side-irradiating a 5 cm length of fibre using a LED and optical diffuser. On the out-coupling side, an Olympus 10x objective was used to form an intermediate image plane at the aperture (A2), after passing through a 450 nm long-pass (LP) filter. The beam was then collimated using a f = 250 mm lens and passed through a 50/50 beam splitter (BS). One path was focused onto a CCD using a f = 500 mm lens, whilst the other path was coupled into a 400 μm multi-mode fibre (MMF) using an Olympus 20x objective, and delivered to the spectrometer.

Incompressible Newtonian fluids undergoing laminar flow through a long cylindrical channel can be described by the Hagen–Poiseuille equation.

$$|\Delta p| = \frac{8A\bar{v}L\eta}{\pi r^4} \tag{3.2}$$

where $|\Delta p|$ is the pressure drop across the cylindrical channel of length L, radius r and cross-sectional area A.[173] These parameters are shown in Figure 3.7b. Substituting Equation 3.2 into Equation 3.1 gives

$$|\Delta p| = \frac{4\eta^2 L}{\rho r^3} Re \tag{3.3}$$

which means the pressure drop we must apply to a 20 cm long channel to achieve a fluid velocity of 10 cm s^{-1} is 1.6×10^6 Pa in water and 5.4×10^4 Pa in acetonitrile. This pressure difference results in a parabolic velocity profile with a peak velocity given by $\bar{v}$.

Component	Part Identifier	Description
Camera	IDS uEye UI-3240LE-NIR-GL	
Spectrometer	Ocean Optics QE65000	
405 nm Laser Diode	Thorlabs CPS405	
M1-M9	Thorlabs PF05-03-P01	
O1, O3, O4	Edmund Optics 86-813	10x
O2	Edmund Optics 86-815	40x
O5	Edmund Optics 86-814	20x
A1-A2	Thorlabs D25S	Aperture
BS	Thorlabs BS010	Non-Polarizing
SMF	SM300	
MMF	Thorlabs M131L02	Fibre Patch Lead
f=150mm	Thorlabs AC254-150-A-ML	
f=250mm	Thorlabs AC254-250-A-ML	
f=500mm	Thorlabs AC254-500-A-ML	
450nm LP Filter	Thorlabs FEL0450	

Table 3.2: Optical components used in the fluorescence setup to realise fibre-based spectroscopy.
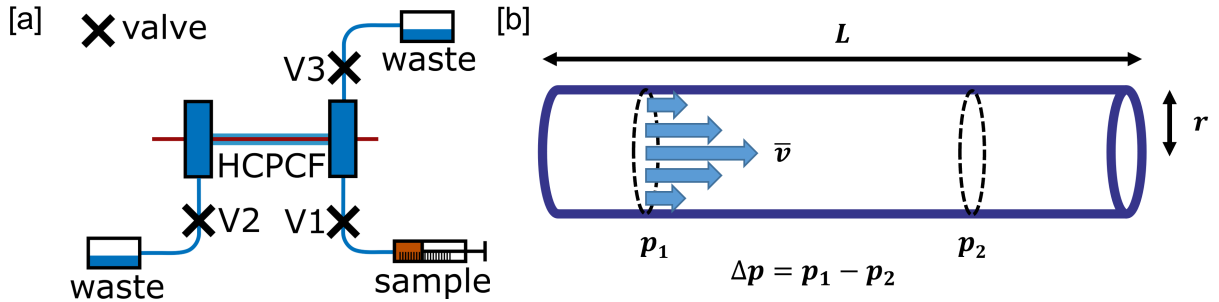
Figure 3.7: Fluidic setup with pressure cells and valves are shown in (a) with the parameters in the Hagen-Poiseuille equation shown in (b).

To grasp the volume required to clear through the delivery tubing and HC-PCF, defined here as the *dead volume*, it is useful to consider the volumes of both the delivery tubing and pressure cell. PEEK tubing with an inner diameter of 130 µm was utilised for the sample delivery line. This reduced the tubing dead volume to 2 µL for the 15 cm length of tubing employed. The thick wall of the PEEK tubing also lowered the elastic compliance of the sample delivery line, which prevented residual flows during the static measurements in fibre. The dead volume in the pressure cell is estimated to be 50 µL, giving a total dead volume of 52 µL.

3.3   Fibre characterisation

The resonance condition in air specified in Section 2.3.3, together with the shift in the loss wavelength in a liquid-filled fibre described in Section 2.3.4, can be used to model the transmission properties of a liquid-filled fibre. The condition for resonance and anti-

resonance are described by

$$\lambda_r = \frac{2t}{m}\sqrt{n_2^2 - n_1^2} \qquad \lambda_a = \frac{4t}{2m-1}\sqrt{n_2^2 - n_1^2} \tag{3.4}$$

where λ_r refers to the resonance wavelength, λ_a refers to the anti-resonance wavelength, t refers to the fibre strut thickness, m is the order, n_1 is the refractive index of the liquid and n_2 is the refractive index of silica. Figure 3.9 shows the resonance and anti-resonance bands expected in an air-filled ($n_1 = 1.00$), water-filled ($n_1 = 1.33$) and acetonitrile-filled ($n_1 = 1.34$) HC-PCF.

HC-PCFs were designed to avoid resonance losses in the visible region of the electromagnetic spectrum. Restrictions on current fabrication methods places a lower limit of 150 nm on the strut thickness. Fibres utilised in this project were fabricated by Michael Frosz at the Max Plank Institute for the Science of Light, Erlangen. Two types of hollow-core photonic crystal fibre were fabricated for this project, namely kagomé-type (Figure 3.8b) and single-ring HC-PCFs (Figure 3.8c-d). A HC-PBGF is shown for comparison of the glass micro-structure (Figure 3.8a), although this class of HC-PCF was not considered for performing broadband spectral measurements given their narrow transmission windows.
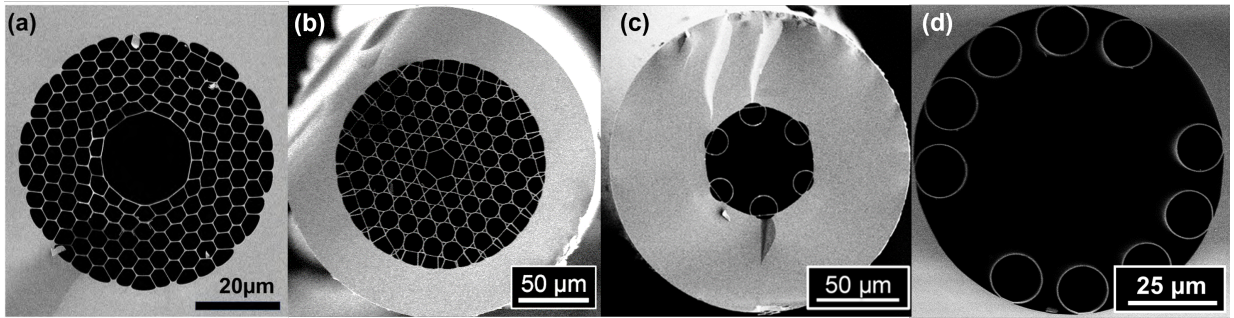
Figure 3.8: (a) SEM micrograph of a 19-cell bandgap-type fibre with a 21 µm core. (b) SEM micrograph of a kagomé-type fibre with a 20 µm core and 160 nm strut thickness. Fibre ID: 20110315-02. (c) SEM micrograph of a single-ring fibre with a 43 µm core and 500 nm strut thickness. Fibre ID: 20190930-1. (d) SEM micrograph of a single-ring fibre with a 71 µm core and 300 nm strut thickness. Fibre ID: 20181019-12-2. All SEM micrographs were obtained from Michael Frosz at the Max Plank Institute for the Science of Light, Erlangen.

3.3.1   Transmission in air

The transmission and modal profiles of a 20 cm length of both NCF 20181019-12-2 and NCF 20190930-1 were characterised in air initially, to determine whether the modelled resonant losses at 630 nm and 560 nm respectively were evident in experiment. Characterisation was performed using a broadband supercontinuum laser (NKT Photonics EXR-15) with a variable bandpass filter (NKT SuperK Varia, 480 nm to 840 nm). The collimated laser beam had a mode field diameter of 429 µm at the objective lens, measured by directing the laser spot onto a CCD and fitting the incident counts to a 2D-Gaussian function. The mode field diameter encloses 86% of the beam's power and is defined where the counts drop off from the central peak by e^{-2}.
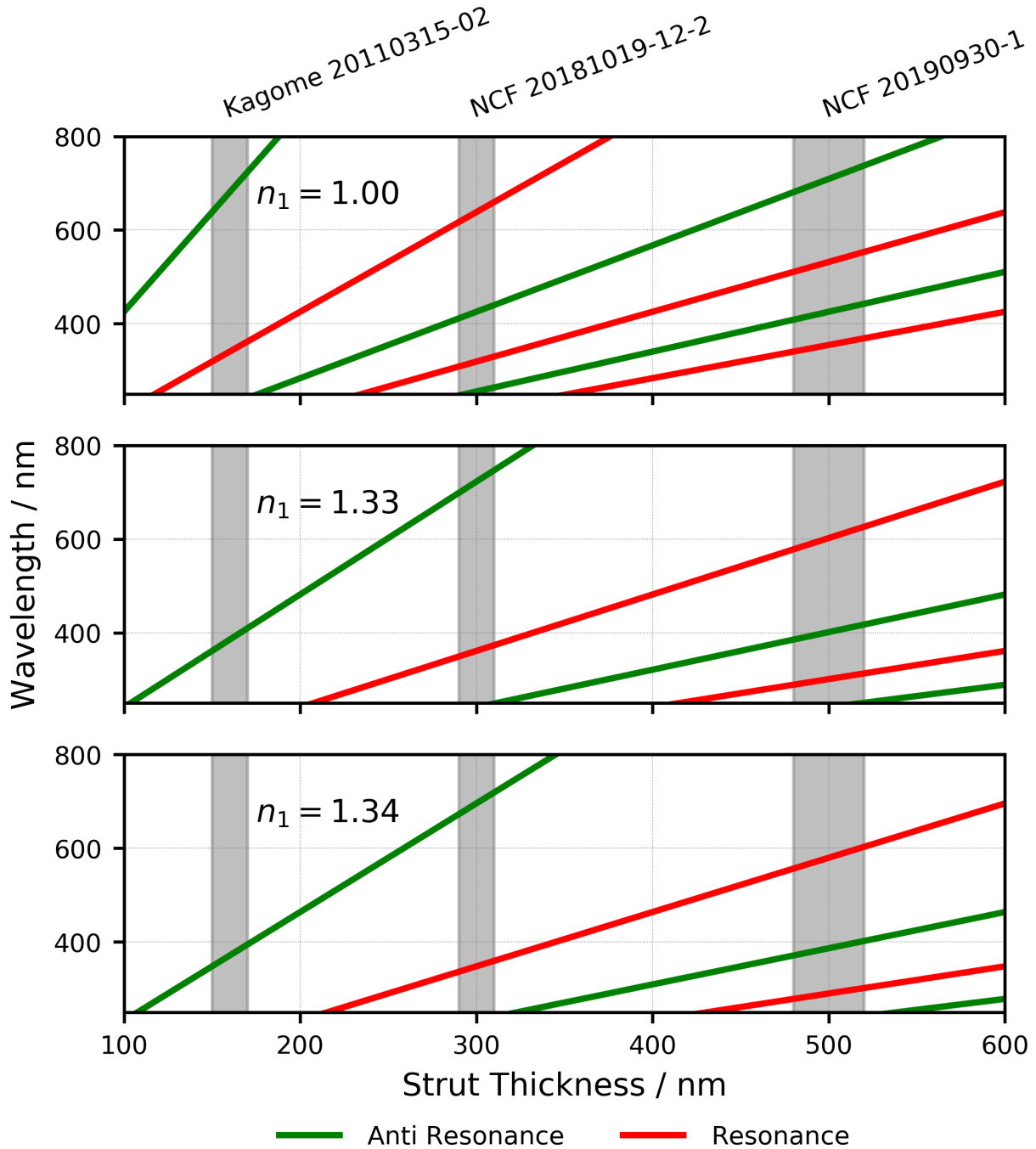
Figure 3.9: Modelled resonances (red) and anti-resonances (green) as a function of silica strut thickness and solvent refractive index, based on the ARROW model. Three HC-PCFs available for experiments are highlighted in grey (fibre references are listed). Higher order resonances and anti-resonances are depicted at increasingly shorter wavelengths. The refractive index of silica was taken as $n_2 = 1.46$. For attributing to specific solvents, a refractive index of $n_1 = 1.33$ corresponds to water and $n_1 = 1.34$ corresponds to acetonitrile.

Optimal coupling can be achieved when the beam waist of a Gaussian beam is equivalent to the HC-PCF core diameter, and is located at the fibre's end facet with the laser beam directed along the longitudinal axis of the fibre (Figure 3.10. The relationship between divergence, θ, and beam waist, ω_0, for a Gaussian beam at a given wavelength, λ, can be

defined by

$$\theta = \frac{2\lambda}{\omega_0 \pi} \qquad (3.5)$$

and the required lens to achieve a divergence, θ, has a focal length, f, defined by

$$f = \frac{d}{2\theta} \qquad (3.6)$$

where d is the mode field diameter of the laser beam incident at the lens. Calculated divergence values are shown in Table 3.3 with the HC-PCFs they correspond to.
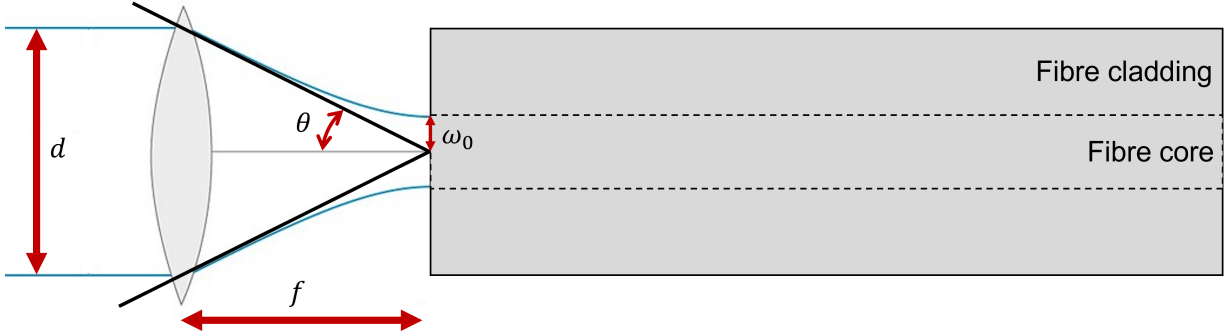
Figure 3.10: Schematic of beam divergence matching to the HC-PCF core size. θ, divergence; ω_0, beam waist; d, mode field diameter; f, focal length.

Fibre	Core radius / μM	Beam divergence required / rad
Kagomé 20110315-02	10	0.019
NCF 20181019-12-2	36	0.0053
NCF 20190930-1	22	0.0087

Table 3.3: Fibre core radii and theoretical optimal beam divergences for laser coupling. Beam divergence is defined at a wavelength of 600 nm and for a laser beam with a mode field diameter of 429 μm.

Consequently, the theoretical optimal lenses for coupling into the Kagomé 20110315-02, NCF 20181019-12-2 and NCF 20190930-1 have focal lengths 11 mm, 40 mm and 25 mm respectively. However, a laser beam was coupled into the NCF 20193009-1 fibre using an Olympus PLN 4x objective (focal length 45 mm, and coupled into the NCF 20181019-12-2 fibre using a $f = 100$ mm lens. It was found that these lenses provided the highest coupling efficiencies in experiments. Transmitted light was out-coupled using an Olympus PLN 10x objective and directed towards a camera.

A wavelength sweep was performed with a 50 nm bandwidth. Fine adjustments to the coupling enabled fundamental LP$_{01}$-like modes to be excited at most wavelengths in both fibres, as depicted in Figure 3.11. A LP$_{11}$-like mode is excited with NCF 20190930-1 at 800 nm. Transmission was calculated by measuring the power at each fibre facet, using a Thorlabs S120VC power meter. Power measurements were taking before the lens for the incident counts, and post-objective for the exit counts.
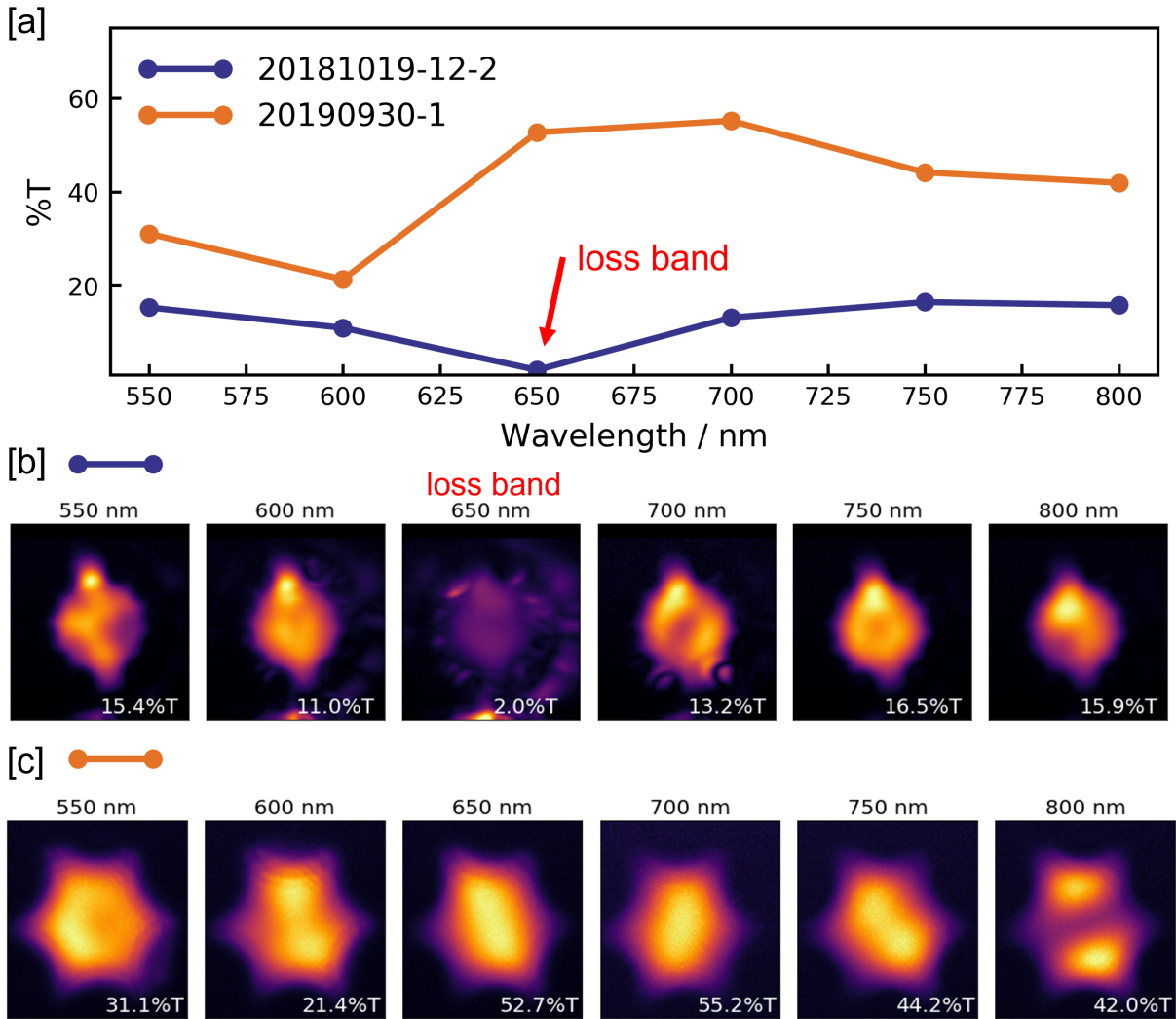
Figure 3.11: (a) Visible light transmission through a 20 cm length of single-ring fibres 20181019-12-2 (core radius 36 μm, Figure 3.8d) and 20190930-1 (core radius 22 μm, Figure 3.8c). (b) Measured mode intensity profiles with fibre 20181019-12-2. (c) Measured mode intensity profiles with fibre 20190930-1. Coupling is optimised for maximum transmission with each data point representing the transmission of a 50 nm band centred at the plotted wavelength.

The maximum transmission achievable in fibre 20181019-12-2 was 17 % at a wavelength of 750 nm, with a loss-band evident at 650 nm. This is clear to see in the mode intensity profile as we have minimal transmission through the core. The maximum transmission achievable in fibre 20190930 was 55 % at a wavelength of 700 nm, with a loss-band evident at 600 nm. Both these result are consistent with the ARROW model. Although efforts were made to match the laser spot size with the fibre core size using different in-coupling lenses, the difference in transmission between the two fibres is likely due to the difference in numerical aperture of each fibre, with the smaller core size of the 20190930 fibre having a closer match to the numerical aperture of the objective lens.

3.3.2 Transmission in liquids

Once the ARROW model was verified with air-filled fibres, optical transmission was characterised when HC-PCFs were infiltrated with water (Figure 3.12) and acetonitrile (Figure 3.13). HC-PCFs were interfaced with standard PEEK microfluidic tubing through custom-designed stainless steel pressure cells with sapphire windows, enabling the HC-PCF to be loaded with a liquid solution whilst remaining optically accessible. HC-PCFs were sealed with PEEK sleeves and finger-tight fittings. The fluidic aspects are discussed in further detail in Section 3.2. The highest coupling efficiencies in water were achieved with an Olympus PLN 10x objective. Discrepancies from the optimal divergences calculated result from the additional air-sapphire window interface and sapphire window-solvent interface. Coupling was optimised at 600 nm and a wavelength sweep performed with a 10 nm bandwidth. Transmission was calculated as before.

LP_{01}-like modes were excited in the kagomé fibre 20110315-02 infiltrated with water and with acetonitrile at most wavelengths measured. However, LP_{11}-like modes were excited between 500 nm and 550 nm with the water-infiltrated fibre. The maximum transmission achievable was 52 % at a wavelength of 550 nm in water, with no resonant loss-bands evident in the wavelength range studied, as predicted by the ARROW model. The transmission in acetonitrile was considerably lower. Clean modes could not be excited in NCF 20190930. This is likely due to the pressure exerted at the in-coupling fibre facet by the PEEK sleeve, together with the larger core that increases sensitivity to bending losses. Some transmission is discernible through the silica capillaries surrounding the core. Inhomogeneous pressure application and local bending of the fibre is known to result in the excitation of higher order modes and greater transmission losses. The maximum transmission achievable in NCF 20190930 was 15 % at a wavelength of 625 nm in water, with no resonant loss-bands evident. The drop in transmission with acetonitrile is observable with this fibre, although this is unprecedented given the small refractive index contrast between water and acetonitrile and the negligible absorbance of these solvents at visible wavelengths.

3.4 Conclusions

The best transmission characteristics, in terms of broadband guidance at visible wavelengths, and the cleanest optical modes were observed with kagomé fibre 20110315-02. Consequently, lengths of this fibre were used to perform spectroscopy measurements on photochemical reactions facilitated in water and acetonitrile.
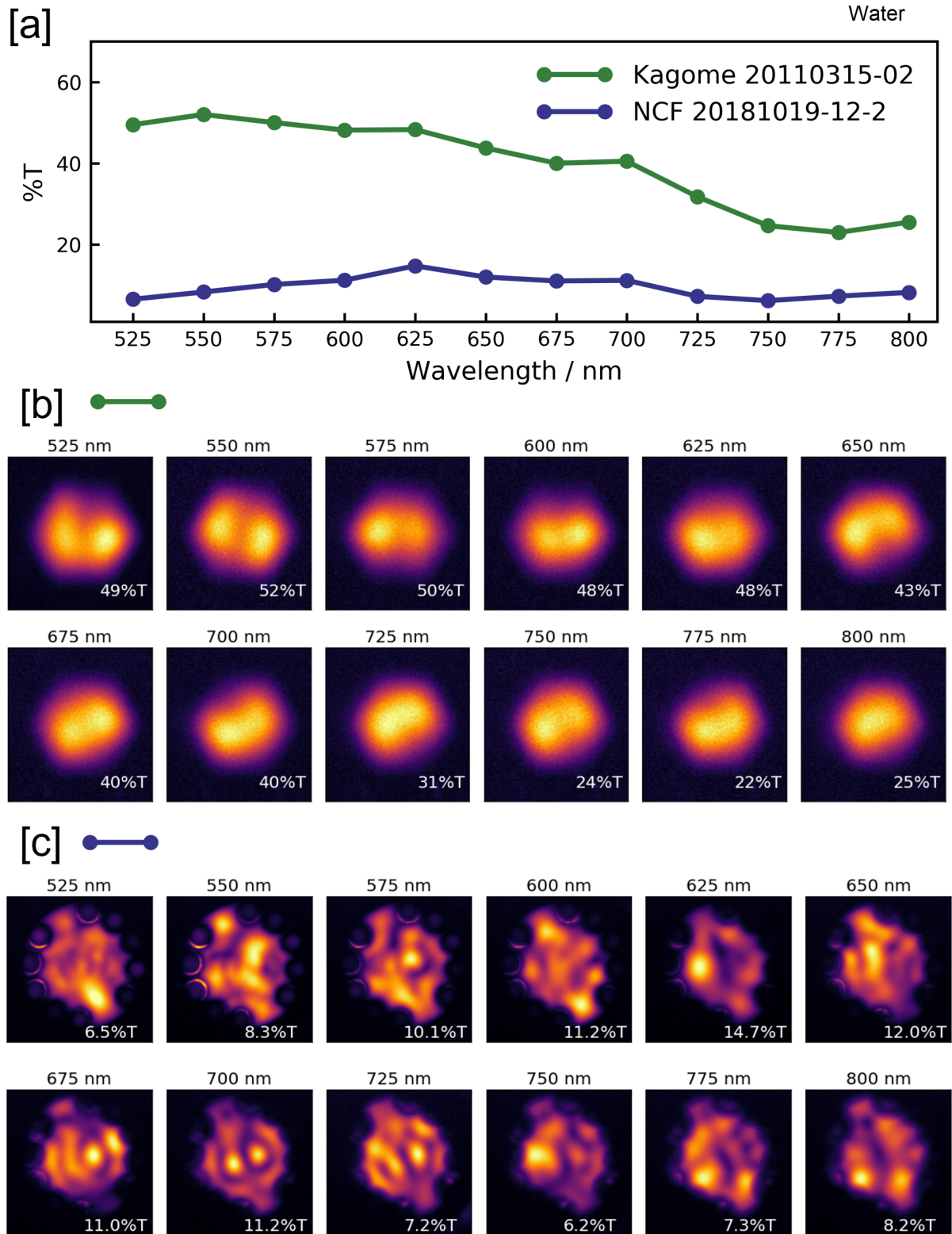
Figure 3.12: (a) Visible light transmission through a 20 cm length of kagomé fibre 20110315-02 (core radius 10 μm, Figure 3.8b) and single-ring fibre 20181019-12-2 (core radius 36 μm, Figure 3.8d) infiltrated with water. (b) Measured mode intensity profiles with fibre 20110315-02. (c) Measured mode intensity profiles with fibre 20181019-12-2. Coupling is optimised for maximum transmission with each data point representing the transmission of a 10 nm band centred at the plotted wavelength.

51
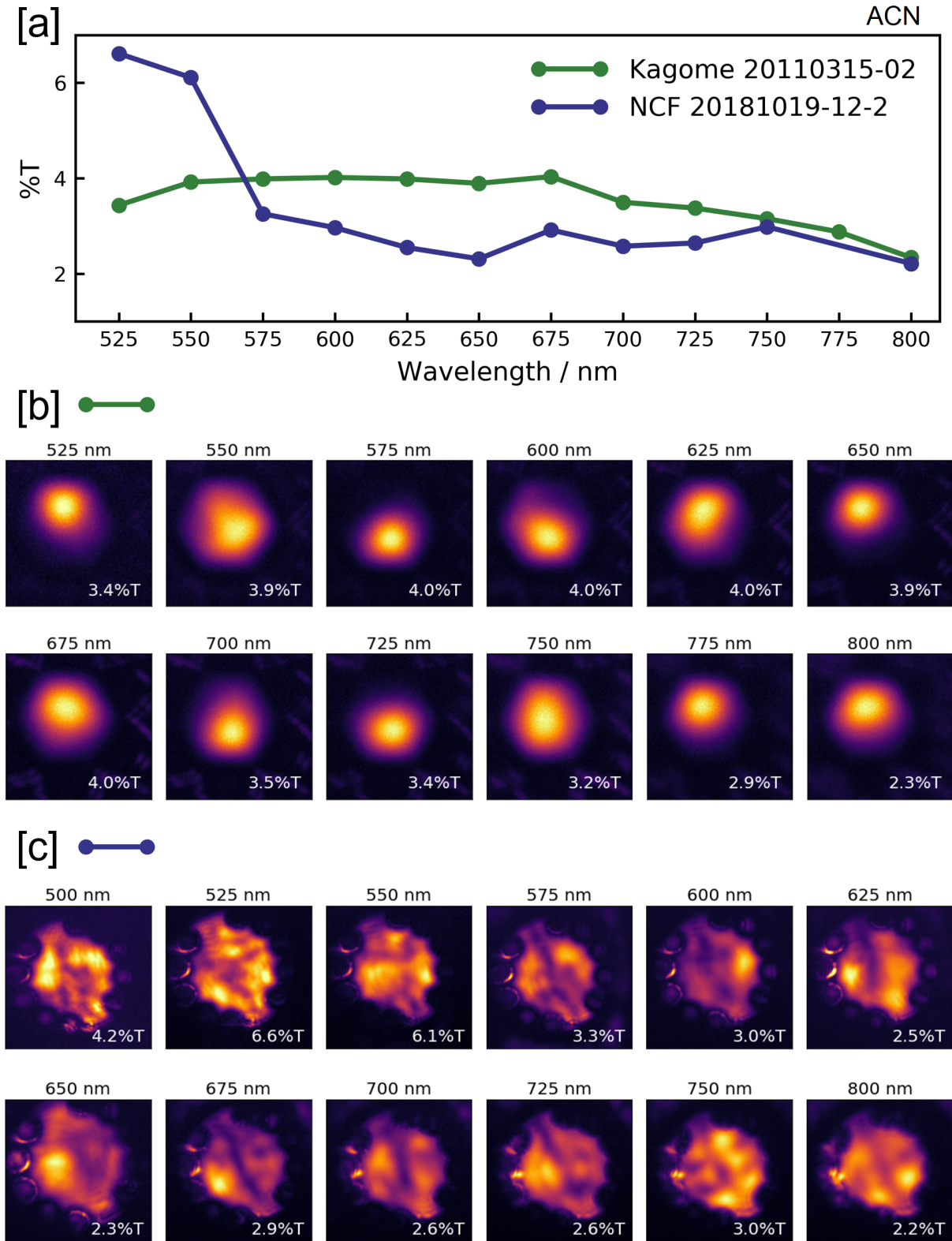
Figure 3.13: (a) Visible light transmission through a 20 cm length of kagomé fibre 20110315-02 (core radius 10 μm, Figure 3.8b) and single-ring fibre 20181019-12-2 (core radius 36 μm, Figure 3.8d) infiltrated with acetonitrile. (b) Measured mode intensity profiles with fibre 20110315-02 (c) Measured mode intensity profiles with fibre 20181019-12-2. Coupling is optimised for maximum transmission with each data point representing the transmission of a 10 nm band centred at the plotted wavelength.

Chapter 4

Low volume reaction monitoring of carbon nanodots

The contents of this chapter have resulted in the following publications:

<u>Takashi Lawson</u>, Alexander S. Gentleman, Ava Lage, Carla Casadevall, Michael H. Frosz, Erwin Reisner, and Tijmen G. Euser. 'Low volume reaction monitoring of carbon nanodot light absorbers in optofluidic microreactors'. **(in preparation)**.

Results presented in this chapter were solely obtained and analysed by the author of this thesis. Carbon nanodots were synthesised by Ava Lage.

In this chapter, HC-PCF microreactors are used for *in-situ* reaction monitoring via electronic absorption spectroscopy. Specifically, HC-PCF microreactors are used for optical screening of carbon nanodots (CDs), a nanometer-sized material that is emerging as a homogeneous light-absorber in photocatalysis. The CD-driven photoreduction reaction of viologens (XV^{2+}) to the corresponding radical cation $XV^{\bullet+}$ is monitored as a model reaction, using a sample volume of $1\,\mu L$ per measurement and with a detectability of $<1\,\mu M$.

A range of different reaction conditions have been systemetically studied, including different types of CDs (i.e., amorphous, graphitic, and graphitic nitrogen-doped CDs), viologens and sacrificial electron donors. Furthermore, the excitation irradiance was varied to study its effect on the photoreduction rate.

These findings validate the utility of fibre-based optofluidic microreactors in providing *in-operando* and quantitative kinetic insights whilst conserving sample. Optofluidic microreactors with real-time optical detection form the basis of future automated catalyst screening platforms, where candidates are synthesised on small-scales and at high cost.

4.1 Importance of microreactors

Although the application of carbon dots (CDs) in hydrogen-evolving photocatalysis has been clearly demonstrated,[62,61] the quantum yield of CD-based systems is relatively low ($< 6\%$).[45] Optimisation of these hybrid colloidal photocatalytic systems requires comprehensive knowledge of the reaction kinetics that can only be obtained through screening of different types of CDs, SEDs, and other reaction conditions. For example, the effect of the SED on the reaction rate is poorly understood and hard to rationalise.[20]

Unfortunately, screening processes are challenging as they typically rely on *ex-situ* methods for analysis, which may not necessarily reflect the system under real catalytic conditions and therefore lead to poor reaction optimisation decisions. Consequently, there is a growing need for microreactors, allowing rapid changes in reaction conditions to be monitored *in-operando* under minute reaction volumes.[174,175] HC-PCFs have emerged as an attractive optofluidic platform for such analytical chemistry. A key advantage is that they allow light to be guided along a microfluidic channel over extended lengths, while keeping the internal sample volume very low. HC-PCFs thus enable highly sensitive liquid-phase spectroscopy on sub-μL sample volumes.[117,116,164]

This chapter builds upon previous work demonstrating the use of HC-PCF microreactors for *in-situ* monitoring of CD-driven photoreduction of viologens on detection volumes less than 36 nL.[176] The screening of a vast array of reaction conditions generates new kinetic insights into the photoactivity of CDs. Viologens are used as indicators of electron transfer from CDs, due to their distinctive absorption peaks and their ability to provide insight into single electron transfers. CD-Viologen reactions thus form an excellent test system to understand redox mechanisms independently from catalysis requirements. The performance of CD light absorbers is benchmarked against the conventional photosensitiser $[Ru(bpy)_3]^{2+}$ (bpy = 2,2'-bipyridine). This work aims to demonstrate how fibre-based optofluidic microreactors can provide comprehensive quantitative kinetic insight into photochemical systems, and identify optimal reaction conditions for photochemistry.

4.2 Exploratory cuvette measurements

The absorption of aqueous samples of carbon dots (amorphous - aCDs, graphitic - gCDs and nitrogen-doped graphitic - NgCDs) were measured in a Cary 300 UV-Vis spectrophotometer to deduce the absorption coefficient as a function of wavelength. These results are shown in Figure 4.1. A sample of $[Ru(bpy)_3]^{2+}$ was also analysed. The spectra show that the absorption of the CDs increase towards UV wavelengths and the peak absorption for $[Ru(bpy)_3]^{2+}$ occurs at 450 nm. This peak corresponds to a metal to ligand charge transfer (MLCT) state. Absorption around 365 nm corresponds to electronic *d-d* transitions.

A sample of 0.5 g L^{-1} amorphous carbon dots (aCDs) in an aqueous pH6 phosphate buffer was prepared in a gas-tight cuvette and purged under nitrogen for 15 minutes. A magnetic stirrer ensured sufficient mixing within the cuvette volume, with a nitrogen over pressure
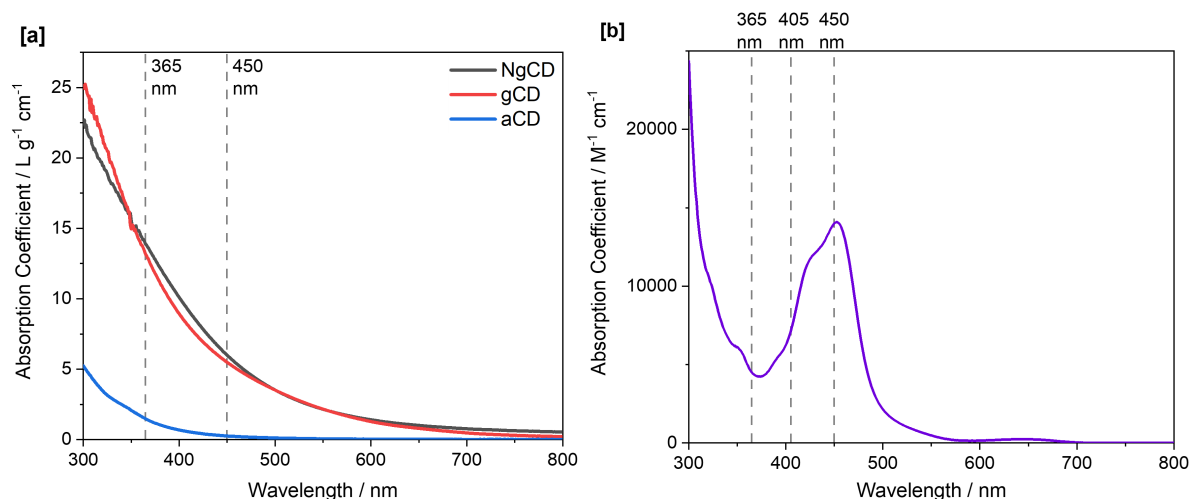
Figure 4.1: Absorption spectra of the three forms of carbon dots in (a) and $[\mathrm{Ru(bpy)_3}]^{2+}$ in (b). Measurements were performed in cuvettes. The wavelengths of the closest excitation sources to the absorption maximum are represented by the dashed lines.

maintained during the spectral measurements. Time-resolved absorption spectra of the sample are shown on XV^{2+} addition in Figure 4.2a and then on addition of EDTA in Figure 4.2b. The aCD sample was subject to UV irradiation ($\lambda = 365\,\mathrm{nm}$, $174\,\mathrm{mW\,cm^{-2}}$) at right angles to the collimated beam from the halogen source (Ocean Optics DH-2000) used to perform absorption spectroscopy. $0.1\,\mathrm{mL}$ of a $1.3\,\mathrm{mM}$ MV^{2+} stock solution was injected using a syringe at $t = 300\,\mathrm{s}$. The spectral measurement was then stopped at $t = 750\,\mathrm{s}$ for the syringe to be cleaned and loaded with EDTA. The measurement was then restarted, and $0.1\,\mathrm{mL}$ of a $0.2\,\mathrm{M}$ EDTA stock solution was added at $t = 120\,\mathrm{s}$. A rapid absorption following EDTA addition was observed, due to the production of the $\mathrm{MV}^{\bullet+}$ radical cation. Both species are required for the radical cation to form. Although the $\mathrm{MV}^{\bullet+}$ radical cation was detectable in cuvette-based measurements with $1\,\mathrm{cm}$ path lengths, the absorbance values are small (0.3), and therefore a longer path length is desirable, while at the same time significantly reducing the sample volume. This is achievable with HC-PCF microreactors and the subject of this chapter.

4.3 Screening scheme

The proposed mechanism of the reaction in the absence of $\mathrm{O_2}$ is summarized in reactions 1-8, based on a study by Mandal *et al.* with $[\mathrm{Ru(bpy)_3}]^{2+}$ as a photosensitiser.[177] The photoexcited CD is reductively quenched,[55] whereby electron transfer to XV^{2+} only proceeds following hole scavenging of CD* by the SED, given the SED is in vast excess relative to XV^{2+} in this study (see Figure 4.4).[20,45] Control measurements confirm that no $\mathrm{XV}^{\bullet+}$ was formed in the absence of a sacrificial electron donor (see Section 4.2). Ideally, the SED will be irreversibly oxidised into inert molecules after electron transfer. However, most SEDs have degradation products which further interact with the photosystem. Reactions (6) and (7) describe the degradation pathway of EDTA, TEA and TEOA, with the deprotonation of the oxidised SED ($\mathrm{SED_{ox}^+}$) followed by a second dark electron transfer.[20]

55
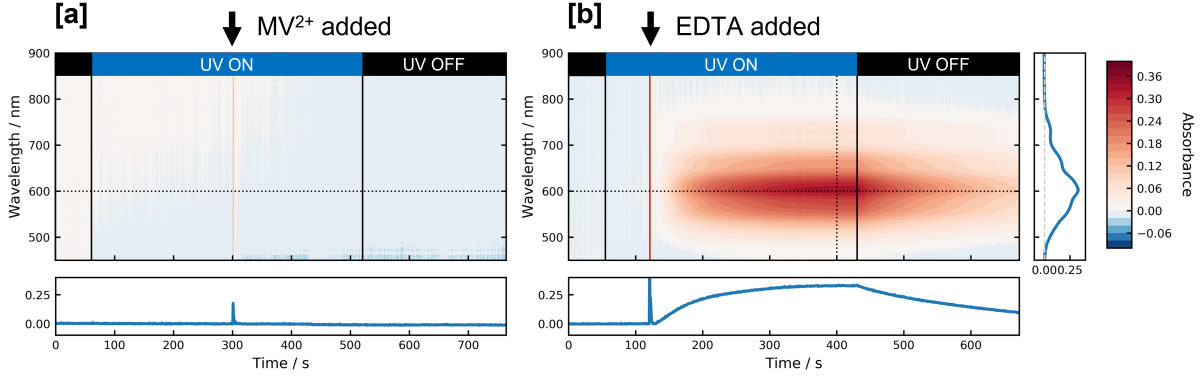
Figure 4.2: Time-resolved absorption spectra of sample containing amorphous carbon dots on addition of the viologen species in (a) and then on addition of EDTA in (b). UV excitation and component addition times are as labelled. The horizontal dotted lines in (a, b) correspond to the absorption time-trace taken at 600 nm, and the vertical dotted line in (b) corresponds to the spectrum shown on the right at $t = 400$ s.

(1) $\text{CD} + \text{h}\nu \rightleftharpoons \text{CD}^*$

(2) $\text{CD}^* + \text{SED} \longrightarrow \text{CD}^- + \text{SED}^+_{\text{ox}}$

(3) $\text{CD}^- + \text{XV}^{2+} \longrightarrow \text{CD} + \text{XV}^{\bullet+}$

(4) $\text{CD}^- + \text{SED}^+_{\text{ox}} \longrightarrow \text{CD} + \text{SED}$

(5) $\text{XV}^{\bullet+} + \text{SED}^+_{\text{ox}} \longrightarrow \text{XV}^{2+} + \text{SED}$

(6) $\text{SED}^+_{\text{ox}} \longrightarrow \text{SED'} + \text{H}^+$

(7) $\text{SED'} + \text{XV}^{2+} \longrightarrow \text{XV}^{\bullet+} + \text{products}$
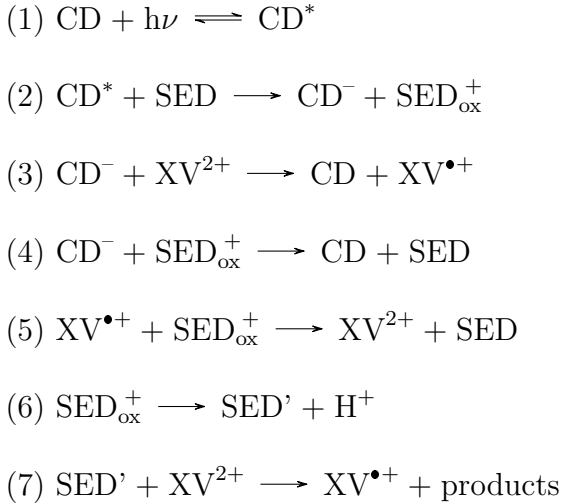
Reaction (1) represents the formation of the photoexcited state of the carbon dot, CD^*, which can be quenched by a sacrificial electron donor in Reaction (2), resulting in an electron-rich carbon dot, CD^- and an oxidised SED species, SED^+_{ox}. Reaction (3) represents the electron transfer from CD^- to XV^{2+} to form a radical cation that we detect via absorption spectroscopy. Reaction (3) competes with the electron transfer described in Reaction (4), where the SED^+_{ox} cannot escape the solvent cage surrounding the carbon dot and reverts back to SED. The $\text{XV}^{\bullet+}$ population can be depleted in an interaction with SED^+_{ox} through Reaction (5), although this contribution is expected to be small in long-term measurements given the SED^+_{ox} species is short lived. For SED^+_{ox}, in the cases of EDTA, TEA and TEOA refers to the aminyl radical species, $\text{R}_2\text{N}^{\bullet+}\text{CH}_2$, which is readily deprotonated to form SED', a carbon-centred radical species and strong reducing agent, $\text{R}_2\text{NC}^{\bullet}\text{H}$, in Reaction (6). SED' can donate a dark electron to XV^{2+} in a secondary route to form $\text{XV}^{\bullet+}$, as shown in Reaction (7). Although this theoretically implies that each SED molecule can participate in two XV^{2+} reductions, in practice the quenching efficiency is 0.5 at best,[20] due to the electron transfer described in Reaction (4).

4.4   Photosensitiser kinetics

Colloidal photoredox catalysis proceeds via electron transfers between the surface states of a nanodot and a substrate. Bloh *et al.* model the reaction kinetics of colloidal systems, considering only the rate-limiting redox half-reaction. Using their approach,[171] the change in reactive surface sites (n^*) in a single carbon nanodot consists of three components. Here we consider the reductive half-reaction.

$$\frac{dn^*}{dt} = c_1 + c_2 + c_3, \tag{4.1}$$

where c_1 refers to the generation of reactive surface sites, c_2 refers to the relaxation of reactive surface sites, and c_3 refers to the electron transfer from reactive surface sites to the substrate.

First, the generation of reactive surface sites (n^*) can be expressed through

$$c_1 = \phi L_p \frac{n}{n_0} \tag{4.2}$$

where ϕ is the quantum yield, L_p is the local volumetric rate of photon absorption (LVRPA), n is the number of surface trap sites in their ground state and n_0 is the total number of available surface trap sites. The quantum yield captures bulk recombination and the migration of excited electrons to surface trap sites.

Second, the relaxation of reactive surface sites can be modelled as a first-order process with a rate constant k_r.

$$c_2 = -k_r \frac{n^*}{n_0} \tag{4.3}$$

Third, the electron transfer from the reactive surface site to the substrate for the simple case of $S + e^- \longrightarrow S^-$ can be described by

$$c_3 = -k_{ET}\theta n^*[S] \tag{4.4}$$

where θ is the surface coverage of the carbon nanodot and $[S]$ is the substrate concentration. Langmuir-Hinshelwood reaction kinetics can be described where θ takes the form of the Langmuir adsorption isotherm and the reaction is photon-limited.[171,178] Taking a steady-state approach, we can assume the population of reactive surface sites remains constant such that

$$0 = \frac{dn^*}{dt} = \phi L_p \frac{n}{n_0} - k_r \frac{n^*}{n_0} - k_{ET}\theta n^*[S]. \tag{4.5}$$

Furthermore, given that we have assumed the reductive half-reaction to be rate-limiting, the replenishment of electrons by the oxidative half-reaction conserves the total number of available states such that $n = n_0 - n^*$. Hence, we can re-arrange for n^* to give

$$n^* = \frac{\phi L_p n_0}{\phi L_p + k_r + \theta k_{ET}[S]n_0}. \tag{4.6}$$

The local rate of formation of S^- is therefore described by

$$\frac{d[S^-]}{dt} = k_{ET}\theta n^*[S] = \frac{\phi L_p \theta k_{ET} n_0 [S]}{\phi L_p + k_r + \theta k_{ET} n_0 [S]}. \tag{4.7}$$

If we normalise the rate constant to a carbon nanodot concentration, $[P]$, such that $n_0 k_{ET} = [P]k'_{ET}$ we can rewrite this as

$$\frac{d[S^-]}{dt} = \frac{\phi L_p \theta k'_{ET} [P][S]}{\phi L_p + k_r + \theta k'_{ET} [P][S]}. \tag{4.8}$$

In the high-photon limit where $\phi L_p \gg (k_r + k'_{ET}[P][S])$, this expression simplifies to the expected second-order rate equation with respect to the carbon nanodot and substrate,

$$\frac{d[S^-]}{dt} = k'_{ET}\theta[P][S]. \tag{4.9}$$

In the low-photon limit where $\phi L_p \ll (k_r + k'_{ET}[P][S])$, this expression simplifies to the expected first-order rate equation with respect to the LVRPA,

$$\frac{d[S^-]}{dt} = \phi L_p \frac{\theta k'_{ET} [P][S]}{k_r + \theta k'_{ET} [P][S]}. \tag{4.10}$$

Here we have not explicitly considered the influence of diffusion on the electron-transfer rate constant, nor have we considered scattering by the carbon nanodots. However, the power-law dependency of the reaction rate (r), with respect to light intensity ($r \propto I^m$), can be explained by the change in the exponent, m, from a low photon limit ($m = 1$) to the high photon limit ($m = 0$). An exemplary dependency of the local reaction rate with LVRPA is shown in Figure 4.3.

4.5 Experimental method

Mechanistic insight into the photoactivity of carbon nanodots was obtained by the systematic screening of four factors, as shown in Figure 4.4a. A 20 cm length of kagomé-style HC-PCF was infiltrated with various aqueous solutions of carbon nanodots, viologens and sacrificial electron donors. The fibre used in this study (Figure 4.4b) was fabricated with a strut thickness of 160 nm to suppress the first resonant loss to 193 nm. Resonant losses were calculated for a fibre infiltrated with water, and assuming a glass refractive index of 1.45. As the fibre is operated at wavelengths above the lowest resonance, broadband light guidance over the entire visible wavelength range is expected.

Additionally, a core region of 30 μm diameter facilitated a UV-Vis detection volume of *ca.* 7 nL cm^{-1}. Further details on the kagomé HC-PCF utilised are discussed in Section 3.3.

Samples were thoroughly purged under nitrogen for at least 15 min prior to loading into the fibre, and inserted through the out-coupling facet to minimise disturbances to the optical coupling. All samples were injected into the pressure cell using gas-tight syringes and a
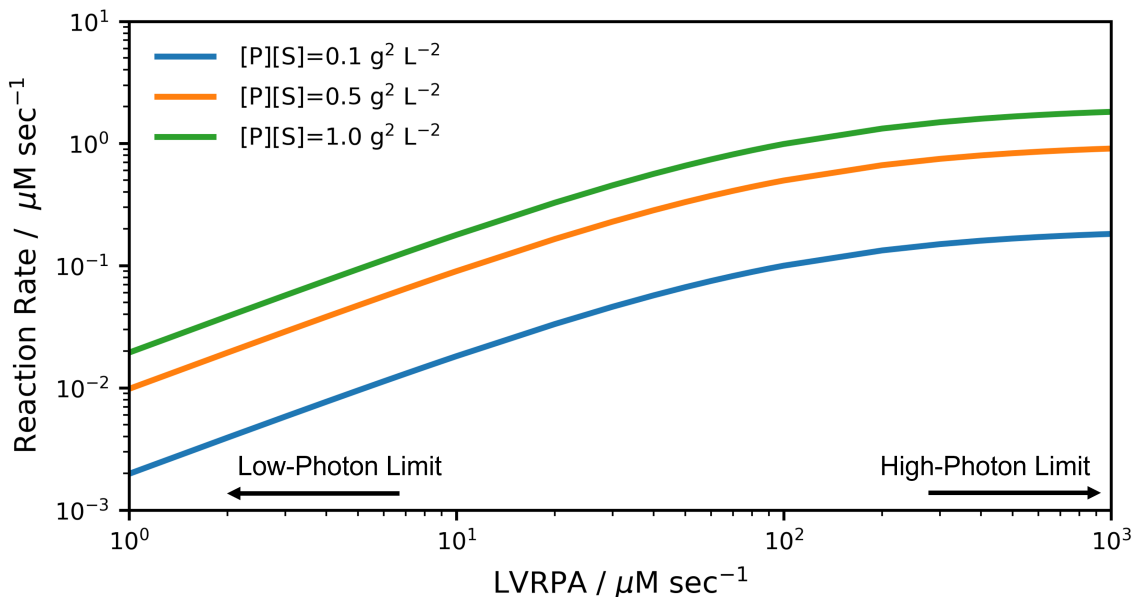
Figure 4.3: Exemplary dependency of the local reaction rate on the LVRPA, plotted at different [P][S] concentrations. Parameters used: $\phi = 1$, $k_r = 100 \, \mu M \, s^{-1}$, $k_{et} = 2 \, \mu M \, g^{-2} \, L^2 \, s^{-1}$, $\theta = 1$.

syringe pump (Aladdin AL-1000), having passed through $0.2 \, \mu m$ pore size cellulose acetate filters to prevent fibre blockages.

Repeat measurement runs were loaded successively into the fibre and started once the spectrum returned to the reference baseline. This ensured that residual reaction products from the previous run had been pushed clear of the fibre. The fibre was cleaned with $200 \, \mu L$ of water ($200\times$ the internal fibre volume) between sample sets of different reaction conditions, and subsequent samples were loaded once the spectrum matched an internal water reference.

A 365 nm UV LED source (HepatoChem EvoluChem 365PF) together with an optical diffuser (Thorlabs DG20-220-MD) was used to side-irradiate a 5 cm section of the HC-PCF, ensuring a homogeneous excitation profile across the 36 nL UV-Vis detection volume (Figure 4.4c). Further details on the optical setup are discussed in Section 3.1.5. The irradiance was varied between $1.6 \, mW \, cm^{-2}$ and $88.4 \, mW \, cm^{-2}$ by placing 2" x 2" absorptive neutral density filters (Thorlabs NE2XXB series) between the excitation source and fibre. A 450 nm blue LED source (HepatoChem EvoluChem 405PF) was additionally utilised to benchmark the performance of NgCDs against $[Ru(bpy)_3]^{2+}$ at an irradiance of $99.1 \, mW \, cm^{-2}$.

4.5.1 Data analysis

Each sample was loaded into the fibre microreactor and subject to UV (365 nm) or blue (450 nm) irradiation, A short period after the excitation source is turned on, a rapid photoinduced absorption peaking at 605 nm is observed, indicating the formation of $XV^{\bullet+}$.[176]
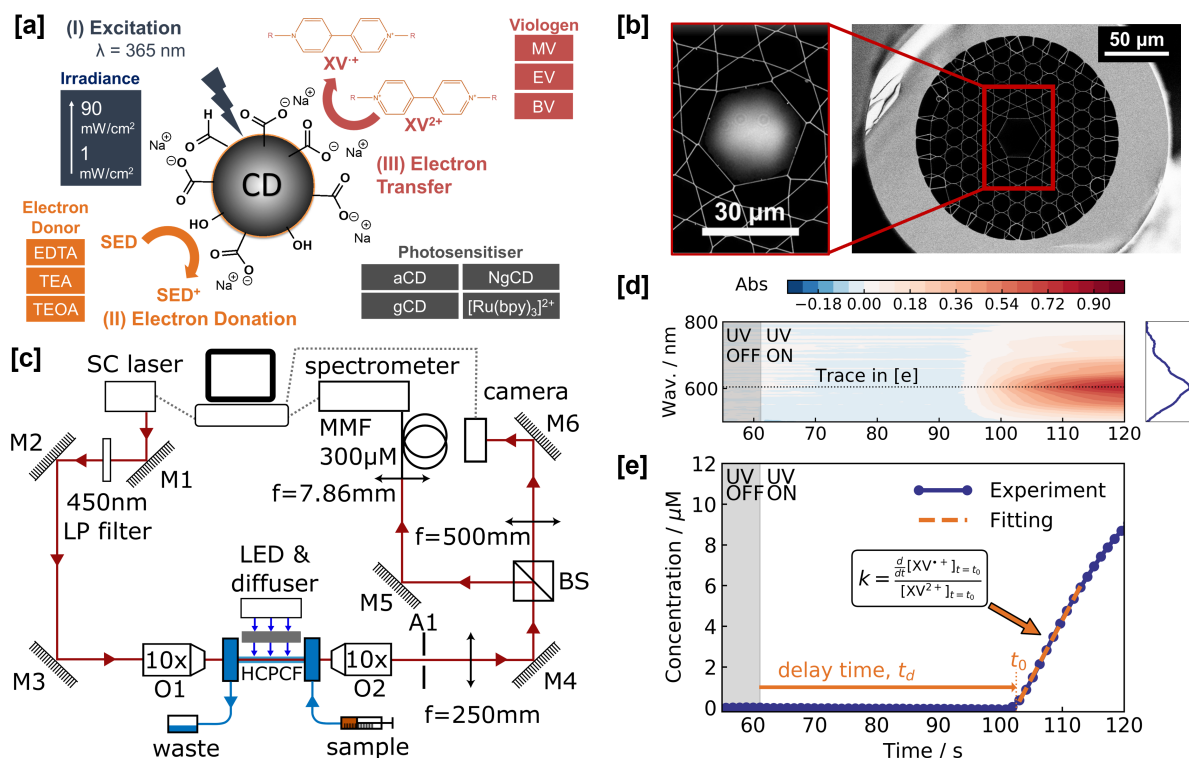
Figure 4.4: Fibre-based carbon dot screening. (a) Schematic of CD-driven photoreduction of viologens and the four screening factors explored in this study: The irradiance, sacrificial electron donor (SED) used, CD photosensitiser type, and viologen species (XV); (b) Scanning electron microscopy (SEM) image of the core region of the kagomé-style hollow-core photonic crystal fibre (HC-PCF) overlaid with the measured mode intensity profile (450 nm - 600 nm). (c) Optical setup enabling the transmitted mode to be simultaneously analysed by a camera (see (c)) and its spectrum by a spectrometer (see (d)). BS, beamsplitter; LP, long-pass; MMF, multimode fibre; SC, supercontinuum. O1 corresponds to the in-coupling objective and O2 corresponds to the out-coupling objective. A1 is an aperture used for alignment. (d) Time-resolved spectra are converted to absorbance with a trace taken at 605 nm to deduce the $XV^{\bullet+}$ concentration in (e). The spectral shape of the absorbance profile is characteristic of a $XV^{\bullet+}$ species; (e) Fitting method for calculating the delay time, t_d, and photoreduction rate constant, k. The time at which the electron transfer starts, t_0 is defined by the x-intercept of the linear fitting function.

Absorbance was converted to concentration by applying the Beer Lambert Law with the reported values of absorption coefficients for MV ($1.3 \times 10^4\,\mathrm{M^{-1}\,cm^{-1}}$), EV ($1.22 \times 10^4\,\mathrm{M^{-1}\,cm^{-1}}$) and BV ($1.4 \times 10^4\,\mathrm{M^{-1}\,cm^{-1}}$).[179,180] The average absorbance within a 10 nm wide band was taken for this conversion around the absorption, following a 1-minute pause in the dark, to ensure that the reference spectrum was stable, and that the probe source (supercontinuum laser) did not drive the reaction, unless stated otherwise (Figure 4.4d). The values of t_d and k were obtained by fitting a linear function to a short time interval following the formation of the $XV^{\bullet+}$ radical cation, as shown in Figure 4.4e. This fitting method ensures that consumable reactants are in excess, and contributions to the formation of $XV^{\bullet+}$ by reduction with SED' are negligible. Therefore, the gradient of the linear fitting function relates to the pseudo first-order photoreduction rate constant, k, by

$$k = \frac{\frac{d}{dt}[XV^{\cdot +}]_{t=t_0}}{[XV^{2+}]_{t=t_0}} \quad (4.11)$$

The x-intercept of the fitted function was used to define the time at which electron transfers start, t_0, and thus define a delay period, t_d, following the excitation source being switched on.

Where rate profiles of the viologen radical cation are presented, a Savitzky-Golay filter was applied to minimise undue noise whilst retaining peak heights.[181] The relevant parameters applied for filtering were a window size of 31 and polynomial order of 3. Savitzky-Golay filtering was not applied to the concentration and percentage conversion profiles presented.

4.5.2 Materials and synthesis of CDs

All chemicals and reagents were purchased from commercial suppliers and used as received unless otherwise noted. Laboratory-grade reagents were used for synthesis, and chemicals for the analytical part were of the highest available purity. Phosphate buffer solutions $(0.2\,\text{M})$ and SED stock solutions $(0.2\,\text{M})$ were prepared and verified using a pH electrode (Mettler Toledo, FiveEasy Plus) at pH 6 and pH 8. The pH of SED stock solutions was adjusted using sodium hydroxide and hydrochloric acid. MV^{2+}, EV^{2+} and BV^{2+} stock solutions were made up by dissolving methyl viologen dichloride, ethyl viologen dibromide and benzyl viologen dichloride salts, respectively. A stock solution of $[\text{Ru(bpy)}_3]^{2+}$ was made up by dissolving tris(bipyridine)ruthenium(II) chloride. All stock solutions were made up using Milli-Q purified water.

All CD types were synthesised and characterised according to previously reported procedures.[62,55] In brief, amorphous carbon nanodots (aCDs) were synthesised by pyrolysis of citric acid at $180\,°\text{C}$ for $40\,\text{h}$, graphitic carbon nanodots (gCDs) were similarly synthesised by pyrolysis of citric acid at $180\,°\text{C}$ for $40\,\text{h}$ followed by pyrolysis at $320\,°\text{C}$ for a further $100\,\text{h}$. Nitrogen-doped carbon nanodots (NgCDs) were synthesized by pyrolysis of aspartic acid at $320\,°\text{C}$ for $100\,\text{h}$. To enhance water solubility, all CD types were neutralised to pH 7 using NaOH and then freeze-dried to obtain the final product as a brown powder.

4.6 Results and discussion

The proposed mechanism in Section 4.3 was verified qualitatively by measuring how the photosystem responded to adjustments in component concentrations. The four component concentrations adjusted in turn were [aCD], [MV^{2+}], [EDTA] and the excitation irradiance. These studies enabled optimal reaction parameters to be determined for aCD-driven photoreduction of methyl viologen in the presence of EDTA . Once these optimal reaction conditions were realised, the effect of changing the viologen species, the SED, pH and the type of CD was explored.

4.6.1 The effect of [aCD]

Samples of $40\,\mu$M MV^{2+} and 0.1 M EDTA were made up in an aqueous pH 6 phosphate buffer, with various concentrations of aCDs. These samples were subject to UV irradiation ($365\,$nm, $90.2\,$mW cm^{-2}), with the corresponding concentration and rate profiles shown in Figures 4.5a-b. As observed, peak radical cation generation is higher when the CD concentration is greater, suggesting a dynamic equilibrium exists between the photoinduced rate of formation of the radical cation and the depletion rate of the radical cation. At higher concentrations of CDs, the position of equilibrium is shifted towards the radical cation given the higher [CD*]. However, a rise in [CD*] is also associated with a rise in [SED$_{ox}^+$], with the oxidised sacrificial electron donor further accumulating with longer irradiation times and thus interacting with MV$^{\bullet+}$ as in Reaction (5), which results in a greater depletion rate following the peak. This is confirmed by cuvette-based UV-Vis absorption measurements where chemically reduced MV$^{\bullet+}$ in the absence of EDTA is stable in aqueous solutions. Interestingly, the depletion consists of a fast and a slow component. The slow depletion component, within the context of the proposed reaction scheme, is likely a result of the accumulating SED' species at longer times, which drives MV^{2+} reduction, albeit at a much slower rate relative to the CD-facilitated photoreduction.
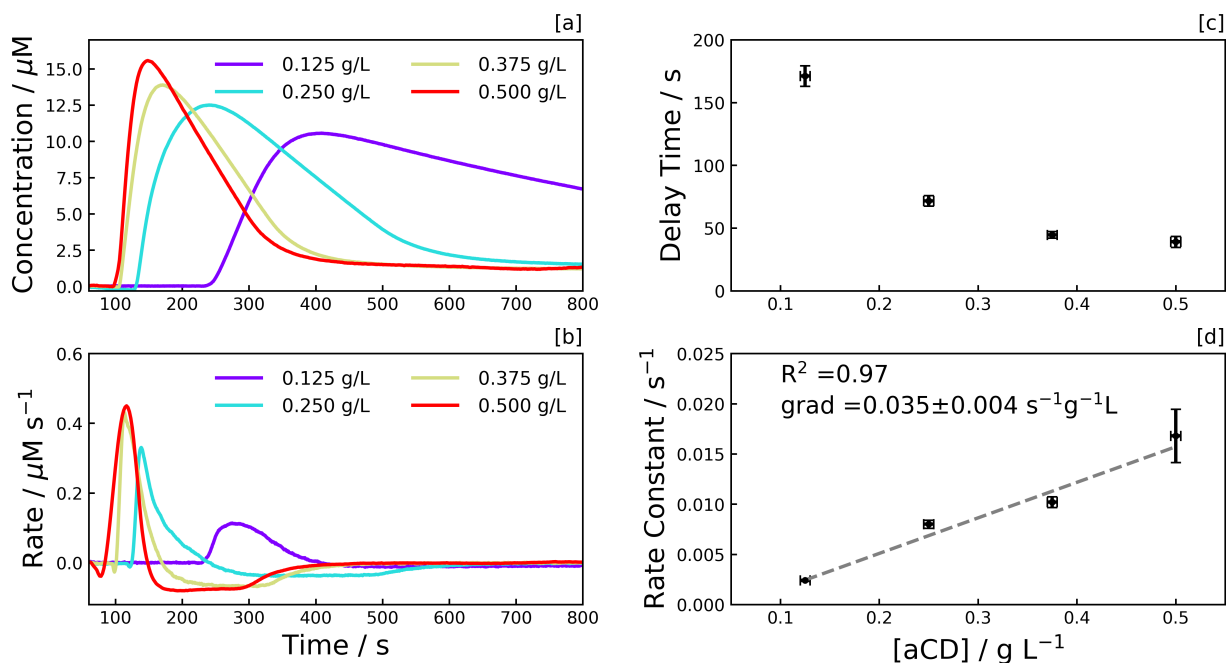
Figure 4.5: Photoreduction dependence on aCD concentration. (a) MV$^{\bullet+}$ concentration, and (b) rate profiles, illustrating the dependence of the reaction kinetics on aCD concentration. Each sample consists of aCDs with $40\,\mu$M MV^{2+} and 0.1 M EDTA in an aqueous pH 6 phosphate buffer. Samples were subject to continuous UV irradiation ($\lambda = 365\,$nm) from $t = 60\,$s at an irradiance of $90.2\,$mW cm^{-2}. (c) Delay time, and (d) photoreduction rate constant, both plotted as a function of aCD concentration, with error bars signifying the standard deviation of triplicates.

Delay time is inversely proportional to carbon dot concentration (Figure 4.5c), implying that the mechanism behind the delay-time is dependent on the number of photons absorbed, and potentially a phenomenon driven by interactions between CDs, such as the collision-

induced filling of trapped states within the CDs with excited electrons from the valence band before the CDs can transfer electrons to MV^{2+}.[176] However, the delay time observed may also be due to residual oxygen present in the system undergoing competing electron transfer with excited-state CDs. Eventually, the concentration of the residual oxygen will deplete completely and the electron transfer between excited-state CDs and MV^{2+} ensues, with the rate of residual oxygen depletion expected to increase as the concentration of aCDs increases.

Additionally, the photoreduction rate is linearly proportional to aCD concentration (Figure 4.5d), with each addition of $0.1\,\mathrm{g\,L^{-1}}$ of CDs contributing $3.5 \times 10^{-3}\,\mathrm{s^{-1}}$ to the photoreduction rate constant.

In conclusion, the linear dependency of rate on [aCD] suggests that a higher aCD concentration is more effective at driving MV^{2+} photoreduction. Hence, in measurements herein, an aCD concentration of $0.5\,\mathrm{g\,L^{-1}}$ was employed.

4.6.2 The effect of [MV]

To provide further insight into the radical cation depletion and delay time phenomenon, the starting concentration of MV^{2+}, $MV^{2+}_{t=0}$, was varied to ascertain the point at which the aCD surface becomes saturated with MV species. This set of samples was made up with $0.5\,\mathrm{g\,L^{-1}}$ aCD and $0.1\,\mathrm{M}$ EDTA in an aqueous pH 6 phosphate buffer.

Once samples were loaded into the fibre, they were subject to UV excitation as before, with the corresponding concentration and percentage conversion profiles shown in Figures 4.6a-b. Here, the greater concentration of $MV^{\bullet+}$ produced and corresponding strong absorption meant that negligible counts were detectable at the spectrometer at $600\,\mathrm{nm}$. Therefore, the conversion from absorbance to concentration was performed by averaging the absorbance within a $10\,\mathrm{nm}$ wide band centred around $670\,\mathrm{nm}$, with a scaled absorption coefficient of $6.2 \times 10^3\,\mathrm{M^{-1}\,cm^{-1}}$ (see Figure 4.7).

The depletion rate of $MV^{\bullet+}$ is constant at all starting concentrations of MV^{2+}, suggesting that the SED_{ox}^{+} species is rate-limiting the depletion. The rate equation takes the form in Equation 4.12. This suggests the rate of electron donation to the CDs is not coupled to the rate of electron transfer to the MV^{2+}, and similar amounts of SED_{ox}^{+} exist at all starting concentrations of MV^{2+}.

$$\frac{d[MV^{\cdot+}]}{dt} = k[MV^{2+}] \tag{4.12}$$

In contrast to the sweep in CD concentration, no clear correlation between $MV^{2+}_{t=0}$ and delay time is observed, signifying that the delay time phenomenon is not regulated by MV^{2+}, but is intrinsic to the carbon dots themselves and possibly controlled by the SED. A drop in the photoreduction rate constant was observed above a starting concentration of $100\,\mathrm{\mu M}$ MV^{2+}, with a maximum conversion to the radical cation of 38%. Above this

Figure 4.6: Photoreduction dependence on MV^{2+} concentration. (a) $MV^{\bullet+}$ concentration, and (c) percentage conversion profiles, illustrating the dependence of the reaction kinetics on the starting concentration of the methyl viologen dication, $MV^{2+}_{t=0}$. Conversion was calculated by dividing the concentration profile by the starting concentration of the methyl viologen dication. Each sample consists of MV^{2+} with $0.5\,\mathrm{g\,L^{-1}}$ aCDs and $0.1\,\mathrm{M}$ EDTA in an aqueous pH 6 phosphate buffer. Samples were subject to continuous UV irradiation ($\lambda = 365\,\mathrm{nm}$) from $t = 60\,\mathrm{s}$ at an irradiance of $90.2\,\mathrm{mW\,cm^{-2}}$. (b) Delay time, and (d) photoreduction rate constant. both plotted as a function of $MV^{2+}_{t=0}$ concentration, with error bars signifying the standard deviation of triplicates.

threshold, the photoreduction rate is no longer pseudo-first order with respect to MV^{2+}, and the local volumetric rate of photon absorption (L_p, LVRPA) should be considered as part of the rate equation. This new second order rate equation takes the form in Equation 4.13.

$$\frac{d[MV^{\cdot+}]}{dt} = k'[MV^{2+}]L_p \tag{4.13}$$

In general, a decrease in photoreduction rate constant could be linked to the available surface area on each carbon dot that MV^{2+} molecules can adsorb to (described as the surface coverage, θ, in Section 4.4). To give insight into this, a conversion is applied to the mass concentration of aCDs to give an approximate number concentration. This is achieved using their average diameter deduced by TEM ($8\,\mathrm{nm}$), together with their density, $1.5\,\mathrm{g\,cm^{-3}}$,[182] yielding a number concentration of $2\,\mathrm{\mu M}$. This indicates that each aCD can drive 50 conversions to $MV^{\bullet+}$ per second before limitation by the amount of photoexcited electrons at this particular irradiance ($90.2\,\mathrm{mW\,cm^{-2}}$). It is estimated that it takes on average $20\,\mathrm{ms}$ for a MV^{2+} to attach to the aCD, accept an electron to form $MV^{\bullet+}$, then escape the solvent cage. MV^{2+} adsorption is in competition with other adsorbing species, such as: (a) the SED and its oxidised counterparts and (b) $MV^{\bullet+}$ that has not been able to escape the solvent cage, given the negatively charged surface of the CDs. $MV^{\bullet+}$
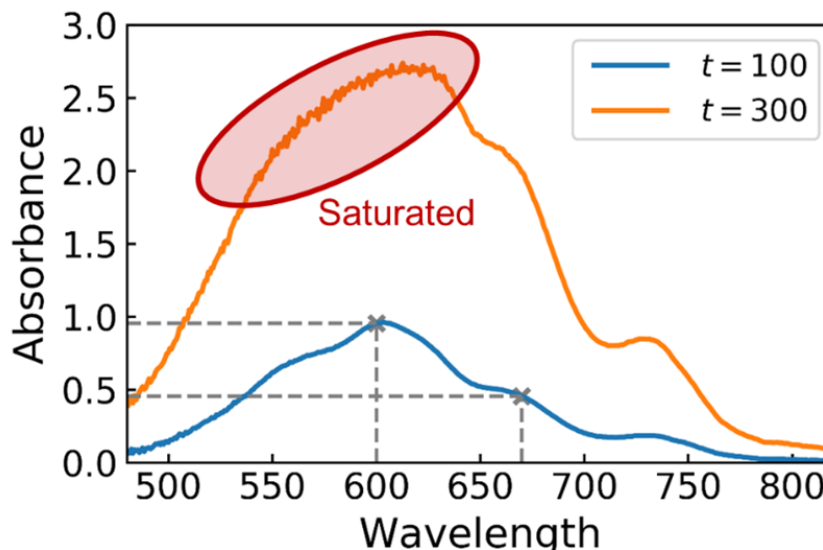
Figure 4.7: Scaling of the absorption coefficient of methyl viologen. The absorbance at $600\,\text{nm}$ and $670\,\text{nm}$ was extracted at $t = 100\,\text{s}$ and the fraction taken to scale the known absorption coefficient of methyl viologen at $600\,\text{nm}$. The absorption spectrum at $t = 300\,\text{s}$ shows that although the absorbance at $600\,\text{nm}$ was saturated, the absorbance at $670\,\text{nm}$ is not.

formation rate, and the number of MV^{2+} attaching per second to the aCD, increases at higher irradiances, as discussed in Section 4.6.4.

In conclusion, the optimal concentration for CD-driven photocatalysis with MV in this system is $[MV^{2+}] < 100\,\mu\text{M}$.

4.6.3 The effect of [EDTA]

To confirm whether the sacrificial electron donor (EDTA) was rate-limiting and to validate the pseudo-first order rate equation in Equation 4.12 with respect to $MV^{2+}_{t=0}$, the concentration of EDTA was varied between $1\,\text{mM}$ and $100\,\text{mM}$. This set of samples were prepared with $0.5\,\text{g}\,\text{L}^{-1}$ aCD and $40\,\mu\text{M}$ MV^{2+} in an aqueous pH 6 phosphate buffer. Once samples were loaded into the fibre, they were subject to UV excitation as before, with the corresponding concentration and rate profiles shown in Figures 4.8a-b.

The concentration profiles of the $25\,\text{mM}$, $50\,\text{mM}$ and $100\,\text{mM}$ measurement runs are similar in Figure 4.8a with the photoreduction rate constant starting to saturate above $25\,\text{mM}$ in Figure 4.8d. This suggests there is a sufficient reservoir of EDTA above $25\,\text{mM}$ for the photoreduction not to be rate-limited by the sacrificial electron donor and as such, the rate-limiting step is attributed to photon absorption when $[\text{EDTA}] > 25\,\text{mM}$. This exceeds the aCD concentration by 10^4 times. However, given EDTA is in competition with MV^{2+} to access the CD surface, excessively large EDTA concentrations may counter-productively reduce the photoreduction rate constant. It is challenging to deduce whether this is the case at $100\,\text{mM}$ within the margins of error. The $1\,\text{mM}$ and $10\,\text{mM}$ samples appear to be limited by the EDTA reservoir, and the depletion rate is noticeably smaller at these concentrations. Based on the proposed reaction scheme, it is assumed that above $25\,\text{mM}$
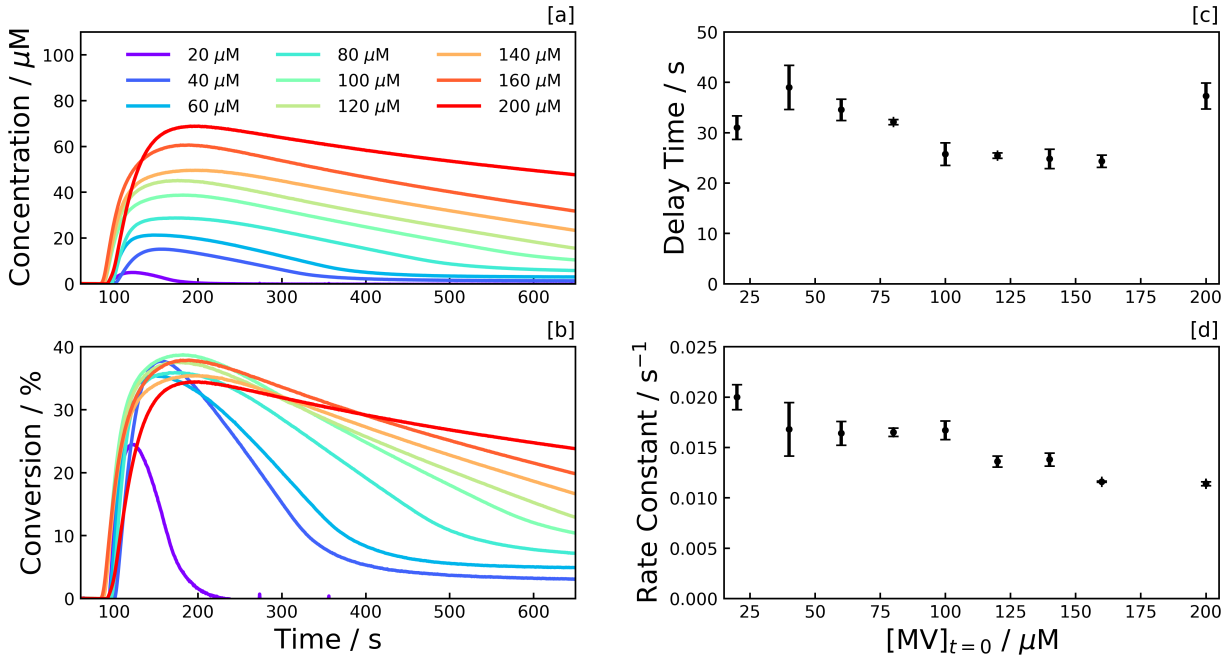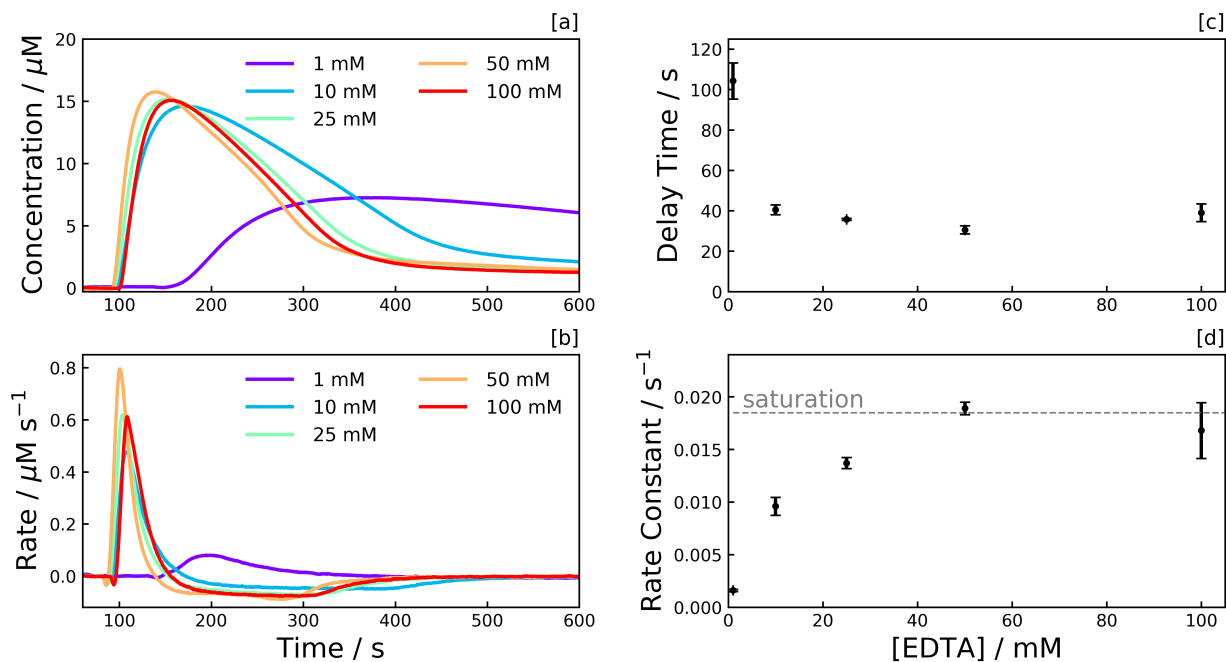
Figure 4.8: Photoreduction dependence on EDTA concentration. (a) $MV^{\bullet+}$ concentration, and (b) rate profiles, illustrating the dependence of the reaction kinetics on EDTA concentration. Each sample consists of EDTA with $40\,\mu M\ MV^{2+}$ and $0.5\,g\,L^{-1}$ aCDs in an aqueous pH 6 phosphate buffer. Samples were subject to continuous UV irradiation ($\lambda = 365\,nm$) from $t = 60\,s$ at an irradiance of $90.2\,mW\,cm^{-2}$. (c) Delay time, and (d) photoreduction rate constant. both plotted as a function of EDTA concentration, with error bars signifying the standard deviation of triplicates.

EDTA, SED_{ox}^{+} also saturates to a constant value given the very similar $MV^{\bullet+}$ depletion rates observed in the concentration profiles. The decrease in the rate of depletion at $1\,mM$ and $10\,mM$ is then a result of less SED_{ox}^{+} being available to oxidise $MV^{\bullet+}$ back to MV^{2+}.

Given EDTA exists in solution at pH 6 as $2-$ and $3-$ ions, the immediate surroundings of the negatively charged CD surface likely consists of an inner-sphere of positively charged methyl viologen species and an outer-sphere of EDTA. Therefore, the electron transfer from the CD to the MV^{2+} is likely an inner-sphere electron transfer, and the electron donation from the EDTA to the CD is likely an outer-sphere transfer event.

The delay time is relatively consistent in the $10\,mM$ to $100\,mM$ range, with a significant increase noticeable at $1\,mM$. This behaviour suggests the delay time is linked to the electron donation phenomenon to the carbon dots, and this phenomenon is limited by EDTA at $1\,mM$. Additional experiments substituting the CDs for the conventional photosensitiser $[Ru(bpy)_3]^{2+}$ found that the delay time was not intrinsic to the carbon dots. It is hypothesised that although great efforts were taken to purge oxygen in our measurement samples, a small amount of residual oxygen trapped at the photosensitiser surface has to be depleted before the MV^{2+} photoreduction can begin. This residual oxygen is depleted by accepting photoexcited electrons from the carbon dot, with a sacrificial electron donor required to fill the remaining holes in the CD valence band.

66

In conclusion, the optimal concentration for CD-driven photocatalysis with EDTA in this system is [EDTA] > 25 mM.

4.6.4 The effect of irradiance

The irradiance-dependence on the photoreduction reaction kinetics was explored using 6 different irradiances in the range $1.6 \, \text{mW cm}^{-2}$ to $88.4 \, \text{mW cm}^{-2}$ with aCDs, methyl viologen and EDTA. Reaction kinetic profiles were used to determine whether the photoreduction process was photon-limited, and to calculate a quantum yield. This set of samples were made up with $0.5 \, \text{g L}^{-1}$ aCDs, 0.1 M EDTA and $40 \, \mu\text{M} \, \text{MV}^{2+}$ in an aqueous pH 6 phosphate buffer. The results are shown in Figure 4.9.
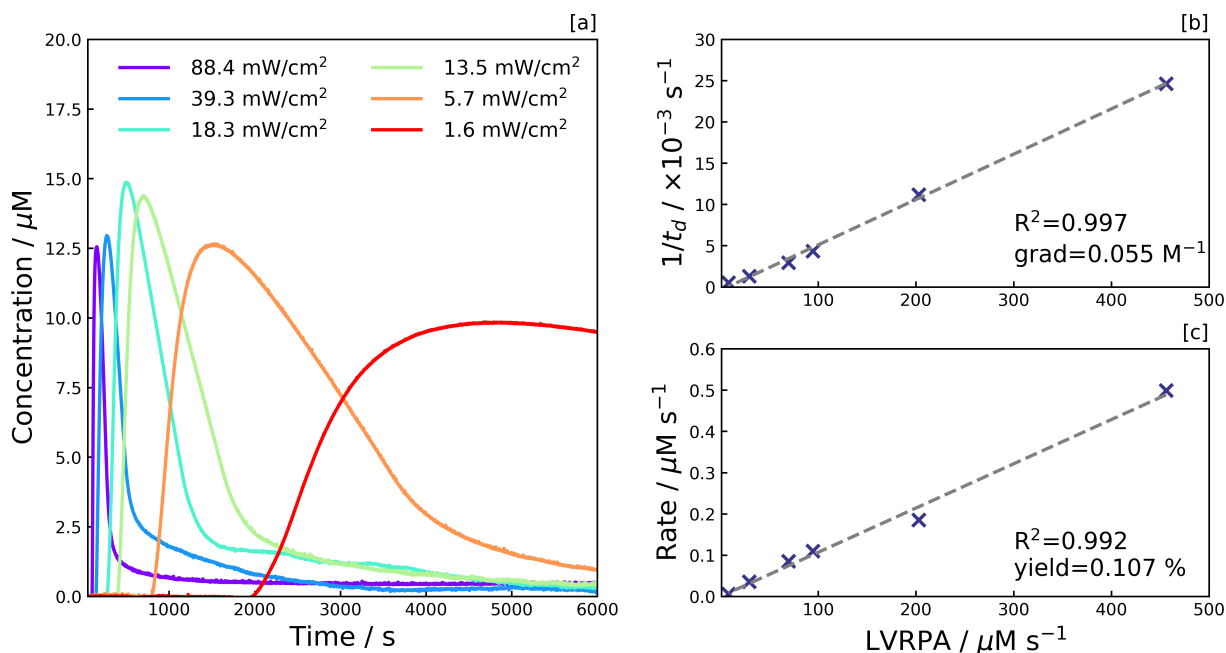
Figure 4.9: Photoreduction dependence on the local volumetric rate of photon absorption (LVRPA). (a) $\text{MV}^{\bullet+}$ concentration, and (c) rate profiles, illustrating the dependence of the reaction kinetics on EDTA concentration. Each sample consists of $0.5 \, \text{g L}^{-1}$ aCDs, 0.1 M EDTA and $40 \, \mu\text{M} \, \text{MV}^{2+}$ in an aqueous pH 6 phosphate buffer. Samples were subject to continuous UV irradiation ($\lambda = 365 \, \text{nm}$) at $t = 60 \, \text{s}$. (b) Delay time, and (c) photoreduction rate constant, both plotted as a function of LVRPA.

Irradiances, I, were measured using a Thorlabs S130 photodiode at the same distance below the optical diffuser as the HC-PCF (1 cm), with the values converted to a local volumetric rate of photon absorption (LVRPA) by considering the CD absorption coefficient, ϵ_λ, (see Figure 4.1a) together with the CD concentration, [CD], and the excitation wavelength, λ, as shown in Equation 4.14.

$$L_p = (\ln 10)\epsilon_\lambda [CD] \frac{\lambda}{hc} \frac{I}{N_A} \tag{4.14}$$

It is worth noting that adjustments to the irradiance are equivalent to adjustments to the CD concentration, as both quantities are directly proportional to the LVRPA. As such,

the effect of increasing the irradiance on the shape of the concentration profile is similar to increasing the CD concentration as depicted in Figure 4.5a. However, high LVRPA regimes are challenging to reach with highly concentrated solutions of carbon dots. At high [CD] concentrations, viologen photoreduction cannot be analysed in fibre due to substantial absorption at 600 nm from the CDs over the 20 cm optical path length. In these cases, high LVRPA regimes can be accessed by increasing the irradiance.

The delay time (t_d) was found to be inversely proportional to the LVRPA (Figure 4.5b), suggesting the delay time phenomenon is also light-driven (in addition to be dependent on CD concentration). The strong correlation supports the hypothesis that MV^{2+} photoreduction begins once a fixed amount of oxygen is depleted.

A clear linear trend is observed between LVRPA and initial photoreduction rate (Figure 4.5c), indicating that the photoreduction process is indeed photo-limited, giving a quantum yield of 0.11%. This low yield relates to the fast relaxation of photoexcited CDs on the picosecond timescale, with only a small proportion of photoexcited electrons surviving long enough to take part in an electron transfer to the viologen dication.[45]

In conclusion, the linear dependency of rate on LVRPA suggests that a higher LVRPA is more effective at driving MV^{2+} photoreduction. Comparing to the model described in Section 4.4, at all irradiances tested, the reaction is in the low photon limit where rate $\propto$ LVRPA, and therefore $\phi L_p \ll (k_r + k_{ET}[P][S])$ (see Equation 4.10). Hence, in the following set of measurements, the highest irradiances achievable in the measurement setup were employed ($\lambda = 365$ nm: 88.4 mW cm^{-2} or $\lambda = 450$ nm: 99.1 mW cm^{-2}).

4.6.5 Comparing Carbon Dots, Sacrificial Electron Donors, and Different Viologens

The concentration sweeps of each component in the photosystem provide insight into the reaction kinetics of CD-driven photoreduction and support the reaction scheme presented. Moreover, optimal conditions were identified for this photosystem for [aCD] = 0.5 g L^{-1}, namely [MV^{2+}] < 100 µM and [EDTA] > 25 mM. The rate was also found to vary linearly with irradiance in the accessible range (1.6 mW cm^{-2} to 88.4 mW cm^{-2}), hence this parameter should be maximised for optimal photoreduction of MV^{2+}.

Armed with these optimal conditions, to corroborate the reaction mechanism further, individual components of the photosystem were altered to probe their effects on the photoreduction rate constant and delay time, with the results shown in Figure 4.10.

Viologen Small changes in the molecular structure of the viologen species were used to gain insight into the electron transfer process at the surface of aCDs, with EDTA as the sacrificial electron donor (Figures 4.10a-b). The viologens studied comprised methyl viologen (MV), ethyl viologen (EV) and benzyl viologen (BV); each expected to form electrostatically-bound complexes together with aCDs, but with modified binding affinities.
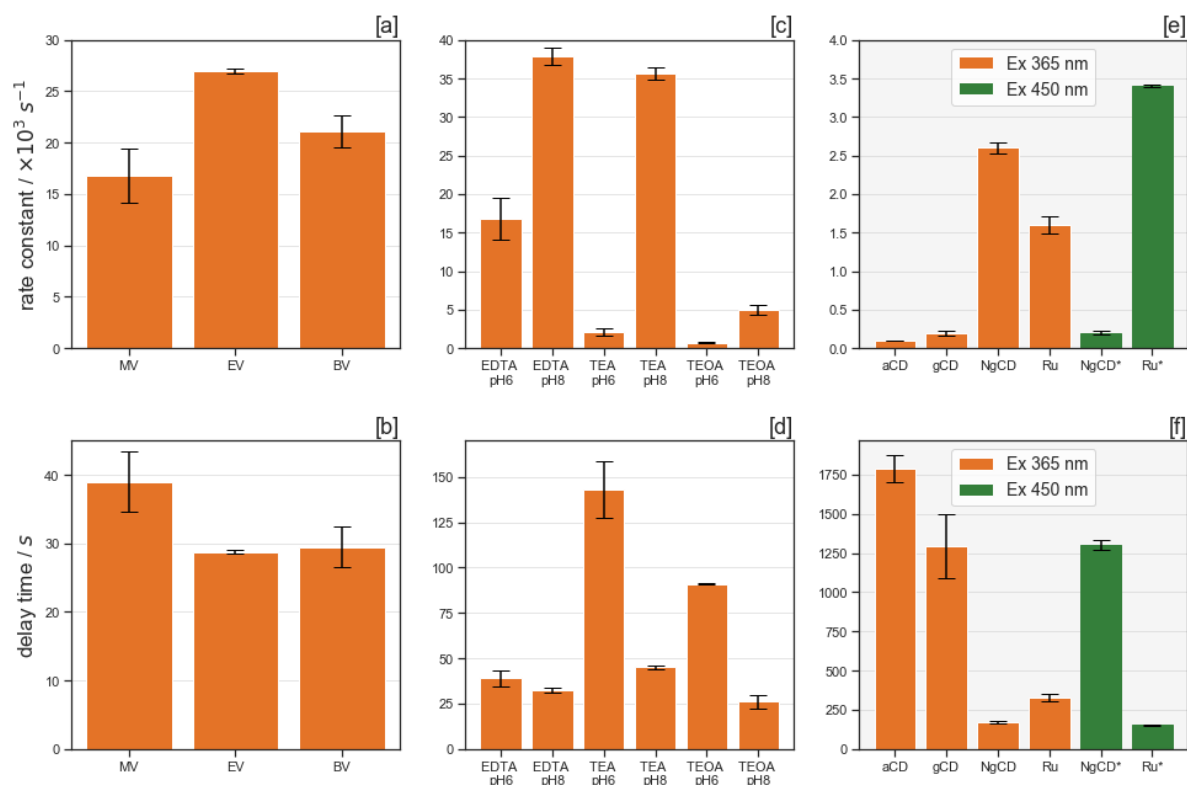
Figure 4.10: Photoreduction dependence on individual photosystem components. (a)-(b) Varying the viologen species: (a) photoreduction rate constants and (b) delay time. Each sample consists of $40\,\mu M$ XV^{2+}, $0.1\,M$ EDTA and $0.5\,g\,L^{-1}$ aCD. (c)-(d) Varying the sacrificial electron donor and pH: (c) photoreduction rate constants and (d) delay time. Each sample consists of $40\,\mu M$ MV^{2+}, $0.1\,M$ SED and $0.5\,g\,L^{-1}$ aCD. (e)-(f) Varying the photosensitiser type and excitation wavelength: (e) photoreduction rate constants and (f) delay time. Each sample consists of $40\,\mu M$ MV^{2+}, $0.1\,M$ and $0.01\,g\,L^{-1}$ light absorber. Samples were made up in an aqueous pH 6 phosphate buffer unless the pH is stated otherwise. Samples were subject to continuous UV irradiation ($\lambda = 365\,nm$, $88.4\,mW\,cm^{-2}$) or blue irradiation ($\lambda = 450\,nm$, $99.1\,mW\,cm^{-2}$). Ru = $[Ru(bpy)_3]^{2+}$, with Ru* and NgCD* denoting excitation at 450 nm. Error bars signify the standard deviation of triplicates.

Based on the redox potentials of methyl viologen (MV^{2+} - $E_0 = -0.446\,V$ vs normalized hydrogen electrode (NHE)),[183] ethyl viologen (EV^{2+} - $E_0 = -0.449\,V$ vs NHE),[183] and benzyl viologen (BV^{2+} - $E_0 = -0.359\,V$),[183] the photoreduction rate should be fastest for BV^{2+}, followed by MV^{2+} then EV^{2+} considering the average excited-state potential of COOH-terminated CDs is $-0.55\,V$ vs reversible hydrogen electrode at pH 5.[43] However, this trend is not observed, with electron transfer being the fastest for EV^{2+}. Competing factors, such as the cage escape process and CD binding affinity, contribute to the reaction rate. For example, the bulkiness of the BV^{2+} species restricts the ease of cage escape.

SED and pH   The effect of varying the SED was investigated with EDTA, TEA and TEOA at pH 6 and pH 8, in conjunction with aCDs and methyl viologen (Figure 4.11). Changes in the molecular structure of the SEDs, and the subsequent molecular structures of their oxidation products, were used to understand the depletion of $XV^{\bullet+}$ observed in all measurement runs. Adjustments to pH also tune the SED degradation pathways.

The electron donor has a significant effect on both the photoreduction rate constant (Figure 4.10c) and delay time (Figure 4.10d). EDTA is well-known as an electron donor that can operate in neutral conditions, with TEA and TEOA working best under alkaline conditions.[20] The deprotonation step in Reaction (6) is pH sensitive, with more basic conditions favouring the strongly reducing SED' over SED_{ox}^{+}. Therefore, increasing the pH results in a greater rate of $MV^{\bullet+}$ production with all the electron donors tested. The poor performance of TEA and TEOA at pH 6 is attributed to disfavoured deprotonation of the aminyl radical at pH 6 (TEA pKa = 10.7, TEOA pKa = 7.9).[20] EDTA displays an improved performance as its relevant pKa value is 6.1,[20] with both singly-protonated and doubly-protonated forms of EDTA coexisting at pH 6 in solution. It is surprising to see a ×7 higher photoreduction rate with TEA over TEOA, given TEOA has a lower pKa. Therefore, the cage escape efficiency is postulated to be faster with TEA over TEOA, thus producing the radical cation more rapidly.

Overall, the delay time is dependent on the type of SED used. At pH 6, TEA and TEOA have considerably longer delay times before the onset of viologen photoreduction. This is linked to the poor electron-donating ability of both these SEDs at pH 6, resulting in a longer amount of time to remove residual oxygen in the sample. When viologen photoreduction was performed at pH 8 with the different SEDs, the delay times are observed to be more similar, meaning that each SED was not inhibited under slightly alkaline conditions.

Photosensitiser   The performance of different photosensitisers were probed by comparing the rate of photoreduction of amorphous carbon dots (aCDs), graphitic carbon dots (gCDs) and nitrogen-doped graphitic carbon dots (NgCDs). NgCDs were benchmarked against $[Ru(bpy)_3]^{2+}$ under UV 365 nm and blue 450 nm irradiation. For this set of measurements, methyl viologen was utilised as the electron acceptor and EDTA as the electron donor (Figures 4.10e-f).

By comparing carbon dots at the same mass loading ($10\,mg\,L^{-1}$), we find that NgCDs perform the best out of the carbon dots by a considerable margin – with a ×10 higher photoreduction rate observed over its un-doped graphitic counterpart. This increase corroborates well with the increase in reported turnover frequencies (TOF) for proton reduction when gCDs and NgCDs are used in conjunction with the molecular $[Ni(P_2N_2)_2]^{2+}$ DuBois-type catalyst (NiP).[43] Given that the size distributions of both gCDs and NgCDs are similar,[55] the difference in delay time cannot be attributed to a difference in the number density of CDs. The absorption coefficients of both gCDs and NgCDs are also similar (see Figure 4.1a), which suggests that the excited state lifetime differentiates the two. Therefore, nitrogen-doping must promote a greater proportion of long-lived species, which is also corroborated by transient absorption spectroscopy measurements.[45]

Benchmarking against $[Ru(bpy)_3]^{2+}$ at the same mass loading shows that although NgCDs drive higher rates of reaction under UV (365 nm) irradiation, $[Ru(bpy)_3]^{2+}$ performs best under blue (450 nm) irradiation. This is partly because NgCDs have a ×2.3 lower absorbance at 450 nm, whereas $[Ru(bpy)_3]^{2+}$ has ×3.1 higher absorbance at this wavelength

(see Figure 4.1b). Consequently, a $\times 7.1$ increase in rate is expected by changes in absorption. Applying a small correction to account for the different photon fluxes incident with the $365\,\text{nm}$ source and $450\,\text{nm}$ sources, we arrive at an expected increase of $\times 9.8$. A $\times 13$ increase in rate is observed, which is in reasonable agreement with the expected increase in rate. The slightly higher experimental values are likely due to the superior ability of $[\text{Ru(bpy)}_3]^{2+}$ in donating an electron to MV^{2+} in this photosystem. This is thought to be due to the extended excited state lifetime of $[\text{Ru(bpy)}_3]^{2+}$ over the NgCDs, as the $450\,\text{nm}$ transition corresponds to the metal-to-ligand charge transfer (MLCT) excited state that is ideally suited for facilitating outer-sphere electron transfer to substrates or co-catalysts.

4.7 Conclusions

Comprehensive *in-operando* spectrokinetic analysis can be performed on a CD-driven photoreduction reaction with a total cumulative sample volume of $< 1.5\,\text{mL}$. This study builds upon our previous proof-of-principle work demonstrating the use of HC-PCF microreactors for studying photochemistry. Systematic screening of 29 reaction conditions gave insight into the complex interplays between each component in a colloidal photosystem, consisting of an electron acceptor, electron donor and photosensitiser. It is important to highlight the significant role of the sacrificial electron donor in controlling the kinetics of viologen photoreduction reactions, with EDTA, TEA and TEOA further interacting with the photosystem at later stages. Our data shows that EDTA and TEA in aqueous pH 8 solutions are the most effective sacrificial electron donors for carbon dot-driven hydrogen evolution, and additionally, viologen electron relays implemented in photocatalytic systems should perform best under these same conditions.
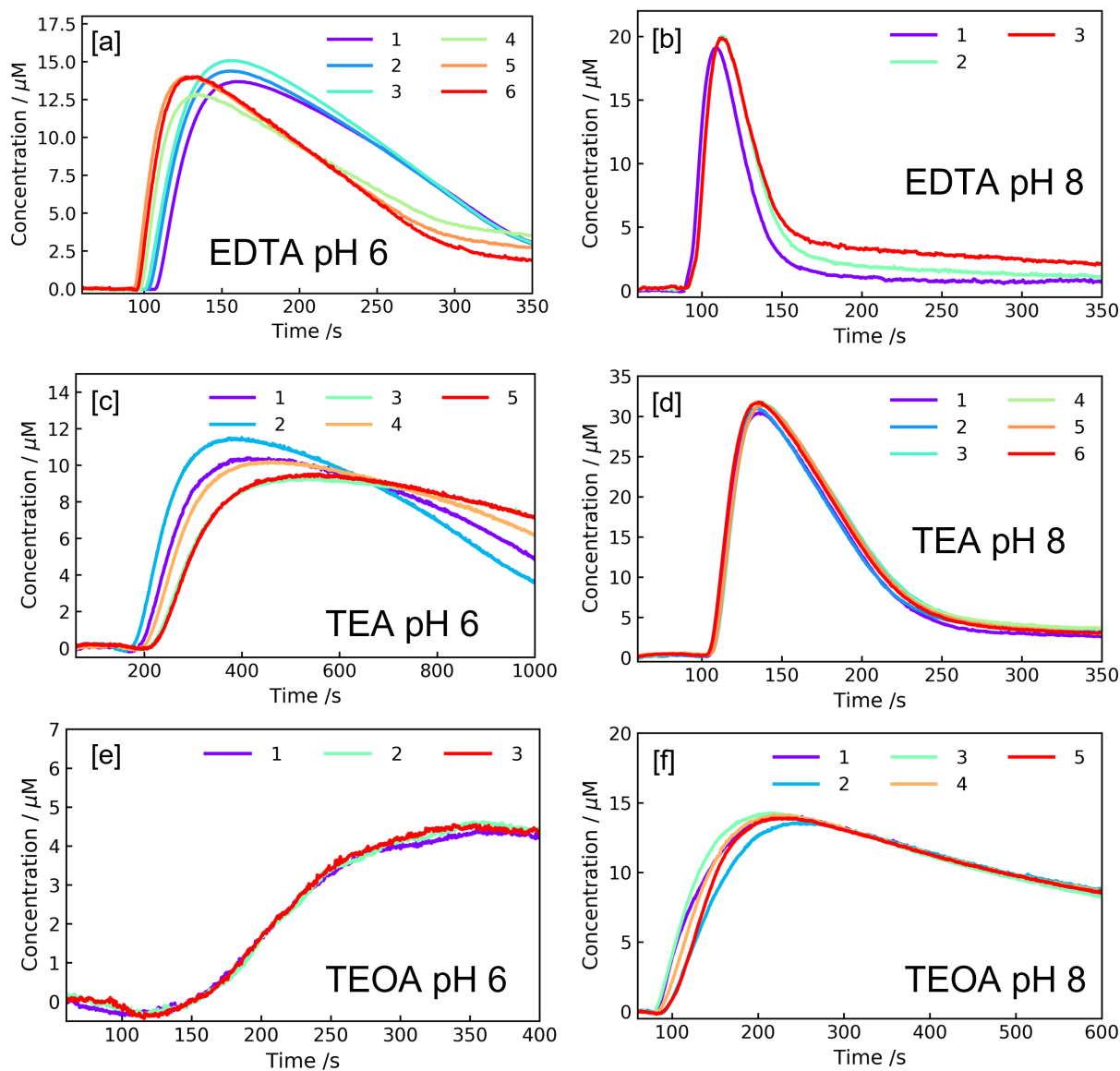
Figure 4.11: Concentration profiles with various sacrificial electron donors. Numbers 1-6 refer to measurement repeats. Each sample consisted of $0.5\,\mathrm{g\,L^{-1}}$ amorphous carbon dots with $40\,\mathrm{\mu M}$ MV^{2+} and $0.1\,\mathrm{M}$ of the sacrificial electron donor (SED) in an aqueous phosphate buffer. Samples were subject to UV irradiation $\lambda = 365\,\mathrm{nm}$, $88.4\,\mathrm{mW\,cm^{-2}}$) at $t = 60\,\mathrm{s}$. The SEDs tested include EDTA pH 6 (a) TEA pH 6 (c) TEOA pH 6 (e) EDTA pH 8 (b) TEA pH 8 (d) and TEOA pH 8 (f). Error bars presented in Figure 4.10 were calculated by extracting rate constants and delay times from each measurement repeat.

Chapter 5

Cobaloxime catalyst speciation in fibra

The contents of this chapter have resulted in the following publications:

<u>Takashi Lawson</u>,[†] Alexander S. Gentleman,[†] Annika Eisenschmidt, Daniel Antón-García, Michael H. Frosz, Erwin Reisner, and Tijmen G. Euser. 'In-operando detection of cobaloxime intermediate states during photocatalytic water-splitting'. **(in preparation)**.

[†] authors contributed equally

Experimental results presented in this chapter were solely obtained and analysed by the author of this thesis. Cobaloximes were synthesised by Daniel Antón-García. Density functional theory (DFT) calculations were performed by Annika Eisenschmidt.

Previously, methyl viologen was used as an indicator to optimise the photoactivity of carbon nanodots with sacrificial electron donors. Here, for the first-time, the electron transfer to the active state of a cobaloxime electrocatalyst is observed *in-situ*. This hydrogen evolving system was coupled with $[Ru(bpy)_3]^{2+}$ as a photosensitiser and two sacrificial electron donors (TEOA and ascorbate). During the catalytic cycle, the Co atom at the metal centre of the cobaloxime is reduced to form Co(II) and Co(I) species as two electrons are required to produce a hydrogen molecule from two protons. Each Co species possesses distinct visible absorption bands that can be monitored by absorption spectroscopy. This optical characteristic was exploited to understand the two electron transfer from $[Ru(bpy)_3]^{2+}$ to the cobaloxime.

5.1 Importance of *in-operando*

Routine quantitative analyses of photocatalysts include cyclic voltammetry (CV) measurements,[184,185] fluorescence quenching (Stern-Volmer) analysis,[184,186] and measurement of product yields.[83] However, these methods give little mechanistic insight into the sequence of steps that enable the photocatalytic reaction to proceed. Mechanistic studies of multistep photocatalytic reactions often relate to elucidating factors that influence catalyst turnover or regulate product yields.[83,187] These investigations centre on characterising catalytic intermediates either by isolation,[188,189] spectroscopic identification,[184,190,191] or through computational methods such as density functional theory (DFT).[192,193] Experimentally identifying catalytic intermediates remains highly challenging as these species typically exist on limited time scales at very low concentrations.[194,195,196,197] Therefore, the improved light-matter interaction and long optical path lengths within HC-PCFs is advantageous.

A system comprising of a photosensitiser in conjunction with a hydrogen evolution catalyst (HEC) has been proposed for H_2 generation from water.[19,31,198] One such system consists of a $[Ru(bpy)_3]^{2+}$ light absorber and a cobaloxime electrocatalyst.[31] Cobaloximes are cobalt-based metal complexes, with those containing dimethylglyoximato (dmgH) ligands shown to be effective proton reduction catalysts in aqueous solutions.[74,76] Moreover, the addition of a pendant pyridine ligand to the Co ion is reported to enhance the catalytic activity of the catalyst.[77] In the generally accepted mechanism for H_2 evolution, reduction to the Co^+ state is followed by protonation to produce a metal-hydride, $Co^{3+}-H$.[82,199,200,201] Conclusive evidence of subsequent reaction steps remains difficult to collect. A second electron transfer to $Co^{3+}-H$ could form a $Co^{2+}-H$ species which then accepts a second proton to release H_2. Alternatively, a bimolecular pathway with two $Co^{3+}-H$ species could interact to form two Co^{2+} species and H_2 (see Section 2.1.3).[80] *In-operando* methods are well-placed to identify the nature of cobaloxime intermediate states, and therefore these methods provide utility in elucidating the correct reaction mechanism.

Importantly, cobaloximes have characteristic absorption spectra dependent on the oxidation state of the cobalt metal centre.[72,80,79] Therefore, *in-operando* spectroscopy can be used to identify the intermediate states with the added benefits of fibre-based microreactors as discussed in Section 2.4. The Co(I) state has been detected in CH_2Cl_2 for the selective synthesis of alkenylphosphine oxides under visible light,[202] and has been detected via spectroelectrochemical methods where cobaloximes have been immobilised on mesoporous ITO electrodes.[79] However the Co(I) state has not been detected in aqueous solvents *in-operando* because the absorption is too low at relevant concentrations and cannot be measured with conventional techniques.

5.2 Experimental method

To maximise the optical path length and therefore detection sensitivity, a 20 cm length of kagomé-style HC-PCF was infiltrated with various aqueous solutions of $[Ru(bpy)_3]^{2+}$, cobaloximes, and sacrificial electron donors (SEDs). Samples were thoroughly purged under nitrogen for at least 15 min prior to loading into the fibre, and inserted through the out-coupling facet to minimise disturbances to the optical coupling. All samples were injected into the pressure cell using gas-tight syringes and a syringe pump (Aladdin AL-1000), having passed through 0.2 μm pore size cellulose acetate filters to prevent fibre blockages.

Repeat measurement runs were loaded successively into the fibre and started once the spectrum returned to the reference baseline. This ensured that residual reaction products from the previous run had been pushed clear of the fibre. The fibre was cleaned through with water between different sample sets, and subsequent samples were loaded once the spectrum matched an internal water reference. The irradiance could be varied between $99\,\mathrm{mW\,cm^{-2}}$ and $323\,\mathrm{mW\,cm^{-2}}$ for the 450 nm LED, $60\,\mathrm{mW\,cm^{-2}}$ and $281\,\mathrm{mW\,cm^{-2}}$ for the 405 nm LED, and $13\,\mathrm{mW\,cm^{-2}}$ and $88\,\mathrm{mW\,cm^{-2}}$ for the 365 nm LED. This was achieved by placing a 2" x 2" absorptive neutral density filter (Thorlabs NE205B) between the excitation source and fibre. The excitation source was switched on after a 1-minute pause in the dark to ensure that the reference spectrum was stable, and that the probe source (supercontinuum laser) did not drive the reaction. Further details on the absorption set-up are provided in Section 3.1.5.

HC-PCFs have been reported to withstand pressures of above 150 bar,[203] which is an important factor when it comes to studying gas-evolving photocatalysts. High pressures are required to suppress bubble formation, which can be fatal for guidance down a HC-PCF if not adequately controlled. By application of Henry's Law (see Equation 5.1),[204] the turnover number before bubble formation occurs can be calculated.

$$C_{\mathrm{limit}} = \frac{P}{k_H} \tag{5.1}$$

where k_H is the Henry's law constant, P is the pressure and C_{limit} is the solubility limit. For hydrogen gas in water, $k_H = 1282\,\mathrm{M\,bar^{-1}}$ at 298 K,[204] meaning the solubility limit is 0.12 M at 150 bar. Typical working concentrations of cobaloximes are μM, allowing $\sim 12,000$ chemical conversions without bubble formation.

5.2.1 Materials and synthesis

CoP[1] was synthesised by Daniel Antón-García as previously reported.[78,205] Other chemicals and reagents were purchased from commercial suppliers and used as received unless otherwise noted. Laboratory-grade reagents were of the highest available purity. Phosphate buffer solutions (0.2 M) and SED stock solutions (0.2 M) were prepared and verified using a pH electrode (Mettler Toledo, FiveEasy Plus) at pH 6 and pH 8. The pH of SED stock solutions was adjusted using sodium hydroxide and hydrochloric acid. A stock solu-

tion of $[Ru(bpy)_3]^{2+}$ was made up by dissolving tris(bipyridine)ruthenium(II) chloride. All stock solutions were made up using Milli-Q purified water.

5.2.2 DFT calculations

Time-dependent density functional theory (TD-DFT) calculations were performed by Annika Eisenschmidt. Fully optimised molecular structures were obtained through geometry optimisations applying the B3LYP[206,207,208] or TPSSh[209,210,211] density functional in conjunction with either the def2-TZVP[212,213] or the 6-31G(d,p)[214,215,216] basis set. Solvation was approximated by the conductor-like model CPCM[217] with the refractive index and dielectric constant set to water. Long-range Coulomb and HF exchange interactions were included using the *rijcosx* approximation. All calculations were conducted using ORCA 4.0.1.2.[218]

5.3 Exploratory cuvette measurements

The absorption spectra of aqueous samples of two cobaloximes (CoP^1 and $Co(dmgH)_2Cl_2$) were measured in a Cary 300 UV-Vis spectrophotometer to deduce the absorption coefficient as a function of wavelength. These results are shown in Figure 5.1a. The absorption of the cobaloxime species falls off sharply between 300 nm and 400 nm, with very limited absorption for wavelengths longer than 500 nm. A shoulder exists in both absorption spectra at 365 nm.

A sample of $[Ru(bpy)_3]^{2+}$ was also analysed (see Figure 5.1b), with the absorption peak at 450 nm corresponding to a metal-to-ligand charge transfer (MLCT) state. This excited state is effectively quenched by a cobaloxime via electron transfer due to the greater electron density on the ligands compared to the ground state.
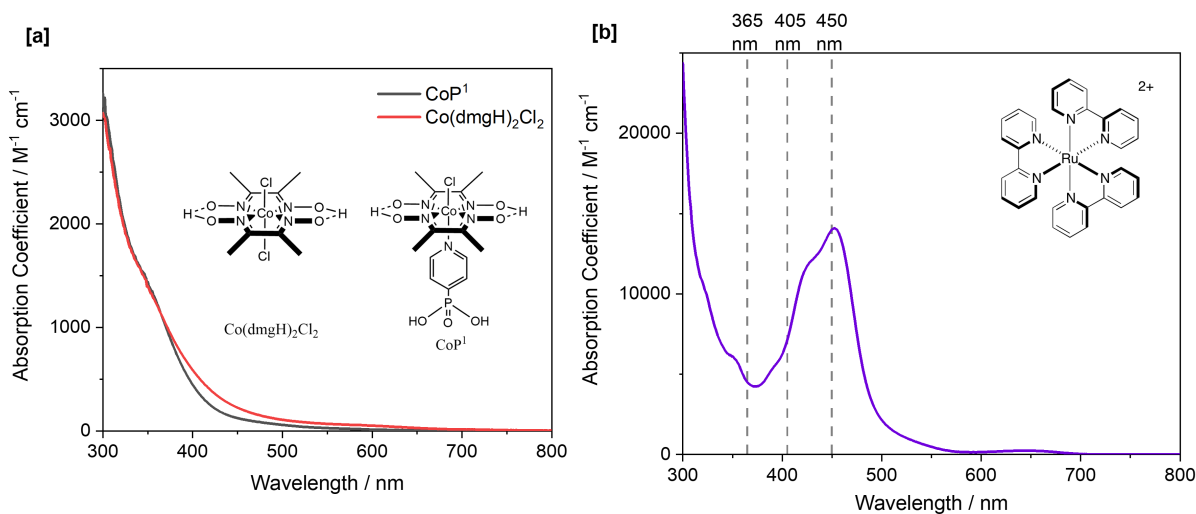

Figure 5.1: UV-Vis absorption spectra of; (a) cobaloxime species, and (b) $[Ru(bpy)_3]^{2+}$. Measurements were performed in cuvettes and all samples were recorded in aqueous solution. The wavelengths of the closest excitation sources to the absorption maximum are represented by the dashed lines.

5.4 Results and discussion

Cobaloximes were spectroscopically characterised with various electron donors and excitation sources. Optimum conditions to observe a photoinduced absorption signal were identified. Following the identification of optimum conditions, three different cobaloximes species were characterised under the same reaction conditions to identify subtle differences in the absorption spectra and reaction kinetics.

5.4.1 Comparing reaction conditions

Samples containing $44\,\mu M$ $[\text{Ru(bpy)}_3]^{2+}$, $0.1\,M$ sacrificial electron donor (SED) and $86\,\mu M$ CoP^1 were prepared, with the results shown in Figure 5.3. In this study, ascorbate was used as the SED as this was reported to work well with $[\text{Ru(bpy)}_3]^{2+}$ in previous studies.[44,27,31] The $[\text{Ru(bpy)}_3]^{2+}$ triplet excited manifold undergoes reductive quenching by the ascorbate ion, with subsequent electron transfer from the photogenerated $[\text{Ru(bpy)}_3]^{+}$ species to the cobaloxime catalyst.[31]

Although the optimum pH for H$_2$ evolution for this system is pH 5,[31] cobaloximes have been reported to work best between pH 7 and pH 10.[82,75] The inconsistency in optimal pH is a result of the different solvents and sacrificial electron donors employed. Alkaline conditions were employed to limit H$_2$ turnover and build up the population of catalytic intermediates.

TEOA as a sacrificial electron donor was also tested as a comparison to the ascorbate ion, although the optimum pH for H$_2$ evolution for this system is reported as pH 7.[219] The decrease in the rate of H$_2$ formation at pH $<$ 7 is likely a result of the protonation of TEOA which renders it a less effective sacrificial electron donor.[219]

A rapid photo-induced absorption (PIA) is observed following the $365\,\text{nm}$ excitation source being switched on when sodium ascorbate is employed as the SED (Figures 5.3a-d). The PIA disappears within one minute. This behaviour is similar to that observed with methyl viologen in Section 4.2, indicative of an electron transfer event, and the formation of a new species. This species is postulated to be the Co(I) intermediate state, which most likely arises due to the reductive quenching of an excited state of $[\text{Ru(bpy)}_3]^{2+}$. Importantly, the small magnitude of this absorption (0.1) is only detectable over a $20\,\text{cm}$ path length, and a conventional $1\,\text{cm}$ cuvette measurement would not be able to resolve this signal above noise (Abs 0.005 in cuvette).

Following the disappearance of the PIA, the depletion of a ground state species absorbing at a $\lambda_{\text{max}} = 560\,\text{nm}$ is apparent when the photoexcitation is driven at $365\,\text{nm}$ (Figures 5.3a-b), whereas the emergence of a new absorbing species with the same λ_{max} is observed when the photoexcitation is driven at $450\,\text{nm}$ (Figures 5.3c-d). The ground state species can be attributed to CoP^1 as this behaviour is not observed when methyl viologen is employed as the electron acceptor. Moreover, the spectral shape of the bleach matches the absorption tail of CoP^1, and ascorbate degradation products are not expected to absorb in

the visible region. The spectral shape of the CoP[1] absorption is discussed in further detail in Section 5.4.2. Radical-induced degradation of the catalyst becomes more likely with UV excitation, which could explain the degradation of CoP[1]. Moreover, CoP[1] absorbs at 365 nm (see Figure 5.1a), meaning this degradation mechanism is likely connected to the photoexcited state of CoP[1]. The magnitude of the absorbance does not change when the LED source is switched off, confirming that the degradation is UV-driven.

The new absorbing species evident in Figures 5.3c-d builds up linearly with time when the LED source is on and remains stable at a fixed absorbance when the LED source is off. This suggests that this absorbing species is generated by a light-driven process and is stable in solution. The native Co(III) state of CoP[1] has two axial substituents (Cl and the pyridine group with phosphate anchor), with reduction to lower oxidation states leading to Cl dissociation and leaving a free site for catalysis and the formation of a stable Co(II) state.[74] Cl dissociates as aqua ligands can labilise Cl ligands, and given the cobaloxime is made up in aqueous solvents, neutral aqua ligands are ligated over Cl.[220] A Co(II) species is therefore postulated to be the new absorbing species that builds with time. However, specific assignment of the Co(II) species is difficult without access to DFT-simulated UV-Vis spectra. This is the focus of the next section. However, at this stage, as alkaline conditions limit proton uptake by Co metal centres, it is hypothesised that Co(II) is favoured over its Co(II)-hydride counterpart. The proposed electron and proton transfer steps are provided in Figure 5.2.
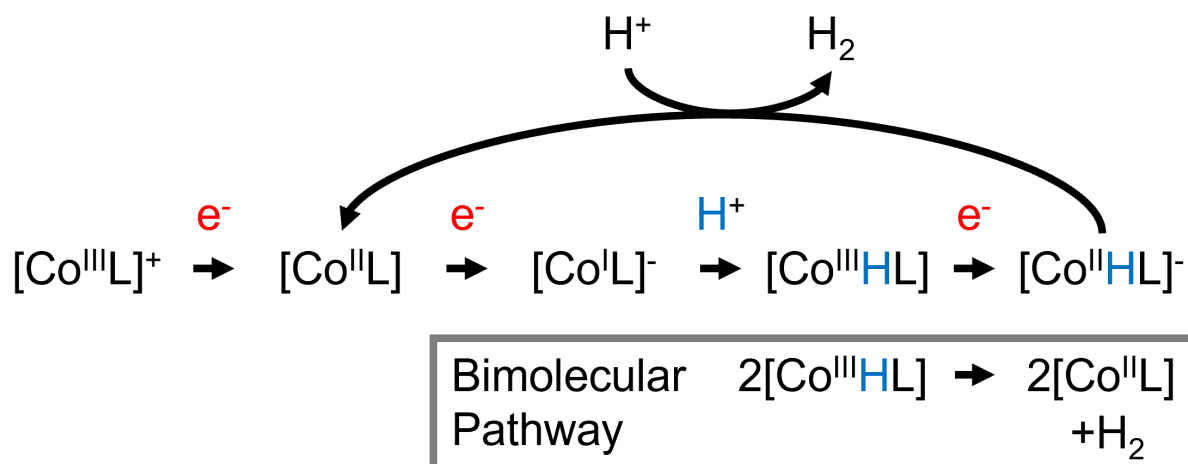
Figure 5.2: Unimolecular reaction mechanism for hydrogen evolution with cobaloxime catalysts.[80,82,199,200,201] L depicts the ligands. An alternative bimolecular pathway comprises two Co(III)-hydrides interacting to form two Co(II) species and H_2, without the formation of a Co(II)-hydride species.[80]

Only limited photoactivity was observed when the SED was replaced with TEOA in Figures 5.3e-f. A stock solution at a higher pH was prepared, as solar fuel catalysis with TEOA is generally performed at pH values above 8.[20] A weak absorption signal arises over long irradiation times, with photoexcitation by a 405 nm LED source being slightly more effective at producing the onset of this absorption signal than the 365 nm LED source.

No changes in absorbance above noise were observed when $[Ru(bpy)_3]^{2+}$ was replaced by nitrogen-doped graphitic carbon nanodots (NgCDs, data not shown), where the reaction was driven by a 405 nm or 450 nm source. This is likely due the limited absorption of NgCDs at 405 nm and 450 nm, where the degradation processes are less dominant. As such, ascorbate was employed as the SED with $[Ru(bpy)_3]^{2+}$ for the rest of the experiments due to the strong changes in absorption observed.
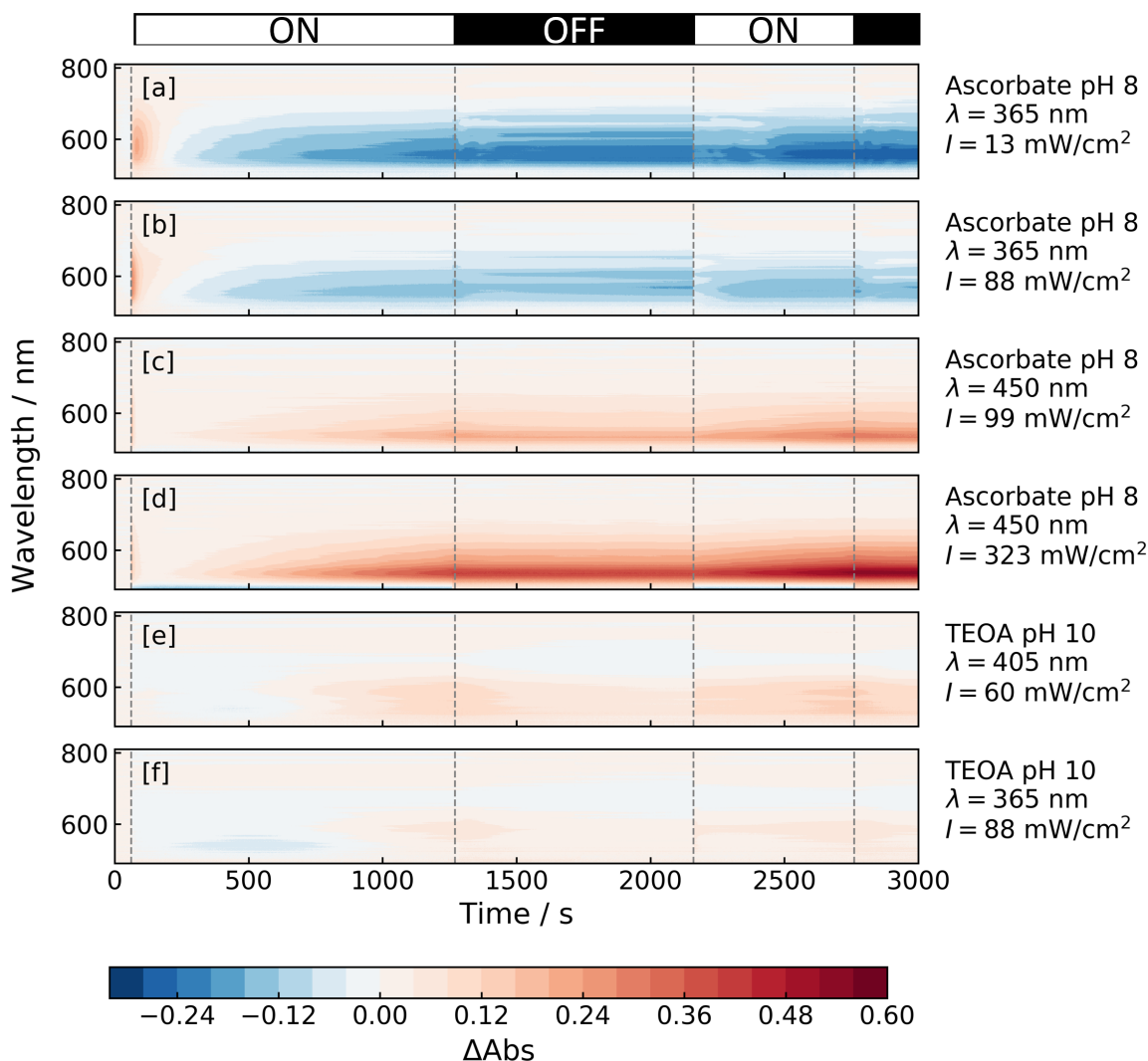
Figure 5.3: *In-fibra* colour maps detailing the time evolution of absorption as a function of wavelength for the CoP[1] catalyst with $[Ru(bpy)_3]^{2+}$ as a photosensitiser. Each sample was made up of 44 µM $[Ru(bpy)_3]^{2+}$, 100 µM CoP[1] and 0.1 M SED. The sacrificial electron donor was varied between pH 8 sodium ascorbate (a-d) and TEOA (e-f). Profiles (a,b,f) were driven by a 365 nm LED source, (c-d) a 450 nm LED source and (e) a 405 nm LED source.

5.4.2   Comparing cobaloximes

Three different cobaloximes were compared at a concentration of 86 µM with 0.1 M ascorbate and 44 µM $[Ru(bpy)_3]^{2+}$ in a pH 8 phosphate buffer. Samples were photoexcited with a 450 nm source (99 mW cm^{-2} or 323 mW cm^{-2}). The absorption time-traces at 540 nm, together with the spectral profiles at key times, are shown in Figure 5.4. The three differ-

ent cobaloximes consisted of $Co(dmgH)_2Cl_2$, $Co(dmgH)_2pyCl$, which were self-assembled by adding 1 equivalent of pyridine to $Co(dmgH)_2Cl_2$, and CoP^1 with a phosphate anchor, which was originally designed to facilitate efficient electron transfer from metal oxides and carbon nanodots when used in hydrogen production experiments in previous work.[78,77]
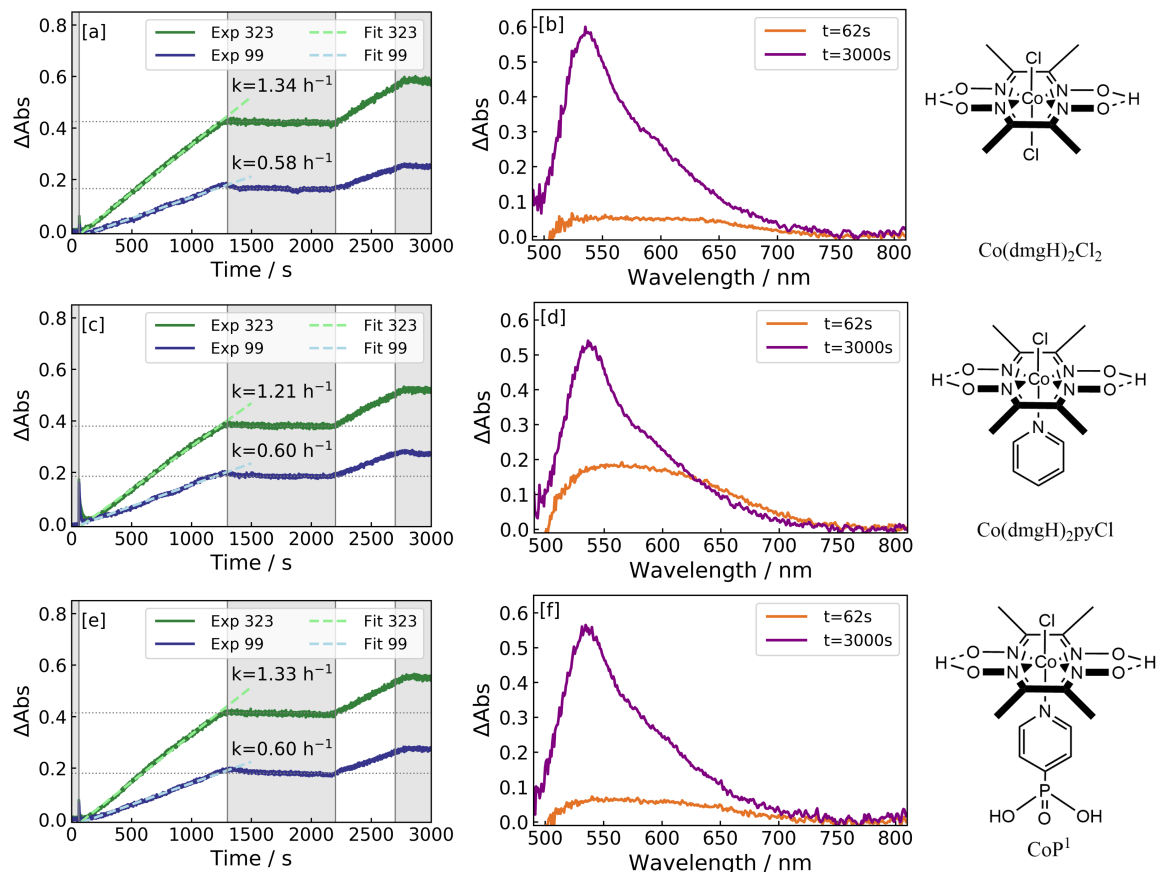
Figure 5.4: Photoinduced absorption profiles of three cobaloximes with axial Cl ligands (a-b), an axial pyridine ligand (c-d) and an axial phosphate ligand (e-f) under $\lambda = 450\,\text{nm}$ irradiation. The excitation source was switched on at $t = 60\,\text{s}$. Absorption time traces (a,c,e) are taken at $540\,\text{nm}$ under $99\,\text{mW cm}^{-2}$ and $323\,\text{mW cm}^{-2}$ irradiances, with a linear fit applied to extract a zero-order rate constant. Spectral profiles (b,d,f) are shown for each cobaloxime studied at $t = 62\,\text{s}$ and $t = 3000\,\text{s}$ under an irradiance of $323\,\text{mW cm}^{-2}$. These correspond to the initial photoinduced absorption of a Co(I) species, and the growing population of a Co(II) species, respectively. Grey shading indicates time periods where the excitation source was switched off.

As discussed previously, the time-resolved absorbance for each cobaloxime consists of a transient component (Figure 5.4 - $t = 62\,\text{sec}$) and a steady-state component that increases linearly with irradiation time (Figure 5.4 - $t = 3000\,\text{sec}$). The transient component absorbs broadly in the range $500\,\text{nm}$ to $700\,\text{nm}$. It is most prominent for the cobaloxime with the pyridine group attached (see Figure 5.4d). The steady-state component has an absorbance profile that is narrower, with a shoulder evident at $570\,\text{nm}$. The steady-state component grows at a similar rates with all three Co species under $99\,\text{mW cm}^{-2}$ irradiation. However, a lower rate is observed with $Co(dmgH)_2pyCl$ compared to the other Co species under $99\,\text{mW cm}^{-2}$ irradiation.

Based on DFT-simulated UV-Vis spectra presented in Figure 5.5c, the Co(III) state is expected to have the weakest visible light absorption out of the three oxidation states investigated. Only the TPSSh functional and 6-31G(d,p) basis set combination predicts any appreciable absorption in the visible region for the Co(III) species. This absorption is limited to wavelengths shorter than 550 nm, with a maximum intensity of 1000. The Co(III) state relates to the ground state of cobaloximes, whose absorbance was experimentally measured and presented in Figure 5.1. Indeed, this confirms that absorbance is limited to below 450 nm for the Co(III) state.

The intensity can be viewed as a relative measure for comparing the absorption coefficients calculated using the same functional and basis set. Therefore, by considering the TPSSh functional with the 6-31G(d,p) basis set, absorption from Co(III) states (Figure 5.5c) is expected to be $\times 8$ weaker than the Co(II) state (Figure 5.5b), and $\times 70$ weaker than the Co(I) state (Figure 5.5a). DFT simulations predict that Co(III)-hydride species (Figure 5.5h) have a stronger absorption peak at 510 nm over their Co(III) counterpart, and have limited absorption at wavelengths longer than 550 nm. The addition of a pyridine ligand weakens this Co(III)-hydride absorption, and in fact, only the TPSSh functional and 6-31G(d,p) basis set combination predicts any appreciable absorption above 500 nm.

The Co(II) state without a pyridine ligand is predicted to have a peak absorbance at 550 nm with a shoulder at 570 nm using the B3LYP functional and 6-31G(d,p) basis set combination (Figure 5.5b). This spectral shape matches well with the steady-state component of absorption observed in experiments, and therefore the absorption observed can be assigned to the Co(II) state. The shape and position of the absorption peak in the experimentally-measured UV-Vis spectra does not match the predicted UV-Vis spectra of the Co(II)-hydride species, so the Co(II)-hydride species is excluded as a potential assignment. Although the addition of a pendant pyridine ligand is predicted to perturb the absorption profile of the Co(II) species (Figure 5.5e), this was not observed in experiment. This could be due to a combination of factors, such as the incomplete self-assembly of pyridine ligands with Co metal complexes in solution to start with, and/or poor binding efficiency of the pyridine to the Co(II) metal centre, resulting in the pyridine group detaching and re-attaching to the Co metal centre as part of the photocatalytic cycle.

The Co(I) state is quadratically planar in its lowest energy configuration and expected to absorb the most strongly out of the three oxidation states considered. In the interest of consistency, DFT simulations using the B3LYP functional and 6-31G(d,p) basis set combination are considered. An absorbance centred at 580 nm is expected with an $8\times$ stronger signal than the Co(II) state (Figure 5.5a). A double absorption peak predicted by DFT (560 nm, 600 nm) was not evident in experiments on addition of pyridine (Figure 5.5d). This may indicate that the pyridine group does not bind efficiently to the Co(I) metal centre, similar to the Co(II) metal centre described above. In this case, this suggests that the pyridine group only re-attaches to the Co(III) metal centre.

Comparing the spectra from DFT and experiment provides strong support for the steady-state formation of $Co^{II}(dmgH)_2(H_2O)_2$ with irradiation time. The transient signal is most likely the Co(I) state that disappears within a minute. This species is highly nucleophilic and is rapidly protonated to form Co(III)-hydrides. The rapid nature of this reaction step, coupled with the limited reservoir of H^+ at pH 8, fits well with the transient signal observed. In addition, the shape of the absorption spectra assigned to Co(I) species by Lazarides *et al.* and Muresan *et al.* match well with the broad absorption profiles observed here.[219,79] However, it must be noted that in both these studies a different solvent was used (CH_2Cl_2 and DMF respectively), which is likely to perturb the cobaloxime absorption spectra measured in water.

The absorbance of Co(I), and hence its population, is greatest with the addition of pyridine (Figure 5.5d), which lends support to the greater hydrogen turnover observed by Willkomm *et al.* with this ligand.[77] The addition of a pendant pyridine therefore increases the rate of formation of the Co(I) state from the Co(II) state. The Co(II) state is negligible at early times, which can be explained by its lower intensity and its small population at early times. The absorption from the Co(I) state likely engulfs the weak Co(II) signal.

Panagiotopoulos *et al.* report that cobaloximes without pyridine ligands (i.e., with two chloride ligands) display significantly lower stability than cobaloximes with a pyridine group.[220] Moreover, they show that pyridine ligands with electron withdrawing groups (such as a phosphate group) slow down the rate of photocatalytic hydrogen evolution when sensitised by porphyrins. However, addition of TiO_2 nanoparticles allowed the attachment of the cobaloxime catalyst to the surface of the TiO_2 and the catalytic performance was shown to be improved by 5×.[220] The greater population of the Co(I) state for $Co(dmgH)_2pyCl$, evidenced by this species displaying the highest amount of absorption for its transient absorption feature (Figure 5.4d) relative to its other two cobaloxime counterparts (Figures 5.4d and f), corroborates the conclusions reported by Panagiotopoulos *et al.*.

Unfortunately, the weak predicted absorption of Co(III) species means it is challenging to detect the first protonation to form Co(III)-H species. However, the Co(II) state can be tracked, and the population of this state grows linearly with time.

5.5   Conclusions

Catalytic intermediate states can be observed via spectroscopic methods on microlitre volumes in-operando. The hydrogen-evolving reaction driven by the combination of cobaloxime electrocatalysts with $[Ru(bpy)_3]^{2+}$ light absorbers revealed the formation of a transient Co(I) species and a steady-state Co(II) species. Hydrogen turnover was limited by employing alkaline conditions to prolong the lifetime of Co(II) states. The addition of an axial pendant pyridine unit was found to increase the stability and absorption of the transient feature assigned to the Co(I) state.

This proof-of-principle study forms a promising basis for future work, which should in the first instance investigate the pH-dependence on the formation of cobaloxime catalytic intermediates. Moreover, there is potential in future work for dry organic solvents to be utilised to artificially accumulate intermediate species.

This fibre-based technique is more powerful in complex multi-electron molecular catalysis, such as those employed in CO_2 reduction and N_2 fixation. The only requirement is that the spectroscopic signature of intermediate species changes with the oxidation state of the metal centre.
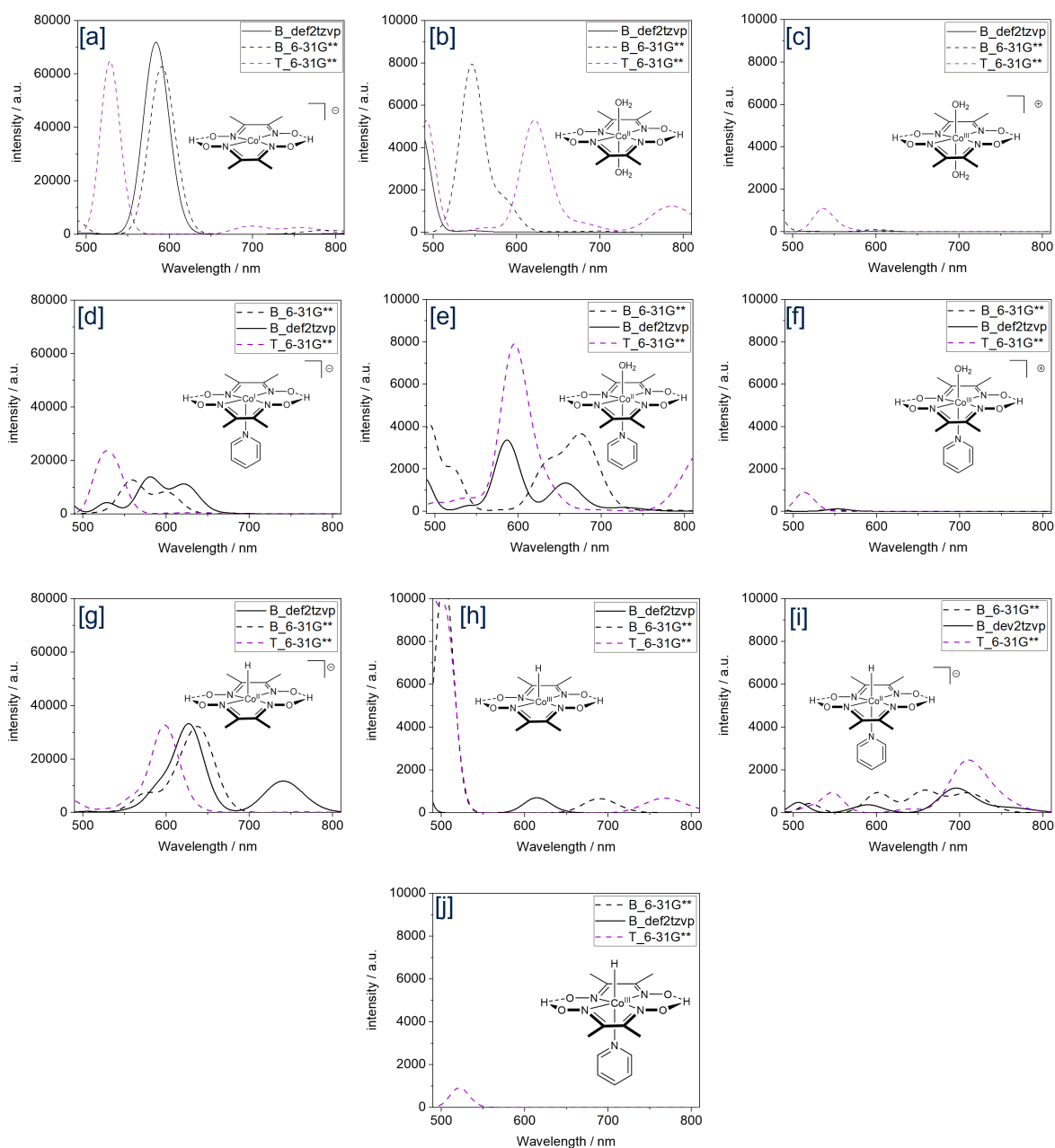
Figure 5.5: Computationally calculated UV-Vis absorption spectra for (a-c) $Co(dmgH)_2(H_2O)_2$ and (d-f) $Co(dmgH)_2(H_2O)py$ via density functional theory (DFT). (a,d) depict the Co(I) oxidation state, (b,e) depict the Co(II) oxidation state and (c,f) depict the Co(III) oxidation state. (g) and (i) represent the DFT-simulated UV-Vis spectra for Co(II)-hydrides, in the case of $Co(dmgH)_2$ and $Co(dmgH)_2py$ respectively. (h) and (j) represent the DFT-simulated UV-Vis spectra for Co(III)-hydrides, in the case of $Co(dmgH)_2$ and $Co(dmgH)_2py$ respectively. B_ corresponds to the B3LYP functional and T_ corresponds to the TPSSh functional. DFT calculations were performed by Annika Eisenschmidt.

Chapter 6

Stern-Volmer analysis in fibra

The contents of this chapter have resulted in the following publications:

Alexander S. Gentleman[†], Takashi Lawson[†], Molly Davis, Jacob Turner-Dore, Michael Frosz, Alexander J. Cresswell, Erwin Reisner and Tijmen G. Euser. 'Stern-Volmer analysis of fluorescence quenching of photocatalysts within hollow-core photonic crystal fibre microreactors'. **(in preparation)**.

[†] authors contributed equally

4CzIPN was synthesised by Jacob Tuner-Dore. Results presented in this chapter were solely obtained and analysed by the author of this thesis. Section 6.4.2 was written together with Alexander Gentleman.

The use of quantitative fluorescence spectroscopy within optofluidic hollow-core photonic crystal fibre microreactors can give insight into electron transfer dynamics and energy dispersal mechanisms of homogeneous photocatalysts. Specifically, the mechanism of a recently developed visible-light photoredox reaction for the α-C-H alkylation of unprotected primary amines with methyl acrylate is interrogated. This transformation deploys the organic photocatalyst 2,4,5,6-tetra(9H-carbazol-9-yl)isophthalonitrile (4CzIPN) in combination with an azide ion (N_3^-) co-catalyst that also serves as the primary reductive quencher for 4CzIPN*. Stern-Volmer analysis on 170 nL sample volumes was performed on a model system consisting of 4CzIPN with tetrabutylammonium azide (Bu_4NN_3) and cyclohexylamine (CHA), the latter being a representative amine substrate for the photocatalytic α-C-H alkylation reaction. The results obtained from in-fibre Stern-Volmer analysis compare well with those obtained via conventional fluorimeter-based methods for the Bu_4NN_3 quencher, and show marked improvement to results obtained for the CHA quencher via the same conventional methods. This work provides a starting point for automated, nanolitre-volume fluorescence quenching analysis, enabling the high-throughput screening of photocatalysts or quenchers for the discovery of new photocatalytic transformations.

6.1 Importance of fluorescence

The development of photocatalytic systems that efficiently and sustainably convert UV-Vis light into chemically stored energy ('solar fuels'), or harness photonic energy in the chemical synthesis of high-value chemicals, is a major scientific and technological challenge, and a route that remains largely untapped despite its potential significance. Solar fuels include small molecule feedstocks such as H_2, CO, CH_4, HCO_2H and CH_3OH,[45,221] whereas high-value chemicals include complex organic molecules in pharmaceuticals and crop protection agents.[222]

In the case of solar fuels, photonic energy is converted into chemical potential energy - a process inspired by natural photosynthesis, for the endergonic conversion of carbon dioxide and water into carbohydrates and dioxygen in living organisms. On the contrary, the use of visible-light photocatalysis in organic synthesis harnesses this photonic energy to surmount an activation barrier in the reaction mechanism, but the net transformations are intrinsically exergonic (i.e., the photon's energy is harnessed but not ultimately stored).[223]

Both fields share the fundamental commonality of a photocatalyst (PC) - a chemical entity that is capable of absorbing UV-Vis light and whose excited state (PC*) then interacts with a non-absorbing molecular species (a 'quencher') in order to induce a chemical reaction. The collision-induced quenching step can proceed via either an energy transfer pathway (EnT) (i.e., indirectly exciting the quencher),[224] or via a single electron transfer pathway (SET) (i.e., oxidising or reducing the quencher to generate a radical species).[225] The term 'photosensitiser' is used in the former case and 'photoredox catalyst' in the latter case, but some catalysts can operate via either pathway and so the broader term 'photocatalyst' is preferable.

Regardless of the application or precise mechanism, one particular aspect of photocatalytic systems that requires further elucidation is the competitive nature of energy dispersal mechanisms of the catalyst's excited state, PC*, between productive quenching (which leads to the chemical reaction of interest) versus non-productive relaxation. Once generated, the excess energy contained within PC* can be dispersed, returning the PC to its ground state in the process. The relaxation of PC* can be either radiative (i.e., fluorescence from ^{1}PC* or phosphorescence from ^{3}PC*) or it can be non-radiative (e.g., $S_1 \rightarrow S_0$ internal conversion followed by vibrational relaxation), transferring thermal energy to the bulk medium in the latter case.

As the kinetics associated with these energy dispersal mechanisms govern the efficiency and catalytic turnover[171] of a particular photocatalytic system, gaining an enhanced understanding of these competing dispersal mechanisms will allow a more judicious choice of PC when designing a photocatalytic system. For instance, the experimental quantification of fractionation between quenching and relaxation for a given PC-quencher combination can be used for mechanistic interrogation in photocatalytic reaction development, to identify or confirm which molecular species is engaging with the excited photocatalyst.

A common technique is Stern-Volmer analysis, which measures the rate of quenching of PC* by a given quencher species, as a function of its concentration, in competition with radiative decay processes. [150,151,226] In fact, this technique has found application beyond the provision of mechanistic insight, and has recently been leveraged as a high-throughput screening technology for the discovery of novel synthetic organic transformations. [227]

It was shown in Chapter 4 and Chapter 5 that electron transfers under reaction conditions can be studied with UV-Vis absorption spectroscopy within HC-PCFs. In this chapter, a new fibre-based optofluidic microreactor approach is employed to perform fluorescence spectroscopy on ultra-small volumes of 4CzIPN, in the presence of fluorescence quenchers, Bu_4NN_3 and CHA, with the results obtained being used to perform a Stern-Volmer analysis.

The 4CzIPN photocatalyst and Bu_4NN_3 / CHA quencher combinations were chosen to interrogate the mechanism of a visible-light photoredox reaction for α-C-H alkylation of unprotected primary amines with methyl acrylate. [228] This transformation deploys the popular organic photocatalyst 4CzIPN in combination with an azide ion (N_3^-) as a hydrogen atom transfer (HAT) co-catalyst. [229] The azide ion is introduced experimentally as Bu_4NN_3, which affords solubility in the organic solvent utilised for the chemistry (acetonitrile).

Cresswell *et al.* have previously utilised cuvette-based Stern-Volmer analyses to ascertain that the azide ion (N_3^-) co-catalyst serves as the primary reductive quencher for 4CzIPN*, with some very minor competitive quenching by the primary amine substrate. [228] Hence, to provide a head-to-head comparison with these results, the same reaction is investigated via Stern-Volmer fluorescence quenching analysis in a HC-PCF. This provides a pretext for future use in the analysis of other photocatalytic processes.

In the first instance, to ensure that fluorescence light can be collected in the fibre geometry, the applicability of side-irradiation and in-coupled excitation was investigated. As part of these preliminary studies, Coumarin dyes [230] were utilised as the fluorescent emitter.

6.2 Preliminary measurements

6.2.1 Coumarin dyes

Coumarin dyes are chromenones that undergo photo-induced electron transfer in the presence of an amine, resulting in a drop in fluorescent counts. [230] Preliminary measurements with Coumarin 515 and Coumarin 490 were undertaken in acetonitrile with the fluorescence quencher N-methylaniline (MAN). These experiments ensured that the change in fluorescent counts on addition of a quencher (in this case MAN) were sufficient to detect within a HC-PCF environment.

Two excitation geometries were considered: in-coupling a laser diode into a HC-PCF and side-irradiating the HC-PCF with a LED source. Further details on both these geometries are provided in Section 3.1.6.

Side excitation A solution of $5\,mM$ Coumarin 490 in acetonitrile was infiltrated into a kagomé-style HC-PCF (20110315-02) following $15\,min$ of purging to remove residual O_2. This sample was subject to $405\,nm$ excitation using a HepatoChem EvoluChem 405PF LED source ($272\,mW\,cm^{-2}$), by side-irradiating a $5\,cm$ length of the HC-PCF. On addition of N-methylaniline to additional samples, the fluorescent counts decreased, as shown in Figure 6.1a. The fluorescent counts were primarily guided through the core as shown in Figure 6.1b. An aperture was employed to spatially select the fluorescent counts from the core for taking the fluorescent spectra.

In-coupled excitation A solution of $50\,\mu M$ Coumarin 515 in ethanol was infiltrated into a HC-NCF (20190930-1) following $15\,min$ of purging to remove residual O_2. This sample was subject to $405\,nm$ excitation using a Thorlabs CPS405 laser diode ($613\,\mu W$), which was coupled into the fibre with a transmission efficiency of $3.4\%T$ (in ethanol). The fluorescent counts from a sample with $475\,\mu M$ N-methylaniline decreased by $\times 6$, as shown in Figure 6.1c. Interestingly the fluorescent counts were primarily guided through the cladding as shown in Figure 6.1d. This corroborates the low index coating model discussed in Section 8.1, with the polymer coating substituted for air. In-coupled light was efficiently absorbed by the Coumarin dye infiltrated in the core, as no additional counts were detected at the spectrometer when the $450\,nm$ long-pass filter was removed.

Fluorescence was guided and detectable in both excitation geometries, however, to ensure a homogeneous excitation profile, side-irradiation was selected for fluorescence studies herein. Moreover, a kagomé-style fibre was chosen for these further studies, due to the fluorescence mainly being confined to the core, making the analysis easier via spatial filtering. These preliminary measurements show that although the angular range of fluorescence collection is small, this is compensated for by integrating the counts along the length of the fibre. As a result, sufficient counts are detectable at the spectrometer to measure a low-noise fluorescence spectrum, without the need for a photomultiplier tube (PMT) that are common in fluorimeters. Given this optofluidic setup works with conventional Coumarin dyes, the fluorescence of the photoredox catalyst 4CzIPN was then measured in fibre.

6.2.2 4CzIPN

The absorbance of 4CzIPN, tetrabutylammonium azide (Bu_4NN_3) and cyclohexylamine (CHA) was measured using a Cary 300 UV-Vis Spectrophotometer, with the profiles shown in Figure 6.2a. The absorption of the two quenchers is minimal at $365\,nm$, meaning 4CzIPN is the chemical entity solely responsible for photon absorption. The absorption edge of 4CzIPN tails off at $470\,nm$; thus any fluorescence emitted by 4CzIPN shorter than this wavelength is increasingly likely to be re-absorbed.
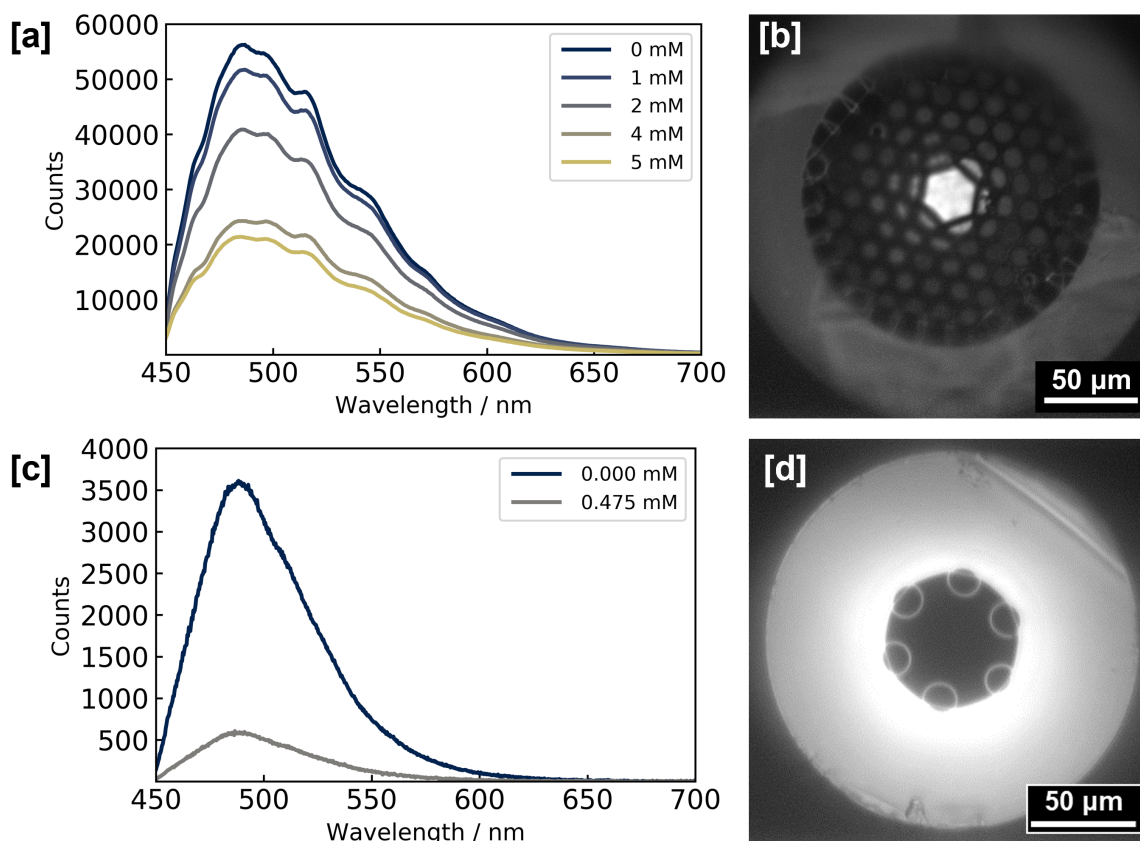
Figure 6.1: (a) Fluorescent counts of Coumarin 515 as a function of N-methylaniline (MAN) quencher concentration. (b) Image of the fibre facet showing the fluorescence emanating from the core of the fibre. (c) Fluorescent counts of Coumarin 490 as a function of MAN concentration. (d) Image of the fibre facet showing the fluorescence coming mainly from the cladding.

A Cary Eclipse Fluorescence Spectrophotometer was then used to produce an excitation-emission map to identify an excitation wavelength which maximises the fluorescent counts. This data is presented in Figure 6.2b. A 365 nm source was identified as the most appropriate for performing fluorescence spectroscopy on 4CzIPN. Fluorescence spectra with the addition of various concentrations of Bu_4NN_3 were then collected for Stern-Volmer analysis, under the same sample preparation procedures as fibre-based measurements. These methods are detailed in Section 6.3. Fluorescence spectra were measured under three different excitation wavelengths (455 nm, 425 nm and 365 nm). As expected from the absorption profile (Figure 6.2a) and excitation-emissions maps (Figure 6.2b) of 4CzIPN, the fluorescent counts decrease with increasingly longer wavelengths, and the bimolecular quenching process becoming less efficient.

6.3 Experimental method

A 20 cm length of kagomé-style fibre (20110315-02) was injected with various samples of photosensitiser and quencher. As the refractive indices are very similar for water (1.33) and acetonitrile (1.34), the ARROW model predicts that light guidance should be maintained in acetonitrile. See Section 3.3 for further details.

Figure 6.2: (a) UV-Vis absorption spectra of 4CzIPN (0.03 mM), tetrabutylammonium azide (Bu$_4$NN$_3$, 0.6 mM) and cyclohexylamine (CHA, 12 mM). An Agilent Cary 300 UV-Vis Spectrophotometer was used to collect the absorption spectra. Absorbance is referenced to a cuvette of acetonitrile.(b) Emission spectra as a function of excitation wavelength, as measured by a Cary Eclipse Fluorescence Spectrophotometer. (c) Peak emission counts from (b) plotted against excitation wavelength.

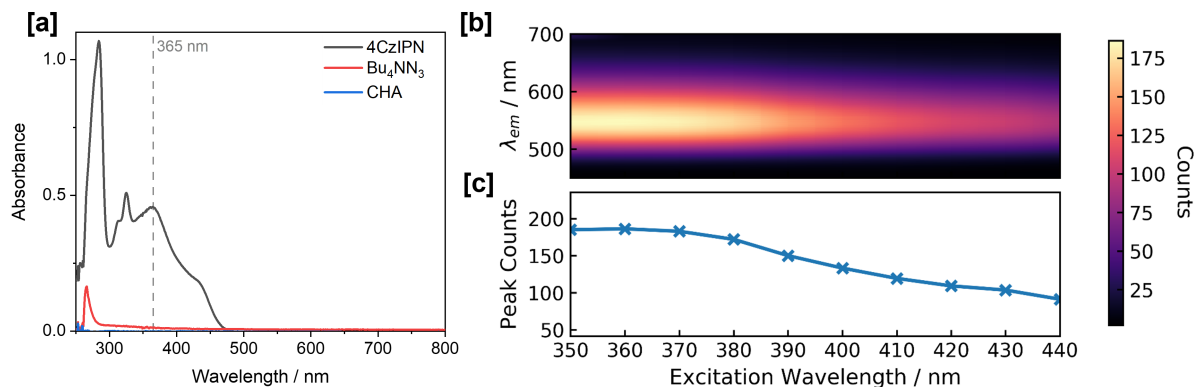0.03 mM samples of 4CzIPN in acetonitrile were prepared at five different quencher concentrations to perform a Stern-Volmer analysis. CHA and Bu$_4$NN$_3$ were compared as fluorescence quenchers for these purposes.

A 365 nm UV LED source (HepatoChem EvoluChem 365PF) together with an optical diffuser (Thorlabs DG20-220-MD) was used to side-irradiate a 5 cm section of the HC-PCF, ensuring a homogenous excitation of 95 mW cm^{-2} across a 36 nL volume. Further details on the optical setup are discussed in Section 3.1.6. A 365 nm excitation wavelength was chosen to match the absorption peak of 4CzIPN in acetonitrile, proposed to correspond to the S_3 electronic state (mainly HOMO $\rightarrow$ LUMO + 1 transition).[231]

A beamsplitter (BS) cube divided the guided fluorescent light over an imaging CCD (IDS UI-3240LE-NIR-GL) and a fibre-coupled spectrometer (Ocean Optics QE 65000). Spatial filtering through an aperture (A1) was employed to selectively collect fluorescent counts from the core region of the HC-PCF. Fluorescence spectra were generated by integrating the spectrometer counts over a 1 s period and subtracting a background spectrum measured over the same integration period.

Samples were purged under nitrogen for at least 20 min prior to loading into the fibre and were injected into the pressure cell using gas-tight syringes and a syringe pump (Aladdin AL-1000). Fibres were thoroughly cleaned with acetonitrile before use, and a background fluorescence spectrum was taken. Samples were then inserted sequentially into the fibre.

The 4CzIPN photosensitiser was synthesized via a procedure outlined by Engle *et al.* with inconsequential modifications.[232] All other chemicals and reagents were purchased from commercial suppliers and used as received unless otherwise noted. Laboratory-grade reagents were of the highest available purity. All stock solutions were made up using extra dry acetonitrile ($<$ 50 ppm water).
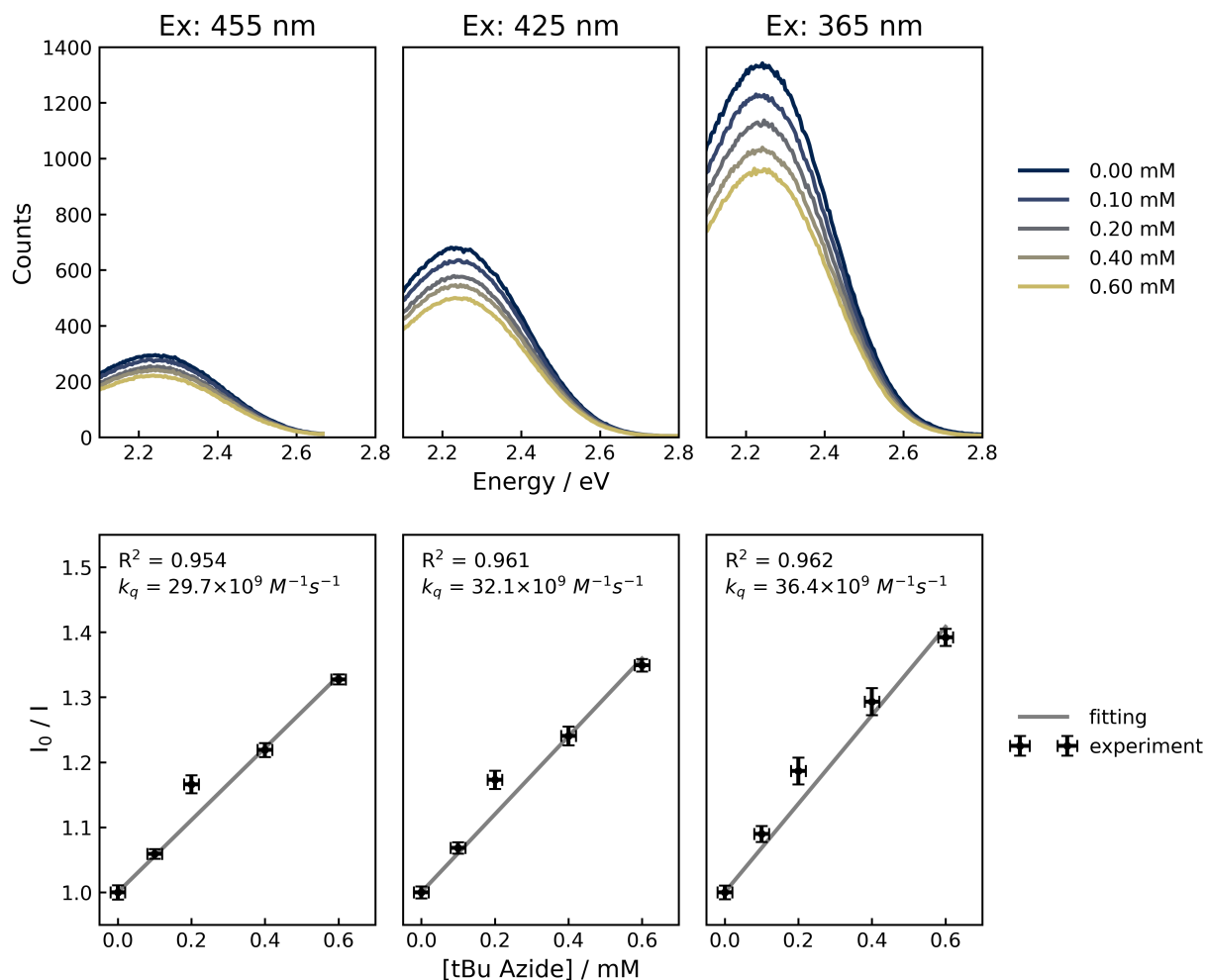
Figure 6.3: Fluorimeter-based Stern-Volmer analysis on 4CzIPN with the fluorescence quencher Bu_4NN_3. Fluorescence spectra at different quencher concentrations (top) and Stern-Volmer plots (bottom) at three different excitation wavelengths (455 nm, 425 nm, and 365 nm). Error bars indicate the standard error of triplicate measurements. A Cary Eclipse Fluorescence Spectrophotometer was used to collect the fluorescence spectra, with Stern-Volmer analysis performed by the same method as the fibre-based measurements. Spectra were truncated to remove counts from the excitation source from the Stern-Volmer analysis where relevant.

6.3.1 Data analysis

0.03 mM samples of 4CzIPN in acetonitrile were prepared at 5 different quencher concentrations to perform Stern-Volmer analysis. CHA and Bu_4NN_3 were compared as fluorescence quenchers for these purposes.

Background-subtracted fluorescent counts recorded in units of wavelength ($f(\lambda)$) were truncated to wavelengths between 400 nm and 700 nm, then converted to units of energy ($f(E)$) via scaling by the Jacobian transformation in Equation 6.1. [233]

$$f(E) = -f(\lambda)\frac{hc}{E^2} \tag{6.1}$$
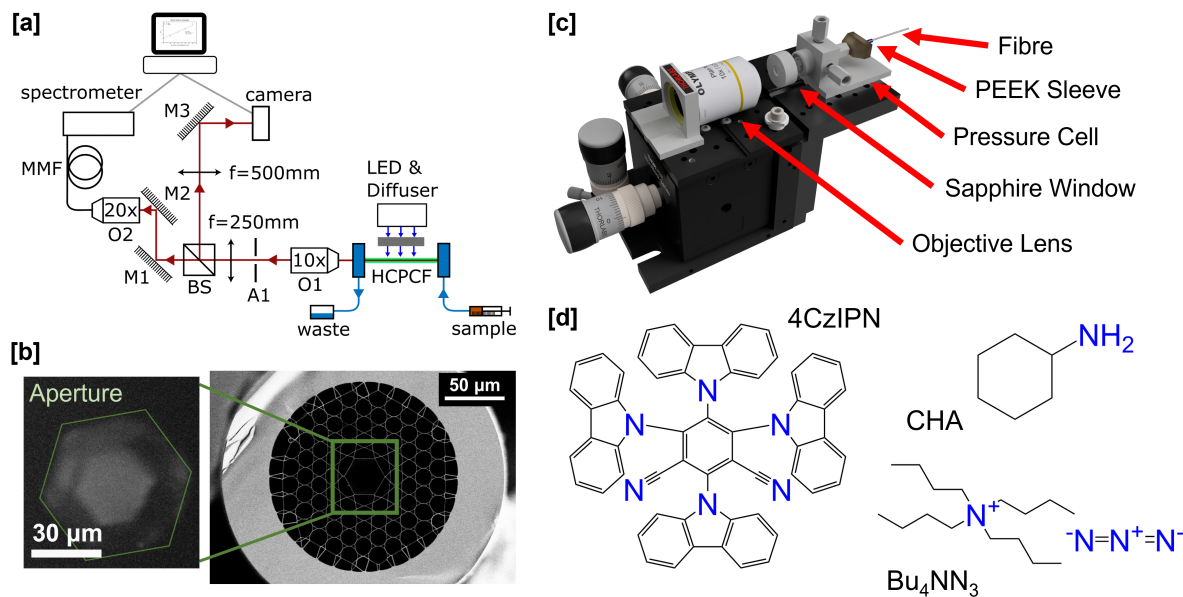
Figure 6.4: Fibre-based optofluidic microreactor for ultralow-volume fluorescence spectroscopy. (a) Optical setup enabling the fluorescence to be simultaneously analysed by a camera (see (b)), and its spectrum by a spectrometer. BS, beamsplitter; MMF, multimode fibre; O1, fluorescence out-coupling objective; O2, objective lens used to fibre-couple the fluorescence to a spectrometer; A1, aperture used to spatially select the core region (green hexagon in (b)). (b) Scanning electron microscopy (SEM) image of the kagomé-style hollow-core photonic crystal fibre (HC-PCF) with a corresponding camera image of the fluorescent light captured from the core. (c) 3D schematic of the pressure cells used in these experiments that interface the optics with commercially available PEEK microfluidics components. (d) Chemical structures of the photosensitiser (4CzIPN) together with the two fluorescence quenchers tested, cyclohexylamine (CHA) and tetrabutylammonium azide (Bu$_4$NN$_3$).

Plotting fluorescent counts against photon energy provides superior physical insight for quantitative fluorescence analysis. A Jacobian transformation is required to convert the counts measured on a spectrometer, as those signals are recorded per unit wavelength. As the intervals $d\lambda$ are not evenly sized across the energy spectrum, data is falsely represented if a Jacobian transformation on the counts is not carried out.[233]

A Stern-Volmer analysis was then performed using the integrated counts (Equation 6.2),[5] by normalising the integrated counts (I_n) at each of the five quencher concentrations ($[Q]_n$) to the sample without quencher (I_0). Three separate measurements were taken at each of the five quencher concentrations, and a linear function fitted to the mean normalised counts to extract the bimolecular Stern-Volmer quenching rate constant, k_q. The fluorescence lifetime in the absence of quencher, τ_0, was taken as 18.7 ns.[231]

$$\frac{I_0}{I_n} = 1 + k_q \tau_0 [Q]_n \qquad (6.2)$$

6.4 Results and discussion

6.4.1 Fluorescence quenching measurements and Stern-Volmer analysis

A Stern-Volmer analysis was first conducted with Bu_4NN_3 to determine the rate at which it can quench the excited state of 4CzIPN, with the results presented in Figure 6.5. The azide anion (N_3^-) is oxidized to the azidyl radical ($N_3^\bullet$) as part of the quenching process.[234] A background ('control') fluorescence spectrum taken prior to loading with 4CzIPN samples shows that the background fluorescence from the HC-PCF infiltrated with pure acetonitrile was negligible. Fitting the normalized counts to the linear function in Equation 6.2 gives a Stern-Volmer bimolecular quenching rate constant, k_q, of $30.5 \times 10^9 \pm 1.1 \times 10^9 \, \mathrm{L \, mol^{-1} \, s^{-1}}$ with strong confidence ($R^2 = 0.995$).

Fluorimeter-derived measurements (see Figure 6.3) with the same data analysis methodology and triplicate repeats, gave a similar k_q of $36.4 \times 10^9 \pm 1.8 \times 10^9 \, \mathrm{L \, mol^{-1} \, s^{-1}}$ with a slightly lower confidence $R^2 = 0.962$, showing the reproducibility of our Stern-Volmer measurements between separate measurement platforms. In addition, fibre-based measurements enabled a bimolecular rate constant to be extracted on a 10^4 times smaller sample volume than fluorimeter-based measurements ($2 \, \mathrm{mL}$ compared to $140 \, \mathrm{nL}$ per measurement).

Figure 6.5: Fluorescence quenching of $30 \, \mu\mathrm{M}$ 4CzIPN by Bu_4NN_3. Fluorescence profiles at each quencher concentration are shown in (a) with a Stern-Volmer plot presented in (b). A control measurement in (a) confirms that fluorescence from the HC-PCF is insignificant compared to 4CzIPN. Error bars in (b) correspond to the standard error of triplicates.

Reabsorption of fluorescence by 4CzIPN or Bu_4NN_3 is expected to be negligible due to the marginal overlap between absorbance and fluorescence profiles (see Figure 6.2 for the absorbance profile). Any reabsorption effects would be most dominant above $2.6 \, \mathrm{eV}$ where our fluorescent counts are low. However, over the $20 \, \mathrm{cm}$ fibre length, reabsorption effects may become more important as absorbance scales proportionally with optical path length

as described by the Beer-Lambert Law. By comparing the spectral shape of the fluorescence in the absence of Bu_4NN_3 to that with $1.2\,mM\ Bu_4NN_3$ (see Figure 6.6), it is estimated that less than 4% of fluorescent photons are reabsorbed over the fibre length.
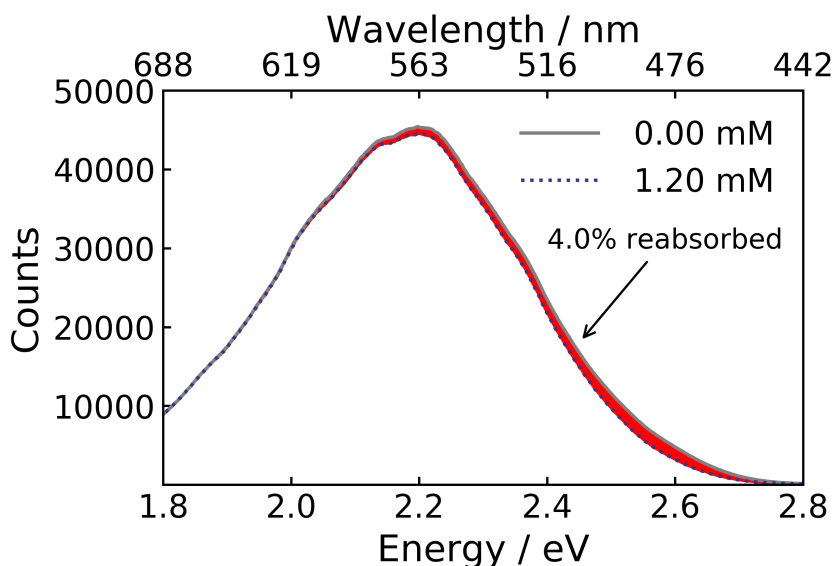
Figure 6.6: Fluorescence profiles of 4CzIPN with and without $1.2\,mM\ Bu_4NN_3$. The $1.2\,mM$ Bu_4NN_3 profile is scaled by a factor 1.65 such that the spectral counts at low energies are equivalent. The resulting differences at higher energies, filled in red, then correspond to the photons reabsorbed by either 4CzIPN or Bu_4NN_3. Each curve is integrated, and the difference in integrand gives the proportion of photons reabsorbed - 4.0%.

A similar Stern-Volmer analysis was conducted with CHA to compare against Bu_4NN_3. We find that CHA as a quencher for 4CzIPN is less effective and report a bimolecular quenching rate constant, k_q, of $1.6 \times 10^9 \pm 0.1 \times 10^9\,L\,mol^{-1}\,s^{-1}$ with moderate confidence ($R^2 = 0.849$).

To give a clear interpretation of the azide anion and CHA as quenchers, the proportion of excited states which interact with each quencher is calculated from the fluorescence lifetime and bimolecular quenching rate constant, as shown in Equation 6.3. It is observed that 36% of the excited state of 4CzIPN is quenched by $1\,mM$ of azide compared to 3% with $1\,mM$ of CHA.

$$F_q = \frac{k_q[Q]}{\tau_0 + k_q[Q]} \tag{6.3}$$

Cuvette-based measurements in a commercial fluorimeter with CHA were inconclusive, with immaterial changes in detected fluorescence. This may partly be due to trace O_2 which competes with CHA in quenching the 4CzIPN excited state, but also due to the lower sensitivity of the fluorimeter over its fibre-based counterpart.
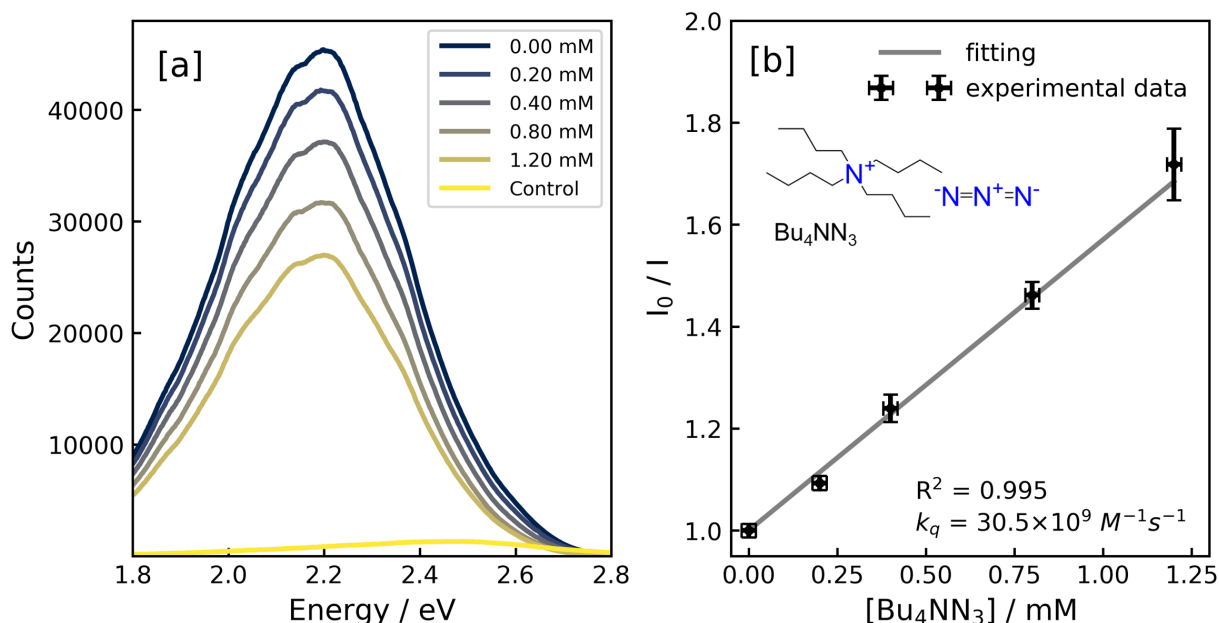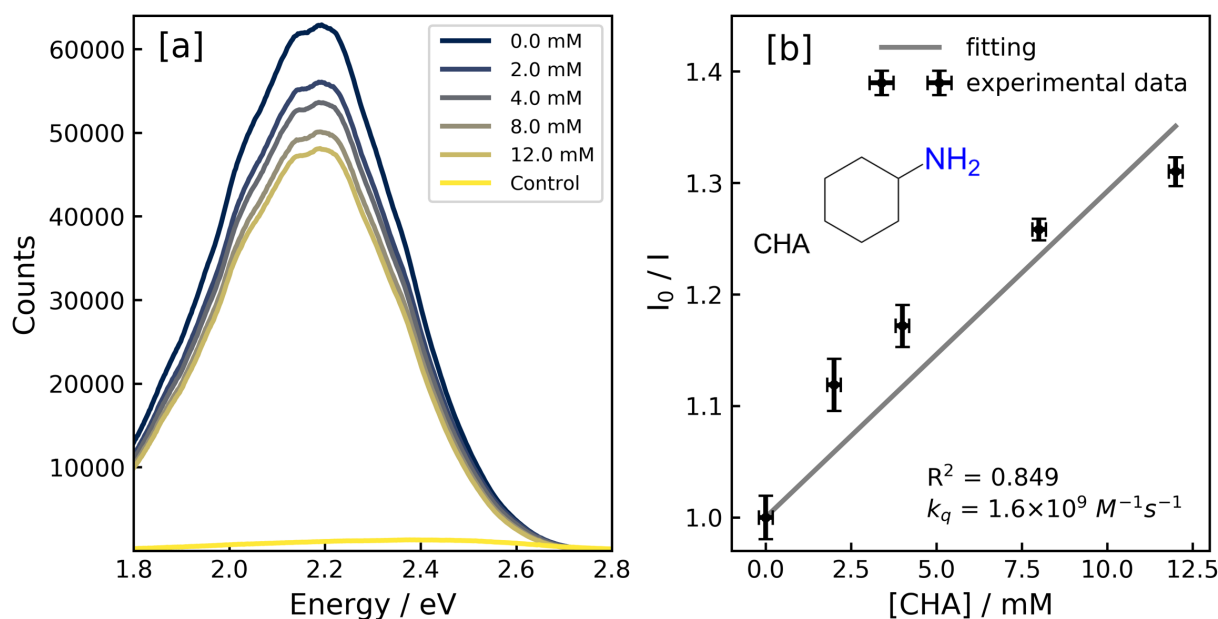
Figure 6.7: Fluorescence quenching of $30\,\mu M$ 4CzIPN by CHA. Fluorescence profiles at each quencher concentration are shown in (a) with a Stern-Volmer plot presented in (b). A control measurement in (a) confirms that fluorescence from the HC-PCF is insignificant compared to 4CzIPN. Error bars in (b) correspond to the standard error of triplicates.

6.4.2 Mechanistic insight obtained from Stern-Volmer analysis

Stern-Volmer analysis allows fundamental mechanistic insight into photoredox processes to be obtained, ensuring that the quenching dynamics between photocatalysts and substrates can be quantitatively analysed in order to ascertain the extent to which each component in the reaction mixture quenches the excited-state of the photocatalyst. Unfortunately, Stern-Volmer analysis cannot provide any insight into the nature of the quenching, for example, whether energy transfer or electron transfer is responsible for the quenching process. However, it can provide kinetic information regarding the extent to which various components in a catalytic mixture are quenching the fluorescence of the photocatalyst, in addition to whether static or dynamic (collisional) quenching is responsible.

For the synthetic photoredox protocol newly-developed by Cresswell *et al.* for synthesising α-tertiary amines and their corresponding γ-lactum derivatives, the 4CzIPN photocatalyst is used in conjunction with a HAT catalyst and an electrophilic Michael acceptor in order to yield the desired products via the generation of unprotected α-amino radicals from primary amines. After screening various HAT catalysts using CHA as a representative primary amine and butyl acrylate (BA) as the Michael acceptor, Bu_4NN_3 was found to be the most effective for this synthetic photoredox protocol. As these experiments were conducted using 4CzIPN as the photocatalyst, CHA as the representative primary amine, and Bu_4NN_3 as the HAT catalyst, it is pertinent to investigate the fluorescence quenching dynamics of 4CzIPN with Bu_4NN_3 and CHA within HC-PCF microreactors to demonstrate their enhanced capability over fluorimeter-based approaches for performing Stern-Volmer analysis.

From *in-fibra* Stern-Volmer analysis, the Bu_4NN_3 is shown to be much more efficient than CHA at quenching the excited state of 4CzIPN, with more reliable values of the bimolecular quenching coefficient when compared to fluorimeter-based measurements for the 4CzIPN/CHA quenching pair. Even though the bimolecular quenching rate coefficient obtained for Bu_4NN_3 is of a similar magnitude to the rate of diffusion ($k_{diff} \approx 10^{10}\,\mathrm{s}^{-1}$),[225] static and dynamic (collisional) quenching pathways cannot be distinguished without excited state lifetime studies. Despite this, the comparison of k_q values for Bu_4NN_3 and CHA indicates that when the two components are present in the photoredox reaction mixture, Bu_4NN_3 is mechanistically more engaged than CHA in the excited-state quenching process. As such, it can be inferred that the photoredox process is initiated via energy or electron transfer between the excited state 4CzIPN (4CzIPN*) and Bu_4NN_3, with single electron transfer (SET) being the more likely scenario. This is further justified by the enhanced reducing power of N_3^- over CHA with respect to 4CzIPN* ($E_{p/2}$ of N_3^- = + 0.87 V; $E_{p/2}$ of CHA = + 1.53 V; $E_{1/2}$ (4CzIPN*/4CzIPN·⁻) = + 1.35 V - all vs. SCE in acetonitrile),[228] ensuring that SET from N_3^- to 4CzIPN* is a thermodynamically-feasible process. The *in-fibra* Stern-Volmer analysis confirms that the photoredox-catalysed α-C-H alkylation of unprotected primary amines to directly synthesise α-tertiary amines and their γ-lactum derivatives[228] relies on an electron transfer event between 4CzIPN* and Bu_4NN_3 to proceed. The alternative is an electron transfer event between 4CzIPN* and CHA, which this analysis shows will not occur due to the lower k_q value obtained.

6.5 Conclusions

Quantitative fluorescence spectroscopy can be performed on 140 nL volumes using optofluidic hollow-core photonic crystal fibre microreactors. Fibre-based Stern-Volmer analysis was successfully carried out on a 4CzIPN photocatalyst together with the azide anion fluorescence quencher. These are key reagents used in the photoredox-catalysed synthetic protocol newly-developed by Cresswell *et al.* for synthesising α-tertiary amines and their corresponding γ-lactum derivatives. The resulting bimolecular quenching rate constant was found to be comparable to conventional fluorimeter-derived methods, despite the 10^4 times reduction in sample volume.

Additionally, upon performing *in-fibra* Stern-Volmer analysis in the fluorescence quenching of 4CzIPN with cyclohexylamine, another key reagent in the synthetic photoredox protocol developed by Cresswell *et al.*, more reliable values of the bimolecular quenching coefficient were determined when compared to fluorimeter-based measurements. Thus, this work provides a foundation for fully automated fluorescence screening of photoredox catalysts with quencher concentrations adjusted in continuous flow, whilst minimising the consumption of precious and expensive reagents.

Chapter 7

Transient absorption spectroscopy on carbon nanodots

Measurements in this chapter were interpreted by Takashi Lawson. Samples were prepared by Takashi Lawson and Alexander Gentleman. Data were analysed and plotted by Stuart Macpherson. Carbon nanodots were synthesised by Ava Lage. CoP[1] was synthesised by Daniel Antón-García.

In this chapter, transient absorption spectroscopy is used to provide additional insight into the electron-transfer processes occurring at the carbon nanodot (CD) surface. The CD-driven photoreduction of methyl viologen (MV^{2+}) to the radical cation ($MV^{\bullet+}$) is monitored as a model reaction with various sacrificial electron donors (Ascorbic Acid and EDTA). The co-catalyst CoP[1] is also utilised as a reductive indicator. Although these measurements were performed in cuvette, future work aims to perform TA spectroscopy *in-fibra*, to enhance weak absorption signals and detect optically-evasive intermediate states.

7.1 Importance of ultra-fast spectroscopy

Time-resolved absorption spectroscopy with carbon nanodot-driven photochemistry has been shown in previous chapters. However, the resolution afforded by these steady-state measurements is restricted to 1×10^{-4} s. Full mechanistic insights into the nanodot-catalyst interface can only be generated by probing the electron-transfer timescales in the 1×10^{-9} s to 1×10^{-3} s regime (see Section 2.2), which is possible with pump-probe techniques such as transient absorption (TA) spectroscopy.[32,44,235,236,40] TA spectroscopy can probe the photophysical properties of carbon nanodot (CD) systems, in terms of their intrinsic relaxation processes, the nature of photogenerated intermediate species, and CD charge transfer reactions. Crucially, charge carrier lifetime (the average elapsed time between the generation and recombination of excited electrons/holes) can be determined, which must be longer than the reaction time scales to allow any significant amount of catalysis to occur.[90]

Stationary-state UV-Vis absorption spectroscopy measures the ground-state sample, whereas in TA spectroscopy both the ground state and excited states are measured. The transient absorption signal (ΔOD) is defined as the difference between the absorbance of the excited and ground state samples

$$\Delta OD(\lambda, \tau) = OD^*(\lambda, \tau) - OD^0(\lambda) \qquad (7.1)$$

where $OD^*(\lambda, \tau)$ and $OD^0(\lambda)$ correspond to the optical density (absorbance) of the excited state and ground state, respectively. The transient absorption signal is a function of the wavelength, λ, and the time delay, τ, defined as time elapsed after excitation.

In general, three components can contribute to the TA signal: a ground state bleach, stimulated emission and photoinduced absorption.[90] In a ground state bleach, a fraction of the molecules have been promoted to the excited state through the action of the pump pulse, and therefore the number of molecules in the ground state has decreased. Hence, the ground-state absorption in the excited sample is less than that in the non-excited sample and a negative signal in the ΔOD spectrum is observed. Stimulated emission also manifests as a negative signal. The probe source can stimulate further coherent emission, where photons emitted have the same phase and direction as the incoming photon. This results in a higher number of counts at the detector compared to the ground state, and hence a negative absorption signal. A positive signal results from photoinduced absorption ('PIA'), where intermediate reaction products are generated that absorb in the UV-Vis region of the electromagnetic spectrum. These intermediates can be short-lived, but are importantly detectable on the time-scales of TA spectroscopy.

TA spectroscopy was first reported by George Porter in 1950 for the identification of reaction intermediates,[237] but TA-derived mechanistic insights into useful photocatalytic reactions remain relatively scarce. Recently, Orr-Ewing and co-workers investigated the organocatalyzed atom-transfer radical polymerization with TA spectroscopy and showed the electron transfer from short-lived excited singlet states can exert control of polymer molecular weight.[236] Additionally, Durrant and co-workers showed that bimolecular reactions with carbon dots, in combination with a molecular Ni bis(diphosphine) catalyst, was limited by fast geminate recombination.[55] However, *in-operando* detection of catalytic intermediates under real operating conditions remains challenging in CD-driven photochemistry. This cuvette-based work aims to determine timescales and spectral features of interest ahead of building an *in-fibra* TA spectroscopy setup.

7.2   Experimental method

Short-time (100 fs - 2 ns) measurements were carried out using the second harmonic of a Ti:sapphire amplifier (Spectra-Physics Solstice) as the pump beam (90 fs pulse width, 500 Hz repetition rate, 3.1 eV photon energy). A motor-driven delay stage was used to mechanically vary the pump-probe delay. Long-time (1 ns - 1 ms) measurements were

carried out using the third harmonic of an electro-optical Q-switched laser (InnoLas picolo AOT) as the pump beam ($< 800\,\text{ps}$ pulse width, $500\,\text{Hz}$ repetition rate, $3.49\,\text{eV}$ photon energy). A delay generator was used to electronically vary the pump–probe delay.

For both short and long-time measurements, the probe spectrum was generated using a home-built noncollinear optical parametric amplifier, pumped by the second harmonic of the same Ti:sapphire amplifier (Spectra-Physics Solstice).

A common detection method was used. Transmitted probe and reference pulses were focussed into a calibrated diffraction grating spectrograph (Andor SR303i) and the spectrally-separated light was recorded with an n-type metal–oxide–semiconductor (NMOS) linear image sensor (Hamamatsu S8381-1024Q) and processed by a customized peripheral component interconnect (PCI) interface from Entwicklungsbüro Stresing.

Sample solutions were made up under ambient conditions in quartz cuvettes ($1\,\text{mm}$ path length, Hellma), and sealed with a screw cap. Except where stated, samples were continuously purged with nitrogen during measurements to minimise the oxygen content within the cuvette. Unless stated otherwise, samples were prepared and purged for $10\,\text{min}$ directly before starting a measurement.

7.2.1 Materials

CoP[1] was synthesised by Daniel Antón-García as previously reported.[78,205] All other chemicals and reagents were purchased from commercial suppliers and used as received unless otherwise noted. Laboratory-grade reagents were used for synthesis, and chemicals for the analytical part were of the highest available purity. Phosphate buffer solutions (0.2 M) and sacrificial electron donor (SED) stock solutions (0.2 M) were prepared and verified using a pH electrode (Mettler Toledo, FiveEasy Plus) at pH 6 and pH 8. The pH of SED stock solutions was adjusted using sodium hydroxide and hydrochloric acid. A methyl viologen (MV^{2+}) stock solution was made up by dissolving methyl viologen dichloride. All stock solutions were made up using Milli-Q purified water.

Nitrogen-doped carbon nanodots (NgCDs) were synthesised and characterised according to a previously reported procedure.[55] In brief, NgCDs were synthesized by pyrolysis of aspartic acid at $320\,^\circ\text{C}$ for $100\,\text{h}$. To enhance water solubility, they were neutralised to pH 7 using NaOH and then freeze-dried to obtain the final product as a brown powder.

7.3 Results and discussion

7.3.1 Ultrafast NgCD kinetics

Control measurements with EDTA and EDTA in combination with MV displayed no photo-induced signal. However, the combination of EDTA (0.1 M) with NgCDs ($0.25\,\text{g\,L}^{-1}$) at pH 6 gave rise to a photoinduced signal in the $1\,\text{ps}$ to $2\,\text{ns}$ timescale as shown in Figure 7.1. The CDs were excited with a $400\,\text{nm}$ pump at two different pulse fluences ($14\,\mu\text{J\,cm}^{-2}$,

$140\,\mu J\,cm^{-2}$). The instrument response function, capturing the delay in the detection electronics, was limited to $< 100\,fs$ and does not convolute the absorption signal appreciably for pump-probe delays of $> 1\,ps$.
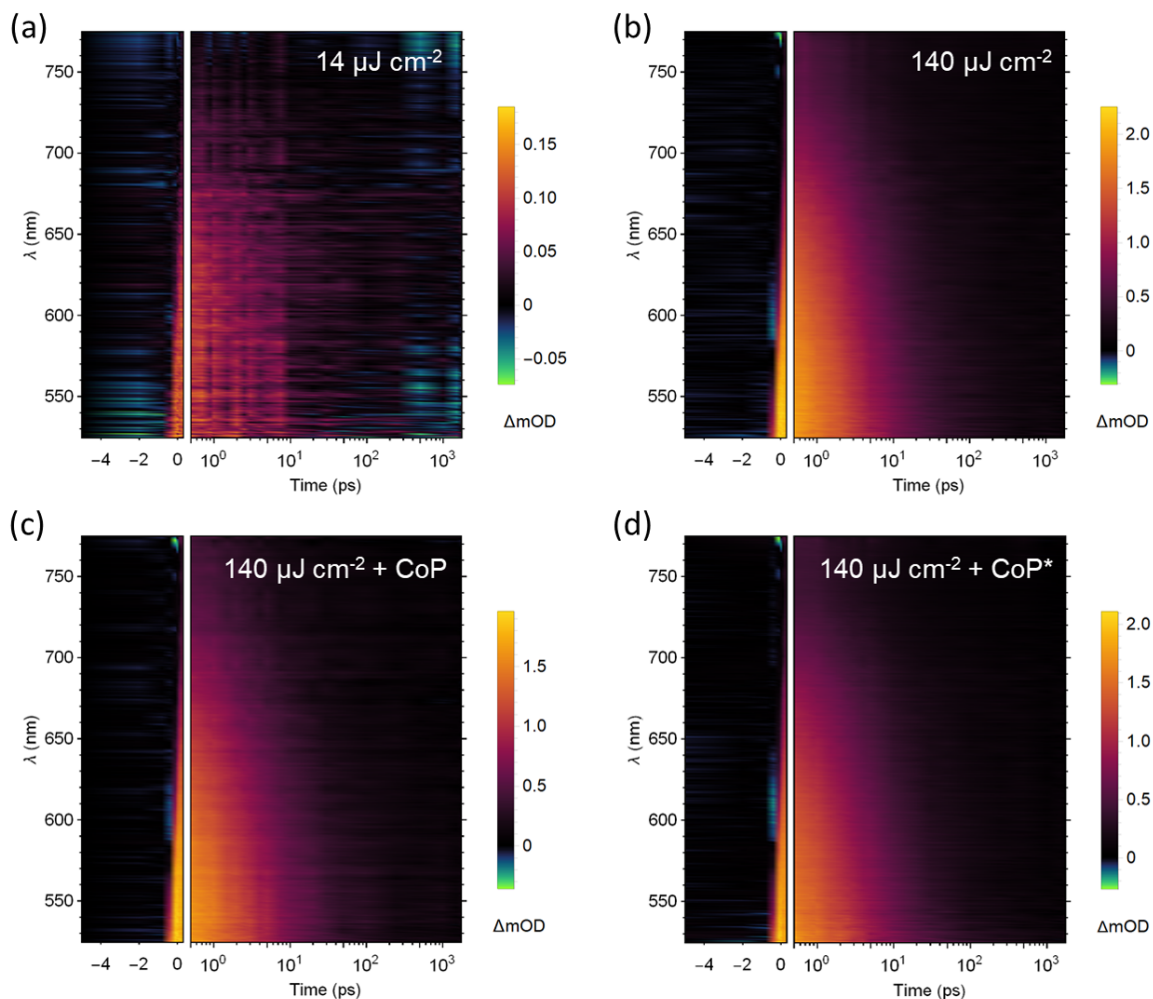
Figure 7.1: Ultrafast transient absorption measurements of nitrogen-doped graphitic carbon nanodots (NgCDs) in a pH 6 phosphate buffer. 2D picosecond TA plots of NgCD absorbers $(0.25\,g\,L^{-1})$ in aqueous solution with EDTA $(0.1\,M)$, under pulsed excitation of (a) $14\,\mu J\,cm^{-2}$ per pulse and (b) $140\,\mu J\,cm^{-2}$ per pulse. (c) 2D TA plot of NgCD absorbers with CoP[1] additive $(340\,\mu M)$ (d) 2D TA plot with the same additive configuration but sample was pre-irradiated with UV light $(365\,nm, 1\,mW\,cm^{-2}, 15\,min)$. All ultrafast TA measurements were pumped at $400\,nm$, with $500\,Hz$ repetition rate.

The increase in absorbance across the full spectral range of the probe source ($510\,nm$ - $775\,nm$) arises due to the greater number of optically allowed transitions from the excited (populated) states of CDs to higher excited states. The absorbance signal then bleaches and is reduced to $< 8\%$ of the initial signal intensity by $1\,ns$. This observation is indicative of the thermalisation of excited state species, and matches well with the residual 6% of long-lived carriers ($> 5\,ns$) reported by Martindale *et al.*.[55]

The magnitude of the absorption signal, and the signal-to-noise ratio, increased as the pump fluence was raised from $14\,\mu J\,cm^{-2}$ per pulse to $140\,\mu J\,cm^{-2}$ per pulse. However, the decay time $(1/e)$ of the absorption feature on ultrafast timescales appears independent of pulse energy, suggestive of a first-order relaxation process with respect to the irradiance.

The addition of electron-accepting CoP[1] $(340\,\mu M)$ had limited effect on the picosecond photophysics, and did not perturb the absorption characteristics of the NgCDs. A pre-irradiated sample $(365\,nm, 15\,min)$ was also measured to ensure that the delay-time phenomenon described in Section 4.6 did not affect the picosecond photophysics. Again, no kinetic variation was observed. This is expected as electron transfer processes usually occur at $10\,\mu s$ (see Section 2.2).

7.3.2 SEDs

Having confirmed that no electron transfer processes occur on timescales $< 1\,ns$, longer pump-probe delays were utilised to measure absorbance on timescales ranging from $1\,ns$ to $1\,ms$. The SED was varied to investigate how this affected the photophysics at these longer timescales. The CDs were excited with a $355\,nm$ pump with a pulse fluence of $240\,\mu J\,cm^{-2}$. The instrument response function, capturing the delay in the detection electronics, was limited to $< 500\,ps$ and does not convolute the absorption signal appreciably for pump-probe delays of $> 1\,ns$. These results are shown in Figure 7.2.

Lifetimes of seconds are inconsistent with typical nanosecond kinetics of excited singlet states and are more in line with trapped charges in semiconductors or potentially long-lived triplet states formed in CDs.[55,61] Therefore, it is likely that absorption contributions at early times arise from bulk transitions within the NgCDs $(< 1\,ns)$, whereas contributions at later times $(> 1\,ns)$ arise from surface (trap) states. These trap states are effectively quenched by O_2 (see Section 7.3.5) and hence must originate primarily from electrons, rather than holes.

The PIA decay profile in the presence of EDTA in a pH 6 phosphate buffer is initially very rapid (Figure 7.2c). Given the EDTA is in abundance around the NgCDs, it is likely that an EDTA coordination sphere forms around the NgCDs, which influences the excited state dynamics of surface trap states through repulsive electrostatic interactions. In this case, EDTA promotes recombination and a faster excited state decay. However, a small plateau appears at $1\,\mu s$ in Figure 7.2b. It could be argued that the plateau is where the decay profile starts to match the form of the NgCD profile alone. Alternatively, this plateau can be interpreted as an electron transfer process to fill the photoinduced holes in the valence band of the CDs, preventing recombination and the elongation of excited state lifetime. Past $5\,\mu s$, the absorption decay matches that of the NgCDs alone.

The PIA decay profile in the presence of ascorbic acid (AA) at pH 4.5 (no phosphate buffer) is initially slower than in the absence of AA, however, this behaviour switches over at $20\,ns$. The AA appears to increase the rate of excited state decay, with no electron transfer processes apparent, in contrast to the behaviour observed with EDTA. It is hypothesised
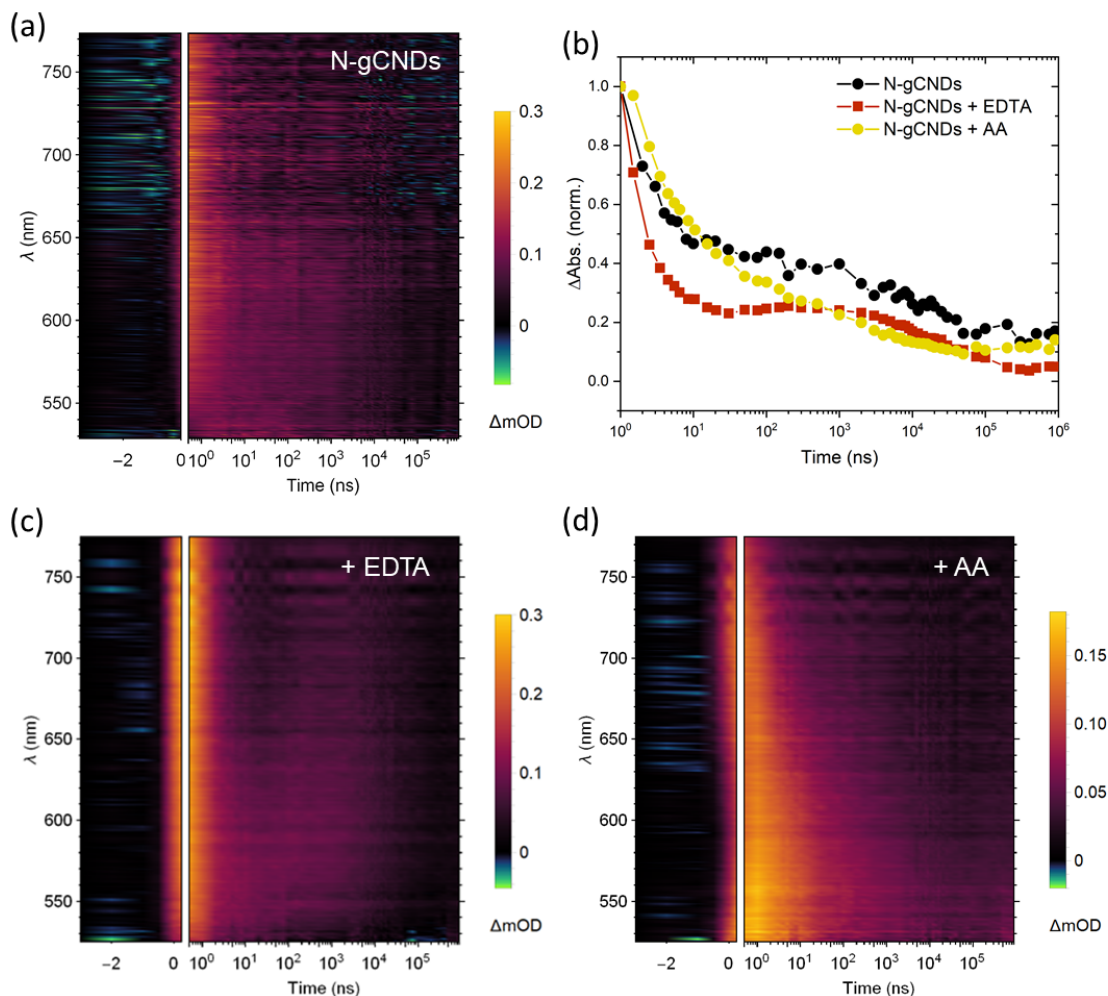
Figure 7.2: Influence of sacrificial electron donors on TA dynamics of NgCDs in solution. (a) Spectral map with NgCDs only $(0.25\,\mathrm{g\,L^{-1}})$. (b) Normalised average absorbance in the range 530 nm to 700 nm with the addition of EDTA pH 6 and ascorbic acid pH 4.5. (c) Spectral map of NgCDs with the addition of 0.1 M EDTA pH 6. (d) Spectral map of NgCDs with the addition of 0.1 M ascorbic acid pH 4.5.

that this is due to AA being an oxidative quencher and EDTA being a reductive quencher. In the case of AA, the excited state electrons prefer to be transferred to an electron acceptor before the holes in the valence band are filled by a SED, whereas in the case of EDTA, the photoinduced holes in the valence bands are preferentially filled first by a SED, with subsequent electron transfer of excited state electrons to an electron acceptor.

Both oxidative and reductive quenching mechanisms with CDs have been shown to occur by Achilleos *et al.* with EDTA and a Ni bis(diphosphine) H_2 evolution co-catalyst.[61] The changes observed are also likely affected by the contrasting electrostatic interactions between EDTA and ascorbic acid with the NgCD surface. For example, at pH 6 EDTA exists in solution as a 2− and 3− ion, whereas at pH 4.5 ascorbic acid exists as a 1− ion. This will directly impact on the coordination of SEDs around the NgCDs, and subsequent electron transfers.

7.3.3   Ascorbic acid with methyl viologen

Once the influence of SEDs without an electron acceptor was understood, MV was introduced as an electron acceptor in combination with AA (0.1 M) at pH 4.5 (no buffer). The TA spectra as a function of MV^{2+} were measured with the results presented in Figure 7.3.

The addition of AA results in the formation of an absorption peak centred at 600 nm on a 1 µs to 100 µs timescale. Figure 7.4 shows the spectral shape of this absorption, which matches well with the known UV-Vis absorption spectrum of the $MV^{\bullet+}$ radical cation across the concentration series.[65] Therefore, this absorption is assigned to $MV^{\bullet+}$.

The magnitude of this absorption peak increases with higher starting concentrations of MV^{2+} (Figure 7.5a), and the onset of the absorption peak occurs earlier (Figure 7.5b-c). The 5× increase in absorbance can be explained by the greater population of $MV^{\bullet+}$ species that forms. The decrease in onset time is suggestive of a diffusion-limited process, where the concentration of MV^{2+} is limiting $MV^{\bullet+}$ formation.

It is interesting to note that the $MV^{\bullet+}$ has a short lifetime, with the population falling rapidly to 0 by 1 ms. $MV^{\bullet+}$ is expected to be stable in N_2-purged aqueous solutions. This depletion is attributed to the formation of deyhydroascorbic acid (DHA) in the AA degradation pathway described in Section 2.1.4. DHA is a mild oxidant that can counterproductively take an electron from $MV^{\bullet+}$. Diffusion of $MV^{\bullet+}$ outside the probed volume is precluded as an explanation for the diminishing absorption signal. The 355 nm pump had a laser spot size of 1 mm, whereas the broadband probe had a laser spot size of 150 µm. Therefore, 1 ms is insufficient time for $MV^{\bullet+}$ to diffuse out of the probed volume ($D \approx 1 \times 10^{-5}$ cm^2 s^{-1}). This, in part, explains why ascorbic acid did not display any photoactivity in combination with CDs and AA in steady-state measurements under continuous UV irradiation (results not shown). The $MV^{\bullet+}$ does not survive long enough in the presence of DHA, which means it cannot accumulate at a sufficient rate and be detectable on timescales longer than 1 ms.

Quantitative analysis in terms of reaction kinetics can be performed by truncating the absorbance to the period where the $MV^{\bullet+}$ initially forms at a constant rate (Figure 7.5d). Applying a linear fitting routine enables a rate, R, to be extracted, which is plotted again the starting concentration of MV^{2+} in Figure 7.5e. The gradient of this plot is 1.20 ± 0.05, indicative of first-order kinetics with respect to MV^{2+}. Equation 7.3 shows that the order of reaction with respect to MV^{2+}, n, can be extracted in Figure 7.5e under the condition that the CD concentration and irradiance are held constant.

$$R = k[MV^{2+}]^n \tag{7.2}$$

$$\log R = \log k + n \log [MV^{2+}] \tag{7.3}$$

Figure 7.3: TA dynamics of NgCDs $(0.25\,\mathrm{g\,L^{-1}})$ with MV^{2+} as an electron acceptor and ascorbic acid$(0.1\,\mathrm{M})$ as a SED at pH 4.5. (a) No MV; (b) $4\,\mu\mathrm{M}$ MV^{2+}; (c) $12\,\mu\mathrm{M}$ MV^{2+}; (d) $40\,\mu\mathrm{M}$ MV^{2+}; (e) $120\,\mu\mathrm{M}$ MV^{2+} and (f) $400\,\mu\mathrm{M}$ MV^{2+}.
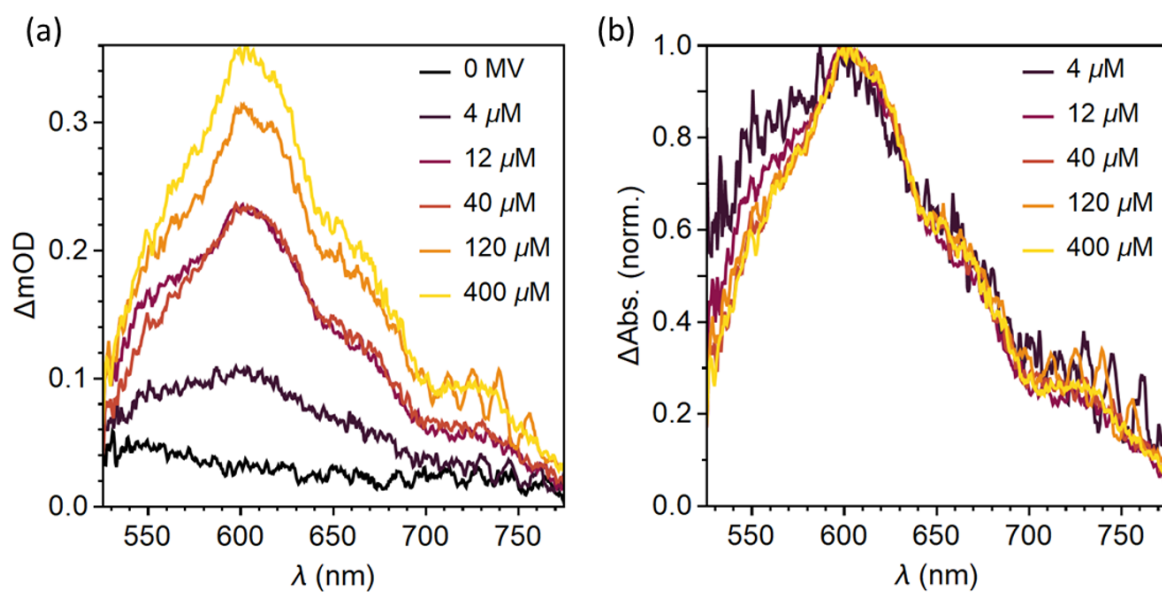
Figure 7.4: Spectral plots of the $MV^{\bullet+}$ absorption peak with different starting concentrations of MV^{2+} (a) without normalisation and (b) with normalisation to the peak counts. The spectra presented were extracted at times where the absorption at $600\,\mathrm{nm}$ was at a maximum.
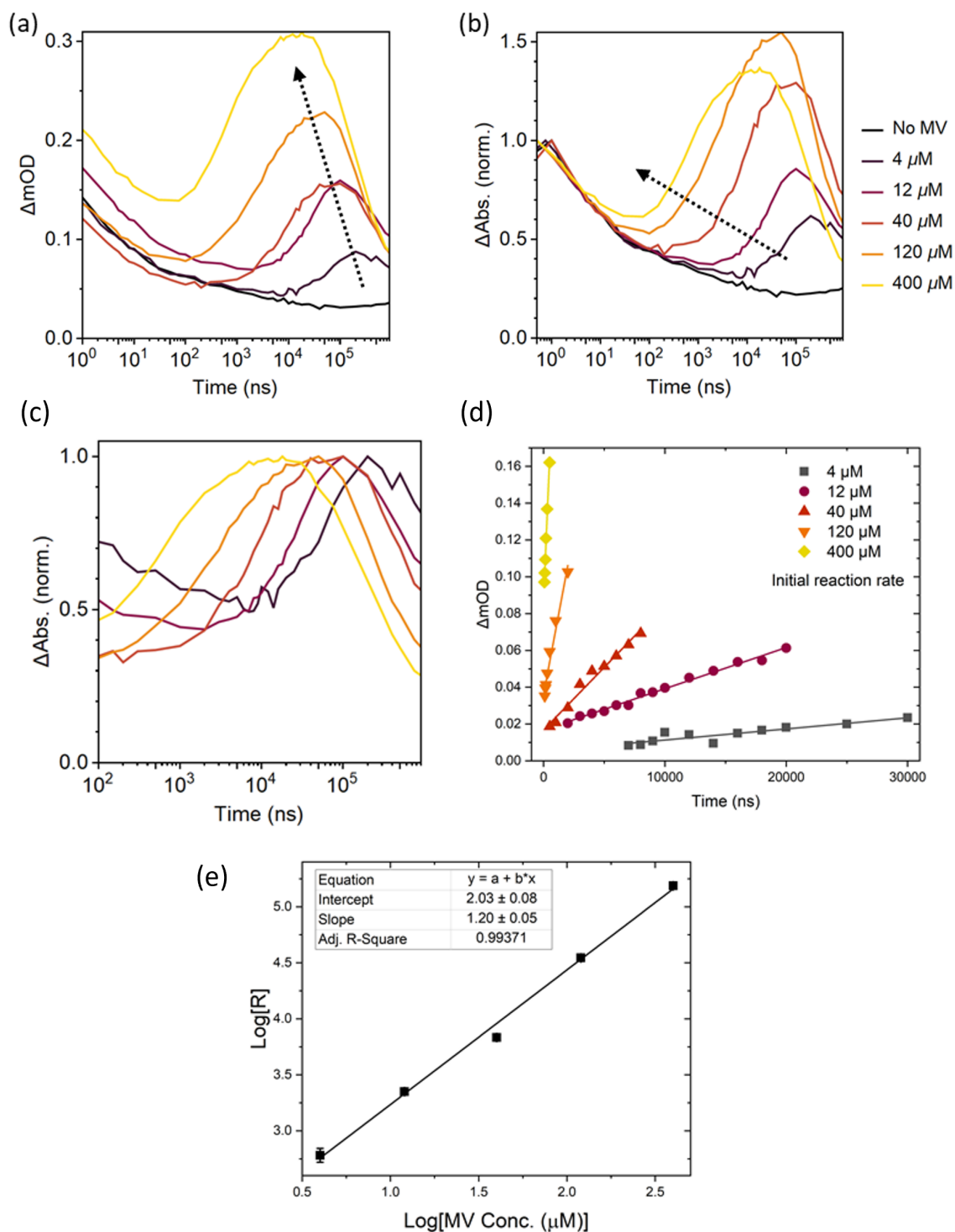
Figure 7.5: Reaction kinetics of NgCDs ($0.25\,\mathrm{g\,L^{-1}}$) with $\mathrm{MV^{2+}}$ as an electron acceptor and ascorbic acid ($0.1\,\mathrm{M}$) as a SED at pH 4.5. (a) Average ΔOD in the range $530\,\mathrm{nm}$ to $700\,\mathrm{nm}$, showing an increase in absorption with increasing amounts of $\mathrm{MV^{2+}}$. (b) Average absorbance normalised to $1\,\mathrm{ns}$ showing a shift in the onset of absorption to earlier times with increasing amounts of $\mathrm{MV^{2+}}$. (c) Same as (b) but normalised to the maximum $\mathrm{MV^{\bullet+}}$ absorption. (d) Initial absorption as $\mathrm{MV^{\bullet+}}$ is generated as a function of $[\mathrm{MV^{2+}}]$, with linear fittings applied to extract a rate constant. (e) Rate constants from (d) plotted as a function of $[\mathrm{MV^{2+}}]$, showing that the rate of formation of $\mathrm{MV^{\bullet+}}$ is first order with respect to $\mathrm{MV^{2+}}$.

The influence of pH on electron-transfer to form $MV^{\bullet+}$ was then investigated with NgCDs $(0.25\,\mathrm{g\,L^{-1}})$ and AA $(0.1\,\mathrm{M})$ in the presence of MV^{2+} $(40\,\mu M)$. The results are shown in Figure 7.6. The onset of $MV^{\bullet+}$ absorption was similar at the pH values tested $(4.5, 6.0, 8.0)$, however the decay profiles of $MV^{\bullet+}$ differed, where more alkaline pH led to a faster decay in the $MV^{\bullet+}$ population. At pH 4.5, the $1/e$ decay time was $500\,\mu s$, whereas at pH 8.0 this value decreased to $200\,\mu s$. This can be explained by the AA degradation pathway that forms the oxidant DHA. The formation of DHA requires a deprotonation step that becomes easier at higher pH, resulting in a greater rate of oxidation of $MV^{\bullet+}$.
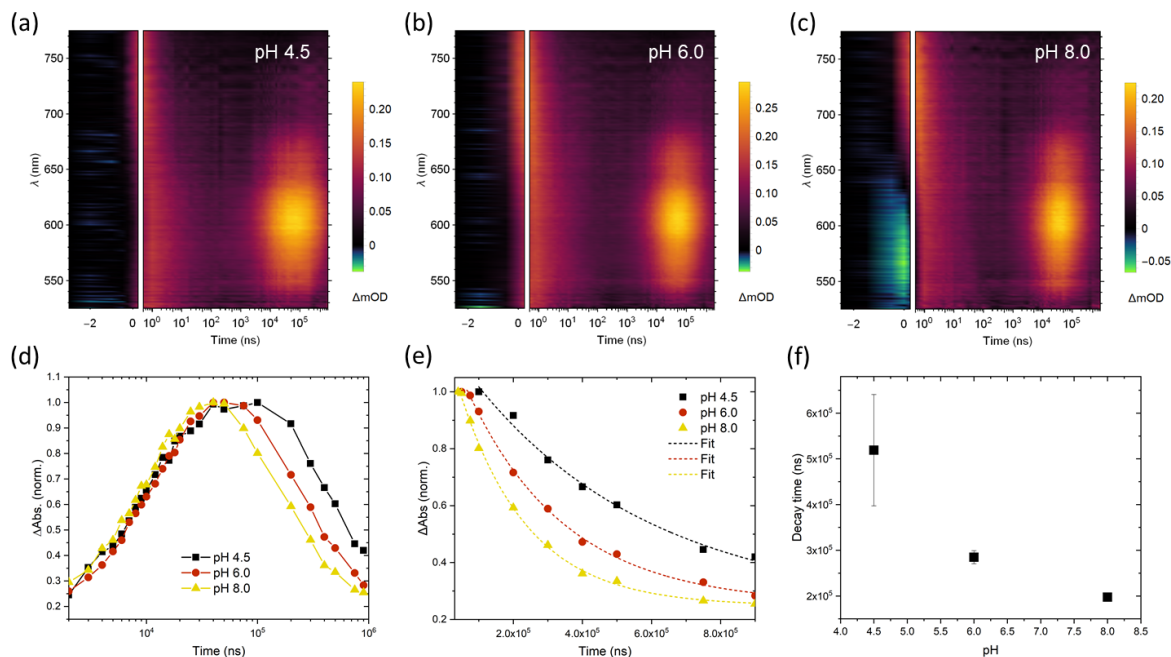
Figure 7.6: pH-dependent charge transfer in the presence of NgCDs $(0.25\,\mathrm{g\,L^{-1}})$ and ascorbic acid $(0.1\,\mathrm{M})$ with MV $(40\,\mu M)$. (a) Spectral map at pH 4.5 (no buffer); (b) spectral map at pH 6 (phosphate buffer) and (c) spectral map at pH 8 (phosphate buffer). (d) Average absorbance in the range $530\,\mathrm{nm}$ to $700\,\mathrm{nm}$, normalised to the absorption peak. (e) Plot of the absorption decay with exponential fittings applied. (f) $1/e$ decay time from (e) as a function of pH.

7.3.4 EDTA with methyl viologen

The SED was then changed to EDTA $(0.1\,\mathrm{M})$ in a pH 6 phosphate buffer, with the results presented in Figure 7.7. The absorption changes were less pronounced than with AA, and no clear-cut $MV^{\bullet+}$ radical formation was observed. However, with $120\,\mu M$ MV, an absorption peak that could be attributed $MV^{\bullet+}$ can be observed at $1 \times 10^5\,\mathrm{ns}$ in Figure 7.7e.

The time evolution of absorbance (averaged over $530\,\mathrm{nm}$ to $700\,\mathrm{nm}$) is shown in Figures 7.8a-b and the spectral profiles are shown in Figures 7.8c-f. In the presence of a small amount of MV, the small peak at $1\,\mu s$ disappears. With the addition of $> 120\,\mu M\,MV^{2+}$, a small trough is formed instead. This small trough consists of an extra drop in absorption at $10\,\mu s$ followed by a recovery in absorption at $100\,\mu s$.
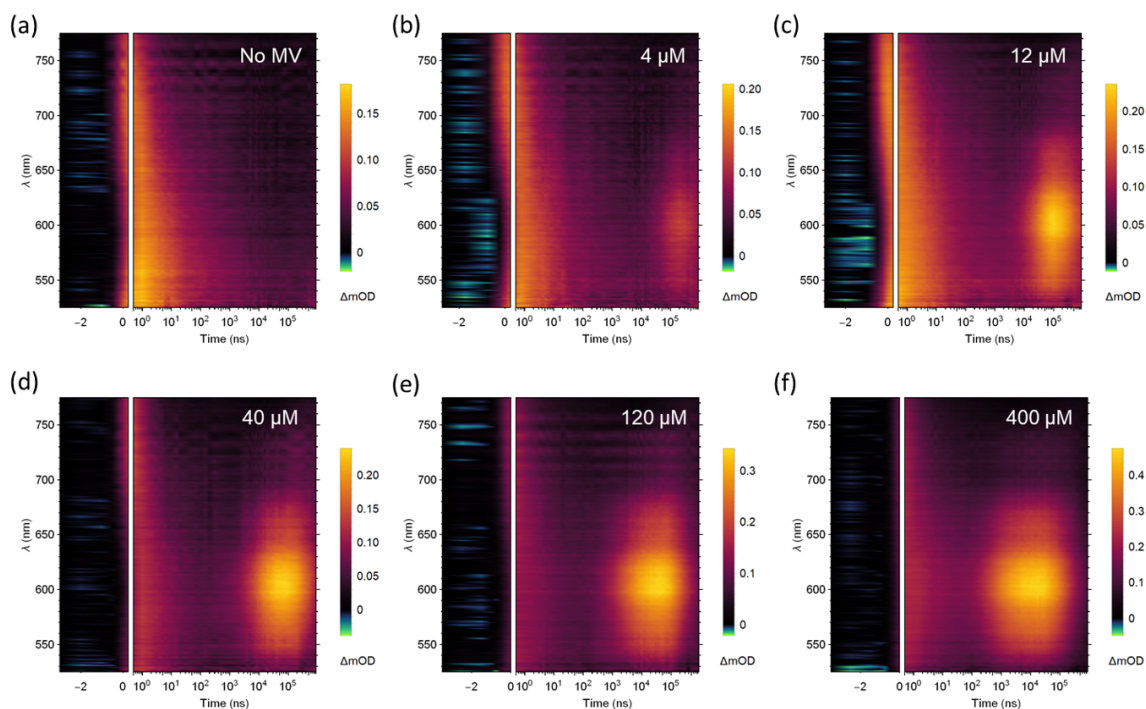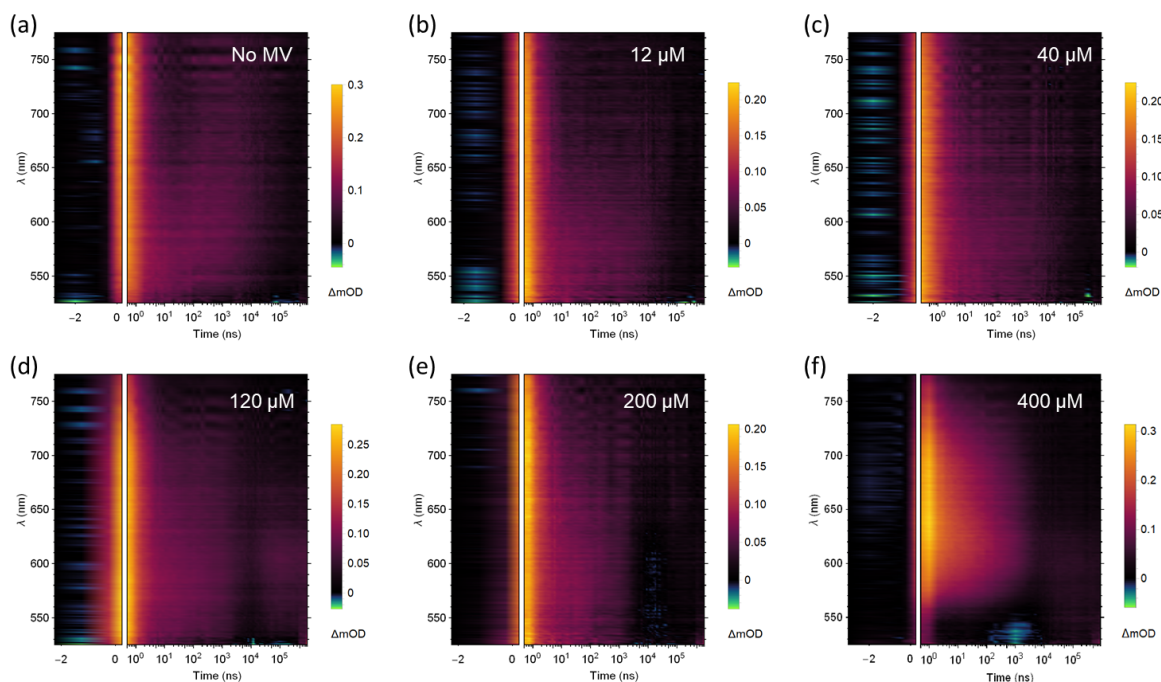
Figure 7.7: TA dynamics of NgCD ($0.25\,\mathrm{g\,L^{-1}}$) with MV^{2+} as an electron acceptor and EDTA (0.1 M) as a SED at pH 6. (a) No MV; (b) $4\,\mu M\ MV^{2+}$; (c) $12\,\mu M\ MV^{2+}$; (d) $40\,\mu M\ MV^{2+}$; (e) $120\,\mu M\ MV^{2+}$ and (f) $400\,\mu M\ MV^{2+}$.
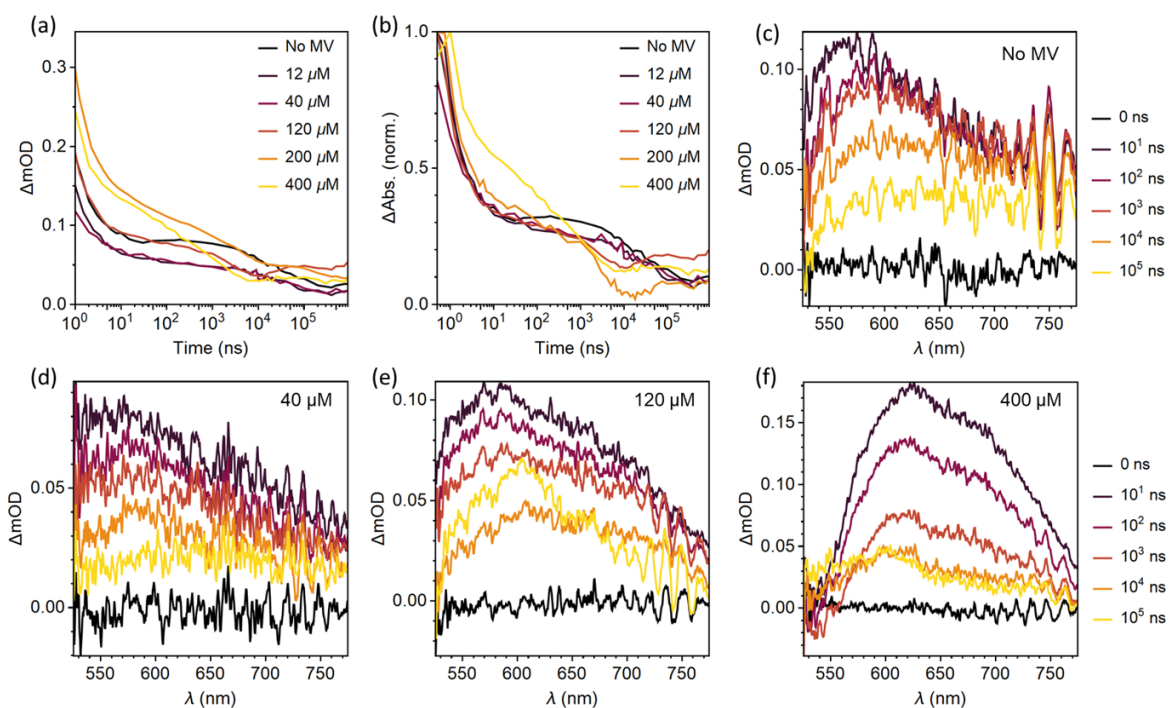

Figure 7.8: TA kinetics and spectra for a system comprising of NgCDs with MV^{2+} as an electron acceptor and EDTA as a SED. (a) Average ΔOD in the range $530\,\mathrm{nm}$ to $700\,\mathrm{nm}$. (b) Average absorbance normalised to peak at $\approx 1\,\mathrm{ns}$. (c)-(f) Spectral plots as a function of $[MV^{2+}]$.

It is challenging to attribute the absorption behaviour observed to a specific chemical species. The absorption is broad over the full probe range. However, given a clear $MV^{\bullet+}$ absorption peak is not evident, in contrary to the measurements with AA, the absorption must be affected by interactions between EDTA and MV^{2+} at the CD surface. This could be due to photoinduced changes in EDTA-MV complexation, which are known to exist in solution and reported by Hoffman *et al.*.[238]

Differences in the ionic strength of samples containing EDTA and AA may also play a role. Ionic strength affects the electrostatic screening of the NgCD surface. This phenomenon would then affect the interaction between the MV^{2+} and the NgCD surface.

In steady-state measurements (see Chapter 4), the formation of $MV^{\bullet+}$ with EDTA is clearly observed. However, $MV^{\bullet+}$ formation is not observed between $1\,ns$ and $1\,ms$ in these TA spectroscopy measurements. Therefore, the formation of $MV^{\bullet+}$ must occur on timescales longer than $1\,ms$. EDTA must slow the formation of $MV^{\bullet+}$ over ascorbic acid, perhaps by reducing the cage escape yield of $MV^{\bullet+}$ from the NgCD surface.

This lends support to the hypothesis that EDTA is a reductive quencher that fills the photoinduced holes in the CDs before the CDs can transfer an electron to MV^{2+}. This is in contrast to AA, which is hypothesised to be an oxidative quencher. This means the CDs transfer an electron to the MV^{2+} first, before the AA fills the photoinduced holes in the CD valence band. This is supported by the lack of a detectable electron transfer event with AA in the absence of MV, as shown in Figure 7.2b. This hypothesis requires further evidence, namely studies into other SEDs, such as TEA and TEOA, alongside pump-probe spectroscopy at delays longer than $1\,ms$ to confirm the formation of $MV^{\bullet+}$ with EDTA.

7.3.5   Effect of oxygen

The influence of N_2 purging and UV ($365\,nm$) pre-irradiation was explored with NgCDs ($0.25\,g\,L^{-1}$) in a pH 6 phosphate buffer, with the results shown in Figure 7.9.

The combination of the pump light and air exposure leads to a rapid quenching of the CD photoinduced absorption feature (Figure 7.9b). This quenching happens in ~$10\,ns$ and appears to be suppressed by purging the solution with N_2 before and during measurements (Figure 7.9c). Air (likely O_2) results in a ground state bleach feature, meaning the CDs become less-absorbing than their non-irradiated state.

7.4   Conclusions

Mechanistic insight into the electron transfer processes occurring at the surface of nitrogen-doped graphitic carbon nanodots were gained via TA spectroscopy. The results suggest that EDTA is a reductive quencher that fills the photoinduced holes in the CDs before the CDs can transfer an electron to MV^{2+}. The formation of $MV^{\bullet+}$ in the presence of EDTA is predicted to arise on timescales longer than $1\,ms$. This is in contrast to ascorbic acid (AA), which is hypothesised to be a oxidative quencher. This means the CDs transfer

Figure 7.9: Influence of N_2 purging and UV pre-irradiation on TA dynamics of NgCDs ($0.25\,\mathrm{g\,L^{-1}}$) in a pH 6 phosphate buffer. (a) Fresh sample that is purged continuously with a N_2 flow during the measurement. (b) Sample exposed to air for a few hours with no purging during the measurement. The sample is pre-irradiated with UV light (365 nm) for 10 min. (c) Sample purged with N_2 and pre-irradiated with UV light (365 nm) for 10 min. The measurement is then performed with a continuous N_2 flow.

an electron to the MV^{2+} first after $\approx 10\,\mu s$, before the AA fills the photoinduced hole in the CD valence band. The $MV^{\bullet+}$ has a short lifetime in the presence of AA, with the population falling rapidly to 0 by 1 ms. This depletion is attributed to the formation of deyhydroascorbic acid (DHA) in the AA degradation pathway, which is a mild oxidant that can counter-productively take an electron from $MV^{\bullet+}$.

These results provide a good basis for *in-fibra* studies with cobaloxime or nickel DuBois catalysts, whose reactive intermediates possess much weaker absorption cross sections than $MV^{\bullet+}$. Fibre-based microreactors can amplify the weak ΔmOD signals by increasing the optical path length from 1 mm to >10 cm. This is discussed further in Section 8.2.

Chapter 8

Conclusions and outlook

8.1 Conclusions

Fibre-based optofluidic microreactors for ultra-low volume reaction kinetics analysis have been developed, and new mechanistic insights into elusive photocatalytic systems have been delivered. Utilising the wave-guiding properties of hollow-core photonic crystal fibres (HC-PCFs), an assortment of optical techniques were employed to study photochemical reactions *in-situ*. This chapter summarises the key conclusions from these studies.

Fibre-based microreactors   Two optical setups employing hollow-core photonic crystal fibre (HC-PCF) microreactors with nanolitre reaction volumes were tested. The maximum transmission through a water-filled HC-PCF was achieved using a kagomé-style HC-PCF - 52 % at a wavelength of 550 nm over a 20 cm length. Absorbance and fluorescence spectroscopy were performed on minimal sample volumes ($< 1\,\mu$L), and photochemical reactions tracked *in-operando*.

Modular LED excitation sources were used to side-irradiate the microreactor, and in the case of fluorescence spectroscopy, excitation was also demonstrated by optically coupling a laser diode into the fibre core. Pressure cells enabled a fluidic system to be interfaced with the HC-PCFs, where samples were loaded into the HC-PCF with a syringe, whilst retaining unobstructed optical access to the fibre facets.

Carbon dot screening   Comprehensive *in-operando* spectrokinetic analysis was performed on carbon nanodots (CDs) by using the photoreduction of methyl viologen as an indicator of electron transfer from the CDs, with a total cumulative sample volume of < 1.5 mL. The quantum yield of the photoreduction process with amorphous CDs in the presence of EDTA (pH 6) was measured as 0.11%. Moreover, optimal conditions were identified for this photosystem for [aCD] $= 0.5\,\mathrm{g\,L^{-1}}$, namely [MV^{2+}] $< 100\,\mu$M and [EDTA] > 25 mM. The rate was also found to vary linearly with irradiance in the accessible range ($1.6\,\mathrm{mW\,cm^{-2}}$ to $88.4\,\mathrm{mW\,cm^{-2}}$), hence this parameter should be maximised for optimal photoreduction of MV^{2+}.

It is predicted that EDTA and TEA in aqueous pH 8 solutions are the most effective sacrificial electron donors for carbon dot-driven hydrogen evolution, and additionally, viologen electron relays implemented in photocatalytic systems should perform best under these same conditions.

Cobaloxime catalyst intermediates Cobaloxime catalytic intermediate states were observed via absorption spectroscopy during a hydrogen evolution reaction *in-operando*. The photocatalytic reaction was driven by the combination of cobaloxime electrocatalysts with $[Ru(bpy)_3]^{2+}$ light absorbers revealed the formation of a transient Co(I) species and a steady-state Co(II) species, as corroborated by density functional theory (DFT) simulations. The addition of an axial pendant pyridine unit was found to increase the rate of formation of the Co(I) state.

In-operando spectra of $Co(dmgH)_2Cl_2$, $Co(dmgH)_2pyCl$ and CoP^1 indicate that the pyridine group does not bind efficiently to the Co(I) and Co(II) metal centres. Therefore is it postulated that the pyridine group detaches during the catalytic cycle and only re-attaches when the Co(III) state is reformed.

Stern-Volmer analysis Bimolecular quenching rate constant were determined via Stern-Volmer analysis on a model system consisting of 4CzIPN, together with the fluorescence quencher, tetrabutylammonium azide (Bu_4NN_3), which are both key reagents used in the synthetic photoredox for synthesising α-tertiary amines and their corresponding γ-lactum derivatives. The bimolecular quenching coefficient for the 4CzIPN/Bu_4NN_3 pair was determined as $30.5 \times 10^9 \pm 1.1 \times 10^9 \, \mathrm{L\,mol^{-1}\,s^{-1}}$ with strong confidence ($R^2 = 0.995$). The value obtained is comparable to conventional fluorimeter-derived methods ($36.4 \times 10^9 \pm 1.8 \times 10^9 \, \mathrm{L\,mol^{-1}\,s^{-1}}$, $R^2 = 0.962$).

Moreover, more reliable values over fluorimeter-derived methods of the bimolecular quenching coefficient were determined for the 4CzIPN/cyclohexylamine (CHA) quenching pair. The bimolecular quenching coefficient for the 4CzIPN/CHA pair was determined as $1.6 \times 10^9 \pm 0.1 \times 10^9 \, \mathrm{L\,mol^{-1}\,s^{-1}}$.

Transient absorption spectroscopy Transient absorption (TA) spectroscopy on nitrogen-doped graphitic carbon nanodots (NgCDs) revealed that ascorbic acid (AA) is an oxidative quencher and EDTA is a reductive quencher. NgCDs transfer an electron to the MV^{2+} in the presence of AA after $\approx 10\,\mu s$, but this transfer is postulated to occur on timescales longer than $1\,ms$ in the presence of EDTA. The formation of the degradation product dehydroascorbic acid (DHA) with AA was found to counter-productively take an electron from $MV^{\bullet+}$, resulting in the $MV^{\bullet+}$ population falling rapidly to 0 by $1\,ms$.

These results provide a good basis for *in-fibra* studies with cobaloxime or nickel DuBois catalysts, whose reactive intermediates possess much weaker absorption cross sections than $MV^{\bullet+}$. Fibre-based microreactors can amplify the weak *in-operando* ΔmOD signals by increasing the optical path length.

8.2 Outlook

Optical spectroscopy is a powerful tool to monitor photocatalytic reactions. Although a one electron process (methyl viologen reduction) and two electron process (hydrogen evolution) have been monitored here, insight into more complex multi-photon, multi-electron and/or multi-proton molecular catalysis can be provided by optical techniques. *In-operando* methods can give insight into the coupling of light absorption with catalytic chemical change, which is at the heart of photocatalysis. The only requirement is that the spectroscopic signature of intermediate species changes with the oxidation state of the metal centre.

There continues to be scope to develop new photocatalytic systems, particularly in enhancing catalytic activity and stability in water. The optofluidic techniques reported here have generated new kinetic and mechanistic insights into how photocatalysts function, which could not be obtained by conventional techniques. These insights can be used to design more efficient photocatalysts in the future. Additional optofluidic techniques can be explored to provide new insight - these promising areas are briefly discussed below.

Raman spectroscopy   Absorption and fluorescence spectroscopy for reaction monitoring *in-fibra* has been demonstrated here, however guidance of Raman scattering along HC-PCFs can enhance the detectability of this inherently weak phenomenon and provide additional insight into photochemical processes (see Section 2.3.6), particularly the formation of new functional groups in the course of a chemical reaction.

Higher order modes   The ability to control the spatial extent of light using higher order modes within liquid-filled HC-PCF microreactors (see Section 2.3.5) enables surface adhesion and diffusion dynamics to be probed on a micrometer scale. For example, a higher order mode (i.e. LP_{31}) can be used to selectively excite photocatalysts attached to the fibre walls, then a fundamental mode (LP_{01}) used to probe the formation of products as they diffuse from the fibre wall to the centre of the fibre core.

Flow microreactors   HC-PCFs can be utilised to perform reaction monitoring in flow. One method by which this objective can be achieved is by interfacing HC-PCFs with microfluidic chips. This has the potential to reduce the dead-volume to below $50\,\mu L$ - a limitation of the pressure cells employed in this project. Reactions in flow are a stepping stone towards automation of catalyst screening. For example, fluorescence screening of photoredox catalysts can be performed with quencher concentrations adjusted in continuous flow, with minimal consumption of precious and expensive reagents. Moreover, the output of the HC-PCF can be connected to a gas chromatograph or mass spectrometer for further insight into the reaction products produced. Furthermore, a heat stage can be integrated for temperature-dependent measurements.

Low index coatings A capillary with no internal structure can function as an effective waveguide if the outer protective polymer layer is substituted for a low index coating (LIC). The low index coating must have a refractive index below that of the solvent. The extremity of guidance is the limit of total internal reflection, as depicted in Figure 8.1. For each interface we can write an expression using Snell's Law

$$n_{LIC} = n_{sil} \sin \theta_c \tag{8.1}$$

$$n_{sil} \sin \theta_c = n_{sol} \sin (90 - \theta_a) \tag{8.2}$$

such that the acceptance angle of the LIC, θ_a, is given by

$$\cos \theta_a = \frac{n_{LIC}}{n_{sol}} \tag{8.3}$$
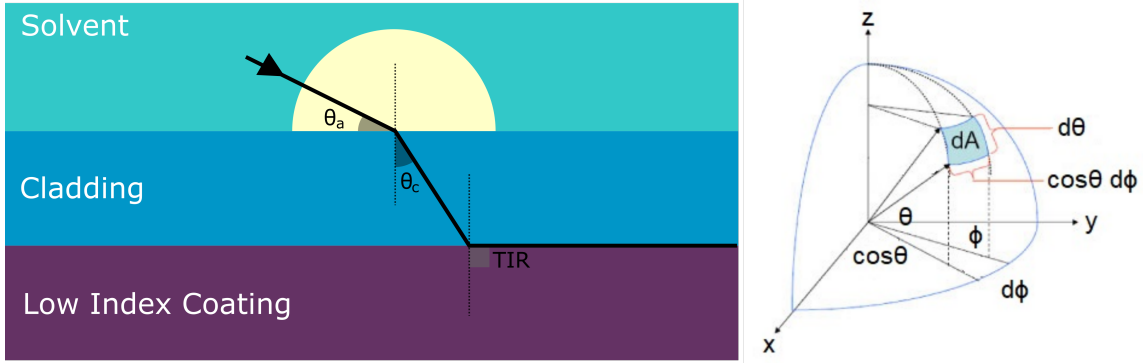
Figure 8.1: Low index coating guidance is achieved through total internal reflection. The fraction of fluorescence captured can be derived by considering a hemisphere, from the refractive indices of the low index coating and the solvent.

Considering a hemispherical volume enclosing the solvent-silica interface, we can calculate the fraction of light that is collected by the LIC, f,

$$f = \frac{1}{2\pi} \int_0^\pi \int_0^{\theta_a} \cos \theta \, d\phi \, d\theta = \frac{1}{2\pi} \int_0^\pi d\phi \int_0^{\theta_a} \cos \theta \, d\theta = \frac{1}{2} \sin \theta_a \tag{8.4}$$

So our fraction collected in terms of refractive indices is

$$f = \frac{1}{2} \sqrt{1 - \frac{n_{LIC}}{n_{sol}}} \tag{8.5}$$

This shows that air as the outer layer is the most effective medium for capturing the most fluorescence, however, it is important to note that capillaries cannot guide light effectively through the solvent. Instead, the light is guided through the silica cladding. So although the efficiency of fluorescent light capture is greater, in-coupled excitation sources will suffer from poor light-matter interaction lengths with the sample. There is scope to optimise capillaries and LICs in future work.

Fibre-based TA spectroscopy The weak ΔmOD signals in cuvette, measured over a 1 mm path length, can be enhanced by using fibre-based microreactors, with path lengths of 10 cm. In the first instance, the fibre's effect on the temporal evolution of the pump and probe pulses should be fully characterised. Cladding-pumping can be employed to guide the pump light through the fibre cladding, allowing it to traverse the hollow-core as it propagates. This would result in a homogeneous irradiance across the sample volume. The absorption can then be measured by a broadband probe source, which is coupled into the fibre core, exciting a fundamental LP_{01}-like mode. LICs can also be employed to reduce leakage of the pump out of the cladding. This is summarised in Figure 8.2.
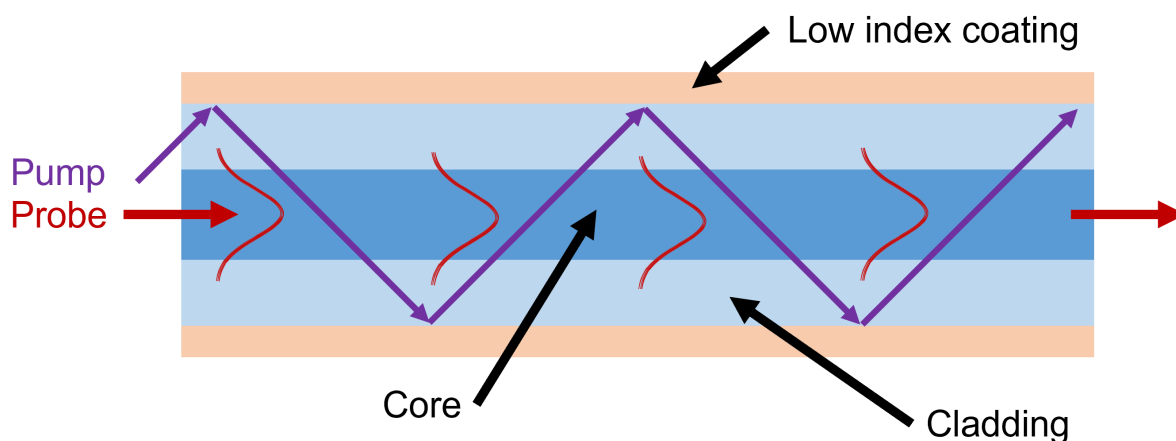

Figure 8.2: Schematic for fibre-based TA spectroscopy, which employs cladding-pumping and low index coatings.

Bibliography

[1] International Energy Agency. The Future of Hydrogen. Technical report, Paris, 2019.

[2] O. S. Bushuyev, P. De Luna, C. T. Dinh, L. Tao, G. Saur, J. Van De Lagemaat, S. O. Kelley, and E. H. Sargent. What Should We Make with CO2 and How Can We Make It? *Joule*, 2:825–832, 2018.

[3] J. Jia, L. C. Seitz, J. D. Benck, Y. Huo, Y. Chen, J. W. D. Ng, T. Bilir, J. S. Harris, and T. F. Jaramillo. Solar water splitting by photovoltaic-electrolysis with a solar-to-hydrogen efficiency over 30%. *Nature Communications*, 7(1):13237, 2016.

[4] H. Nishiyama, T. Yamada, M. Nakabayashi, Y. Maehara, M. Yamaguchi, Y. Kuromiya, H. Tokudome, S. Akiyama, T. Watanabe, R. Narushima, S. Okunaka, N. Shibata, T. Takata, T. Hisatomi, and K. Domen. Photocatalytic solar hydrogen production from water on a 100 m2-scale. *Nature*, pages 1–7, 2021.

[5] D. M. Arias-Rotondo and J. K. McCusker. The photophysics of photoredox catalysis: a roadmap for catalyst design. *Chemical Society Reviews*, 45(21):5803–5820, 2016.

[6] D. Erickson, D. Sinton, and D. Psaltis. Optofluidics for energy applications. *Nature Photonics*, 5(10):583–590, 2011.

[7] M. Kozlowski and T. Yoon. Editorial for the Special Issue on Photocatalysis. *The Journal of Organic Chemistry*, 81(16):6895–6897, 2016.

[8] J. Barber. Photosynthetic energy conversion: natural and artificial. *Chem. Soc. Rev.*, 38(1):185–196, 2009.

[9] J. Twilton, C. Le, P. Zhang, M. H. Shaw, R. W. Evans, and D. W. C. MacMillan. The merger of transition metal and photocatalysis. *Nature Reviews Chemistry*, 1: 0052, 2017.

[10] H. Yu, R. Shi, Y. Zhao, G. I. N Waterhouse, L.-Z. Wu, C.-H. Tung, T. Zhang, H. Yu, R. Shi, Y. Zhao, L.-z. Wu, C.-h. Tung, T. Zhang, and G. I. N Waterhouse. Smart Utilization of Carbon Dots in Semiconductor Photocatalysis. *Advanced Materials*, 28:9454–9477, 2016.

[11] X. Huang, J. Wang, T. Li, J. Wang, M. Xu, W. Yu, A. El Abed, and X. Zhang. Review on optofluidic microreactors for artificial photosynthesis. *Beilstein Journal of Nanotechnology*, 9:30–41, 2018.

[12] M. Graetzel. Artificial photosynthesis: water cleavage into hydrogen and oxygen by visible light. *Accounts of Chemical Research*, 14(12):376–384, 1981.

[13] Y. Tachibana, L. Vayssieres, and J. R. Durrant. Artificial photosynthesis for solar water-splitting. *Nature Photonics*, 6(8):511–518, 2012.

[14] M. Crespo-Quesada and E. Reisner. Emerging approaches to stabilise photocorrodible electrodes and catalysts for solar fuel applications. *Energy & Environmental Science*, 10(5):1116–1127, 2017.

[15] Z. W. Seh, J. Kibsgaard, C. F. Dickens, I. Chorkendorff, J. K. Nørskov, and T. F. Jaramillo. Combining theory and experiment in electrocatalysis: Insights into materials design. *Science*, 355(6321):eaad4998, 2017.

[16] T. J. Meyer. Chemical approaches to artificial photosynthesis. *Accounts of Chemical Research*, 22(5):163–170, 1989.

[17] H. Takeda and O. Ishitani. Development of efficient photocatalytic systems for CO2 reduction using mononuclear and multinuclear metal complexes based on mechanistic studies. *Coordination Chemistry Reviews*, 254(3-4):346–354, 2010.

[18] A. J. Medford and M. C. Hatzell. Photon-Driven Nitrogen Fixation: Current Progress, Thermodynamic Considerations, and Future Outlook. *ACS Catalysis*, 7 (4):2624–2643, 2017.

[19] J. Willkomm, K. L. Orchard, A. Reynal, E. Pastor, J. R. Durrant, and E. Reisner. Dye-sensitised semiconductors modified with molecular catalysts for light-driven H2 production. *Chemical Society Reviews*, 45(1):9–23, 2016.

[20] Y. Pellegrin and F. Odobel. Sacrificial electron donor reagents for solar fuel production. *Comptes Rendus Chimie*, 20(3):283–295, 2016.

[21] A. Kudo and Y. Miseki. Heterogeneous photocatalyst materials for water splitting. *Chemical Society Reviews*, 38(1):253–278, 2009.

[22] S. S. Ahsan, A. Gumus, and D. Erickson. Redox mediated photocatalytic water-splitting in optofluidic microreactors. *Lab on a Chip*, 13(3):409–414, 2013.

[23] D. R. Prasad and M. Z. Hoffman. Photodynamics of the tris(2,2'-bipyrazine)ruthenium(2+)/methylviologen/EDTA system in aqueous solution. *Journal of the American Chemical Society*, 108(10):2568–2573, 1986.

[24] K. Yatsuzuka, K. Yamauchi, K. Kawano, H. Ozawa, and K. Sakai. Improving the overall performance of photochemical H 2 evolution catalyzed by the Co-NHC complex via the redox tuning of electron relays. *Sustainable Energy & Fuels*, 5(3):740–749, 2021.

[25] K. Maeda, M. Higashi, D. Lu, R. Abe, and K. Domen. Efficient Nonsacrificial Water Splitting through Two-Step Photoexcitation by Visible Light using a Modified Oxynitride as a Hydrogen Evolution Photocatalyst. *Journal of the American Chemical Society*, 132(16):5858–5868, 2010.

[26] Y. Wang, H. Suzuki, J. Xie, O. Tomita, D. J. Martin, M. Higashi, D. Kong, R. Abe, and J. Tang. Mimicking Natural Photosynthesis: Solar to Renewable H2 Fuel Synthesis by Z-Scheme Water Splitting Systems. *Chemical Reviews*, 118(10):5201–5241, 2018.

[27] A. Reynal, E. Pastor, M. A. Gross, S. Selim, E. Reisner, and J. R. Durrant. Unravelling the pH-dependence of a molecular photocatalytic system for hydrogen production. *Chemical Science*, 6(8):4855–4859, 2015.

[28] K. Kalyanasundaram. Photophysics, photochemistry and solar energy conversion with tris(bipyridyl)ruthenium(II) and its analogues. *Coordination Chemistry Reviews*, 46:159–244, 1982.

[29] Q. Lam, M. Kato, and L. Cheruzel. Ru(II)-diimine functionalized metalloproteins: From electron transfer studies to light-driven biocatalysis. *Biochimica et Biophysica Acta (BBA) - Bioenergetics*, 1857(5):589–597, 2016.

[30] J. R. Winkler and H. B. Gray. Electron transfer in ruthenium-modified proteins. *Chemical Reviews*, 92(3):369–379, 1992.

[31] M. Natali. Elucidating the Key Role of pH on Light-Driven Hydrogen Evolution by a Molecular Cobalt Catalyst. *ACS Catalysis*, 7(2):1330–1339, 2017.

[32] A. J. Cowan and J. R. Durrant. Long-lived charge separated states in nanostructured semiconductor photoelectrodes for the production of solar fuels. *Chem. Soc. Rev.*, 42 (6):2281–2293, 2013.

[33] A. Reynal, F. Lakadamyali, M. A. Gross, E. Reisner, and J. R. Durrant. Parameters affecting electron transfer dynamics from semiconductors to molecular catalysts for the photochemical reduction of protons. *Energy & Environmental Science*, 6(11): 3291–3300, 2013.

[34] K. E. Dalle, J. Warnan, J. J. Leung, B. Reuillard, I. S. Karmel, and E. Reisner. Electro- and Solar-Driven Fuel Synthesis with First Row Transition Metal Complexes. *Chemical Reviews*, 119(4):2752–2875, 2019.

[35] A. Mills and S.-K. Lee. A web-based overview of semiconductor photochemistry-based current commercial applications. *Journal of Photochemistry and Photobiology A: Chemistry*, 152(1-3):233–247, 2002.

[36] B. C. Hodges, E. L. Cates, and J.-H. Kim. Challenges and prospects of advanced oxidation water treatment processes using catalytic nanomaterials. *Nature Nanotechnology*, 13(8):642–650, 2018.

[37] Y. Park, W. Kim, D. Monllor-Satoca, T. Tachikawa, T. Majima, and W. Choi. Role of Interparticle Charge Transfers in Agglomerated Photocatalyst Nanoparticles: Demonstration in Aqueous Suspension of Dye-Sensitized TiO 2. *The Journal of Physical Chemistry Letters*, 4(1):189–194, 2013.

[38] A. Fujishima and K. Honda. Electrochemical Photolysis of Water at a Semiconductor Electrode. *Nature*, 238(5358):37–38, 1972.

[39] G. Hutton. *Surface-functionalised carbon dots as versatile light harvesters for solar driven catalysis.* PhD thesis, University of Cambridge, 2017.

[40] S. Corby, R. R. Rao, L. Steier, and J. R. Durrant. The kinetics of metal oxide photoanodes from charge generation to catalysis. *Nature Reviews Materials*, 2021.

[41] J. Greeley, T. F. Jaramillo, J. Bonde, I. Chorkendorff, and J. K. Nørskov. Computational high-throughput screening of electrocatalytic materials for hydrogen evolution. *Nature Materials*, 5(11):909–913, 2006.

[42] R. B. Gordon, M. Bertram, and T. E. Graedel. Metal stocks and sustainability. *Proceedings of the National Academy of Sciences*, 103(5):1209–1214, 2006.

[43] B. C. M. Martindale, E. Joliat, C. Bachmann, R. Alberto, and E. Reisner. Clean Donor Oxidation Enhances the H 2 Evolution Activity of a Carbon Quantum Dot–Molecular Catalyst Photosystem. *Angewandte Chemie International Edition*, 55(32):9402–9406, 2016.

[44] M. A. Gross, A. Reynal, J. R. Durrant, and E. Reisner. Versatile Photocatalytic Systems for H2 Generation in Water Based on an Efficient DuBois-Type Nickel Catalyst. *Journal of the American Chemical Society*, 136(1):356–366, 2014.

[45] G. A. M. Hutton, B. C. M. Martindale, and E. Reisner. Carbon dots as photosensitisers for solar-driven catalysis. *Chemical Society Reviews*, 46:6111–6123, 2017.

[46] X. Xu, R. Ray, Y. Gu, H. J. Ploehn, L. Gearheart, K. Raker, and W. A. Scrivens. Electrophoretic Analysis and Purification of Fluorescent Single-Walled Carbon Nanotube Fragments. *Journal of the American Chemical Society*, 126(40):12736–12737, 2004.

[47] I. Y. Goryacheva, A. V. Sapelkin, and G. B. Sukhorukov. Carbon nanodots: Mechanisms of photoluminescence and principles of application. *TrAC Trends in Analytical Chemistry*, 90:27–37, 2017.

[48] M. A. Melo and F. E. Osterloh. Defect States Control Effective Band Gap and Photochemistry of Graphene Quantum Dots. *ACS Applied Materials & Interfaces*, 10(32):27195–27204, 2018.

[49] S. N. Baker and G. A. Baker. Luminescent Carbon Nanodots: Emergent Nanolights. *Angewandte Chemie International Edition*, 49(38):6726–6744, 2010.

[50] H. Luo, N. Papaioannou, E. Salvadori, M. M. Roessler, G. Ploenes, E. R. H. Eck, L. C. Tanase, J. Feng, Y. Sun, Y. Yang, M. Danaie, A. Belen Jorge, A. Sapelkin, J. Durrant, S. D. Dimitrov, and M. Titirici. Manipulating the Optical Properties of Carbon Dots by Fine-Tuning their Structural Features. *ChemSusChem*, 12(19): 4432–4441, 2019.

[51] J. T. Margraf, V. Strauss, D. M. Guldi, and T. Clark. The Electronic Structure of Amorphous Carbon Nanodots. *The Journal of Physical Chemistry B*, 119(24): 7258–7265, 2015.

[52] C. Rao, S. Yamantakk Han, N. C. Verma, and C. Nandi. Labelling Proteins with Carbon Nanodots. *ChemBioChem*, 18:2385–2389, 2017.

[53] W. Jia, B. Tang, and P. Wu. Carbon dots with multi-functional groups and the application in proton exchange membranes. *Electrochimica Acta*, 260:92–100, 2018.

[54] G. Murali, J. K. R. Modigunta, S. Park, S. Lee, H. Lee, J. Yeon, H. Kim, Y. H. Park, S. Y. Park, J. R. Durrant, H. Cha, T. K. An, and I. In. Enhancing Light Absorption and Prolonging Charge Separation in Carbon Quantum Dots via Cl-Doping for Visible-Light-Driven Photocharge-Transfer Reactions. *ACS Applied Materials & Interfaces*, 13(29):34648–34657, 2021.

[55] B. C. M. Martindale, G. A. M. Hutton, C. A. Caputo, S. Prantl, R. Godin, J. R. Durrant, and E. Reisner. Enhancing Light Absorption and Charge Transfer Efficiency in Carbon Dots through Graphitization and Core Nitrogen Doping. *Angewandte Chemie International Edition*, 56(23):6459–6463, 2017.

[56] T. T. Meiling, R. Schürmann, S. Vogel, K. Ebel, C. Nicolas, A. R. Milosavljević, and I. Bald. Photophysics and Chemistry of Nitrogen-Doped Carbon Nanodots with High Photoluminescence Quantum Yield. *Journal of Physical Chemistry C*, 122(18): 10217–10230, 2018.

[57] Y. Zhang, X. Liu, Y. Fan, X. Guo, L. Zhou, Y. Lv, and J. Lin. One-step microwave synthesis of N-doped hydroxyl-functionalized carbon dots with ultra-high fluorescence quantum yields. *Nanoscale*, 8(33):15281–15287, 2016.

[58] H. Liu, T. Ye, and C. Mao. Fluorescent Carbon Nanoparticles Derived from Candle Soot. *Angewandte Chemie International Edition*, 46(34):6473–6475, 2007.

[59] H. Ming, Z. Ma, Y. Liu, K. Pan, H. Yu, F. Wang, and Z. Kang. Large scale electrochemical synthesis of high quality carbon nanodots and their photocatalytic property. *Dalton Transactions*, 41(31):9526, 2012.

[60] J. Shen, Y. Zhu, X. Yang, and C. Li. Graphene quantum dots: emergent nanolights for bioimaging, sensors, catalysis and photovoltaic devices. *Chemical Communications*, 48(31):3686, 2012.

[61] D. S. Achilleos, W. Yang, H. Kasap, A. Savateev, Y. Markushyna, J. R. Durrant, and E. Reisner. Solar Reforming of Biomass with Homogeneous Carbon Dots. *Angewandte Chemie International Edition*, 59(41):18184–18188, 2020.

[62] B. C. M. Martindale, G. A. M. Hutton, C. A. Caputo, and E. Reisner. Solar Hydrogen Production Using Carbon Quantum Dots and a Molecular Nickel Catalyst. *Journal of the American Chemical Society*, 137(18):6018–6025, 2015.

[63] D. Reyes, M. Camacho, M. Camacho, M. Mayorga, D. Weathers, G. Salamo, Z. Wang, and A. Neogi. Laser Ablated Carbon Nanodots for Light Emission. *Nanoscale Research Letters*, 11:424, 2016.

[64] L. Tang, R. Ji, X. Cao, J. Lin, H. Jiang, X. Li, K. S. Teng, C. M. Luk, S. Zeng, J. Hao, and S. P. Lau. Deep Ultraviolet Photoluminescence of Water-Soluble Self-Passivated Graphene Quantum Dots. *ACS Nano*, 6(6):5102–5110, 2012.

[65] T. Watanabe and K. Honda. Measurement of the extinction coefficient of the methyl viologen cation radical and the efficiency of its formation by semiconductor photocatalysis. *Journal of Physical Chemistry*, 86(14):2617–2619, 1982.

[66] J. Ding, C. Zheng, L. Wang, C. Lu, B. Zhang, Y. Chen, M. Li, G. Zhai, and X. Zhuang. Viologen-inspired functional materials: synthetic strategies and applications. *Journal of Materials Chemistry A*, 7(41):23337–23360, 2019.

[67] V. Strauss, J. T. Margraf, C. Dolle, B. Butz, T. J. Nacken, J. Walter, W. Bauer, W. Peukert, E. Spiecker, T. Clark, and D. M. Guldi. Carbon Nanodots: Toward a Comprehensive Understanding of Their Photoluminescence. *Journal of the American Chemical Society*, 136(49):17308–17316, 2014.

[68] H. Ogata and W. Lubitz. Bioenergetics Theory and Components — Hydrogenases Structure and Function. In *Encyclopedia of Biological Chemistry III*, pages 66–73. Elsevier, 2021.

[69] B. M. Hockin, C. Li, N. Robertson, and E. Zysman-Colman. Photoredox catalysts based on earth-abundant metal complexes. *Catalysis Science & Technology*, 9(4): 889–915, 2019.

[70] J. R. McKone, N. S. Lewis, and H. B. Gray. Will Solar-Driven Water-Splitting Devices See the Light of Day? *Chemistry of Materials*, 26(1):407–414, 2014.

[71] A. P. Walsh, J. A. Laureanti, S. Katipamula, G. M. Chambers, N. Priyadarshani, S. Lense, J. T. Bays, J. C. Linehan, and W. J. Shaw. Evaluating the impacts of amino acids in the second and outer coordination spheres of Rh-bis(diphosphine) complexes for CO 2 hydrogenation. *Faraday Discussions*, 215:123–140, 2019.

[72] T. E. Rosser and E. Reisner. Understanding Immobilized Molecular Catalysts for Fuel-Forming Reactions through UV/Vis Spectroelectrochemistry. *ACS Catalysis*, 7 (5):3131–3141, 2017.

[73] A. K. Pal, C. Li, G. S. Hanan, and E. Zysman-Colman. Blue-Emissive Cobalt(III) Complexes and Their Use in the Photocatalytic Trifluoromethylation of Polycyclic Aromatic Hydrocarbons. *Angewandte Chemie International Edition*, 57(27):8027–8031, 2018.

[74] D. W. Wakerley and E. Reisner. Development and understanding of cobaloxime activity through electrochemical molecular catalyst screening. *Phys. Chem. Chem. Phys.*, 16(12):5739–5746, 2014.

[75] D. Wakerley, M. Gross, and E. Reisner. Proton reduction by molecular catalysts in water under demanding atmospheres. *Chem. Commun.*, 50(100):15995–15998, 2014.

[76] F. Lakadamyali, M. Kato, N. M. Muresan, and E. Reisner. Selective Reduction of Aqueous Protons to Hydrogen with a Synthetic Cobaloxime Catalyst in the Presence of Atmospheric Oxygen. *Angewandte Chemie International Edition*, 51(37):9381–9384, 2012.

[77] J. Willkomm, N. M. Muresan, and E. Reisner. Enhancing H 2 evolution performance of an immobilised cobalt catalyst by rational ligand design. *Chemical Science*, 6(5):2727–2736, 2015.

[78] F. Lakadamyali and E. Reisner. Photocatalytic H2 evolution from neutral water with a molecular cobalt catalyst on a dye-sensitised TiO2 nanoparticle. *Chemical Communications*, 47(6):1695–1697, 2011.

[79] N. M. Muresan, J. Willkomm, D. Mersch, Y. Vaynzof, and E. Reisner. Immobilization of a Molecular Cobaloxime Catalyst for Hydrogen Evolution on a Mesoporous Metal Oxide Electrode. *Angewandte Chemie International Edition*, 51:12749–12753, 2012.

[80] J. Willkomm and E. Reisner. Photo- and electrocatalytic H2 evolution with cobalt oxime complexes. *Bulletin of Japan Society of Coordination Chemistry*, 71:18–29, 2018.

[81] S.-W. Cao, X.-F. Liu, Y.-P. Yuan, Z.-Y. Zhang, J. Fang, S. C. J. Loo, J. Barber, T. C. Sum, and C. Xue. Artificial photosynthetic hydrogen evolution over g-C3N4 nanosheets coupled with cobaloxime. *Physical Chemistry Chemical Physics*, 15(42):18363–18366, 2013.

[82] J. L. Dempsey, B. S. Brunschwig, J. R. Winkler, and H. B. Gray. Hydrogen Evolution Catalyzed by Cobaloximes. *Accounts of Chemical Research*, 42(12):1995–2004, 2009.

[83] D. G. Blackmond. Kinetic Profiling of Catalytic Organic Reactions as a Mechanistic Tool. *Journal of the American Chemical Society*, 137(34):10852–10866, 2015.

[84] G. Neshvad and M. Z. Hoffman. Reductive quenching of the luminescent excited state of tris(2,2'-bipyrazine)ruthenium(2+) ion in aqueous solution. *The Journal of Physical Chemistry*, 93(6):2445–2452, 1989.

[85] H.-S. Chang, G. V. Korshin, and J. F. Ferguson. Investigation of Mechanisms of Oxidation of EDTA and NTA by Permanganate at High pH. *Environmental Science & Technology*, 40(16):5089–5094, 2006.

[86] Q. G. Mulazzani, M. Venturi, and M. Z. Hoffman. Radiolytically induced one-electron reduction of methylviologen in aqueous solution. Reactivity of EDTA radicals toward methylviologen. *The Journal of Physical Chemistry*, 89(4):722–728, 1985.

[87] C. Turró, J. M. Zaleski, Y. M. Karabatsos, and D. G. Nocera. Bimolecular Electron Transfer in the Marcus Inverted Region. *Journal of the American Chemical Society*, 118(25):6060–6067, 1996.

[88] J. Ren, D. S. Achilleos, R. Golnak, H. Yuzawa, J. Xiao, M. Nagasaka, E. Reisner, and T. Petit. Uncovering the Charge Transfer between Carbon Dots and Water by In Situ Soft X-ray Absorption Spectroscopy. *The Journal of Physical Chemistry Letters*, 10(14):3843–3848, 2019.

[89] R. Berera, R. van Grondelle, and J. T. M. Kennis. Ultrafast transient absorption spectroscopy: principles and application to photosynthetic systems. *Photosynthesis Research*, 101:105–118, 2009.

[90] T. J. Miao and J. Tang. Characterization of charge carrier behavior in photocatalysis using transient absorption spectroscopy. *The Journal of Chemical Physics*, 152: 194201, 2020.

[91] Y. Zhu and J.-X. Cheng. Transient absorption microscopy: Technological innovations and applications in materials science and life science. *The Journal of Chemical Physics*, 152:020901, 2020.

[92] W. Yang, R. Godin, H. Kasap, B. Moss, Y. Dong, S. A. J. Hillman, L. Steier, E. Reisner, and J. R. Durrant. Electron Accumulation Induces Efficiency Bottleneck for Hydrogen Production in Carbon Nitride Photocatalysts. *Journal of the American Chemical Society*, 141(28):11219–11229, 2019.

[93] L. Li, R. Chen, X. Zhu, H. Wang, Y. Wang, Q. Liao, and D. Wang. Optofluidic Microreactors with TiO2 -Coated Fiberglass. *ACS Applied Materials & Interfaces*, 5 (23):12548–12553, 2013.

[94] D. Psaltis, S. R. Quake, and C. Yang. Developing optofluidic technology through the fusion of microfluidics and optics. *Nature*, 442:381–386, 2006.

[95] C. Monat, P. Domachuk, V. Jaouen, C. Grillet, I. Littler, M. Croning-Golomb, B. J. Eggleton, S. Mutzenich, T. Mahmud, G. Rosengarten, and A. Mitchell. Micron-scale tunability in photonic devices using microfluidics. In *Proceedings of the SPIE*, volume 6329, pages 1–12. International Society for Optics and Photonics, 2006.

[96] C. Monat, P. Domachuk, and B. J. Eggleton. Integrated optofluidics: A new river of light. *Nature Photonics*, 1(2):106–114, 2007.

[97] W. Yang, D. B. Conkey, B. Wu, D. Yin, A. R. Hawkins, and H. Schmidt. Atomic spectroscopy on a chip. *Nature Photonics*, 1(6):331–335, 2007.

[98] G. Testa, G. Persichetti, and R. Bernini. Liquid Core ARROW Waveguides: A Promising Photonic Structure for Integrated Optofluidic Microsensors. *Micromachines*, 7(47):1–19, 2016.

[99] P. Measor, L. Seballos, D. Yin, J. Z. Zhang, E. J. Lunt, A. R. Hawkins, and H. Schmidt. On-chip surface-enhanced Raman scattering detection using integrated liquid-core waveguides. *Applied Physics Letters*, 90:211107, 2007.

[100] C. Li, G. Bai, Y. Zhang, M. Zhang, and A. Jian. Optofluidics Refractometers. *Micromachines*, 9(3):136, 2018.

[101] M. Haque, K. K. C. Lee, S. Ho, L. A. Fernandes, and P. R. Herman. Chemical-assisted femtosecond laser writing of lab-in-fibers. *Lab Chip*, 14(19):3817–3829, 2014.

[102] N. Wang, F. Tan, Y. Zhao, C. C. Tsoi, X. Fan, W. Yu, and X. Zhang. Optofluidic UV-Vis spectrophotometer for online monitoring of photocatalytic reactions. *Scientific Reports*, 6(1):28928, 2016.

[103] X. Fan and I. M. White. Optofluidic microsystems for chemical and biological analysis. *Nature Photonics*, 5(10):591–597, 2011.

[104] T. Van Gerven, G. Mul, and J. Moulijn. A review of intensification of photocatalytic processes. *Chemical Engineering and Processing: Process Intensification*, 46(9):781–789, 2007.

[105] J. Kim, B. Jang, J. Gargiulo, J. Bürger, J. Zhao, S. Upendar, T. Weiss, S. A. Maier, and M. A. Schmidt. The Optofluidic Light Cage – On-Chip Integrated Spectroscopy Using an Antiresonance Hollow Core Waveguide. *Analytical Chemistry*, 93(2):752–760, 2021.

[106] C. Le, M. K. Wismer, Z.-C. Shi, R. Zhang, D. V. Conway, G. Li, P. Vachal, I. W. Davies, and D. W. C. MacMillan. A General Small-Scale Reactor To Enable Standardization and Acceleration of Photocatalytic Reactions. *ACS Central Science*, 3 (6):647–653, 2017.

[107] J. C. Knight. Photonic crystal fibres. *Nature*, 424(6950):847–851, 2003.

[108] J. E. Saunders, C. Sanders, H. Chen, and H.-P. Loock. Refractive indices of common solvents and solutions at 1550 nm. *Applied Optics*, 55(4):947, 2016.

[109] A. M. Cubillas, X. Jiang, T. G. Euser, N. Taccardi, B. J. M. Etzold, P. Wasserscheid, and P. S. J. Russell. Photochemistry in a soft-glass single-ring hollow-core photonic crystal fibre. *The Analyst*, 142(6):925–929, 2017.

[110] E. A. Marcatili and R. A. Schmeltzer. Hollow Metallic and Dielectric Waveguides for Long Distance Optical Transmission and Lasers. *Bell System Technical Journal*, 43(4):1783–1809, 1964.

[111] K. Kitayama. Light propagation in optical fibers. In *Optical Code Division Multiple Access*, chapter 3, pages 65–106. Cambridge University Press, Cambridge, 2014.

[112] A. R. Hawkins and H. Schmidt. *Handbook of optofluidics*. CRC Press, 1st edition, 2017. ISBN 9781138113602.

[113] W. M. Haynes. *CRC Handbook of Chemistry and Physics*. CRC Press, 96th edition, 2015. ISBN 9781482260977.

[114] P. Russell. Photonic Crystal Fibers. *Science*, 299(5605):358–362, 2003.

[115] F. Amrani, J. H. Osório, F. Delahaye, F. Giovanardi, L. Vincetti, B. Debord, F. Gérôme, and F. Benabid. Low-loss single-mode hybrid-lattice hollow-core photonic-crystal fibre. *Light: Science & Applications*, 10(1):7, 2021.

[116] A. M. Cubillas, M. Schmidt, T. G. Euser, N. Taccardi, S. Unterkofler, P. S. J. Russell, P. Wasserscheid, and B. J. M. Etzold. In Situ Heterogeneous Catalysis Monitoring in a Hollow-Core Photonic Crystal Fiber Microflow Reactor. *Advanced Materials Interfaces*, 1:1300093, 2014.

[117] M. Schmidt, A. M. Cubillas, N. Taccardi, T. G. Euser, T. Cremer, F. Maier, H.-P. Steinrück, P. S. J. Russell, P. Wasserscheid, and B. J. M. Etzold. Chemical and (Photo)-Catalytical Transformations in Photonic Crystal Fibers. *ChemCatChem*, 5 (3):641–650, 2013.

[118] F. Benabid and P. Roberts. Linear and nonlinear optical properties of hollow core photonic crystal fiber. *Journal of Modern Optics*, 58(2):87–124, 2011.

[119] A. M. Cubillas, S. Unterkofler, T. G. Euser, B. J. M. Etzold, A. C. Jones, P. J. Sadler, P. Wasserscheid, and P. S. Russell. Photonic crystal fibres for chemical sensing and photochemistry. *Chemical Society Reviews*, 42(22):8629–8648, 2013.

[120] J. D. Joannopoulos, S. G. Johnson, J. N. Winn, and R. D. Meade. *Photonic crystals: molding the flow of light*. Princeton University Press, second edition, 2008. ISBN 9780691124568.

[121] R. F. Cregan, B. J. Mangan, J. C. Knight, T. A. Birks, P. S. J. Russell, P. J. Roberts, and D. C. Allan. Single-Mode Photonic Band Gap Guidance of Light in Air. *Science*, 285(5433):1537–1539, 1999.

[122] C. Markos, J. C. Travers, A. Abdolvand, B. J. Eggleton, and O. Bang. Hybrid photonic-crystal fiber. *Reviews of Modern Physics*, 89(4):045003, 2017.

[123] B. Debord, A. Amsanpally, M. Chafer, A. Baz, M. Maurel, J. M. Blondy, E. Hugonnot, F. Scol, L. Vincetti, F. Gérôme, and F. Benabid. Ultralow transmission loss in inhibited-coupling guiding hollow fibers. *Optica*, 4(2):209, 2017.

[124] B. J. Mangan, L. Farr, A. Langford, P. J. Roberts, D. P. Williams, F. Couny, M. Lawman, M. Mason, S. Coupland, R. Flea, H. Sabert, T. A. Birks, J. C. Knight, and P. S. J. Russell. Low loss (1.7 dB/km) hollow core photonic bandgap fiber. In *Optical Fiber Communication Conference*, Los Angeles, 2004. Optical Society of America.

[125] F. Benabid, J. C. Knight, G. Antonopoulos, and P. S. J. Russell. Stimulated Raman Scattering in Hydrogen-Filled Hollow-Core Photonic Crystal Fiber. *Science*, 298 (5592):399–402, 2002.

[126] F. Couny, F. Benabid, and P. S. Light. Large-pitch kagome-structured hollow-core photonic crystal fiber. *Optics Letters*, 31(24):3574, 2006.

[127] M. Maurel, M. Chafer, A. Amsanpally, M. Adnan, F. Amrani, B. Debord, L. Vincetti, F. Gérôme, and F. Benabid. Optimized inhibited-coupling Kagome fibers at Yb-Nd:Yag (85 dB/km) and Ti:Sa (30 dB/km) ranges. *Optics Letters*, 43(7):1598, 2018.

[128] S. Février, B. Beaudou, and P. Viale. Understanding origin of loss in large pitch hollow-core photonic crystal fibers and their design simplification. *Optics Express*, 18(5):5142–5150, 2010.

[129] N. M. Litchinitser, A. K. Abeeluck, C. Headley, and B. J. Eggleton. Antiresonant reflecting photonic crystal optical waveguides. *Optics Letters*, 27(18):1592, 2002.

[130] J.-L. Archambault, R. Black, S. Lacroix, and J. Bures. Loss calculations for antiresonant waveguides. *Journal of Lightwave Technology*, 11(3):416–423, 1993.

[131] G. J. Pearce, G. S. Wiederhecker, C. G. Poulton, S. Burger, and P. St. J. Russell. Models for guidance in kagome-structured hollow-core photonic crystal fibres. *Optics Express*, 15(20):12680, 2007.

[132] M. A. Finger, N. Y. Joly, T. Weiss, and P. S. Russell. Accuracy of the capillary approximation for gas-filled kagomé-style photonic crystal fibers. *Optics Letters*, 39 (4):821, 2014.

[133] A. D. Pryamikov, A. S. Biriukov, A. F. Kosolapov, V. G. Plotnichenko, S. L. Semjonov, and E. M. Dianov. Demonstration of a waveguide regime for a silica hollow - core microstructured optical fiber with a negative curvature of the core boundary in the spectral region > 35 μm. *Optics Express*, 19(2):1441–1448, 2011.

[134] S.-f. Gao, Y.-y. Wang, X.-l. Liu, C. Hong, S. Gu, and P. Wang. Nodeless hollow-core fiber for the visible spectral range. *Optics Letters*, 42(1):61, 2017.

[135] S.-F. Gao, Y.-Y. Wang, W. Ding, D.-L. Jiang, S. Gu, X. Zhang, and P. Wang. Hollow-core conjoined-tube negative-curvature fibre with ultralow loss. *Nature Communications*, 9(1):2828, 2018.

[136] P. Uebel, M. C. Günendi, M. H. Frosz, G. Ahmed, N. N. Edavalath, J.-M. Ménard, and P. S. Russell. Broadband robustly single-mode hollow-core PCF by resonant filtering of higher-order modes. *Optics Letters*, 41(9):1961, 2016.

[137] F. Poletti. Nested antiresonant nodeless hollow core fiber. *Optics Express*, 22(20): 23807–23828, 2014.

[138] G. Antonopoulos, F. Benabid, T. A. Birks, D. M. Bird, J. C. Knight, P. J. St Russell, R. F. Cregan, B. J. Mangan, P. J. Roberts, and D. C. Allan. Experimental demonstration of the frequency shift of bandgaps in photonic crystal fibers due to refractive index scaling. *Optics Express*, 14(7):3000–3006, 2006.

[139] G. O. S. Williams, T. G. Euser, J. Arlt, P. S. Russell, and A. C. Jones. Taking Two-Photon Excitation to Exceptional Path-Lengths in Photonic Crystal Fiber. *ACS Photonics*, 1(9):790–793, 2014.

[140] J. S. Y. Chen, T. G. Euser, N. J. Farrer, P. J. Sadler, M. Scharrer, and P. S. J. Russell. Photochemistry in Photonic Crystal Fiber Nanoreactors. *Chemistry - A European Journal*, 16(19):5607–5612, 2010.

[141] A. Cubillas, M. Schmidt, M. Scharrer, T. G. Euser, B. Etzold, N. Taccardi, P. Wasserscheid, and P. S. Russell. Monitoring of catalytic reactions in photonic crystal fiber. In *2011 Conference on Lasers and Electro-Optics Europe and 12th European Quantum Electronics Conference (CLEO EUROPE/EQEC)*. IEEE, 2011. ISBN 978-1-4577-0533-5.

[142] T. G. Euser, G. Whyte, M. Scharrer, J. S. Y. Chen, A. Abdolvand, J. Nold, C. F. Kaminski, and P. S. J. Russell. Dynamic control of higher-order modes in hollow-core photonic crystal fibers. *Optics Express*, 16(22):17972, 2008.

[143] A. Ruskuc, P. Koehler, M. A. Weber, A. Andres-Arroyo, M. H. Frosz, P. S. Russell, and T. G. Euser. Excitation of higher-order modes in optofluidic photonic crystal fiber. *Optics Express*, 26(23):30245, 2018.

[144] C. Maurer, A. Jesacher, S. Bernet, and M. Ritsch-Marte. What spatial light modulators can do for optical microscopy. *Laser & Photonics Reviews*, 5(1):81–101, 2011.

[145] R. Brüning, Y. Zhang, M. McLaren, M. Duparré, and A. Forbes. Overlap relation between free-space Laguerre Gaussian modes and step-index fiber modes. *Journal of the Optical Society of America A*, 32(9):1678, 2015.

[146] V. A. J. M. Sleiffer, Y. Jung, N. K. Baddela, J. Surof, M. Kuschnerov, V. Veljanovski, J. R. Hayes, N. V. Wheeler, E. R. N. Fokoua, J. P. Wooler, D. R. Gray, N. H.-L. Wong, F. R. Parmigiani, S.-u. Alam, M. N. Petrovich, F. Poletti, D. J. Richardson, and H. de Waardt. High Capacity Mode-Division Multiplexed Optical Transmission in a Novel 37-cell Hollow-Core Photonic Bandgap Fiber. *Journal of Lightwave Technology*, 32(4):854–863, 2014.

[147] G. Epple, N. Y. Joly, T. G. Euser, P. St.J. Russell, and R. Löw. Effect of stray fields on Rydberg states in hollow-core PCF probed by higher-order modes. *Optics Letters*, 42(17):3271, 2017.

[148] O. A. Schmidt, T. G. Euser, and P. S. Russell. Mode-based microparticle conveyor belt in air-filled hollow-core photonic crystal fiber. *Optics Express*, 21(24):29383, 2013.

[149] J. W. Verhoeven. Glossary of terms used in photochemistry (IUPAC Recommendations 1996). *Pure and Applied Chemistry*, 68(12):2223–2286, 1996.

[150] K. P. L. Kuijpers, C. Bottecchia, D. Cambié, K. Drummen, N. J. König, and T. Noël. A Fully Automated Continuous-Flow Platform for Fluorescence Quenching Studies and Stern-Volmer Analysis. *Angewandte Chemie International Edition*, 57(35): 11278–11282, 2018.

[151] S. Bold, L. Zedler, Y. Zhang, J. Massin, V. Artero, M. Chavarot-Kerlidou, and B. Dietzek. Electron transfer in a covalent dye–cobalt catalyst assembly – a transient absorption spectroelectrochemistry perspective. *Chemical Communications*, 54(75): 10594–10597, 2018.

[152] S. Smolka, M. Barth, and O. Benson. Highly efficient fluorescence sensing with hollow core photonic crystal fibers. *Optics Express*, 15(20):12783, 2007.

[153] G. O. S. Williams, T. G. Euser, P. S. J. Russell, and A. C. Jones. Spectrofluorimetry with attomole sensitivity in photonic crystal fibres. *Methods and Applications in Fluorescence*, 1:015003, 2013.

[154] G. O. S. Williams, T. G. Euser, P. S. J. Russell, A. J. MacRobert, and A. C. Jones. Highly Sensitive Luminescence Detection of Photosensitized Singlet Oxygen within Photonic Crystal Fibers. *ChemPhotoChem*, 2(7):616–621, 2018.

[155] H. Rigneault and P. Berto. Tutorial: Coherent Raman light matter interaction processes. *APL Photonics*, 3(9):091101, 2018.

[156] D. Tuschel. Raman Thermometry. *Spectroscopy*, 31(12):8–13, 2016.

[157] M. Li, S. K. Cushing, and N. Wu. Plasmon-enhanced optical sensors: a review. *Analyst*, 140(2):386–406, 2015.

[158] W. R. Fenner, H. A. Hyatt, J. M. Kellam, and S. P. S. Porto. Raman cross section of some simple gases. *Journal of the Optical Society of America*, 63(1):73, 1973.

[159] F. Schorn, M. Aubermann, R. Zeltner, M. Haumann, and N. Y. Joly. Online Monitoring of Microscale Liquid-Phase Catalysis Using in-Fiber Raman Spectroscopy. *ACS Catalysis*, 11(11):6709–6714, 2021.

[160] S. Kasera, L. O. Herrmann, J. del Barrio, J. J. Baumberg, and O. A. Scherman. Quantitative multiplexing with nano-self-assemblies in SERS. *Scientific Reports*, 4 (1):6785, 2015.

[161] E. C. Le Ru, E. Blackie, M. Meyer, and P. G. Etchegoint. Surface enhanced raman scattering enhancement factors: A comprehensive study. *Journal of Physical Chemistry C*, 111(37):13794–13803, 2007.

[162] V. S. Tiwari, A. Khetani, M. Naji, and H. Anis. Study of surface enhanced Raman scattering (SERS) within hollow core photonic crystal fiber. In *2009 IEEE Sensors*, pages 367–370. IEEE, 2009. ISBN 978-1-4244-4548-6.

[163] V. S. Tiwari, A. Khetani, A. Momenpour, and H. Anis. Optimum size and volume of nanoparticles within hollow core photonic crystal fiber. *IEEE Journal on Selected Topics in Quantum Electronics*, 20(3), 2014.

[164] R. J. McQuitty, S. Unterkofler, T. G. Euser, P. S. Russell, and P. J. Sadler. Rapid screening of photoactivatable metallodrugs: photonic crystal fibre microflow reactor coupled to ESI mass spectrometry. *RSC Advances*, 7(59):37340–37348, 2017.

[165] S. Unterkofler, R. J. McQuitty, T. G. Euser, N. J. Farrer, P. J. Sadler, and P. S. Russell. Microfluidic integration of photonic crystal fibers for online photochemical reaction analysis. *Optics Letters*, 37(11):1952, 2012.

[166] R. Chen, L. Li, X. Zhu, H. Wang, Q. Liao, and M.-X. Zhang. Highly-durable optofluidic microreactor for photocatalytic water splitting. *Energy*, 83:797–804, 2015.

[167] C. W. Coley, M. Abolhasani, H. Lin, and K. F. Jensen. Material-Efficient Microfluidic Platform for Exploratory Studies of Visible-Light Photoredox Catalysis. *Angewandte Chemie International Edition*, 56(33):9847–9850, 2017.

[168] J. Parmar, S. Jang, L. Soler, D.-P. Kim, and S. Sánchez. Nano-photocatalysts in microfluidics, energy conversion and environmental applications. *Lab on a Chip*, 15 (15):2352–2356, 2015.

[169] N. Wang, F. Tan, L. Wan, M. Wu, and X. Zhang. Microfluidic reactors for visible-light photocatalytic water purification assisted with thermolysis. *Biomicrofluidics*, 8 (5):054122, 2014.

[170] M. J. Muñoz-Batista, M. M. Ballari, A. Kubacka, O. M. Alfano, and M. Fernández-García. Braiding kinetics and spectroscopy in photo-catalysis: the spectro-kinetic approach. *Chemical Society Reviews*, 48(2):637–682, 2019.

[171] J. Z. Bloh. A Holistic Approach to Model the Kinetics of Photocatalytic Reactions. *Frontiers in Chemistry*, 7:128, 2019.

[172] P. Koehler. *Optofluidic Microreactors for Advanced Photocatalysis*. PhD thesis, University of Cambridge, 2019.

[173] S. Unterkofler. *Optofluidic Photonic Crystal Fibres for Biomedical Research in fibra*. PhD thesis, University of Erlangen-Nuremberg, 2013.

[174] T. Wirth. *Microreactors in Organic Chemistry and Catalysis*. Wiley, Weinheim, 2nd edition, 2013. ISBN 978-3-527-33299-1.

[175] Y. Liu, M. M. Aziz, A. Shalini, C. D. Wright, and R. J. Hicken. Crystallization of Ge2Sb2Te5 films by amplified femtosecond optical pulses. *Journal of Applied Physics*, 112(12), 2012.

[176] P. Koehler, T. Lawson, J. Neises, J. Willkomm, B. C. M. Martindale, G. A. M. Hutton, D. Antón-García, A. Lage, A. S. Gentleman, M. H. Frosz, P. S. Russell, E. Reisner, and T. G. Euser. Optofluidic Photonic Crystal Fiber Microreactors for In Situ Studies of Carbon Nanodot-Driven Photoreduction. *Analytical Chemistry*, 93 (2):895–901, 2021.

[177] K. Mandal and M. Z. Hoffman. Quantum yield of formation of methylviologen radical cation in the photolysis of the Ru(bpy)32+/methylviologen/EDTA system. *The Journal of Physical Chemistry*, 88(23):5632–5639, 1984.

[178] Y. Deng. Developing a Langmuir-type excitation equilibrium equation to describe the effect of light intensity on the kinetics of the photocatalytic oxidation. *Chemical Engineering Journal*, 337:220–227, 2018.

[179] K. Tsukahara and R. G. Wilkins. Kinetics of reduction of eight viologens by dithionite ion. *Journal of the American Chemical Society*, 107(9):2632–2635, 1985.

[180] S.-I. Imabayashi, N. Kitamura, S. Tazuke, and K. Tokuda. The role of intramolecular association in the electrochemical reduction of viologen dimers and trimers. *Journal of Electroanalytical Chemistry and Interfacial Electrochemistry*, 243(1):143–160, 1988.

[181] A. Savitzky and M. J. E. Golay. Smoothing and Differentiation of Data by Simplified Least Squares Procedures. *Analytical Chemistry*, 36(8):1627–1639, 1964.

[182] A. B. Siddique, A. K. Pramanick, S. Chatterjee, and M. Ray. Amorphous Carbon Dots and their Remarkable Ability to Detect 2,4,6-Trinitrophenol. *Scientific Reports*, 8(1):9770, 2018.

[183] C. L. Bird and A. T. Kuhn. Electrochemistry of the viologens. *Chemical Society Reviews*, 10(1):49, 1981.

[184] K. J. Lee, N. Elgrishi, B. Kandemir, and J. L. Dempsey. Electrochemical and spectroscopic methods for evaluating molecular electrocatalysts. *Nature Reviews Chemistry*, 1(5):0039, 2017.

[185] N. Elgrishi, K. J. Rountree, B. D. McCarthy, E. S. Rountree, T. T. Eisenhart, and J. L. Dempsey. A Practical Beginner's Guide to Cyclic Voltammetry. *Journal of Chemical Education*, 95(2):197–206, 2018.

[186] N. Kandoth, J. Pérez Hernández, E. Palomares, and J. Lloret-Fillol. Mechanisms of photoredox catalysts: the role of optical spectroscopy. *Sustainable Energy & Fuels*, 5(3):638–665, 2021.

[187] A. Pougin, M. Dilla, and J. Strunk. Identification and exclusion of intermediates of photocatalytic CO2 reduction on TiO2 under conditions of highest purity. *Physical Chemistry Chemical Physics*, 18(16):10809–10817, 2016.

[188] C. Casadevall, V. Martin-Diaconescu, W. R. Browne, S. Fernández, F. Franco, N. Cabello, J. Benet-Buchholz, B. Lassalle-Kaiser, and J. Lloret-Fillol. Isolation of a Ru(iv) side-on peroxo intermediate in the water oxidation reaction. *Nature Chemistry*, 13 (8):800–804, 2021.

[189] R. Beck and S. A. Johnson. Mechanistic implications of an asymmetric intermediate in catalytic C–C coupling by a dinuclear nickel complex. *Chemical Communications*, 47(32):9233, 2011.

[190] G. Neri, J. J. Walsh, G. Teobaldi, P. M. Donaldson, and A. J. Cowan. Detection of catalytic intermediates at an electrode surface during carbon dioxide reduction by an earth-abundant catalyst. *Nature Catalysis*, 1(12):952–959, 2018.

[191] S. M. Sartor, Y. M. Lattke, B. G. McCarthy, G. M. Miyake, and N. H. Damrauer. Effects of Naphthyl Connectivity on the Photophysics of Compact Organic Charge-Transfer Photoredox Catalysts. *The Journal of Physical Chemistry A*, 123(22):4727–4736, 2019.

[192] C. A. Mesa, L. Francàs, K. R. Yang, P. Garrido-Barros, E. Pastor, Y. Ma, A. Kafizas, T. E. Rosser, M. T. Mayer, E. Reisner, M. Grätzel, V. S. Batista, and J. R. Durrant. Multihole water oxidation catalysis on haematite photoanodes revealed by operando spectroelectrochemistry and DFT. *Nature Chemistry*, 12(1):82–89, 2020.

[193] X. Zhang, K. Yamauchi, and K. Sakai. Earth-Abundant Photocatalytic CO2 Reduction by Multielectron Chargeable Cobalt Porphyrin Catalysts: High CO/H2 Selectivity in Water Based on Phase Mismatch in Frontier MO Association. *ACS Catalysis*, 11(16):10436–10449, 2021.

[194] B. M. Weckhuysen. Determining the active site in a catalytic process: Operando spectroscopy is more than a buzzword. *Physical Chemistry Chemical Physics*, 5(20): 4351, 2003.

[195] M. A. Bañares. Operando Spectroscopy: the Knowledge Bridge to Assessing Structure-Performance Relationships in Catalyst Nanoparticles. *Advanced Materials*, 23(44):5293–5301, 2011.

[196] I. L. C. Buurmans and B. M. Weckhuysen. Heterogeneities of individual catalyst particles in space and time as monitored by spectroscopy. *Nature Chemistry*, 4(11): 873–886, 2012.

[197] J. Dou, Z. Sun, A. A. Opalade, N. Wang, W. Fu, and F. F. Tao. Operando chemistry of catalyst surfaces during catalysis. *Chemical Society Reviews*, 46(7):2001–2027, 2017.

[198] D. Dolui, S. Khandelwal, P. Majumder, and A. Dutta. The odyssey of cobaloximes for catalytic H2 production and their recent revival with enzyme-inspired design. *Chemical Communications*, 56(59):8166–8181, 2020.

[199] B. H. Solis, Y. Yu, and S. Hammes-Schiffer. Effects of Ligand Modification and Protonation on Metal Oxime Hydrogen Evolution Electrocatalysts. *Inorganic Chemistry*, 52(12):6994–6999, 2013.

[200] A. Bhattacharjee, E. S. Andreiadis, M. Chavarot-Kerlidou, M. Fontecave, M. J. Field, and V. Artero. A Computational Study of the Mechanism of Hydrogen Evolution by Cobalt(Diimine-Dioxime) Catalysts. *Chemistry - A European Journal*, 19(45):15166–15174, 2013.

[201] N. Queyriaux, R. T. Jane, J. Massin, V. Artero, and M. Chavarot-Kerlidou. Recent developments in hydrogen evolving molecular cobalt(II)–polypyridyl catalysts. *Coordination Chemistry Reviews*, 304-305:3–19, 2015.

[202] W.-Q. Liu, T. Lei, S. Zhou, X.-L. Yang, J. Li, B. Chen, J. Sivaguru, C.-H. Tung, and L.-Z. Wu. Cobaloxime Catalysis: Selective Synthesis of Alkenylphosphine Oxides under Visible Light. *Journal of the American Chemical Society*, 141(35):13941–13947, 2019.

[203] M. Azhar, G. K. L. Wong, W. Chang, N. Y. Joly, and P. S. Russell. Raman-free nonlinear optical effects in high pressure gas-filled hollow core PCF. *Optics Express*, 21(4):4405, 2013.

[204] R. Sander. Compilation of Henry's law constants (version 4.0) for water as solvent. *Atmospheric Chemistry and Physics*, 15(8):4399–4981, 2015.

[205] F. Lakadamyali, A. Reynal, M. Kato, J. R. Durrant, and E. Reisner. Electron transfer in dye-sensitised semiconductors modified with molecular cobalt catalysts: Photoreduction of aqueous protons. *Chemistry - A European Journal*, 18(48):15464–15475, 2012.

[206] C. Lee, W. Yang, and R. G. Parr. Development of the Colle-Salvetti correlation-energy formula into a functional of the electron density. *Physical Review B*, 37(2): 785–789, 1988.

[207] A. D. Becke. Density-functional exchange-energy approximation with correct asymptotic behavior. *Physical Review A*, 38(6):3098–3100, 1988.

[208] A. D. Becke. Density-functional thermochemistry. III. The role of exact exchange. *The Journal of Chemical Physics*, 98(7):5648–5652, 1993.

[209] P. A. M. Dirac. Quantum mechanics of many-electron systems. *Proceedings of the Royal Society of London. Series A, Containing Papers of a Mathematical and Physical Character*, 123(792):714–733, 1929.

[210] J. Tao, J. P. Perdew, V. N. Staroverov, and G. E. Scuseria. Climbing the Density Functional Ladder: Nonempirical Meta–Generalized Gradient Approximation Designed for Molecules and Solids. *Physical Review Letters*, 91(14):146401, 2003.

[211] V. N. Staroverov, G. E. Scuseria, J. Tao, and J. P. Perdew. Comparative assessment of a new nonempirical density functional: Molecules and hydrogen-bonded complexes. *The Journal of Chemical Physics*, 119(23):12129–12137, 2003.

[212] F. Weigend and R. Ahlrichs. Balanced basis sets of split valence, triple zeta valence and quadruple zeta valence quality for H to Rn: Design and assessment of accuracy. *Physical Chemistry Chemical Physics*, 7(18):3297, 2005.

[213] F. Weigend. Accurate Coulomb-fitting basis sets for H to Rn. *Physical Chemistry Chemical Physics*, 8(9):1057, 2006.

[214] M. M. Francl, W. J. Pietro, W. J. Hehre, J. S. Binkley, M. S. Gordon, D. J. DeFrees, and J. A. Pople. Self-consistent molecular orbital methods. XXIII. A polarization-type basis set for second-row elements. *The Journal of Chemical Physics*, 77(7): 3654–3665, 1982.

[215] V. A. Rassolov, J. A. Pople, M. A. Ratner, and T. L. Windus. 6-31G * basis set for atoms K through Zn. *The Journal of Chemical Physics*, 109(4):1223–1229, 1998.

[216] W. J. Hehre, R. Ditchfield, and J. A. Pople. Self—Consistent Molecular Orbital Methods. XII. Further Extensions of Gaussian—Type Basis Sets for Use in Molecular Orbital Studies of Organic Molecules. *The Journal of Chemical Physics*, 56(5):2257–2261, 1972.

[217] V. Barone and M. Cossi. Quantum Calculation of Molecular Energies and Energy Gradients in Solution by a Conductor Solvent Model. *The Journal of Physical Chemistry A*, 102(11):1995–2001, 1998.

[218] F. Neese. The ORCA program system. *WIREs Computational Molecular Science*, 2 (1):73–78, 2012.

[219] T. Lazarides, T. McCormick, P. Du, G. Luo, B. Lindley, and R. Eisenberg. Making Hydrogen from Water Using a Homogeneous System Without Noble Metals. *Journal of the American Chemical Society*, 131(26):9192–9194, 2009.

[220] A. Panagiotopoulos, K. Ladomenou, D. Sun, V. Artero, and A. G. Coutsolelos. Photochemical hydrogen production and cobaloximes: The influence of the cobalt axial N-ligand on the system stability. *Dalton Transactions*, 45(15):6732–6738, 2016.

[221] A. Bachmeier, B. Siritanaratkul, and F. A. Armstrong. Enzymes as Exploratory Catalysts in Artificial Photosynthesis. In E. A. Rozhkova and K. Ariga, editors, *From Molecules to Materials*, pages 99–123. Springer International Publishing, Cham, 2015. ISBN 9783319138008.

[222] V. Balzani, G. Bergamini, and P. Ceroni. Photochemistry and photocatalysis. *Rendiconti Lincei 2016 28:1*, 28(1):125–142, 2016.

[223] A. Studer and D. P. Curran. Catalysis of Radical Reactions: A Radical Chemistry Perspective. *Angewandte Chemie International Edition*, 55(1):58–102, 2016.

[224] Q.-Q. Zhou, Y.-Q. Zou, L.-Q. Lu, and W.-J. Xiao. Visible-Light-Induced Organic Photochemical Reactions through Energy-Transfer Pathways. *Angewandte Chemie International Edition*, 58(6):1586–1604, 2019.

[225] N. A. Romero and D. A. Nicewicz. Organic Photoredox Catalysis. *Chemical Reviews*, 116(17):10075–10166, 2016.

[226] M. H. Gehlen. The centenary of the Stern-Volmer equation of fluorescence quenching: From the single line plot to the SV quenching map. *Journal of Photochemistry and Photobiology C: Photochemistry Reviews*, 42:100338, 2020.

[227] M. N. Hopkinson, A. Gómez-Suárez, M. Teders, B. Sahoo, and F. Glorius. Accelerated Discovery in Photocatalysis using a Mechanism-Based Screening Method. *Angewandte Chemie International Edition*, 55(13):4361–4366, 2016.

[228] A. S. H. Ryder, W. B. Cunningham, G. Ballantyne, T. Mules, A. G. Kinsella, J. Turner-Dore, C. M. Alder, L. J. Edwards, B. S. J. McKay, M. N. Grayson, and A. J. Cresswell. Photocatalytic a-Tertiary Amine Synthesis via C-H Alkylation of Unmasked Primary Amines. *Angewandte Chemie International Edition*, 59 (35):14986–14991, 2020.

[229] J. D. Grayson and A. J. Cresswell. γ-Amino phosphonates via the photocatalytic α-C–H alkylation of primary amines. *Tetrahedron*, 81:131896, 2021.

[230] S. Nad and H. Pal. Electron Transfer from Aromatic Amines to Excited Coumarin Dyes: Fluorescence Quenching and Picosecond Transient Absorption Studies. *The Journal of Physical Chemistry A*, 104(3):673–680, 2000.

[231] R. Ishimatsu, S. Matsunami, K. Shizu, C. Adachi, K. Nakano, and T. Imato. Solvent Effect on Thermally Activated Delayed Fluorescence by 1,2,3,5-Tetrakis(carbazol-9-yl)-4,6-dicyanobenzene. *The Journal of Physical Chemistry A*, 117(27):5607–5612, 2013.

[232] S. Engle, T. R. Kirkner, and C. B. Kelly. Preparation of 2,4,5,6-Tetra(9H-carbazol-9-yl)isophthalonitrile. *Organic Syntheses*, 96:455–473, 2019.

[233] J. Mooney and P. Kambhampati. Get the Basics Right: Jacobian Conversion of Wavelength and Energy Scales for Quantitative Analysis of Emission Spectra. *The Journal of Physical Chemistry Letters*, 4(19):3316–3318, 2013.

[234] M. Shee, S. S. Shah, and N. D. P. Singh. Photocatalytic Conversion of Benzyl Alcohols/Methyl Arenes to Aryl Nitriles via H-Abstraction by Azide Radical. *Chemistry – A European Journal*, 26(62):14070–14074, 2020.

[235] E. Pastor, F. Le Formal, M. T. Mayer, S. D. Tilley, L. Francàs, C. A. Mesa, M. Grätzel, and J. R. Durrant. Spectroelectrochemical analysis of the mechanism of (photo)electrochemical hydrogen evolution at a catalytic interface. *Nature Communications*, 8:14280, 2017.

[236] D. Koyama, H. J. A. Dale, and A. J. Orr-Ewing. Ultrafast Observation of a Photoredox Reaction Mechanism: Photoinitiation in Organocatalyzed Atom-Transfer Radical Polymerization. *Journal of the American Chemical Society*, 140(4):1285–1293, 2018.

[237] G. Porter. Flash photolysis and spectroscopy. A new method for the study of free radical reactions. *Proceedings of the Royal Society of London. Series A. Mathematical and Physical Sciences*, 200(1061):284–300, 1950.

[238] D. R. Prasad and M. Z. Hoffman. Charge-transfer complexation between methylviologen and sacrificial electron donors EDTA, triethanolamine, and cysteine. *Journal of Physical Chemistry*, 88(23):5660–5665, 1984.

[239] G. T. Reed and A. P. Knights. *Silicon Photonics: An Introduction.* John Wiley & Son Ltd, 2004. ISBN 0-470-87034-6.

[240] K. Okamoto. *Fundamentals of optical waveguides.* Elsevier/Academic Press, Burlington, 2nd edition, 2006. ISBN 9780125250962.

[241] D. Gloge. Weakly Guiding Fibers. *Applied Optics*, 10(10):2252–2258, 1971.

Appendix A

Derivation of waveguide equation

Propagation of light through a waveguide can be understood by considering Maxwell's equations and following the derivation of Reed *et al.*.[239]

$$\nabla \cdot \mathbf{D} = \rho \quad , \quad \nabla \cdot \mathbf{B} = 0 \quad , \quad \nabla \times \mathbf{E} = -\frac{\partial \mathbf{B}}{\partial t} \quad , \quad \nabla \times \mathbf{H} = \mathbf{J} + \frac{\partial \mathbf{D}}{\partial t} \tag{A.1}$$

where $\mathbf{D}$ is the electric flux density, $\mathbf{B}$ is the magnetic flux density, $\mathbf{E}$ is the electric field, $\mathbf{H}$ is the magnetic field, ρ is the charge density and $\mathbf{J}$ is the current density. For homogeneous and isotropic materials, these quantities are further related by

$$\mathbf{B} = \mu_r \mathbf{H} \quad , \quad \mathbf{D} = \epsilon_r \mathbf{E} \quad , \quad \mathbf{J} = \sigma \mathbf{E} \tag{A.2}$$

where μ_r is the relative magnetic permeability, ϵ_r is the relative electrical permittivity and σ is the conductivity of the material. For harmonic electromagnetic waves of the form $e^{i\omega t}$ with angular frequency ω

$$\nabla \times \mathbf{E} = -i\omega \mathbf{B} \tag{A.3}$$

$$\nabla \times \mathbf{H} = \mathbf{J} + i\omega \mathbf{D}. \tag{A.4}$$

Taking the curl of Equation A.3 and making appropriate substitutions gives

$$\nabla \times (\nabla \times \mathbf{E}) = -i\omega \mu_r (\sigma \mathbf{E} + i\omega \epsilon_r \mathbf{E}). \tag{A.5}$$

However for a dielectric, $\sigma \to 0$, and making further substitutions $\omega = ck_0$, $1/v^2 = \mu_r \epsilon_r$ and $c = nv$

$$\nabla \times (\nabla \times \mathbf{E}) - k_0^2 n^2 \mathbf{E} = 0. \tag{A.6}$$

where k_0 is the wavenumber in free space and n is the refractive index. Using the vector identity

$$\nabla \times (\nabla \times \mathbf{E}) = \nabla(\nabla \cdot \mathbf{E}) - \nabla^2 \mathbf{E} \tag{A.7}$$

and for wave propagation through dielectric without free electrons

$$\nabla \cdot \mathbf{E} = 0 \tag{A.8}$$

we arrive at the Helmholtz equation

$$\nabla^2 \mathbf{E} + k_0^2 n^2 \mathbf{E} = 0. \tag{A.9}$$

For an infinite two-dimensional waveguide, with solutions of the form $\mathbf{E} = \tilde{\mathbf{E}}(x,y)e^{-i\beta z}e^{i\omega t}$, this differential equation reduces to

$$\nabla_T^2 \mathbf{E} + [k_0^2 n^2(x,y) - \beta^2]\mathbf{E} = 0 \tag{A.10}$$

with ∇_T representing the transverse del operator and β representing the phase change per unit length in the z-direction. This can also be expressed as an eigenvalue equation[240]

$$\hat{\mathbf{O}}\,|\Psi\rangle = \beta^2\,|\Psi\rangle \qquad , \qquad \hat{\mathbf{O}} = \nabla_T^2 + k_0^2 n^2(x,y) \tag{A.11}$$

where $\mathbf{E} = |\Psi\rangle$. β is related to the effective modal index, N_{eff}, by

$$\beta = k_0 \cdot N_{\text{eff}} \tag{A.12}$$

Solutions to the Helmholtz equation correspond to the transverse modes, $|\Phi_e\rangle$, and corresponding eigenvalues, β_e^2, that can propagate through the waveguide. For optical fibres, it is useful to convert from a Cartesian basis to a cylindrical basis (r, ϕ, z), where in general we have radial symmetry such that the refractive index depends only on the radial coordinate, r, and not the azimuthal coordinate, ϕ. In such cases our differential equation is modified to

$$\frac{\partial^2 \Psi(r,\phi)}{\partial r^2} + \frac{1}{r}\frac{\partial \Psi(r,\phi)}{\partial r} + \frac{1}{r^2}\frac{\partial^2 \Psi(r,\phi)}{\partial \phi^2} + [k_0^2 n^2(r) - \beta^2]\Psi(r,\phi) = 0 \tag{A.13}$$

where

$$\Psi(r,\phi) = R(r)\Phi(\phi). \tag{A.14}$$

This can be simplified to

$$\frac{r^2}{R}\frac{d^2 R}{dr^2} + \frac{r}{R}\frac{dR}{dr} + r^2[k_0^2 n^2(r) - \beta^2] = -\frac{1}{\Psi}\frac{d^2\Phi}{d\phi^2} = l^2 \tag{A.15}$$

where $l \in N^+$ given that $\Phi(\phi)$ is 2π-periodic. Equations A.16 and A.17 below are the analytical solutions to Equation A.15, assuming a small refractive index contrast between the cladding and core (named the *weak guidance* condition).[240,241,145]

These solutions are the linearly polarised LP_{lm} modes (see Figure 2.10), where l and m represent the azimuthal and radial orders of the modes respectively. In typical step-index fibres, the refractive index of core and cladding materials differs by around a percent.[107]

$$\text{LP}_{lm} = \text{N}_{lm}\frac{\text{J}_l(\nu_{lm}\frac{r}{a})}{\text{J}_l(\nu_{lm})}e^{il\phi}e^{i\beta z}e^{-i\omega t} \qquad \text{for } r < a \tag{A.16}$$

$$\text{LP}_{lm} = \text{N}_{lm} \frac{\text{K}_l(\mu_{lm}\frac{r}{a})}{\text{K}_l(\mu_{lm})} e^{il\phi} e^{i\beta z} e^{-i\omega t} \qquad \text{for } r \geq a \qquad (\text{A}.17)$$

where N_{lm} is a normalisation constant, J_l is the lth-order Bessel function of the first kind, K_l is the lth-order modified Bessel function of the second kind and a is the core radius. For each LP_{lm} mode, there are two degenerate polarisation modes.

ν_{lm} is a normalized propagation constant of the core defined as

$$\nu_{lm} = a\sqrt{k_0^2 n_{core}^2 - \beta_{lm}^2} \qquad (\text{A}.18)$$

where n_{core} is the refractive index of the core and β_{lm} is the propagation constant of the LP_{lm} mode.[241] μ_{lm} is a normalized propagation constant of the cladding defined as

$$\mu_{lm} = a\sqrt{\beta_{lm}^2 - k_0^2 n_{clad}^2} \qquad (\text{A}.19)$$

where n_{clad} is the refractive index of the cladding and β_{lm} is the propagation constant of the LP_{lm} mode.[241]